

Universitat Politècnica de València
Programa de Doctorado en Ingeniería del Agua y
Medioambiental



**UNIVERSITAT
POLITÈCNICA
DE VALÈNCIA**

Ph.D. Thesis.

**Study and design of a sensor system for the
detection of illicit discharges in sewers and
water bodies**

Author

Javier Rocher Morant

Supervised by

Jaime Lloret Mauri
Jesús Mengual Cuquerella

Enero, 2023

Abstract

The use of water in our society is of great importance. This is used not only for human consumption but also for industrial and livestock activities. Once the water has been used and is no longer helpful for the activity, it becomes a waste called residual water. These waters contain substances that endanger human health and ecosystems. To reduce environmental damage, there are treatment plants that treat these waters to reduce their levels of contamination. We can find two types of sewage treatment plants, those that purify water from urban centres and industrial sewage treatment plants. Industrial treatment plants are responsible for reducing the contaminant load of the water so that it can be discharged into the public sewer system or into the environment.

The presence of illegal discharges and overflows in the sewage system pose a threat to water bodies. Illegal discharges occur when a company or person discharges a volume of water into the sewer without authorization. These discharges can cause a drop in the performance of the treatment plant, which will cause an effluent of poorer quality. On the other hand, overflows are generated when the sewer cannot carry all the water that enters and it is necessary to use the sewer overflows. Overflows can cause pollution of water bodies. In many cases, it is not possible to detect who is responsible for the spills. What makes these go unpunished violating the environmental principle of that whoever pollutes pays.

To solve this problem, the development of a low-cost system for monitoring water parameters to detect problems in sewers within the context of smart cities is proposed. Our working hypothesis is that in the presence of a discharge, the concentration of specific water parameters will change enough to be detected. When the site of the spill is detected, it will be possible to quickly go to the place in order to stop the spill in addition to taking the necessary legal actions against the person who is carrying out the spill.

For our system, we have compiled information on the different parameters that are incorporated into other systems to monitor sewage, such as water level, temperature, conductivity, turbidity and other water contaminants such as organic matter, nutrients, pH and heavy metals. With this information, we have determined that the most exciting parameters that we are able to measure at a low cost are temperature, conductivity, turbidity, water and oil level. In addition, the use of rain sensors for storm sewers is included.

To monitor these parameters, low-cost commercial sensors are chosen to monitor temperature, level and rainfall. For the other parameters, the low cost commercial options that currently exist are not helpful. That is why we decided to develop our own sensors. We decided to use inductive type sensors for conductivity and optical sensors for turbidity and oil control.

Regarding the inductive sensors, we have determined that there are interferences of the solids and the water level in the response of the sensor. We have verified that these two parameters have an effect on the response of the sensor. However, in the case of solids, this interference is minor in the concentration of solids that exists in the sewage system (0.078 V/gram). On the other hand, the amount of water does affect the response of the coil significantly. Therefore, the sensor must be submerged.

Regarding turbidity, we have made two different prototypes. One prototype has been developed for bodies of water and the other for sewage. The prototype developed for bodies of water is capable of determining the percentage of algae that exist in the water, knowing the amount of solids in the water. To determine the amount of solids, we use an algorithm that transforms the turbidity measurement to solids. Regarding the turbidimeter for sewage, we have tested with two similar turbidimeter prototypes with different coloured LEDs, an infrared LED and a photoreceptor at 0° and 180°.

For oil detection, we have developed another optical sensor. We have done tests at different heights of water. Seeing that we were able to identify if the oil came from a gasoline engine or a Diesel engine, and in the case of oil used by a gasoline engine, we were able to quantify it.

Finally, regarding our system, we have analyzed through simulations the usefulness of a level sensor in the sewage system. We have detected that in the case of storm sewage, this can be useful. In addition, we have tested the inductive sensor and the oil sensor in a pipe with different concentrations of salt and oil to see how they work.

Our system (sensor node) uses a microcontroller connected to different sensors. The estimated cost of each sensor node is 120 €. Our system will use a star type network topology. Where the different sensor nodes will send the information to a central point (cluster head). The cluster head will have Internet connection which allows the connection to a database placed in a server.

The developed sensors can be used in other environments. For this reason, we show other works carried out during the thesis period with the developed sensors. These works are: (I) The use of coils for soil moisture monitoring, (II) the use of optical sensors to detect diesel B (low tax) in unauthorized vehicles, (III) the use of sensors and bioabsorption technology in irrigation canals affected by wastewater, and (IV) the use of the oil sensor in irrigation canals.

Resumen

El uso del agua en nuestra sociedad es de gran importancia. Esta se utiliza no solo para el consumo humano sino también para actividades industriales y ganaderas. Una vez el agua se ha utilizado y deja de ser útil para la actividad, esta se convierte en un residuo llamado aguas residuales. Estas aguas contienen sustancias que ponen en peligro la salud humana y de los ecosistemas. Para reducir el daño medio ambiental existen las depuradoras que tratan estas aguas para reducir sus niveles de contaminación. Podemos encontrar dos tipos de depuradoras, las que depuran el agua de los núcleos urbanos y las depuradoras industriales. Las depuradoras industriales se encargan de reducir la carga contaminante del agua para que pueda ser vertida al alcantarillado público o al medio ambiente.

La presencia de vertidos ilegales y desbordamientos en el alcantarillado suponen una amenaza para las masas de agua. Los vertidos ilegales se producen cuando una empresa o persona vierte al alcantarillado un volumen de agua sin autorización. Estos vertidos pueden provocar una bajada en el rendimiento de la depuradora lo que provocará un efluente de peor calidad. Por otro lado, los desbordamientos se generan cuando el alcantarillado no puede transportar toda el agua que entra y es necesario utilizar los aliviaderos del alcantarillado. Los desbordamientos pueden provocar la contaminación de las masas de agua. En muchos casos no es posible detectar al responsable de los vertidos. Lo que hace que estos queden impunes violando el principio ambiental de quien contamina paga.

Para solucionar este problema se propone el desarrollo de un sistema de bajo coste para la monitorización de parámetros del agua para detectar problemas en los alcantarillados dentro del contexto de las ciudades inteligentes (Smart cities). La hipótesis de trabajo radica que ante la presencia de un vertido la concentración de ciertos parámetros del agua cambiará lo suficiente como para que pueda ser detectado. Al detectarse el sitio del vertido se podrá acudir rápidamente al lugar a fin de cesar el vertido además de tomar las acciones legales que sean necesarias contra la persona que está realizando el vertido.

Para el sistema hemos recopilado información sobre los diferentes parámetros que se incorporan en otros sistemas para monitorizar el alcantarillado como son el nivel de agua, temperatura, conductividad, turbidez, pH y de otros contaminantes del agua como son la materia orgánica, nutrientes y metales pesados. Con esta información se determina que los parámetros más interesantes y que pueden ser medidos con un bajo coste son temperatura, conductividad, turbidez, nivel de agua y aceite. Además, se incluye el uso de sensores de lluvia para el alcantarillado de pluviales.

Para la monitorización de estos parámetros se escogen sensores comerciales de bajo coste para la monitorización de la temperatura, el nivel y la lluvia. Para los otros parámetros las opciones de bajo coste comerciales que existen en la actualidad no son útiles. Por ello se decidió desarrollar nuestros propios sensores. Para ello se utilizó sensores del tipo inductivos para la conductividad y sensores ópticos para el control de la turbidez y el aceite.

Respecto a los sensores inductivos, se ha determinado que existen interferencias de los sólidos y del nivel de agua en la respuesta del sensor. Se ha comprobado que estos dos parámetros tienen un efecto en la respuesta del sensor. Sin embargo, en el caso de los sólidos esta interferencia es pequeña en la concentración de sólidos que existe en el alcantarillado, siendo esta de 0.078 V/gramo. En cambio, la cantidad de agua sí que afecta a la respuesta de la bobina de forma significativa. Por tanto, el sensor deberá estar sumergido.

Respecto a la turbidez se han realizado dos prototipos diferentes. Un prototipo ha sido desarrollado para cuerpos de agua y el otro para el alcantarillado. El prototipo desarrollado para cuerpos de agua es capaz de determinar el porcentaje de algas que existen en el agua conociendo la cantidad de sólidos en el agua. Para determinar la cantidad de sólidos utilizamos un algoritmo que transforma la medida de la turbidez a sólidos. Respecto al turbidímetro para alcantarillado hemos testeado con dos prototipos similares de turbidímetro con diferentes LEDs de colores, un LED infrarrojo y un fotoreceptor a 0° y 180°.

Para la detección del aceite hemos desarrollado otro sensor óptico. Hemos hecho pruebas a distintas alturas de agua. Viendo que éramos capaces de identificar si el aceite provenía de un motor gasolina o de un motor Diesel, y en el caso de aceite usado por un motor de gasolina éramos capaces de cuantificarlo.

Por último, respecto a nuestro sistema hemos analizado mediante simulaciones la utilidad de un sensor de nivel en el alcantarillado. Hemos detectado que en el caso de alcantarillado pluvial este sí que puede ser útil. Además, hemos testeado en una tubería el sensor inductivo y el de aceite con diferentes concentraciones de sal y aceite para ver su funcionamiento.

Para nuestro sistema utilizaremos un microcontrolador donde irán los diferentes sensores. El coste estimado de cada uno de los nodos sensores es de 120 €. Nuestro sistema utilizara una topología del tipo estrella, donde los diferentes nodos sensores enviaran la información a un punto central (cluster head) este tendrá conexión por internet al ordenador central.

Los sensores desarrollados pueden ser utilizados en otros ambientes. Por ello, mostramos otros trabajos realizados durante el periodo de la tesis con los sensores desarrollados. Estos trabajos son: (I) el uso de bobinas para la monitorización de la humedad del suelo, (II) el uso de sensores ópticos para detectar gasóleo B (bajo en impuestos) en vehículos no autorizados, (III) el uso de sensores y tecnología de bioabsorción en canales de riego afectados por aguas residuales y (IV) el uso del sensor de aceite en canales de riego.

Resum

L'ús de l'aigua a la nostra societat és de gran importància. Aquesta s'utilitza no sols per al consum humà, sinó també per a activitats industrials i ramaderes. Un cop l'aigua s'ha utilitzat i deixa de ser útil per a l'activitat, aquesta es converteix en un residu anomenat aigües residuals. Aquestes aigües contenen substàncies que posen en perill la salut humana i dels ecosistemes. Per reduir el danys mediambientals existeixen les depuradores que tracten aquestes aigües per reduir contaminació la seua carrega contaminants. Podem trobar-hi dos tipus de depuradores, les que depuren l'aigua de nuclis urbans i les depuradores industrials. Les depuradores industrials s'encarreguen de reduir la càrrega contaminant de l'aigua perquè es pugui abocar al clavegueram públic o al medi ambient.

La presència d'abocaments d'aigua il·legals i els desbordaments al clavegueram suposen una amenaça per a les masses d'aigua. Els abocaments il·legals es produeixen quan una empresa o una persona aboca al clavegueram un volum d'aigua sense autorització. Aquests abocaments poden provocar una baixada en el rendiment de la depuradora, lo que provocarà un efluent de pitjor qualitat. D'altra banda, els desbordaments es generen quan el clavegueram no pot transportar tota l'aigua que entra i cal utilitzar els sobreeixidors del clavegueram. Els desbordaments poden provocar la contaminació de les masses d'aigua. En molts casos no és possible detectar el responsable dels abocaments. Això fa que aquests queden impunes violant el principi ambiental de qui contamina paga.

Per solucionar aquest problema es proposa el desenvolupament d'un sistema de baix cost per a la monitorització de l'aigua per detectar problemes als claveguerams dins del context de les ciutats intel·ligents (Smart cities). La hipòtesi de treball consisteix que davant la presència d'un abocament la concentració de certs paràmetres de l'aigua canviarà lo suficient perquè es pugui detectar. En detectar-se el lloc de l'abocament es podrà acudir ràpidament al lloc per cessar l'abocament a més de prendre les accions legals que siguin necessàries contra la persona que està realitzat l'abocament.

Per al sistema hem recopilat informació sobre els diferents paràmetres que s'incorporen en altres sistemes per monitoritzar el clavegueram com són el nivell d'aigua, temperatura, conductivitat, pH, terbolesa i altres contaminants de l'aigua com són la matèria orgànica, nutrients, i metalls pesants. Amb aquesta informació s'ha determinat que els paràmetres més interessants i que poden ser mesurats amb un baix cost són temperatura, conductivitat, terbolesa, nivell d'aigua i oli. A més, s'hi inclou l'ús de sensors de pluja per al clavegueram de pluvials.

Per monitoritzar aquests paràmetres s'escullen sensors comercials de baix cost per monitoritzar la temperatura, el nivell i la pluja. Per als altres paràmetres, les opcions de baix cost comercials que hi ha actualment no són útils. Per això es decideix desenvolupar els nostres propis sensors. Decidim utilitzar sensors del tipus inductius per a la conductivitat i sensors òptics per al control de la terbolesa i l'oli.

Pel que fa als sensors inductius, s'ha determinat que hi ha interferències dels sòlids i del nivell d'aigua en la resposta del sensor. S'ha comprovat que aquests dos paràmetres tenen un efecte a la resposta del sensor. No obstant això, en el cas dels sòlids aquesta interferència és petita en la concentració de sòlids que hi ha al clavegueram, aquesta és de 0.078 V/gram. En canvi, la quantitat d'aigua sí que afecta la resposta de la bobina de manera significativa. Per tant, el sensor haurà d'estar submergit.

Pel que fa a la terbolesa s'han realitzat dos prototips diferents. Un prototip ha estat desenvolupat per a cossos d'aigua i l'altre per al clavegueram. El prototip desenvolupat per a cossos d'aigua és capaç de determinar el percentatge d'algues que hi ha a l'aigua coneixent la quantitat de sòlids a l'aigua. Per determinar la quantitat de sòlids utilitzem un algorisme que transforma la mesura de la terbolesa a sòlids. Pel que fa al turbidímetre per clavegueram hem testejat amb dos prototips similars de turbidímetre amb diferents LEDs de colors, un LED infraroig i un fotoreceptor a 0° i 180°.

Per detectar l'oli hem desenvolupat un altre sensor òptic. Hem fet proves a diferents alçades d'aigua. Veient que érem capaços d'identificar si l'oli provenia d'un motor benzina o d'un motor dièsel, i en el cas d'oli usat per un motor de benzina érem capaços de quantificar-lo.

Finalment, respecte al nostre sistema hem analitzat mitjançant simulacions la utilitat d'un sensor de nivell al clavegueram. Hem detectat que en el cas de clavegueram pluvial aquest sí que pot ser útil. A més, hem testejat en una canonada el sensor inductiu i el d'oli amb diferents concentracions de sal i oli per veure'n el funcionament.

Pel nostre sistema utilitzarem un microcontrolador on aniran els diferents sensors. El cost estimat de cadascun dels nodes sensors és de 120 €. El nostre sistema utilitzarà una topologia del tipus estrella, on els diferents nodes sensors enviaran la informació a un punt central (cluster head), aquest tindrà connexió per internet a l'ordinador central.

Els sensors desenvolupats poden ser utilitzats en altres ambients. Per això mostrem altres treballs realitzats durant el període de la tesi amb els sensors desenvolupats. Aquests treballs són: (I) L'ús de bobines per a la monitorització de la humitat del sòl, (II) l'ús de sensors òptics per detectar gasoil B (sota impostos) en vehicles no autoritzats, (III) l'ús de sensors i tecnologia de bioabsorció en canals de reg afectats per aigües residuals, (IV) l'ús del sensor d'oli a canals de reg.

Agradecimientos

Quiero agradecer a mis directores de tesis Jaime Lloret y Jesús Mengual por todo el apoyo en la realización de la escritura de esta tesis y todo el proceso que ha llevado a ello. En segundo lugar, dar las gracias a mis compañeros de laboratorio especialmente a Sandra Sendra, Lorena Parra, Daniel Basterrechea, Jose Miguel y Sandra Viciano por el apoyo que he recibido durante la realización de la tesis y por los buenos momentos que he vivido con ellos durante esta parte de mi vida.

No queriendo olvidar a mis padres y hermana que me han apoyado en toda mi vida y que me han puesto todos los recursos y cariño que tenían al alcance para que este donde actualmente estoy. Por último, nombrar a mis amigos que me han estado apoyando durante todo este tiempo. Especialmente a Hannah y Diego que me han ayudado en los momentos más bajos de esta etapa.

Gracias a todos, esta tesis ha podido salir adelante.

1.	Introduction.....	1
1.1.	Pollution incidents and overflows in sewerage.	3
1.2.	Analyser and sensor.....	5
1.3.	Water scarcity.....	6
1.4.	Smart Cities.....	6
1.5.	Objectives and hypothesis.....	8
1.5.1.	Hypothesis.....	8
1.5.2.	Research goals	9
1.5.3.	Requirements of system.	9
1.6.	Precedents.	11
1.7.	Structure.....	11
2	Related work.....	13
2.1	Wastewater cycle.....	14
2.2	Pollution of wastewater.....	16
2.3	Monitoring in sewerage and water bodies.....	18
2.3.1	Current systems for sewerage.....	18
2.3.2	Related work on water level sensors.....	21
2.3.3	Related work on temperature sensors.....	22
2.3.4	Related work on conductivity meters.....	23
2.3.5	Related work on sensors to measure total solids in water.	24
2.3.6	Related work on oil sensor.	27
2.3.7	Related work on Nutrients, organic matter, acidity and heavy metals.	29
2.4	Discussion and future challenges on sensors.	34
3	Coil inductivity based sensors.	38
3.1	General test bench.	39
3.2	Effect of solids in inductive sensors.	40
3.2.1	Material and methods.....	40
3.2.2	Results.....	41
3.3	Effect of water level.....	44
3.3.1	Difference between water and air.	44
3.3.2	Difference between different water levels.....	46
3.4	Conclusions.....	50
4	Turbidity Sensor.....	51

4.1	Turbidimeter to Eutrophication in water bodies.....	52
4.1.1	System Description.	52
4.1.2	Test Bench.....	54
4.1.3	Results.....	54
4.2	Determine solid. Effect on algae and sediment concentrations in mg/L in the turbidity (NTU).65	
4.2.1	Test Bench.....	65
4.2.2	Results.....	65
4.3	Turbidity Levels.	69
4.3.1	Proposal.....	69
4.3.2	Test Bench.....	73
4.3.3	Results.....	75
4.4	Improve the infrared sensor.....	86
4.4.1	Test Bench.....	86
4.4.2	Results.....	87
4.5	Conclusions.....	93
5	Oil sensor.....	95
5.1	Proposal.	96
5.1.1	Description of the Optical System.	96
5.1.2	Operational Algorithm.	97
5.2	Test Bench.....	97
5.2.1	Electronic Operation.	97
5.2.2	Sources of Oil.	98
5.2.3	Samples for Calibration and Verification.....	98
5.3	Results.....	99
5.3.1	Industrial Oil of Diesel Engine.	99
5.3.2	Industrial Oil of Gasoline Engine.	103
5.3.3	Verification.....	107
5.3.4	Discussion.	108
5.4	Conclusions.....	111
6	Practical deployment analysis.....	112
6.1	Scenarios in storm sewerage.	113
6.1.1	Algorithm.	113
6.1.2	Results.....	113
6.2	Water level, conductivity, and oil sensor.	115

6.2.1	Test bench.....	116
6.2.2	Results.....	119
6.2.3	Conclusions.....	130
7	Application in sewerage.....	132
7.1	Selection and Definition of Communication Technology.....	133
7.2	Topology.....	133
7.3	Algorithms.....	134
7.4	Cost of a sensor node.....	136
8	Application to other environments.....	138
8.1	Design and Calibration of Moisture Sensor-based on Electro-magnetic Field Measurement for Irrigation Monitoring.....	139
8.1.1	Test bench.....	139
8.1.2	Results.....	141
8.1.3	Verification.....	146
8.1.4	Overview and general discussion.....	147
8.2	IoT Sensor to Detect Fraudulent use of Dyed Fuels in Smart Cities.....	148
8.2.1	System description.....	148
8.2.2	Measurement and Results.....	151
8.3.	Sensors and Biosorption for Better Reuse of Wastewater.....	155
8.4.	Development of Optical Sensor to detect Industrial Oil in Agricultural Irrigation System.....	156
8.4.1.	Proposal.....	157
8.4.2.	Test Bench.....	158
8.4.3.	Results.....	159
8.5.	Conclusions.....	161
9	Conclusions.....	163
9.1	Conclusions.....	164
9.2	Future Work.....	164
9.3	Problems Faced and Personal Contributions.....	165
9.4	Publications derived from the PhD.....	165
	Reference.....	168

Figure 1.1. Simulation of solids' evolution throughout the day and the effect of two discharges.	9
Figure 2.1 Scheme of a sewerage network and WWTP.....	14
Figure 2.2. Schematic diagram of domestic wastewater treatment process.	16
Figure 3.1. Coiled direction and powered direction.....	39
Figure 3.2 Circuit coil used in the laboratory.	39
Figure 3.3 Operating scheme.....	40
Figure 3.4. Example of how the measurement is taken.....	40
Figure 3.5 Induced voltage results.....	41
Figure 3.6 Results of model m2.....	41
Figure 3.7. Complete circuit of our Low-cost sensor.....	43
Figure 3.8. Experimental setup.	45
Figure 3.9. Vout in the different depths.	45
Figure 3.10 Experimental test.....	46
Figure 3.11 Placement of the coil inside the tube.	46
Figure 3.12 Gathered data with P1 at different frequencies.	48
Figure 3.13. Gathered data with P2 at different frequencies.	48
Figure 3.14. Gathered data with P3 at different frequencies	48
Figure 3.15. Gathered data with P4 at different frequencies	48
Figure 3.16. Gathered data with P5 at different frequencies.	49
Figure 3.17. Gathered data with P6 at different frequencies	49
Figure 3.18. Gathered data with the different prototypes at its WF.....	49
Figure 3.19. Gathered data with P4 and the mathematical model.	50
Figure 4.1. Prototype of algae turbidimeter.....	53
Figure 4.2. Representation of the used prototype.	53
Figure 4.3. Measured resistance values for sediment.....	56
Figure 4.4. Measured resistance values for algae.	56
Figure 4.5. Measured resistance values for mixture 80% sediment and 20% algae.	56
Figure 4.6. Measured resistance values for mixture 60% sediment and 40% algae.	56
Figure 4.7. Measured resistance values for mixture 40% sediment and 60% algae.	56
Figure 4.8. Measured resistance values for mixture 20% sediment and 80% algae.	56
Figure 4.9. Observed versus predicted values of algae concentration with Equation 4.3.	58
Figure 4.10. Observed vs. predicted values of algae concentration with Eureka.	59
Figure 4.11. Observed vs. predicted values of algae concentration with a solid concentration of 15 mg/L.....	60
Figure 4.12. Observed vs. predicted values of algae concentration with a solid concentration of 50 mg/L.....	60
Figure 4.13. Observed vs. predicted values of algae concentration with a solid concentration of 200 mg/L.....	61
Figure 4.14. Observed vs. predicted values of algae concentration with a solid concentration of 500 mg/L.....	61
Figure 4.15. Observed vs predicted values of algae concentration with a solid concentration of 800 mg/L.....	61
Figure 4.16. Observed vs predicted values of algae concentration with a solid concentration of 1500 mg/L.....	62
Figure 4.17. Observed vs predicted values of algae concentration with a solid concentration of 4000 mg/L.....	62
Figure 4.18. Observed vs predicted values of algae concentration with different models.....	62
Figure 4.19. Prototype algorithm.....	63
Figure 4.20. Training and validation of neural network.....	64

Figure 4.21. NTU in the different concentrations of solids and % of sediments.....	66
Figure 4.22. Turbidity of samples with pure Algae and Sediment	66
Figure 4.23. NTU predicted versus NTU observed in Eureka models.....	68
Figure 4.24. Algorithm to calculate the solid concentration.	69
Figure 4.25. a) Picture of the prototypes; b) electronic scheme of a voltage divider.....	70
Figure 4.26. Operating principle.....	71
Figure 4.27. Connection diagram of our prototype.....	72
Figure 4.28 Proposal deployment	73
Figure 4.29. Tested samples.	74
Figure 4.30. Assembly.	74
Figure 4.31. Prototype 1, yellow LED, LDR 180°	76
Figure 4.32. Prototype 2, yellow LED, LDR 180°	76
Figure 4.33. Prototype 1, red LED, LDR 180°	76
Figure 4.34. Prototype 2, red LED, LDR 180°	76
Figure 4.35. Prototype 1, blue LED, LDR 180°	77
Figure 4.36. Prototype 2, blue LED, LDR 180°	77
Figure 4.37. Prototype 1, green LED, LDR 180°	77
Figure 4.38. Prototype 2, green LED, LDR 180°	77
Figure 4.39. Prototype 1, white LED, LDR 180°	78
Figure 4.40. Prototype 2, white LED, LDR 180°	78
Figure 4.41. Prototype 1, blue LED, LDR 0°	80
Figure 4.42. Prototype 2, blue LED, LDR 0°	80
Figure 4.43. Prototype 1, green LED, LDR 0°	80
Figure 4.44. Prototype 2, green LED, LDR 0°	80
Figure 4.45. Prototype 1, yellow LED, LDR 0°	81
Figure 4.46. Prototype 2, yellow LED, LDR 0°	81
Figure 4.47. Prototype 1, red LED, LDR 0°	82
Figure 4.48. Prototype 2, red LED, LDR 0°	82
Figure 4.49. Prototype 1, white LED, LDR 0°	82
Figure 4.50. Prototype 2, white LED, LDR 0°	82
Figure 4.51. Voltage in resistance photodiode at 180°.....	84
Figure 4.52. Voltage in resistance photodiode at 0°.....	84
Figure 4.53. Prototype 1 infrared LED	84
Figure 4.54. Prototype 2 infrared LED	84
Figure 4.55. Picture of the used samples.....	86
Figure 4.56. Prototype drawing.	87
Figure 4.57. Relation between solids and turbidity.....	88
Figure 4.58. Data obtained for different currents tested for the resistances from 10 to 220 kΩ..	89
Figure 4.59. Data obtained for different currents tested for the resistances from 680 to 8200 kΩ.	89
Figure 4.60. Calibration values of the tested configurations (Solids).....	90
Figure 4.61. Calibration values of the tested configurations (NTU).....	91
Figure 5.1. Sensor working diagram	96
Figure 5.2. Design prototype.....	97
Figure 5.3. Algorithm of oil detection.	97
Figure 5.4. Experimental tank with 0.03 mL _{oil} /cm ² from gasoline engine at 20 cm height.	99
Figure 5.5. Resistance of LDR at 0° in diesel oil in the yellow LED.	100
Figure 5.6. Resistance of the LDR at 0° in diesel oil in the red LED.	100
Figure 5.7. Resistance of the LDR at 0° in diesel oil in the blue LED.	100

Figure 5.8. Resistance of the LDR at 0° in diesel oil in green LED.	101
Figure 5.9. Resistance of the LDR at 0° in diesel oil in white LED.	101
Figure 5.10. Resistance of the LDR at 0° in gasoline oil in the yellow LED.	103
Figure 5.11. Resistance of the LDR at 0° in gasoline oil in red LED.	104
Figure 5.12 The mathematical model for the red light at 10 cm to oil using the gasoline engine.	104
Figure 5.13. The mathematical model for the red LED at 15 cm to oil using the gasoline engine.	105
Figure 5.14. The mathematical model for the red LED at 20 cm to oil using the gasoline engine.	105
Figure 5.15. Resistance in LDR at 0° in gasoline oil in blue LED.	106
Figure 5.16. Resistance in LDR at 0° in gasoline oil in green LED.	106
Figure 5.17. Resistance in LDR at 0° in gasoline oil in white LED.	107
Figure 5.18. Algorithm of the function of our sensor.	110
Figure 6.1. Algorithm for data processing.....	113
Figure 6.2. Normal scenario.	114
Figure 6.3. Blockage scenario	114
Figure 6.4. Low drainage	115
Figure 6.5. Illicit discharge.....	115
Figure 6.6. Hydraulic circuit.....	116
Figure 6.7. Map of the simulation section.....	118
Figure 6.8. Effect of the intensity and fixed resistance in the voltage divider in V_{out} differentiate.	120
Figure 6.9. V_{out} with the use of photodiode in the different oil concentrations.	121
Figure 6.10 Two models.....	122
Figure 6.11 V_{out} in the different oil concentrations whit the use of yellow, red, and blue lights.	123
Figure 6.12 V_{out} in the different oil concentrations whit the use of green, white, and infrared lights.....	124
Figure 6.13. Observed versus predicted concentration of oil in yellow light.	124
Figure 6.14. Observed versus predicted concentration of oil in infrared light in the two models.	125
Figure 6.15. Pipes affected by the different % of blockages and blockage positions.	127
Figure 6.16. Induced voltage in the different conductivities in the frequencies between 150 to 158 kHz.....	127
Figure 6.17. Induced voltage in the different conductivities in the frequencies between 159 to 165 kHz.....	128
Figure 6.18. Induced voltage in the different conductivities in the frequencies between 166 to 176 kHz	128
Figure 6.19. Induced voltage in the different conductivities in the frequencies between 177 to 180 kHz.....	128
Figure 6.20. REs of models	129
Figure 6.21. Summary of the % of RE in the calibration.	130
Figure 6.22. Summary of the % of RE in the verification.....	130
Figure 7.1. Network topologies.	133
Figure 7.2. Master Head algorithm.	135
Figure 7.3. Algorithm to wastewater sewerage.	135
Figure 8.1. Soils C1 to C4	140
Figure 8.2. The V_{out} in the different frequencies tested in the prototype NP1.....	142

Figure 8.3. The V_{out} of prototype NP1 frequency 750 kHz.	142
Figure 8.4. The V_{out} in the different frequencies tested in prototype NP2.....	143
Figure 8.5. V_{out} NP2, 490 kHz, two models (II) Equation 8.11 and 8.12 as mathematical model I and II respectively.	143
Figure 8.6. V_{out} NP2, 490 kHz, one model (I) Equation 8.4.....	143
Figure 8.7. V_{out} NP2, 500 kHz, two models (II) Equation 8.13 and 8.14 as mathematical model I and II respectively.	144
Figure 8.8. V_{out} NP2, 500 kHz one model (I) Equation 8.5.	144
Figure 8.9. The V_{out} in the different frequencies tested in prototype NP3.....	145
Figure 8.10. The V_{out} in the frequency of 760 kHz in prototype NP3.....	146
Figure 8.11. The V_{out} in the different frequencies tested in the prototype NP4.	146
Figure 8.12. General structure of the system.....	149
Figure 8.13. Proposed algorithm.....	150
Figure 8.14. Flow message conversation.	150
Figure 8.15. Light absorption by the samples.....	151
Figure 8.16. Experimental test.....	151
Figure 8.17. The resistance of LDR with different lights.....	152
Figure 8.18. The resistance of LDR with white light.....	152
Figure 8.19. The resistance of a photodiode with infrared light.....	153
Figure 8.20. Box plot resistance of LDR with blue light.	154
Figure 8.21.Box plot resistance of LDR with a green light.....	154
Figure 8.22. Box plot resistance of LDR with yellow light.....	154
Figure 8.23. Box plot resistance of LDR with white light.	155
Figure 8.24. Scheme of the proposed wastewater treatment system.....	156
Figure 8.25. Deployment of the sensors in the Irrigation channels for agriculture.....	158
Figure 8.26. Developed Algorithm.	158
Figure 8.27. Values of V_{out} of the LDR in the different LED colours.....	160
Figure 8.28. Voltage out of the different LEDs, groups classification with a confidence interval of 95% and standard deviation. (a) Yellow (b) Red (c) Blue (d) Green (e) White.	161

Table 3.1. Characteristics of the different coils.	42
Table 3.2. Errors in verification test.	43
Table 3.3. Prices of electronic components of our sensor.	44
Table 3.4 Developed prototypes.	44
Table 3.5 Characteristics of the prototypes.	47
Table 4.1. Dimensions of each section of the prototype.	53
Table 4.2. Characteristics of the LEDs of the prototype employed in these tests.....	53
Table 4.3. Multifactorial ANOVA for the LDR resistances in the different lights.....	55
Table 4.4. Mathematical and standard resistance to fixed resistance in the voltage divider.	57
Table 4.5. The precision of the analogy entry.	58
Table 4.6. Values of R^2	60
Table 4.7. Correctly classified cases in the training dataset.	64
Table 4.8. Correctly classified cases in the validation dataset.....	64
Table 4.9. Samples elaborated.....	65
Table 4.10. Absolute and REs of Eureqa models with NTU.....	67
Table 4.11. Absolute and REs of Eureqa models to determine solids.	69
Table 4.12. Prices of the main components.....	72
Table 4.13. Resistance in voltage divider in LDR top mathematical and standard.....	76
Table 4.14. Resistance in voltage divider in LDR down.....	79
Table 4.15. ANOVA height in LDR 0°	83
Table 4.16. Errors in the LDR 0°	85
Table 4.17. Solid concentrations of the samples used in the experiment.	86
Table 4.18. Values of resistance and intensity used in the led and the resistance in the photodiode.	87
Table 4.19. AEs statgraphics.	92
Table 4.20. REs statgraphics.	92
Table 4.21. AEs Eureqa.....	93
Table 4.22. REs Eureqa.....	93
Table 5.1. Multivariate analysis of variance for the height and concentration of diesel oil.....	102
Table 5.2. Multivariate analysis of variance for the height and concentration of gasoline oil. .	107
Table 5.3. Verification for the red LED.	108
Table 5.4. Maximum and minimum resistance measured when the two oils.	108
Table 6.1. Salt concentration used in calibration and verification.	117
Table 6.2. Oil concentration used in calibration and verification.	117
Table 6.3. Values of the artificial rain.....	118
Table 6.4. Values of length and heights of the different pipes.	119
Table 6.5 Values of R^2 , errors and range of the different equations.	121
Table 6.6. Values of resistance in the fixed resistance.....	122
Table 6.7. Range and errors.....	125
Table 7.1. Parameter algorithm represented in Figure 7.3.	136
Table 7.2. Cost of our sensor node.	137
Table 8.1. Features of the prototypes NP1 to NP4.....	139
Table 8.2. Mathematical models to prototype NP1 frequency 750 kHz.	142
Table 8.3. Values of R^2 and REs in NP2 (I) Without the first values before the trend reversal occurs.	144
Table 8.4. Values of R^2 and REs in NP2 (II) Using two models.	145
Table 8.5. Verification NP1, 750 kHz.....	147
Table 8.6 Verification NP2, 490 kHz, and 500 kHz one model.	147
Table 8.7. Verification NP2, 490 kHz, and 500 kHz two models.....	147

Table 8.8. Value of selected resistance for the different LEDs.	160
Table 8.9. Results of statistical ANOVA tests to analyse measured values.	160

Acronyms

ADC	Analog-to-Digital Converters
AE	Absolute Error
BOD	Biological Oxygen Demand.
C4D	Contactless Conductivity Detection
COD	Chemical Oxygen Demand
Diam	Diameter
DTS	Distributed Temperature Sensing
EF	Electromagnetic Field.
EPSAR	Entity for Wastewater Sanitation in the Valencian Community
GIS	Geographical Information System.
GPS	Global Position System
GSM	Global System for Mobile communications
HPLC	High Performance Liquid Chromatography
IC	Induced Coil
ICT	Information and Communication Technologies
IoT	Internet of Things
ISE	Ion-Selective Electrode.
LDR	Light-Dependent Resistor
LED	Light-Emitting Diode
MODIS	Moderate Resolution Imaging Spectroradiometer.
NTU	Nephelometric Turbidity Unit
ORP	Oxidation Reduction Potential.
PC	Powered Coil.
PI	Pollution Incidents
RE	Relative Error
RTD	Resistance Temperature Device
TH	Threshold
TKN	Total Kjeldahl Nitrogen
USA	United States of America
UWWTP	Urban Wastewater Treatment Plant
Vout	Voltage Output
Wc	Water Level Critical
Wd	Water Level Downstream
Wn	Water Level Now
WF	Working Frequency.
WSN	Wireless Sensor Network
WWTP	Wastewater Treatment Plant
CH	Cluster Head
PVC	Polyvinyl Chloride
TH	Threshold
TRL	Technology Readiness Level

1. Introduction.

In this PhD thesis, we propose a system to monitor the presence of pollutant incidents (PIs) in sewerage and water bodies that can receive untreated wastewater or PIs. In this chapter, we introduce the dissertation topic, the research goals, the precedents, and finally, the structure of the dissertation.

First, it is essential to remember the importance of water because life cannot exist without it. The first human civilisations begin near rivers. The Egyptians were in the Nile, Mesopotamia in Tigris and Euphrates, the Chinese in the yellow river or Indus Valley Civilisation in Indus and Ganges rivers. Thus, water is an indispensable resource for life (UNESCO, 2020). In addition, water is essential in many human activities such as food production, industry, street cleaning, etc. Humanity catches the water of the environment and uses it. After the water is used, it is dumped and considered waste. Thus, it is converted to wastewater. The wastewaters contain polluting substances that pollute the environment. To reduce wastewater pollution, Wastewater Treatment Plants (WWTP) are used. The producers of wastewater and the WWTP are connected by sewerage. The use of sewerage started in 3750 AC. However, the first modern sewerage was designed in Hamburgo in 1842. These infrastructures have been demonstrated to be a measure for reducing the mortality of the population (Alsan and Goldin, 2019), (Naja and Volesky, 2013). We can differentiate between two types of sewerage, separated and combined sewerage (Mannina and Viviani, 2009) (Zgheib, Moilleron and Chebbo, 2012). The difference between these two systems is the drainage of the rainwater. In the combined system, the runoff of rainwater (in urban areas) is collected in the same pipes as the wastewater. This water will go to a WWTP, where it will be treated. In the split systems, the wastewater and runoff go in separate pipes. In addition, in some sewerage-separated systems, domestic wastewater and industrial wastewater have different pipes. The wastewater will go to a WWTP, and the runoff will be poured into a body of water (river, lake, sea, etc.). The combined sewerage is typical of the centre of the cities by inheritance from the constructive methods of past eras. In the new areas of urban expansion, the separate sewage system is more common. The construction of separated sewerage is more expensive than combined sewerage because it is necessary to place two pipes. In separated sewerage, the rainwater is not treated in WWTP, which reduces the maintenance cost.

It is essential to keep water free of pollutants to continue using it. All water used by humans ends up in water bodies (lakes, seas, oceans, rivers, wetlands, etc.). Therefore, we must confirm that water gets to the water bodies as cleanly as possible. This is not an easy task to accomplish, considering the significant amount of water used every day in our society. Pollution comes from many places, from big companies which create tons of waste (Garrido et al. 2016) to the tiny house in which the owner uses soap with phosphates (Mousavi and Khodadoost, 2019). The most important aspect of waste treatment is controlling and accurately monitoring the pollutants. Knowing their origin site and the process through which they are treated is vital to correctly managing them. The astounding percentage of global wastewater which is released to the environment without treatment is 80 % (UNESCO, 2020). The percentage of untreated wastewater release changes in different areas of the world. This percentage is lower in rich countries than in developing countries because the rich countries have specific legislation to prevent pollution and more systems for collecting and treating wastewater. In Europe, wastewater is treated within the activity that has generated it until achieving sufficient quality to be discharged into the public sewer or to the environment (Directive 91/271/EEC). In America, the Clean Water Act regulates the discharge of pollutants into the waters and the standards of surface waters (Clean Water Act, 1972).

1.1. Pollution incidents and overflows in sewerage.

This subsection is focused on the PIs and overflows in the sewerage that affected the WWTP or water bodies. We analyse the problem and number of PIs and overflows that occur in some parts of the world. A PI can be spilt directly into the environment, generate a sewerage overflow or arrive at the WWTP. The overflows are generated when the sewerage cannot transport all the water that reaches it. A solution to reduce illicit dumping into the environment is increasing the control methods (Fujikura, 2011).

The Irish environmental protection agency defines PI in urban wastewater as: "I) any discharge that does not comply with the requirements of this licence or certificate; II) any incident with the potential for environmental contamination of surface water or groundwater, or posing an environmental threat to land, or requiring an emergency response by the relevant Water Services Authority." (EPA, 2021). The presence of illicit discharges in the wastewater can affect the water and sludge's biological and physical treatment of the WWTP (Purschke et al., 2020). In December 2016, the illegal disposal of high volumes of sulfuric acid affected the plant of Baarle-Nassau, Netherlands. The repairs cost between 80,000 and 100,000 euros. In addition, it affected the bioreactor and the capacity to depurate the wastewater (Chachuła, Nowak and Solano, 2021).

The PIs do not follow a determined spatial or time distribution. In the report of Toronto Water in 2018, the company detected 664 notices of violation of sewer by-law (Toronto Water, 2018). In the United Kingdom, the number of PIs were 2,204 in 2019, an increase from 1,863 in 2018 and 1,827 in 2017 (UK government, 2020). In the report by the Public Entity for Wastewater Sanitation in the Valencian Community (EPSAR), in 2018, there was 3,109 illegal PIs were detected in the sewerage of Valencia Community (Spain). Of which, in 559 PIS, the culprits were detected (EPSAR, 2018). In 2020, 3,239 PIS were detected, affecting 217 WWTP (44% of the WWTP in the region) (EPSAR, 2020). These numbers show that the presence of PIs is a severe environmental problem. It violates the environmental principle that the polluter pays. In the Valencia region in 2020, 49.7% of spills were detected in the WWTP entry, 34 % in the sewerage, and the rest in industrial parks or factories. In most of the incidents, the culprits were not detected. The main pollutions were conductivity, organic matter, biological inhibitors, nutrients, and postharvest products (EPSAR, 2020). In addition, the sewerages have a large size and are much branched, which makes it difficult to detect illegal discharges and illegal connections. For solving the problem of detected PIs and illicit connections in sewerage, a solution is the use of Wireless Sensor Networks (WSN) or analysers.

In addition, PIs are a critical problem in cities all over the world because they can cause problems in water bodies (Moreira and Bondelind, 2016). Historically, people have thrown their waste into the rivers to be washed down. Thus, it caused a handful of environmental issues in the surrounding area downstream. Nowadays, we have WWTPs, which process the sewage water so it can be returned to a water stream. They are designed to operate for a calculated range of flow and concentration of pollutants. Therefore, if there is an illegal discharge, the WWTP will be unable to completely process the water. Moreover, this is very important because if the water is not processed correctly, it will affect the ecosystem downstream (Ichinose and Yamamoto, 2011). These discharges contain pollutants such as nitrates, sulphates and, in the worst cases even heavy metals and other pernicious compounds. However, illicit discharge can be produced in the sewerage. Iloms et al. (2020) demonstrated that industrial discharge in the sewerage had a negative effect on the WWTP outflow in Vaal, South Africa. The detection of PIs in the sewerage is challenging. Sometimes, these are detected in the entry of the WWTP or in the sewer spillways (as we have seen with the previous data). Therefore, the bigger problem is not the pollution itself, it is the illicit discharges which are detrimental to the environment. WWTP are designed to work within established pollution thresholds (ONU, 2015). These thresholds are calculated taking into

account the size of the population the WWTP is catering to. They are not prepared for a sudden peak of pollution, which is what happens whenever there is an illegal discharge into the sewage system (Brown, Caraco and Pitt, 2004). When it happens, the water coming out of the WWTP is not fully treated, it still has pollutants. Therefore, that water is not safe to be released back into the environment. An illicit discharge could not only cause an isolated accident, some WWTP use processes done by bacteria. Pollutant levels higher than the threshold could disrupt the ecosystem created for those bacteria, thus causing a significant problem for the WWTP treatment process. There have been some attempts to create frameworks for the management of these discharges (Aulinas et al. 2012).

Nowadays, the most used techniques for the detection of these illicit discharges involve the detection before they reach the WWTP. Early detection in sewage or in storm drains is the best regarded method. In order to identify an illicit discharge, several techniques can be employed. They can be divided in four groups: (i) sensory methods, (ii) temperature, (iii) chemical parameters, and (iv) microbiological parameters (Panasiuk et al., 2015). Among those different approaches, both temperature and microbiological parameters are non-conservative parameters. Moreover, microbiological parameters techniques are still under development. Furthermore, chemical parameters can be expensive to measure. Sensory methods, as well as temperature, are low-cost options. The disadvantage sensory methods present is difficulty in detecting low concentrations of pollutants. Among some unusual methods which have been proposed for the tracking of illicit discharges is scent detection by dogs in storm drains (Van De Werfhorst et al. 2014).

Another problem in sewerage is overflows. An overflow is produced when a sewage network receives more water than can be transported to the WWTP, and the excess water is dumped into spillways. The sewerage networks have overflow channels at different points of distribution for dumping the excess water. These channels are located in the upper bound of the pipeline. Excess water discharge is usually produced in water bodies or ravines. The overflows can be produced by broken pipes, runoff rainwater, lack of power, failure in pumps, and pipeline blockage (EPA, 2003). In addition, an overflow can be produced in the WWTP. If a WWTP receives more wastewater than can be treated, the excess water is dumped. The problem with the overflows is that untreated or partially treated wastewater is dumped into the environment. Overflow problems are common in all sewerage networks. In 2020, there were 14,625 overflows in combined sewerage caused by rains in the United Kingdom. (UK Government, 2020). In the basin of the great lakes in the United States of America (USA), 1,482 overflows were produced (EPA, 2016). In the city of San Diego (USA), the maximum number of spills occurred in 2000, with 365 spills. In the following years, spills were reduced to 41 in 2010, 36 in 2020, and 42 in 2021 (Sandiego, 2021). In the Congaree river (USA), 168 overflows were produced, resulting in more than 1,387,000 gallons (5250 m³) of sewage spilt in 2020 (Congaree riverkeeper, 2020). The pollution problems of overflows do not only occur in combined sewerage. In storm events in separate sewerage, the wastewater can enter into the storm sewerage, if combined sewerage is connected to separate sewerage. Xu, Yin and Li (2014) studied the non-stormwater in storm drains in the city of Shanghai. They concluded that 51% of water was an inappropriate entry of sewage flow into the storm drains. However, different studies have been showing high contamination levels in the runoff rainwater in the separate sewerage. In addition, the presence of illicit connections or wastewater pipes that are discharged in the rainwater is hazardous to water bodies because the water is not treated. To reduce overflow numbers, the water infrastructures must be improved. Nevertheless, the overflows cannot be obliterated by sewerage. However, their environmental effects can be reduced by monitoring water bodies that receive the overflows.

1.2. Analyser and sensor.

In situ monitoring is a tool to control water quality. In this section, we present the two technologies used for continuous monitoring (analysers and sensors). Cambridge dictionary defines an analyser as "a person, machine, or device that examines something in detail to discover exactly what it is or consists of." In the same dictionary, a sensor is "a device that is used to record that something is present or that there are changes in something" (Cambridge University Press, 2022). In the past, laboratory techniques were used to monitor the environment. Nowadays, laboratory analyses are still used but have been reduced using sensors and analysers. Laboratory analyses provide more accurate and reliable values than sensors and analysers. Nevertheless, laboratory analyses are expensive because they require one person to take the samples and procure an external laboratory (Zhang, 2016). Though, there are currently parameters such as emerging contaminants, the determination of solids, pesticides, etc., requiring laboratories.

On the one hand, the analysers are like a small laboratory. It is performed the different steps of an analytic method autonomously. The analysers take a sample and add the different reagents to the sample. Subsequently, the analyser measures some parameters of the sample to determine the concentration of the parameter to be analysed. On the other hand, a sensor is a device that responds to a change in the environment. The sensors use the physical properties of the sample (absorbance, electric conductivity, capacitance, irradiation, fluorescence, etc.) or the change of material properties (change of Young's modulus, dilation, substance filter, ability to provide electrons, etc.) or a combination of both to determine the parameter that we want to monitor. Different sensors and analysers have been developed in the last years. In general, the use of sensors is preferable to analysers, because analysers need the use of reagents and management of the chemical residues generated in the measure. However, any parameter cannot be measured with sensors. Thus, it is necessary the use of analysers. The data collected by these devices is saved internally. These data can be downloaded when the responsible person goes to where the device is located or transmits them wirelessly or wired. The use of wireless technologies has given rise to WSN.

The WSNs are formed by different nodes. Each node is formed by the sensing unit (sensors), a processing unit (microcontroller), and a transmitter/receiver unit (antenna). In addition, the WSNs have an operative system for the nodes and a communication protocol (Jondhale, Maheswar and Lloret, 2022). The use of WSNs has grown in recent years. The use of sensors in underwater condition has been studied previously. The monitoring of water needs knowledge of different parameters. All types of substances can be discharged into the sewerage. For this reason, it is essential to determine the types of industries in an area for selecting the sensors that we will install.

The use of sensors is currently widespread in most of our daily tasks. The application field of sensor is vast, and we can find many sensors-based applications in agriculture, industry processes environment monitoring our e-health, among others (Rawat et al. 2013). The WSNs allow us to follow the real-time evolution of some parameters. With this information, we can take the corrective measures that are necessary or check that everything works correctly.

Nevertheless, the maintenance cost of the sensors can difficult their use in some areas, i.e., if the manufacturing cost of these devices is too high, the monitoring of large areas can be costly. For this reason, there is an increased tendency to develop low cost and low maintenance sensors. Some low cost sensors have been developed for monitoring turbidity (Murphy et al. 2015) or conductivity (Parra, 2014), etc. In this sense, chemical sensors are not recommended for implementing this kind of systems since they require continuous maintenance. Thus, the use of physical sensors is the best option for long-term monitoring.

1.3. Water scarcity.

The PIs affect the available water, because they affect the water quality causing that water to become unusable or increasing its purification costs. Water deficit is one of the most significant problems of nowadays. The exploitation of water resources combined with climate change are precursors of this delicate situation (Gosling and Arnell, 2013). The reuse of purified wastewater is a measure to reduce water scarcity. Now, the reuse of purified wastewater is more commoner in arid or semiarid regions than in humidity regions, because of the humid regions, there are more available water. However, global warming decreases the water available. Therefore, the reuse of wastewater is expected to increase (Verstraete and Vlaeminck, 2011).

Nowadays, four billion people suffer scarcity of water at least one month a year (Mekonnen and Hoekstra, 2016). Approximately 65-70% of fresh water is for agricultural purposes (CDC, 2019). Water is a relatively scarce resource because only 1% of the water in the world is suitable for human consumption and accessible (NASA, 2022). Therefore, its use should be rational and avoid its waste. In cities, water is used for human consumption, irrigation of green areas, ornamental use, cleaning of roads and other uses. One of the sources of fresh water is sub-aquatic water and its protection is vital. The result of excessive water consumption has produced a depletion of groundwater (Wada et al. 2010). Depletion also causes seawater intrusion in coastal areas (Werner et al., 2013). The seawater intrusion affects negatively the water quality because it increases the amount of salt in the water. This negatively affects the irrigation of the fields and can turn the water unfit for human consumption. In addition, we must not forget the use of water in agriculture. It may seem that agriculture is far away from cities. However, it is this that provides the food that is used by cities. Finally, you must control the use of water in green areas. Because although they have an ornamental function has been shown that their presence improves the quality of life of people (Lee and Maheswaran, 2010). Different methodologies have been developed to reduce water use in agriculture. Some of them are: drip irrigation, the use of sensors, reduce the amount of irrigation water, reuse of wastewater, etc. The use of technology, methodology of watering, and study of the variability in crops is englobed in the definition of precision farming.

The quality of water also plays a significant role when it comes to using water to irrigate. In most areas, the water quality is enough to be used for irrigation, but in other places, especially in third world countries or in the process of development, water is not suitable for irrigation due to its high content of pollutants. In Europe, a multitude of projects have been carried out for the reuse of wastewater

Reusing purified wastewater can present risks, such as microorganisms and toxic substances affecting soil, groundwater or food production. For this reason, it is essential to control wastewater reuse and improve WWTP (Ungureanu, Vlăduț and Voicu, 2020). Kirhensteine et al. (2016) studied the different key barriers that difficult the reuse wastewater. (I) Water reuse is more complicated than freshwater use, (II) the price of the water reuse, (III) the perception of the reused wastewater is riskier than freshwater and (IV) the difficulty of selling the food products. The presence of PIs in sewerage that arrives at WWTP affects the quality of the effluent. Therefore it will affect the quality of these waters for reuse.

1.4. Smart Cities.

Currently, there is an increase in the population, which will cause an increase in the demand for resources. This together with the rural exodus generate that the environmental impacts are concentrated in urban areas. It is expected that the population in cities in 2050 will be 6 billion (70% of the world population) (Jin et al. 2014). To face the challenges of the future is necessary the rational use of resources. Therefore, the cities have an important challenge in the management of resources. In this ambit, the cities adopt policies for reducing the use of resources. These policies are grouped into the current of smart cities (Perera et al., 2013) (Hancke, Silva and

Hancke, 2012) (Chourabi et al., 2012). This concept has developed in recent years by different authors and institutions. According to the European Commission, "A smart city is a place where traditional networks and services are made more efficient with the use of digital solutions for the benefit of its inhabitants and business " (European Commission, 2019). Therefore, a smart city must have Information and Communication Technologies (ICT) solutions. The history of smart cities started in late 1960 in Los Angeles using computational statistical analysis. With ICT improvement, more cities have developed plans to become smart cities in recent years. In this process, companies have an essential role. An example is Cisco Systems, which launched its Connected Urban Development program in partnership with San Francisco, Amsterdam, and Seoul with \$25 million from the Clinton foundation in 2006. Therefore, the main purpose of a Smart City is to increase its sustainability through digitisation. It is essential to highlight that sustainability is not only from an environmental point of view. It includes human and economic factors. One of the purposes of smart cities is the increased quality of life of its citizens (Neirotti et al. 2014). Thus, daily problems must be solved or minimised like traffic, air and water pollution, excessive energy consumption, noise, and others. Finally, the cities have the challenge of managing the natural resources that are in their proximity and that the city uses to meet the needs of its inhabitants.

One pillar of smart cities is the Internet of Things (IoT). The IoT is a type of WSN where different objects are connected to Internet. There are different definitions of IoT. However, the majority of authors agree that IoT is based on different objects (smartphones, headphones, washing machines, lamps, wearable devices, etc.) that are connected to Internet and can receive and send information (Berte, 2018).

IoT devices can monitor many parameters of cities, improving citizens' quality of life and avoiding wasting resources (Jin et al. 2014). The usefulness of a smart WSN has been widely proven (Siregar et al., 2018). Many resources were used to develop different technological systems that allow rapid and safe control of the other media that affect cities, such as water channels, lakes, water purification, discharge control, air pollution, light pollution, e-health, traffic, and others. The use of sensors and the communication and monitoring of these are essential to control these environments. IoT is used in smart cities to monitor the environment and improve decision performance. Examples are the use of noise sensors to establish noise maps Liu et al. (2020), e-health devices to improve the health of the people (Rathee, Ahuja and Hailu, 2019), control of the quality of drinking water, control and prevention of forestal fires (Lloret et al. 2009), etc.

The IoT devices have a microcontroller or microprocessor, which is in charge of obtaining the reading of the sensors and controlling their turn on. Microprocessors have more RAM, flash memory, and computing power than microcontrollers. However, microcontrollers are cheaper than microprocessors (Microsoft, 2021). The selection of one of them will depend on the calculation needs. IoT projects generally use microprocessors that send data to Internet, where a device with more power computation proceeds to perform the analysis. One problem with IoT devices is energy consumption. In some cases, these devices are powered by batteries. This implies that their energy consumption must be reduced to reduce energy costs. Different solutions are proposed to reduce the energy use of these devices (Mehmood et al. 2020).

Smart cities are the future of urban development. However, nowadays, present important gaps that need to be solved.

- (I) Smart City requires a considerable investment of capital.
- (II) There is an increase in dependence on technological services and new technologies.
- (III) There are still groups that are reluctant to use new technologies or do not feel comfortable.
- (IV) An increase in housing prices prevents the young's access to housing.

The integration of technologies in Smart cities can help to detect illegal dumps. This proves to be highly beneficial for the citizens, who have more available information, as well as better

services. The services for smart cities do not only benefit the population directly using an app but also provide energy efficiency and environmental management. Both factors affect the lives of the citizens, as well as the planet. A good smart city would be one that covers not only the citizens' primary necessities but also the environmental ones.

As the world is becoming more and more technologically advanced, it is becoming more polluted as well. New products lead to new contaminants and more waste. The industrialisation of cities has always been associated with a higher pollution level. Human activities generate different types of waste, which can be classified into solids, liquids, and gases. The global trend is to increase productivity to move the economy forward. Many times, the underlying consequence of said development is a deterioration of the environmental quality (Cao, You and Liu, 2017). This is a price which has been paid in the past. Nevertheless, it is one we should strive towards never paying again. Not if we want the world to be as it has been so far.

1.5. Objectives and hypothesis.

This subsection presents the hypothesis that we use to develop the PhD thesis, the objectives, and the requirements of the system that we develop.

1.5.1. Hypothesis.

This dissertation starts from the point that it is possible to detect the presence of a PI in the sewerage or spillway with low-cost techniques and detect pollution in water bodies that can receive wastewater. The purpose is to prevent possible damage to the WWTP and the environment. In addition, detect the culprits to take the appropriate legal measures.

In Figure 1.1, we show a simulation of the evolution of the concentration of a pollutant in wastewater (solids) and what happens in the case of two spills. The pollutant concentration at night is less than during the day. It is from 5:00 hours that you begin to see a rise in the concentration of pollutants until noon. In midday, there is a small drop in the pollutant concentration until mid-afternoon. From this time, there is a constant drop until the next day. In the case of a discharge, this can be more, less, or the same concentration as the wastewater. With the monitoring of different parameters, the probability that the discharge concentration is the same as wastewater is reduced. The sensor will detect a change in wastewater concentrations in the other two cases. To discard the change in the concentration due to daily fluctuations, the values must be sent to a central node where the values will be compared with the historical series and the values of other nearby sensors. With this information, it is possible to detect the presence of a spill.

In the case of a water body, the concentration of a substance is more constant. However, with an illicit discharge, overflow, or other problem, a change in the concentration of a pollutant is produced. Therefore, with a sensor system capable of continuous monitoring, we will be able to detect it.

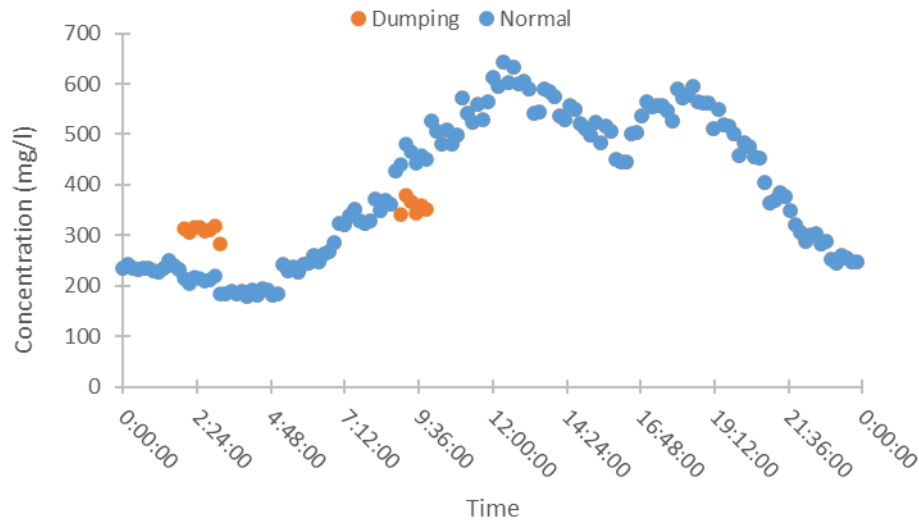


Figure 1.1. Simulation of solids' evolution throughout the day and the effect of two discharges.

1.5.2. Research goals

In this subsection, we present the objectives of the PhD. The main objective is to develop a WSN to detect PIs in sewerage and water bodies. The goals that have been accomplished are shown following:

- Selecting the water parameters present in PIs can be monitored with our system.
 - Determine the main pollutants that are present in PI.
 - Reviewing the techniques used to monitor the pollutants that are in PI.
 - Selecting the techniques that can be used in our system.
 - Searching commercial sensors that accomplish the requisites of our proposal.
- Developing the sensors capable of measuring the water parameters, and there are no viable commercial options.
 - Test the different configurations of the prototype sensor.
 - Obtain the mathematical equations related to pollutant concentration with the sensor's response.
 - Verify the sensor with measures not included in the calibration.
- Creating an algorithm to generate the alarms in case a PI is located in a pipe or water body.
 - Develop the algorithm for nodes located in water bodies.
 - Develop the algorithm for nodes located in storm sewerage.
 - Develop the algorithm for nodes located in combined or wastewater sewerage.

Besides, some of the developed sensors can be implemented in other environments. Thus, some applications of the sensors in other environments, such as agriculture and WWTP, are studied.

1.5.3. Requirements of system.

In this section, we analyse the characteristics that should have the sensors in the WSNs proposed for monitoring the sewerage. Some requirements are similar to the ones presented in other articles. Like the ones presented by (Parra, 2018a) for aquaculture (Sha, Shi and Watkins,

2006) for fire rescue for transportation systems (Khanafer, Guennoun and Mouftah, 2009) and Li et al. (2017) for wastewater. The different characteristics are:

- I. Low cost. An essential parameter for the development of a WSN is the budget. The sewerage in the cities and industrial parks has many kilometres. If we pretend to detect PI, we should use many sensor nodes. It should be at a low cost to ensure the system's economic viability.
- II. Not having moving parts or being that easily clogged. The wastewaters have many materials that can be introduced into the sensors. These materials include wet wipes, oils, food rest, etc. These substances cause problems of blockage in the pipes. Significantly, the wet wipes cause critical blockage in the pipelines of the cities. If our system has mobility or small diameter parts where the water runs, these will clog and stop working. These parts are widespread in the analysers when the system collects a water sample and adds reaction agents. For this reason, using analysers is not recommended in monitoring sewerage on a significant scale. In addition, corrosion is another problem in the underwater system. Corrosion can cause the break of moving parts.
- III. Energy consumption. The sensor nodes are in the sewerage. In many cases, we need uses of battery because we do not have access to the electrical grid or we cannot use alternative energy fonts (solar panels, wind power, etc.). The battery is used for functioning the sensor and sending the data. Many protocols have been developed for reducing the sensors' energy use. Send the data in an alarm situation and one or two times a day. In a system for the sewerage, we recommend that sensors send an alarm in abnormal situation when the user demand information or at determined moments in the day. For this reason, the nodes must have a save system.
- IV. Fault tolerance. The WSN can be composed of different sensor nodes. To save energy, the motes do not send the information directly to the data manager but to a central node that sends the data. In case of failure, the network must be ready to solve it (Parra, 2018b). Depending on the distance between sensors, the sensor nodes send the data directly from the cloud or a central sensor node to the cloud.
- V. Real-time monitoring. The dumping can be produced anytime (especially in untimely hours). Therefore, the sensors must function every time. The time between one reading and another cannot be high. The user should determine this interval. When the interval is smaller, the probability of detecting dumping increases. However, energy demands increase. If we increase, the interval of measuring the opposite happens.

1.6. Precedents.

The idea of creating a system to detect pollutant incidents in sewerage started in 2016. That year, I started my external practices in the WWTP of Gandia (Spain). In the period that I was in the WWTP, different pollutant incidents affected the water purification process. After verifying that the only solution was to file a complaint and that it was a problem that affected more areas, the PhD thesis project was started with my two directors.

To develop a system to monitor the sewerage, it is necessary to use low cost sensors. On the one hand, the director Jaime Lloret is the director of the PhD "Deployment of Efficient Wireless Sensor Nodes for Monitoring in Rural, Indoor and Underwater Environments", where the PhD student developed low cost sensors to monitor the environment (Sendra Compte, 2013). Next to this work, a PhD thesis about using low-cost sensors to monitor aquaculture farms was defended in 2018 (Parra, 2018a). On the other hand, the director Jesus Mengual is an expert in the water cycle with different publications about reducing phosphorus in the water. The two directors have differentiated professional profiles, which causes some positive synergies between both directors for the development of the dissertation.

In this PhD thesis, different sensors have been developed to detect pollutant incidents in the sewerage and the water bodies susceptible to receiving the dumping of crude or purified wastewater. However, the sensors developed can be used in other environments and applications, as demonstrated in the publication of other works unrelated to this PhD thesis.

The following projects and grants partially supported this dissertation:

- “Generalitat Valenciana” through the “Subvencions per a la contractació de personal investigador de caràcter predoctoral (ACIF) (Convocatoria 2017)”. Grant number ACIF/2017/069
- “Ministerio de Educación, Cultura y Deporte”, through the “Ayudas para contratación predoctoral de Formación del Profesorado Universitario FPU (Convocatoria 2016)”. Grant number FPU16/05540.
- European Union through the "ERANETMED (Euromediterranean Cooperation through ERANET joint activities and beyond)" project ERANETMED3-227 SMARTWATIR
- “Ministerio de ciencia e Innovación” Red Heterogenea Inteligente de Sensores Inalambricos para Monitorizar y Estimar el Contenido de Resina de Cistus Ladanifer (PID2020-114467RR-C33)

1.7. Structure.

In this subsection, we show the structure of the thesis.

Chapter 2 presents the wastewater cycle, the main pollutants of wastewater, and the state of art of monitoring the different pollutants of wastewater. It is essential to know the techniques used to monitor the pollutants to adapt them to a low-cost system if there is no low-cost technology for the said parameter. First, we study the technology used nowadays in sewerage. Then we analyze the parameters that can be measured, such as water level, temperature, nutrients, solids, oil, etc. Once we have analyzed and determined the parameters that we want our system to have, we will begin to develop the sensors that must be necessary.

In Chapter 3, we analyze the use of coil inductivity sensors to determine water conductivity. First, it is essential to determine if this type of sensor is affected by other parameters apart from

conductivity. Thus, we test using inductive coils to monitor other parameters. We determine the effect of solid concentration and water level on the induced voltage of this type of sensor.

In Chapter 4, we analyze the turbidity sensor. We develop two different turbidimeters. One is used in water bodies, and the other is used for sewerage. On the one hand, The turbidimeter to water bodies can determine turbidity and differentiate between turbidity caused by solids and algae. This allows us to determine if we are in a body of water that can suffer eutrophication. On the other hand, for the turbidimeter to sewerage, we study the effect of the water height in the measure of turbidity in our sensor.

Then, in chapter 5, we show a new oil sensor based on the optical properties of the oil. For the experiments, we use oil used. In the first experiment, we use used oil from a gasoline engine, and the sensor is located down the sample with oil. In the second experiment, we test with two oils obtained from a diesel and a gasoline engine. The used oil is black if it comes from a diesel engine instead. If it comes from a gasoline engine is black with a brown tonality. Our experiments demonstrated that it could be differentiated between the used oil of a gasoline engine and to diesel engine. In addition, the concentration can be quantified in the gasoline engine's used oil.

In Chapter 6, tests with used oil and inductive sensors in a pipe are shown. We install the sensors of oil and conductivity in a pipe to check the sensor function. In addition, we check the use of water level sensors to detect problems in sewerage. We use simulation software to determine if the water level sensor is valid.

In Chapter 7, we study the different existing topologies to determine the best one for our system. In addition, we have also studied the cost of the sensor nodes.

Chapter 8 presents other work that we developed in the course of this dissertation and that may be of interest to other fields of study. These works are (I) the use of inductive sensors to monitor the moisture in the soil, (II) the use of an optical sensor to detect dyed fuels (low tax) in particular vehicles, (III) a proposal to combine absorption and WSN to reduce the pollution in irrigation channels and (IV) the use of oil sensor in irrigation channels.

Finally, Chapter 9 presents the conclusions, the publications derived from this thesis, the future work, and the fulfilment of the objectives and difficulties found during the process.

2 Related work.

This dissertation proposes a system to detect PIs in sewerage and the effects of wastewater overflows in the environment. To develop our system, first, we need to know the theoretical framework of the current systems proposed for sewerage, the pollutants present in wastewater, and the existing sensors we can use for our proposed system.

This chapter, first explains the wastewater cycle in section 2.1. The main pollutants present in sewerage are shown in section 2.2. Section 2.3 analyses the sensors and systems used in sewerage and water bodies. Finally, section 2.4 presents a discussion and our main conclusions about the already existing systems and sensors. We also determine which sensors or methods are helpful to our proposal.

2.1 Wastewater cycle.

Wastewater is generated in houses, commercial locals, and industries and transported to the WWTP through sewerage networks. The sewerage networks have two main functions preventing flooding by rainwater in urban areas and the connection between human buildings and WWTP. The wastewater treatment capacity in a WWTP is limited and usually cannot be increased easily. When a WWTP is built, this considers the future volume increases in wastewater. Simulation software allows the calculation of the maximum volume and quality of wastewater that WWTP can treat. Mikosz, (2014) used a computer simulation to estimate the maximum pollution load a WWTP could treat. This was done calculating the relationship between required biomass concentration and Chemical Oxygen Demand (COD) load as a function of process temperature. Depending on the temperature range, a range of biomass volumes which could be treated was calculated. For this reason, the presence of PIs are harmful to the WWTP as they can exceed the design capacity and cause a loss of effluent quality.

Figure 2.1 represents the connection between the neighbourhood and the WWTP. The main problems in the sewerage are overflow, the presence of illegal spills, PIs, and blockages. In the following subsections, we analyse the overflow in the sewerage and the presence of illicit spills. A pollution increase of wastewater can produce that WWTP cannot achieve the quality objectives in the effluent. In addition, the presence of toxins can affect the WWTP's biological treatments. In the worst case, the toxins can kill the bioreactor performing the WWTP unable to function properly for months.

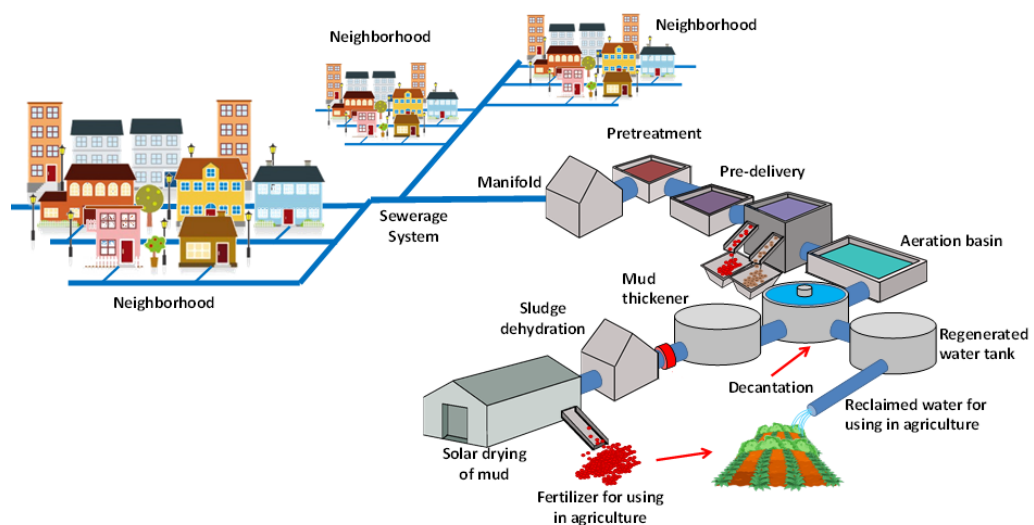


Figure 2.1 Scheme of a sewerage network and WWTP.

The wastewater that reaches the WWTPs remains in these plants between 24 and 48 hours. They must receive treatments for taking advantage of and recovering these waters. Treatments receiving wastewater depend on the size of the WWTP. There are usually two lines, the water line and the sludge line. On the one hand, the purpose of the sludge line is to treat the sludge obtained by decanting the wastewater in the primary and secondary sedimentation tanks. On the other hand, the water line's objective is reducing water pollution and can be divided into preliminary, primary, secondary, and tertiary treatments. Now, we describe the different processes used in the WWTPs to purify wastewater. Each WWTP is different in Figure 2.2, the schematic of a typical WWTP is presented. Therefore, not all the processes described here are present in all WWTPs. Preliminary treatments are used to protect the machinery of the WWTP and adequate the wastewater to the posterior treatments. The first pretreatment is screening. This is based on bars and sieves systems to protect the pipes and machinery from the impact of great solids (such as rocks) and abrasion. After the bars and sieves are located the grit removal. Grit removal eliminates the sands and other big solids that were not previously removed. In addition, if the grit removal is big enough (hydraulic retention times greater than 20 minutes), the oil and fats can be removed from the wastewater. Finally, as the wastewater volume entry in the WWTP is not uniform, some WWTPs have an equalization tank to store excess water during rush hours. This allows better control of the processes that are carried out below. When preliminary treatment is finished, the primary treatment is performed. In primary treatment, the wastewater is stored in large tanks called clarifiers (primary clarifiers). In clarifiers, the separation between solids and water is produced. In these tanks, solids settle to the bottom, from where they will be transported to the sludge line. To improve the sedimentation, some WWTP add chemicals to the water (flocculants and coagulants) that group the solids causing them to increase their sedimentability. Chemical addition can be produced before or after the primary and secondary clarifier or in a clarifier at the final water line. At the end of the primary clarifier, start the secondary treatment. This treatment consists of the use of microorganisms to reduce pollution. The wastewater passes to large rafts (bioreactors) populated by different microorganisms that feed organic remains and nutrients. The organisms can be mixed in the water or fixed on a surface. When organisms are mixed with wastewater, the water is constantly mixed to prevent the sedimentation of the solids. Biological treatment can be anoxic, anaerobic, aerobic, or a combination of them. After the bioreactor, there are clarifiers or a filtration system. The filters are usually found after the clarifiers and are often used to reuse the water in agriculture, and industries or spill in sensible areas. A part of the sludge obtained at the bottom of secondary clarifiers is recirculated to the bioreactor to maintain the concentration of solids (microorganisms). The tertiary treatments consist of sand filters, chemical adsorption, or other processes to increase the water's quality. Finally, the water can be disinfected by ultraviolet light (UV) or chlorine. With all these processes, water is obtained to be suitable for discharge into the environment, making possible to reuse it in agriculture or industrial processes. About the sludge line, the sludge extracted from the clarifiers goes to the sludge line. The sludges have a significant percentage of biodegradable solids. Before the sludge leaves the WWTP, the sludge must stabilisation. The stabilisation can be biological or chemical. Biological stabilisation uses aerobic or anaerobic reactors for it. In the anaerobic process, the sludge is thickened before the anaerobic reactor. In the aerobic process, the thickening process can be produced before or after the aerobic reactor or does not exist. Chemical stabilisation uses chemicals such as Calcium oxide (CaO) to increase the pH of sludge and inert it. Finally, there are mechanical dehydration or drying eras (in small WWTP). The dehydrated sludge can be used on farms as fertiliser, compost, industry process, etc. (EPA, 2004), (Oconomowoc, 2012), (Cole-Parmer, 2021), (Ferrer Polo and Seco Torrecillas, 2007), (Hegab et al., 2018).

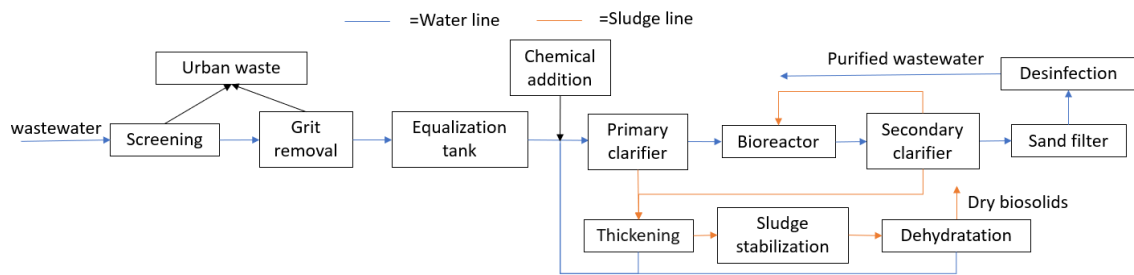


Figure 2.2. Schematic diagram of domestic wastewater treatment process.

2.2 Pollution of wastewater

The main domestic sewage pollutants are solids, organic matter, nutrients, oils and grease, acidity, microorganism, emergent contaminants, and chlorides (Marcos Von Sperling, 2007) (Barnstable County, 2015).

We can divide the solids between suspended or dissolved solids and volatile or not volatile solids. Volatile solids are considered organic compounds, and not volatile solids are mineral compounds, inert or not oxidisable matter. The organic matter is divided into biodegradable and no biodegradable. COD and Biological Oxygen Demand (BOD) are used to measure organic matter. The COD is the quantity of oxygen required to oxidise all the organic matter. The BOD is the quantity of oxygen that requires the organism to degrade the biodegradable organic matter. The difference between volatile solids and COD is the units. Volatile solids are expressed as mg/L, and COD is expressed as mgO₂/l. The solids have effects on WWTP and water bodies. In WWTP, 50% to 70% of solids are sedimented in the primary decanted. The decanted solids (sludge) are digested in aerobic or anaerobic within the sludge stabilisation process (in some plants, there is chemical stabilisation). The solids with no sediment arrive at the biological reactor and are digested if they are biodegradable. However, if the solids are not biodegradable, these will escape through the plant's effluent or sediment in the clarifiers. In water bodies, the presence of solids generates a turbidity increase. This increase causes a reduction of light that arrives at the bottom. That causes the death of vegetation. This supposes a decrease in the oxygen of the water for two reasons: (I) plants no longer generate oxygen, and (II) the aerobic digestion of dead plants. The increase in solids also affects animals. The solids can cause damage to their tissues in addition to making it difficult to hunt other species due to loss of vision.

Organic matter will affect processes depending on whether it is in particulate or dissolved form. In the case of particulate organic matter, this involved the process that we described as we describe in the solids. The biodegradable organic matter in aerobic digestion (bioreactor and aerobic sludge stabilisation) increases oxygen demand. If the WWTP cannot provide enough oxygen, the reactors can enter anoxic or anaerobic conditions, which can cause problems with purifying performance, sedimentation in secondary clarifiers, odours, etc. In addition, in the bioreactors, even if enough oxygen is supplied, sedimentation problems can appear by the proliferation of filamentous bacteria. In anaerobic reactors, the effect of an increase in biodegradable organic matter is not noteworthy. As long as its design capacity is not exceeded and the relationship between nutrients and organic matter is not modified. Currently, some WWTP organic pollutants are injected into the anaerobic reactor as a source of extra income for the plant. In water bodies, organic matter can cause anoxia or anaerobic processes in the water or the sediments.

Like organic matter, nutrients can be in particulate or dissolved form. The presence of organic nitrogen, ammonia, and ammonium Total Kjeldahl Nitrogen (TKN) increases the oxygen demand in aerobic digestion in WWTP and water bodies, because TKN is oxidised by the microorganisms and transformed into nitrate and nitrite (to a lesser extent) by the nitrification process. The nitrate and nitrite cause the rising sludge by forming nitrogen gas in the lower parts

of the WWTP clarifiers. Another effect of WWTP is the contamination of the anaerobic areas of the biological reactor. The phosphorus in the WWTP can unbalance biological processes in biological reactors, leading to unwanted microorganisms' appearance. In water bodies, the most critical problem of nutrients is the generation of eutrophication blooms that cause a reduction of biological diversity, anoxic and anaerobic conditions, the presence of toxins, etc.

Nowadays, there are few studies about emerging pollutants' effects on WWTP. Deblonde, Cossu-Leguille and Hartemann, (2011) review the emerging pollutants in wastewater and show that most cases eliminate these between the influent and effluent of the WWTP. However, in some cases, such as Fenofibric acid, the concentration increases by 148 %. This indicates that these emerging contaminants interact with microorganisms and therefore can affect the plant's performance. In the water bodies, the presence of emergent pollutants is associated with maturing problems in animals, the birth of more males than females (and vice versa) for certain species, the intoxication of the waters due to pesticides, etc.

Finally, heavy metals are substances that are toxic to the organism. The presence of these metals in WWTP and water bodies affects the development of living beings. In WWTPs, this means a reduction in contaminant removal performance. In water bodies, it implies a loss of biodiversity, in addition to the fact that these metals are introduced into food chains, affecting the health of the nearby ecosystem.

The purification of wastewater is produced in WWTP. The most critical process in the depuration is in the biological reactors. The typical performance of an active sludge is $97 \pm 1\%$ for BOD, $93 \pm 1\%$ for COD, and $24 \pm 7\%$ for nitrogen (Ignatev and Tuhkanen, 2019). The biological removal of nitrogen in the active sludge increases the elimination by 85%. However, other systems, such as Anammox or denitrification after the secondary clarifier, can increase nitrogen elimination (McCarty, 2018). However, these systems are not common in Urban Wastewater Treatment Plant (UWWTP). The elimination of solids depends on the technology used. With the use of secondary clarifiers, the performance is $94\% \pm 2\%$ in the elimination of solids regarding an average concentration of 27 mg/L (Hegazy and Gawad, 2016). The option of using filters reduces the solid concentration in the effluent to values near 5 mg/L. Another nutrient is phosphorus. The concentration of this can be reduced with the use of biological removal. However, this reduction is not enough to accomplish the discharge values in sensitive areas. The use of physical chemical treatment is needed. The performance of these depends on the components of the water, the use of filters in the water line, and the chemicals used. Another critical group of pollutants in WWTP is heavy metals. The microorganism in the bioreactor and physical chemical treatments eliminate these compounds from the water line. These are accumulated in the sludge being able to cause the mud cannot be used in the fields.

However, these performances in eliminating the pollution and the WWTP effluents can have adverse effects (Pereda et al. 2020). The presence of high levels of nutrients may cause the eutrophication of the water (Preisner, Neverova-Dziopak and Kowalewski, 2020) or affect the water's biodiversity. Discharging hazardous substances and illicit connections adversely affects the WWTP and the water bodies. Nhapi and Tirivarombo, (2004) determined that the discharge of untreated water increases nutrient levels in the Marimba River, Zimbabwe. Another example is in the corals. Wear and Thurber (2015) studied the effect of the effluent of WWTP in the coral. They observed that the presence of nutrients, endocrine disruptors, solids, toxins, heavy metals, and the reduction of salinity due to the purified wastewater is a cause of the decline of coral reefs.

Some techniques can be used to reduce the effect of wastewater as bioremediation by vegetated drainage ditches (Nsenga Kumwimba et al. 2018), the use of microorganisms (bacteria, algae, fungi) (Saeed et al. 2022), or the use of artificial wetlands (Martín et al. 2020). Bioremediation is a helpful tool to prevent damage to the environment produced by purified wastewater. However, improving the WWTP by reducing PI effects is more interesting than pollution remediation. In addition, bioremediation needs much space and produces biological waste that may be polluted.

2.3 Monitoring in sewerage and water bodies.

This section first analyses the different sewerage sensors to detect PIs. After that, we analyse the different technologies in the sensor and laboratory to determine the concentration of pollutants in sewage and other parameters that can be used to detect PIs and overflows in sewerage.

In the environment, the use of sensors is widespread. Usually, the systems used in the environment are based on one or more sensors to monitor water concentration and parameters. Siregar (2018) proved the need of a low-cost smart environment system to analyse in real-time the wastewater quality. They developed a WSN to detect changes in pH, conductivity, temperature, and dissolved oxygen. Besides, it was equipped with a notification feature that would send an alarm when the parameters exited specified thresholds. Faustine et al. (2014) used pH, conductivity, temperature, and oxygen demand sensors. The conductivity sensor is based on the salt bridge, the pH in an Ion-Selective Electrode (ISE), and the oxygen demand in the electrocatalytic method. They used an Arduino to monitor Lake Victoria with a low cost system and checked that 1250 US \$ could monitor the lake versus the 3400 US \$ commercial sensors. Parameswari and Moses (2019) used IoT to create a WSN endowed with sensing nodes to monitor water quality. They implemented a system to alert the end-user when the pollution levels were too high using SMS. Similarly, Simitha and Subodh Raj, (2019) created an IoT-based WSN system to monitor water quality in a Smart City context. Using a LoRa module based on the LoRaWAN protocol, they were able to create a low-cost, low-power and long-range approach to the issue at hand.

2.3.1 Current systems for sewerage.

In this section, we show different works related to monitor sewerage. Traditionally, PIs are detected with visual inspection in the WWTP or the spillways. This has changed in the last years. Different monitoring technologies have been developed and implemented. Nowadays, the use of continuous monitoring techniques, laboratory analyses, and inspections are used to detect the presence of anomalies in sewerage. The systems used in the sewerage should be different if it is located in a combined or separate sewerage (storm or wastewater sewerage).

One alternative to detect illicit discharges in storm sewerage is visual recognition in combination with other techniques. One technique that does not need laboratory analyses is using trained dogs. These dogs can detect the presence of wastewater mixed with stormwater. Van De Werfhorst et al. (2014) used 2 trained dogs that were taken to the manhole covers where the presence of wastewater was suspected. The results showed that one dog detects 70% of the samples, while another detects 100% of samples with human waste. In another study, Berounsky, Travers and Reynolds, (2018) determined that canines can detect concentrations of bacteria less than 10cfm/100 ml. Then, using trained dogs is an excellent alternative to seeing illicit connections and the presence of wastewater in storm sewerage in urban areas. The use of trained dogs cannot be possible in some locations. For this, the use of an e-nose can be a good option. Moufid et al. (2021) used an electronic nose and a voltammetric electronic tongue to distinguish between clean water and wastewater. They tested it with 7 samples of water obtained from different points of the Oued Fez and Sebou rivers (Morocco), the inlet, and the effluent of WWTP. The two systems showed excellent performance in distinguishing the presence of wastewater. The problem with using an e-nose is that these are very complex. Nowadays, it is tough for the location of many e-noses in the sewerage to detect illicit discharge. However, the e-noses can be used in each case to detect the presence of pollutant incidents in certain places. The e-nose and e-tongue do not detect certain pollutants, so laboratory analysis should be used. Examples of laboratory analysis are presented by Irvine et al. (2011). They developed a program to detect and eliminate illicit discharge in storm sewerage. First, they performed a visual inspection in dry conditions to detect water in the pipes. If water is detected, a sample is taken for analysis in the laboratory. In the laboratory, different low-cost techniques were performed. They determine that the measure of *Escherichia coli*, ammonia, nitrate, fluoride, total chlorine, potassium, detergents, phosphorus,

and turbidity successfully tracks the illicit discharge and the source. Yin et al. (2019) investigated the use of 52 chemical markers in order to identify domestic and industrial flows entering the storm drains. Sodium, potassium, chloride, acesulfame, clarithromycin, and isomaltoligosaccharide presented better results for masses of water coming from the toilet. Meanwhile, glycerol and theanine proved to work better for tracking water coming from other domestic uses. They proved the use of markers as a low-cost option to find misconnected wastewater entries. To prevent the formation of blockage, Rony et al. (2021) proposed an IoT system to control waste entry into channels to prevent it. The system uses an ESP32 microcontroller to send and store the data collected. For collecting the waste of wastewater (insoluble waste), they use two motors and different level sensors to control the water level to prevent overflows and control the amount of waste. The system can send an SMS about the overflows using a Global System for Mobile communications (GSM) module.

For continuous monitoring, it is essential the use of sensors. The viability of a WSN network in sewage is demonstrated by Abbas et al. (2017). They studied a smart sewerage detection system on the Campus of Lille University (France). The system included turbidity, level, and velocity water sensors connected to a data logger with GSM/GPRS connection. By comparing the real values obtained by the sensors and the values obtained by modelling the sewerage, the abnormal and faults situations can be detected. While the system was implemented, it detected the entry of stormwater into the sanitary sewer, and the entry of infiltration water into the sewerage, which is indicative of the poor state of the sewer system. In a WSN, many parameters can be monitored. One of the parameters more studied is temperature. Hoes et al. (2009) investigated the use of fibre-optic Distributed Temperature Sensing (DTS) for detecting illicit connections in stormwater sewerage. They located the sensor in two storm sewerages (Korendijk and Groningen (Netherlands)). There was evidence of illicit connections in these storm sewerages, but the location was unknown. The spatial resolution was 2 m, and the measurement interval was 30 s. The observed temperature values showed that the storm sewerage had a temperature between 5 and 20 °C with low daily variation. However, the wastewater flow of houses or industries had a higher temperature than storm sewerage. The temperature difference generated warm plumes that the optical fibre could detect. The authors showed that there are increases or reductions in the temperature in the case of stormwater runoff. For this reason, in wet conditions, the system cannot detect the presence of illicit discharges. However, the system can detect the presence of illicit connections in dry conditions. In another work, Nienhuis et al. (2013) proposed the use of fibre-optic cables as temperature sensors to detect illicit connections in storm sewerage. They located three sensors in the bottom and top of the sewerage and floating in the water. With the variation in the temperature, they detected illicit connections. Of the three positions tested, the cable in the bottom of the pipe presents deficiencies in detecting spills. However, the other two work well. In addition, the distance between the connection and the sensing point has an essential effect on the detection. Another system based on optical fibre is presented by Vosse (2013). They determined the noise levels in the measurements of the temperature at different distances for 2 hours. Then, they compared the temperature of the water with the value of the noise. The sensor sends an alarm if there is an important difference between the measured temperature and the noise. The measurements were elaborated twice to improve the performance of the sensor. With this system, the authors have detected 99 of 100 artificial spills. Temperature sensors are useful for monitoring illicit connections in the sewerage.

Another parameter that can be controlled in sewerage is the water level. Water level sensors can be helpful to detect blockage in sewerage. See et al. (2009) developed a low-cost WSN for detecting blockages in sewerage based on acoustic sensors in manholes. The collected data were categorised into three categories, low, normal, and high, according to the water level. The different sensor nodes are connected with the protocol Zigbee to the data gathered node. In this study, the maximum distance that sensor nodes and data gathered can be connected was 66.5 m. Granlund and Brännström (2013) tested the use of water level sensors to monitor the presence of abnormal events in sewerage. They located an ultrasonic level sensor above 500 mm of the water

level and a GSM device to send the data gathered. They tested that the system could be extended to other places to monitor the sewerage. In another work, Wahyuni, Wijaya and Nurmalasari (2014) used an ATmega 128 as a microcontroller and monitored the level, velocity, and rainfall in combined sewerage. The different sensor nodes are connected by a radio frequency module (XBee™) if they are close or GSM if the connection is not possible. The topology used was bus when the information of the sensor nodes. The network was organised in a Bus topology. In this case, the information of the sensor nodes is sent to a gateway that transmits all the information to a database server. This database is connected with a Geographical Information System (GIS) to visualise the drainage information.

Until now, we have presented different works to monitor sewerage with temperature and water level sensors. Using these sensors may not be enough to detect PI. Therefore, it is necessary to monitor other parameters. Liu et al. (2014) studied the parameters that can be used to detect PIs in sewerage. They measure temperature, pH, turbidity, conductivity, oxidation reduction potential (ORP), UV-254 (organic matter), nitrate-nitrogen, and phosphate with commercial sensors. The sensors were in a pipe into which water was pumped from a tank without pollutants. This water is internally recirculated and introduced with another pump to the pollutants. Glyphosate, lead, atrazine, chromium, and cadmium were used as pollutants. The sensors used are to monitor other parameters that the introduced into the pipe. However, the detection method is based on the response of the different sensors to the pollution presence (virtual sensing). The correlation between the sensor response and the pollution is evaluated using the Pearson correlation. The researchers concluded that the different pollutants provoke a reaction in the sensors. Therefore, various sensors and correlation coefficients can be used to identify and quantify the different pollutants. The advantage of this versus using only an ideal sensor for each pollutant is that it prevents false positives or negatives. Finally, the time to detect a pollutant dumped was 9 minutes after dumping. In a posterior work, the authors propose an algorithm to improve the detection of PIs (Liu, Smith and Che, 2015). They used the same parameters and Pearson correlation, but they added the use of Euclidean distance. To calculate the Euclidean distance, a matrix with the correlation index of the different sensor responses is created in pairs (for example, pH and turbidity). The matrix values are converted to a vector with the correlation values and compared with the values to the point of origin. An alarm is generated if the value obtained is higher than the threshold alarm. The system presents a detection index of 95% of contamination events and a generation of 2% of false alarms. In another test, Hauser et al. (2019) used pH, chloride, and conductivity electrodes to detect PI. To simulate the PI, the authors performed 4 samples with values of pH, conductivity, and ions remarkably different from the normal values in residual water. These mixed samples were diluted up to 50 times in a static wastewater environment. The results showed that these electrodes could detect an illegal discharge 10 meters downstream of the discharges point but could not characterise the composition and the source of pollutant (illegal waste, household chemicals, or pipe cleaner). Buras and Solano Donado, (2021) study the use of machine learning to location of PI sources. They used pH and conductivity sensors to determine the presence of a PI and its localization. They observed the change of pH and conductivity along the time and observed minor oscillation of them than in the case of a PI. When a PI is produced, the pH and conductivity values rapidly change. The distance can be calculated with the XGBoost algorithm and the peak size. The worst location error of the proposed system is 14.2 m in a range of 210 m, and the mean is 6.3 m. Other authors reduce the number of parameters to detect abnormal values. Li et al. (2017) propose monitoring 4 parameters (temperature, pH, conductivity, and turbidity). They used a pump to capture sewerage water to the sensing unit. The sensing unit has a data processing and communication unit to transfer the data. Its system was tested for 3 years in different sewerages. Due to the presence of solids and the generation of biofilms in the system, the authors studied the use of a diameter channel in the sensing unit of 14 mm, with a current flow between 40 and 60 l/min. They determined that the system is sustained for 12 months without blockage and

significant biofilm formations. Thanks to the system, different abnormal events related to illegal industrial discharges to the sewerage have been detected.

We studied works that used sensors to monitor sewerage. The main parameters measured are turbidity, conductivity, temperature, organic matter, ORP, chloride, etc. In addition, other contaminants such as oil, nutrients or heavy metals are present in the sewerage. In the following subsections, we analyse the different technologies used to measure these contaminants to determine their application in sewerage.

2.3.2 Related work on water level sensors.

In this subsection, we analyse different works about water level sensors. The water level measure provides information about blockage in the pipes and overflows. There are various methods to measure the water level that are shown then.

The electrical conductivity of the water can be used for evaluating the water level in an area or tank. Hernández-Nolasco; et al. (2016) developed a system for floods based on the electrical conductivity of the water. The system consists of a microcontroller Netduino Plus 2 to process and send the information. The sensing part consists of different open circuits that close when the water touches the two ends of the loop. The circuits consist of a copper wire in the base and secondary copper wires located at different heights. When any of the circuits closes, it sends the information to an access point and from this to a computer. The computer processes the information and sends an alarm to the smartphones of the population. Capacitive sensors are another alternative for measuring water levels. Reverter, Li and Meijer, (2007)) used a capacitive sensor for monitoring the water level in a metallic tank. The sensor has two electrodes, and one is insulated. The water level can be calculated due to the change in the difference between the dielectric value of air and water. Chetpattananondh et al. (2014) showed a low cost capacitive sensor for water level measurement in the range of 0 to 30 cm with a resolution of 0.2 cm. They used a comb electrode of 70–80 mm width, 300 mm height, and 1–2 mm spacing between each comb. According to the results, this sensor is highly sensitive. It presents good repeatability and low energy consumption.

In some cases, it is not possible to use the electrical properties of water to measure the water level. For this reason, some authors proposed alternative methods to measure the water level, such as acoustic sound, remote sensing, buoys, optical fibre properties, and light or acoustic reflection. Miček et al. (2016) proposed the measurement of the acoustic signal generated by the water flow with a microphone for measuring the water level. Michailovsky et al. (2012) studied the use of Satellite radar altimetry (obtained from the Earth and Planetary Remote Sensing Lab) for monitoring the surface water in the Zambezi River basin. The objective was to calculate the discharge of the rivers in the basin. They studied three scenarios (I) with an in situ rating curve available, (II) With one simultaneous field measurement of cross-section and discharge, and (III) with historical discharge data available. These scenarios have been compared with the values of the real discharge. They obtained that the first method has an error between 4.1 to 6.5 %, while the other methods have an error of 6.9 to 13.8 %. Another option to measure the water level is the use of buoys. Buoys are sensors that contain a floating element in the element measure. With a limit switch to generate alarms or other electronic devices to know the liquid level. Carlson et al. (2020) presented a buoy to monitor glaciers' meltdown and changes in glacial lakes' water levels. The system uses an Adafruit Feather M0 as a microcontroller, a Global Position System (GPS) to know the position of the buoy, an inertial motion unit sensor to see the acceleration of the buoy's position, batteries to power the system and solar panels to provide energy to batteries. These components are located in a waterproof box that floats. Their results showed the potential of the system to monitor water levels in glacial lakes. Nowadays, the methodology most used is the reflection of an acoustic or light wave. These sensors emit light or acoustic waves that are reflected in the surface of the water. However, these methods present problems when performing measurements in areas with high agitation or with the presence of waves. To solve this problem, Li et al. (2014) proposed the use of multiple-input multiple-output ultrasonic transducers. They

used four transmitting elements and four receiving elements. They achieved an improvement in measurement accuracy. Fisher (2013) proposed the measurement of water level with a system composed of an ultrasonic sensor, a temperature sensor, and a microcontroller. The ultrasonic sensor measures the distance from the sensor to the liquid surface. The temperature sensor is used to compensate for the change in acoustic waves. The use of optical fibre and the change of their characteristics with the pressure of water is another alternative. Antonio-Lopez et al. (2011) showed an optical fibre sensor for measuring the water level. A multimode fibre without cladding was used as an optical fibre. The sensor works due to when the fibre is submerged in a liquid, and the refractive index changes depending on how submerged it is. They concluded that the more the fibre is submerged in water, the more the peak wavelength will be shifted to longer wavelengths. This type of sensor has the same gaps that we explained for capacitive sensors. Li et al. (2016) developed a sensor based on fibre optics formed by the integration of an asymmetrical fibre Mach–Zehnder interferometer with a Bragg fibre grating. The Bragg fibre is used to monitor temperature (this method is explained in section 2.3.3). This method is based on the change of light intensity of the core mode and dominant low-order cladding mode of the asymmetrical fibre Mach–Zehnder. This sensor was able to measure the liquid level (0 to 7.5 cm) and temperature. The sensors' resolution is 0.15 cm in liquid level and 1.01 °C in temperature.

2.3.3 Related work on temperature sensors.

Temperature is a physical parameter indicating a system's hotness or coldness according to a scale. Different methods can be used to measure the temperature.

Some authors proposed the use of optical fibre to monitor the temperature. Leal-Junior et al. (2018) proposed using a polymer optical fibre to control the temperature. This method is based on temperature modifies the mechanical properties of the fibre. One of the properties is Young's module. Therefore, in applying a force (stress) on the fibre, the behaviour of the fibre will be modified according to the temperature. The authors use a light source and measure the wavelength of reflected light in the optical fibre. The results show that the polymer optical fibre has a Relative Error (RE) below 2% and can operate until temperatures of 110 °C. In another work, Gonzalez-Reyna et al. (2015) tested fibre Bragg Grating to monitor the temperature. These fibres transmit specific wavelengths and reflect others. The authors use a laser diode with a central peak at 977 nm as a light source and an optical spectrum analyser to analyse the wavelengths that cross the fibre. Their prototype ranges from 20 to 90 °C. one advantage of using fibre is the possibility of developing DTS. Ukil, Braendle and Krippner (2012) review the different technologies used in this type of sensor. These sensors are based on in measure the light backscattering in optical fibre. The measure of backscattering is produced by 3 principles (I) Raman, (II) Brillouin, and (III) Rayleigh. Brillouin scattering is based on the scattering of a light wave in an acoustic wave due to the interaction with the acoustic phonons in a nonelastic medium. The frequency of the wave is related to temperature. Raman scattering is based on doped quartz with amorphous solid structure that provokes lattice oscillation with the temperature increase. The light interacts with the oscillation generated scattered light with a spectral shift related to the frequency of the lattice oscillation. The fibre imperfections generated that fibre can be modelled as a Fibre Bragg Grating. The Rayleigh dispersion is generated depending on the fibre's temperature and strain.

Optical fibre to measure temperature is complex and requires expensive materials. Thus, other systems are used based on the change of their properties with temperature. The most common temperature sensor are resistance temperature detectors (RTD), thermocouples, and thermistors (Arman Kuzubasoglu and Kursun Bahadir, 2020). In another review, Parra et al. (2018a) determined that the technologies that can be used in water are RTD, thermocouples, semiconductors, capacitance thermometers, and Infrared thermography. A RTD is based on the resistance variation of a conductive element with the temperature. Some elements used in these sensors are platinum, copper, nickel, and molybdenum. Similar to the RTD, there is the thermistor. These types of resistance change the internal resistance according to the temperature. The difference between thermistors and RTD is the materials used. On the one hand, the RTD is

performed with pure materials. On the other hand, the thermistors combined polymeric and ceramic materials. Another technology is the thermocouple. The thermocouple is based on the joining of two metals that, according to the temperature, generate a voltage due to the Seebeck effect. The use of semiconductors is another alternative to monitor the temperature. Semiconductors are materials that are conductors or insulators depending on the electric or magnetic field, pressure, incident radiation or temperature. The semiconductors more used are transistors and diodes. In transistors and diodes, the voltage drop changes with the temperature. The capacitive temperature sensors are based on the change of the electric permittivity. The change in permittivity changes the amount of energy the capacitor can store. Finally, there is the infrared thermography technique. This is based on the radiation emitted by bodies according to their temperature (Ley de Stefan-Boltzmann). (Arman Kuzubasoglu and Kursun Bahadir, 2020), (Parra, 2018a).

2.3.4 Related work on conductivity meters.

Conductivity is defined as the resistance of an aqueous environment to carry an electric current. The conductivity of water is related to the concentration of salt, the kind of salt, and the temperature. The increase of the salts and temperature produces a conductivity increase. The standard methods present two methods for measuring water salinity, conductivity cells, and density method (Rice, Eaton and Baird, 2017). In addition, other methods have developed as the use of inductive sensors (Parra et al., 2015a), (Yin et al. 2008), (Völker, Eberheim and Pechstein, 2008), and optical sensors (Zhao et al., 2009).

The density method is based on sample density being proportional to the square of the vibration's period and density being proportional to salinity. This method places the sample and two solutions of known conductivity in different vibrated tubes. Conductivity is calculated by the period difference between the sample and the two calibrated solutions (Rice, Eaton, and Baird, 2017). Optical sensors are another method to measure the conductivity in water. This method is based on the light's refraction when the water's salinity changes. Zhao et al. (2009) used optical sensors to measure conductivity. They determine that the measurement range is 0‰–45‰, and the measurement repeatability is better than ± 0.25 ‰. These methods are few used currently.

Conductivity cells are the most common method to determine conductivity. It is based on using two or more electrodes and measuring the conductivity bridge between them. One problem of the conductivity cells is the polarization of water, to avoid it, three or more electrodes are used. Huang et al. (2011b) presented a sensor with seven electrodes and a temperature sensor to correct the measures. The precision of the sensor is 0.03 mS/cm in the range of 25 to 55 mS/cm. Ramos et al. (2005) developed and tested an in-situ conductivity sensor using cells for water quality monitoring. The sensor consists in three electrodes and two terminal devices. This system works by exchanging ions creating an electric field. When the water flow passes through this system, the electric field varies. Gong et al. (2008) propose a conductivity sensor based on two flat electrodes built on a PBC board. The author makes the measurements using KCl and milliQ water. This sensor works at 334kHz, obtaining significant variations in a wide range of salinity, suitable for marine environments. The conductivity cell can be performed with different low cost materials. Carminati and Luzzatto-Fegiz, (2017) used a micro-USB cable as the electrode, an Arduino Uno as microcontroller, an AD5933 to convert the signal, and different electronic elements to generate and receive the voltage. They determine that the sensor has a resolution of 0.1% and a good adjustment between measuring a commercial conductivity in the range of 3.5 to 0.5 S/m.

Finally, induced conductivity sensors based on Faraday's law have been developed in the last few years. This law says that when a changing Electromagnetic Field (EF) interacts with an electrical circuit, it generates an induced electrical current. The inductive sensors to monitor the conductivity usually are based on two coils a Powered Coil (PC) and an Induced Coil (IC). Some examples of the use of inductive sensors are presented next. Wood et al. (2010) developed a sensor to measure the salinity in estuaries. The system is based on two coils to monitor the conductivity,

a temperature sensor (LM335), and a microcontroller. The two sensors are controlled by an Automatic Voltage Regulator microcontroller that saves the data in a flashcard and sends the data. The conductivity sensor is composed of two coils in solenoid form (a PC and an IC) covered with 1-dodecanethiol to protect against corrosion. The temperature sensor is used to adjust the values of conductivity to salinity. The maximum measure of the sensor is 67 g/l of table salt. Parra (2014) proposes the development of a low-cost wireless conductivity sensor to control freshwater flooding of lakes and mangrove reserves. The sensor used is composed of a toroidal coil and a solenoid, so that the first is fed by a sinusoidal wave, and this induces the second. The results show a wide range of detection able to detect differences between small and large amounts of salt, typical of the sea. In a posterior work, Parra et al. (2015a) improved the sensor. They tested with 18 prototypes, changing the PC and IC spire number, copper diameter, and coil diameter. They concluded that the best prototype has a copper diameter of 0.4 mm, a diameter of 25 mm, 40 spires in PC and 80 spires in IC. The best prototype functions in the concentration of 0.58 mS/cm to 73 mS/cm. The sensibility of the sensor changes with the conductivity of the sample. The best sensibility is in the range of 0.6 to 5.5 mS/cm with a value of 0.1 mS/cm. The worst sensibility is in the range of 41.1 to 86.7 mS/cm, with a value of 0.6 mS/cm. Yin et al. (2008) used a noncontact coil sensor to monitor the water level and conductivity. They obtained errors of 2% for the level and 3% for conductivity. These sensors are submerged in water. A solution to avoid water contact with the sensor is the use of coupled Contactless Conductivity Detection (C4D). This is a new methodology currently being investigated. Huang et al. (2012) developed a new C4D sensor based on two electrodes. An AC powers one electrode, and the other electrode is induced. These electrodes are located on a pipe of 1.8 and 3.2 mm in diameter. The results show that the sensor can work between 0.1348 to 105.3 mS/cm with less than 3.5% RE. The main gap in the use of C4D is the diameter of the pipe. These proposals are good for small diameter applications but not for big diameters of pipes. Other inductive sensors can be used to monitor water conductivity. Kandur, Harms and Kern (2021) show a transformer type inductive conductivity sensor as a low-cost sensor to measure the conductivity in different temperatures. They used two coils with a core of Mn-Zn encapsulated in resin. The conductivity samples tested are between 0 to 55 mS/cm. With the temperature increase, the sensor presents an error of $\pm 3.5\%$. However, the temperature influence can be compensated, and that way, you obtain an error approximately of 0.9%. In another paper, Kang Hui et al. (2020) propose using an inductive sensor based on coils to measure the conductivity. The coils have a magnetic core of Mn-Zn ferrite and copper wires coiled around them. One coil is the PC the other is the sense coil. The range of the prototype is between 0 to 350 mS/cm.

2.3.5 Related work on sensors to measure total solids in water.

Solids are one pollutant in wastewater and water bodies. That pollutant has three effects on water: (I) the loss of water transparency, (II) the transport of pollutants, and (III) physical damage to living beings. Solid concentration can indicate the presence of pollution problems in water. The standard method to control solid concentration in water is drying at 103-105 °C. This method is based on placing a volume of water in a pre-dried container and known weight. The container is located in an oven. When the water is evaporated, the container is weighed and put back in the oven. The process is repeated until the difference between the container's mass (container+solids) measured at different times is less than 0.5 mg (Rice, Eaton and Baird, 2017). The problem with this technique is that it is not instantaneous. Dried does not allow continuous monitoring because the results take several hours. There is no other method to direct the quantification of solids. Thus some authors propose using turbidity sensors and empirical models that relate solids and turbidity (Gippel, 1995) (Downing, 2006). Nowadays, there are four methods for measuring turbidity: (I) Secchi disk, (II) acoustic sensors, (III) remote sensing, and (IV) optical sensors.

The Secchi disk is based on immersing a disk in the water and keeps checking when it is not visible. The Secchi disk was used first by Angelo Secchi in 1865. For a long time, it was the most

used system for measuring turbidity. However, now it has been substituted for other techniques. Nevertheless, it is still used for surface water monitoring (Philippart et al., 2013). Bigam Stephens et al. (2015) collected individual Secchi disk measurements across the United States performed by volunteers and professionals in different water bodies. They inserted this data into a database for future research and water management. One problem with this technology is that it is subjective since the person who performs the methodology sees or stops seeing the disk. Another method to determine the concentration of solids is presented by Pavanelli and Bigi, (2005). They used an Imhoff cone to determine the concentration of solids in an indirect way. They compared the use of the cone with the nephelometer and concluded that the use of an Imhoff cone has a good correlation with the total solids. They determined that the use of a cone is better than a nephelometer, especially in cases with high concentrations of solids, because it does not need dilutions

The alternatives to the Secchi disk are acoustic and optical turbidity sensors. First, we analyse the acoustic sensors. Acoustic sensors are based on the backscatter of the acoustic waves when colliding with solids. Chanson, Takeuchi and Trevethan (2008) used an acoustic sensor for monitoring the solids in a small subtropical estuary of Eastern Australia. They used a microADV (16 MHz) system to generate the acoustic waves and a YSI™ 6600 probe to check the function of the acoustic sensor. The samples were performed with water from the estuary and solids collected on the stream bed and bank just below the high-water mark. First, they studied that the relation between suspended solids and turbidity was linear. However, the relation between backscatter intensity, turbidity, and solids does not present a linear relation. In each case, the values of correlation are high. The results showed that the sensor's calibration depends on the origin of the solids. Pallarès et al. (2016) studied the use of this sensor in sewerage and rivers. They used two different sensors for the different waters. UB-Flow 156 measured the river water and the WWTP with the UB-Flow 315. Their results showed that the backscatter of solids depended on the size of the solids and the frequency of the acoustic wave. Optical turbidity sensors are based on the absorption or backscattering of infrared light or other electromagnetic radiation. The standard methods indicated that the use of infrared light and a photoreceptor must be at 90° degrees of the incident light. However, other positions of the photoreceptor and light radiation have been studied (Rice, Eaton, and Baird, 2017). The turbidity is related to the Tyndall effect. Due to this effect, the light that passes through a medium is scattered when there are small particles in suspension in it. However, turbidity is specific to liquids and not to any medium. In addition, other substances that are not suspended can contribute turbidity to the water. In the literature, there are many works about the development of optical turbidimeters. Now, we analyse some works. Bilro et al. (2010) showed a turbidity sensor with two photodetectors at 90° and 180°. The light source used was a Light-Emitting Diode (LED) with a centre wavelength of 660 nm (red colour). They tested with different concentrations of solids and different sizes of samples. The distances used in the samples that the light had to go through were 2, 5, and 10 mm. They selected a distance of 5 mm because it had good sensitivity and capacity to operate with suspended particles of large dimensions. In another work, Song et al. (2020) developed a turbidimeter using the FX-11A optical fibre sensor and STM32F407 Microcontroller. This microcontroller is used to power the optical fibre and has ethernet transmission to connect it to a network infrastructure, allowing access through a smartphone or computer webpage. The optical fibre has two sets of fibres. One is used to emit light received at 180° by the other fibre. The results showed an error of 3.5% in the 400 to 1500 Nephelometric Turbidity Unit (NTU) range. The sensor values obtained from 0 to 400 NTU are similar in different concentrations. The same issue occurs in the range of 2500 to 4000 NTU. The solution proposed has an important gap in the monitoring of sewerage. The most popular method used to monitor turbidity is based on optical sensors. Prerana et al. (2012) proposed using optical fibre to monitor turbidity in terms of the total interaction coefficient of light. The optical fibre comprises seven peripheral plastic cladding silica fibres to collect the light scattered in the sample. In addition, the optical fibre has a glass core to provide light to the sample. They used a laser of 632.8 nm to irradiate the glass fibre and a mirror to reflect

the light captured by the peripheral fibres. Their sensor obtained good results in low turbidity levels. Other work is presented by Yeoh et al. (2019). Their proposal is based on a pair of multimode fibres. They used a laser of 808 nm as a light source and tested with 3 angles between the emitting and receiving fibre. They selected the angle of 45° due to it presents the best correlation between the mathematical model and the measurements. The sensor can work between 0 to 110 NTU with a medium quadratic error of 2.38 NTU. Optical fibre can have a high cost. Therefore, other authors propose the use of LEDs as the light source. Wang et al. (2018) proposed a low-cost turbidity sensor for monitoring freshwater. They used an infrared LED of 850 nm, a phototransistor at 90° to detect the scattered light, and a photodiode at 180°. These components are fixed to a transparent acrylic tube of 20 mm. The phototransistor at 90° was used in the range of 0 to 200 NTU (precision 0.1 NTU), and the photodiode at 180° was used in the range of 0 to 1000 NTU (precision 1.0 NTU). In the sewerage, we discard the photoreceptor at 180° due to the water level being variable in time. The use of a photoreceptor at 90° is not recommended because if the photoreceptor is placed inside the water, it can get dirty, and if it is placed outside the pipe, light may not reach the photoreceptor.

In water bodies, eutrophication is an important problem caused by increased algae concentrations produced by high concentrations of nutrients. The increase in nutrient concentration is produced by the supply of nutrients to the water body. In many cases, the nutrient supply is produced by the dump of wastewater or purified wastewater. Eutrophication provokes a solid increase in water. Different solutions have contributed to monitor the presence of algae. Lin et al. (2020) proposed the use of a technique for order preference by Similarity to an ideal solution method and Monte Carlo Simulation for evaluating the eutrophication level in lakes. The technique is a multicriteria decision method to select an alternative. They used the concentration of chlorophyll-a, total nitrogen, Secchi disc, total phosphorus, and COD as criteria. They divided the values of eutrophication in 5 levels (>20, >40, >60, >80, >100). The Monte Carlo Simulation is used to reduce the uncertainty of the data collection. They used this methodology in Lake Erhai and concluded that the results were consistent with the values of eutrophication. Their results pointed out that COD and Secchi disc are the most sensitive factors. In another work, Yao et al. (2019) used a multidimensional similarity cloud model to determine a lake's eutrophication. In this paper, the criteria are the same as the one described by Lin et al. (2020). In this model, the authors use a randomised weighting method to process the information to reduce the effect of possible errors in the values obtained of monitoring criteria. The data are introduced in a reverse cloud generation to obtain digital cloud characteristics, and results are compared with the different eutrophic levels. Another method used in water bodies to detect eutrophication is remote sensing. One of the satellites used in remote sensing is the Landsat satellite. Zhou, Wang and Zhou (2004) used the images of Landsat to measure the chlorophyll in Lake Taihu (China). They demonstrated that the TM4 band is the one with the better single-band relationship. Nevertheless, the TM1, TM2, and TM4/TM3 ratio bands have the best correlation ($R^2 = 0.809$). With this method, they can monitor concentrations between 5 to 100 mg chlorophyll a/m³. This model has been adapted by Sòria-Perpinyà et al. (2018) to monitor Valencia's Albufera (Spain). They used the image of Landsat 5 and 7. In this case, TM1 and TM2 are not used, and they have a Pearson correlation coefficient of 0.83 and an R^2 of 0.93. Another algorithm was proposed by Ha, Koike and Nhuan (2013). They used the Moderate Resolution Imaging Spectroradiometer (MODIS) in the ratio of green and blue band reflectance (bands 9 and 12). The images obtained by MODIS were pre-processed to reduce the specular reflections at the sea surface and atmosphere. In addition, they used an ordinary kriging method to improve the pixel resolution to 100 m. They used a histogram minimum method (dark-object subtraction). The paper's objective is the measurement of Chl-a in a shallow lake (Tien Yen Bay in northern Vietnam). In these cases, they measure the presence of chlorophyll in the water surfaces. Xue et al. (2015) proposed a method to estimate the vertical distribution of Chl-a. They used MODIS (terra and aqua). They calculated the Normalised Difference algal Bloom Index (green and red bands) combined with wind speed value. These

values are inserted in a decision tree for calculating if the vertical distribution is vertically uniform, Gaussian, exponential, or hyperbolic.

Using sensors is an alternative to detect eutrophication in water bodies. We find a few examples of sensors used to monitor the presence of sediment or algae. Parra (2018b) proposed a system based on 4 LEDs (red, yellow, green, and infrared) and light receptors. Their prototype was tested with two species of phytoplankton (green and brown) and sediment. They use an algorithm that determines the turbidity with the infrared led. Afterwards, the red LED is used for determining the type of algae or sediment.

2.3.6 Related work on oil sensor.

The used oil is a pollutant of human origin that can reach the water due to illegal dumping or accidents. Oil-polluted water represents a danger to the crop's quality or safety and the farmers' economy (Lopes et al. 2010). In the literature, there are different methods to monitor the presence of oil in water. Remote sensing is the alternative most used for great surfaces. Laneve and Luciani (2015) suggested the use of Specific Absorption Rate system combined with a multispectral sensor like MODIS to detect oil in water. In this work, the results achievable through the development of dedicated algorithms for automatic image processing from MODIS data and a method to classify and describe oil spill events are presented. Furthermore, Klemas (2012) used remote sensing, satellite, and aircraft, for tracking the oil spills at various resolutions over broad areas and using different frequency intervals. The satellite provides the possibility to drift prediction models, such as oil spill locations. They concluded that the model required a vast range of environmental data to predict the oil spill trajectory. Iler and Hamilton (2015) applied an Integrity Applications Incorporated, which collected electro-optical polarimetric imagery to evaluate its effectiveness for detecting oil in water. They obtained the data at multiple sun angles for vegetable oil and crude oil to demonstrate polarimetric imagery sensitivity to different liquids and collection geometries. Their conclusions highlight the optimal behaviour of the system and the possibilities of applying it to detect agricultural runoff or effluent from industrial facilities. In this context, it is necessary to evaluate the systems based on sensors rather than remote sensing systems. Fingas and Brown (2017) differentiate between passive and active methods. On the one hand, the passive methods use the light reflected by the water bodies to detect the presence of oil. The light regions that can be used are (I) Visible spectrum, (II) infrared, (III) near-infrared, and (IV) ultraviolet. On the other hand, active methods are based on the emission of light or sound to detect the oil spill. The active methods are (I) Laser fluorosensors, (II) Radar, and (III) Acoustic travel time. An example of the passive method is preset by Arslan (2018). Arslan proposed the use of Sentinel 1 C-band SAR and Landsat 8 to study the oil spills. They used a real oil spill in Ildır Bay (Izmir, Turkey) on 18 December 2016. The band selected in Sentinel 11 is vertical transmission and vertical reception of radar images (VV). First, the radar image showed the possible presence of an oil spill near the ship. After, Landsat 8 was used to validate the information. In another work, Srivastava and Singh (2010) analysed the use of Moderate-Resolution Imaging Spectroradiometer (MODIS-Aqua) high resolution bands (250 and 500 m) in Lake Maracaibo, Venezuela on 18, 19 and 20th January 2003. They concluded that radiation at 469, 555 and 645 nm atmospherically not corrected presents a good performance to detect the spill. However, the image treatment to correct the atmospheric perturbation can mask oil stains in these bands. To better the identification of spills, the authors propose that the sum ratio of band 3 (645nm) and band 2 (555nm) normalised with band 1 (469 nm)' produced significant results. Peterson et al. (2015) proposed the use of an airborne visible and infrared imaging spectrometer applying multiple endmember spectral mixture analysis to detect the presence of oil in the marshes of Barataria Bay (Louisiana, USA). The proposed system is based on the similarities in oil and non-photosynthetic vegetation spectra, differing only in two narrow hydrocarbon absorption regions around 1700 nm and 2300 nm. Confusion between non-photosynthetic vegetation and oil is expressed as an increase in oil fraction error with increasing non-

photosynthetic vegetation. The presented study obtained an accuracy ranging from 87.5% to 93.3% in oil detection. Another example of remote sensing is presented by Nezhad et al. (2018). They proposed an oil spill detection system by analysing Sentinel 2 images in the Persian Gulf. Their study followed the evolution of one oil spill event using multi-sensor satellite images in the Al Khafji zone (between Kuwait and Saudi Arabia). Oil slicks were characterised by multi-sensor satellite images over the Persian Gulf. They analysed the bands in order to detect and classify oil spills in this zone. They used ENVI software for analysing satellite images and automated data inquiry for oil spills for oil weathering modelling. In addition, Taravat and Del Frate (2012) presented a study in which they examined Landsat ETM+ images' feasibility to detect oil spill pollution in the Gulf of Mexico. The authors concluded that the bands' difference between 660 nm and 560 nm, and division at 825 nm and 560 nm, normalised by 480 nm provide the best result. Another remote sensing-based approach for oil detection is presented by Zhao (2014). They studied the spectral signature in the visible and infrared domain of oil slicks observed in shallow coastal waters of the Arabian Gulf. They used a MODIS, medium resolution imaging spectrometer, and Landsat data. Images of the floating algae index and estimation of sea currents from hydrodynamic models supported the multi-sensor oil tracking technique. They pointed out that scenes with and without sun glint as a spectral signature of oil slicks in the optical domain depends upon the viewing geometry and the solar angle. Depending on the combination of those factors, oil slicks may exhibit dark or bright contrasts concerning oil-free waters. To track oil slicks and forecast their potential landfall, they used ocean circulation and wind data. Another alternative to detect oil spills was shown by Pisano, Bignami and Santoleri (2015). They used 11 MODIS images, seven of them to develop the methodology and four for validating the method. The ratio image $R = L'GN/LGN$ is used to detect possible areas with oil spills. In this ratio, $L'GN$ is the MODIS-retrieved normalised sun glint radiance. The other variable, LGN is an image correction independent of the wind direction obtained by Cox and Munk isotropic sun glint model. Their results indicated that using a threshold is possible to isolate the spills. As a result, the spills of the validation dataset are successfully detected. Salberg, Rudjord and Solberg (2014) examined the Specific Absorption Rate of images operating in a hybrid-polarimetric mode to detect oil spills. They proposed and reviewed several strategies for oil spill detection based on hybrid-polarimetric SAR data. Their results pointed out that low-wind lookalikes may be suppressed simultaneously as the contrast of the oil spills is maintained using hybrid-polarimetry data. Thus, those multi-feature images may be constructed to enhance the performance of oil spill detection.

Another approach was followed by Hübner and Minceva (2020). They developed a novel method to determine compositions on the bimodal of a biphasic system. They proposed a method based on mass balance. This balance correlates a multicomponent biphasic system with a heterogeneous composition with the position phase interface in the microchannel. Finally, they proposed an extension of the method using the information on the bimodal compositions in a subsequent step to calculate phase equilibrium compositions. In the same context, Ramírez-Miquet et al. (2016) proposed implementing optical feedback interferometry for the analysis at the microscale of multiphase flows, starting with the case of parallel flows of two immiscible fluids. This implementation will be a new tool for studying more complex interactions between immiscible fluids. Nonetheless, its application in irrigation channels might be challenging due to the heterogeneity in the suspended solids, which might cause problems with microfluidic technologies. MacLean et al. (2003) presented an optical sensor which was able to detect the presence of hydrocarbon spills. They used a sensor containing liquid-swelling polymers that convert the swelling into a micro bend force on an optical fibre when activated. This sensor was able to locate 1-meter-long spill events with a location accuracy of 2.5 m over a range of 2 km. Finally, they concluded that the sensor would be able to operate in adverse environmental conditions. A novel modular, mid-infrared, evanescent wave fibre optic sensor for the detection of hydrocarbon pollutants in the water had been designed, constructed, and tested by McCue et al. (2006) design utilised simple, low-cost production of the rugged field-based sensor. Besides,

they use a fibre optic sensing element coated with an analyte-enriching polymer that concentrates the analyte in the sensing region. Then the output signal of the optic fibre is filtered at an analyte absorption peak and coupled to a thermopile detector whose signal is read into a computer for analysis. The results concluded that the system could be used as a pollutant detector, with benzene quantified down to 500 ppm using a PVC polymer coating.

Parra et al. (2015b) proposed an optical sensor for hydrocarbon detection in ocean water. The presented sensor is composed of LEDs as a light source and a photoreceptor as a light detector. They performed several tests using light sources with different wavelengths (violet, blue, green, orange, red, and white). Their results concluded that the white colour provides the best results. This study is performed only to verify the presence of hydrocarbon in water, but the authors do not detail the capacity of their proposal to quantify it. The use of LEDs as a light source (or signal) to monitor the presence of oil, in general terms, is not a new issue. Hou et al. (2017) proposed the use of a sensor based on ultraviolet-induced fluorescence and fluorescence-filter systems to monitor the presence of oil in the yellow sea (China). They used a Xenon lamp (200-300 nm) as a light source, a photomultiplier tube as a light receptor, and a light filter system. The light filter system allows light to pass between 300 and 400 nm. This filter is used to increase the accuracy and reduce the noise in the photoreceptor due to the sunlight. The use of ultraviolet light can be expensive. One solution is the use of LEDs as light sources. Oh and Lee (2012) studied the use of artificial light to detect the presence of oil. They tested different colour LEDs (red, green, blue and orange) submerged at 20 mm, and they illuminated a CCD sensor located at 4 cm to the water surface. In the 4 LEDs, the blue light presents the best relationship between the increase of oil thickness and the light intensity in the CCD sensor. McCue (2006) proposed a new modular mid-infrared evanescent wave fibre optic sensor to detect hydrocarbons in water. The sensor uses a broadband source with back-reflecting optics coupled to a fibre optic sensing element. This is coated with an analyse-enriching polymer that concentrates the analyse in the sensing region. The experiment results indicated an optimal behaviour of the sensor, with a concentration of benzene below 500 ppm. Next, Péron et al. (2009) presented an accurate synthesis of Surface-enhanced Raman scattering/spectroscopy active substrates, based on a gold colloidal monolayer, suitable for in situ environmental analysis. They demonstrated that Au-colloidal hydrophobic films synthesised by quartz salinisation provide polycyclic aromatic hydrocarbon (PAH) pre-concentration as well as a SERS effect. Then, Albuquerque et al., (2004) proposed using poly(dimethylsiloxane) to detect aromatic hydrocarbons in water using near-infrared spectroscopy. They could classify the water into distinct groups, contaminated by gasoline A (without ethanol), gasoline C (with 25% of anhydrous ethanol), or diesel fuel.

2.3.7 Related work on Nutrients, organic matter, acidity and heavy metals.

Nutrients, organic matter, pH and heavy metals are water pollutants well studied due to their environmental effects. The presence of nutrients causes the eutrophication of water. Biodegradable organic matter causes anoxic or anaerobic conditions in the water. Non-biodegradable organic matter is associated with pesticides, plastics, organic solvents, etc. The pH changes the chemical equilibrium. Finally, heavy metals are toxic to living beings and cause bioaccumulation in the food chain. Due to the adverse effects of these pollutants in water, some authors proposed systems to monitor them in an integrated way. Yeh et al. (2017) studied the application of LEDs in optical sensors and chemical sensing devices for the detection of biochemical, heavy metals, and environmental nutrients. This system worked in the range of ultraviolet (UV) and infrared. They found that the less used LEDs are the orange, yellow, and green ones. The research concluded that LEDs had become the prominent light sources of chemical sensors

2.3.7.1 Nutrients

Nutrients are chemical compounds used by the organism to grow and survive. The two more important nutrients are nitrogen and phosphorus, usually the limiting nutrients in water

ecosystems. Generally, nitrogen is the limiting nutrient in salt water and phosphorus in freshwater. These nutrients are present in the wastewater and purify wastewater. In Europe, the dump of nitrogen and phosphorus is regulated by Directive 91/271 CEE.

In water, nitrogen is in the form of organic nitrogen, nitrogen gas, ammonia, ammonium, nitrate, and nitrite (Trygar, 2009). Nitrogen gas comes mostly from water denitrification processes and is few soluble in water. Thus, it will quickly pass into the atmosphere. The summary of the concentration of the other nitrogen compounds is the total nitrogen. The standard methods for measuring total nitrogen are In-line UV/Persulfate Digestion and Oxidation with Flow Injection Analysis and persulfate (Rice, Eaton and Baird, 2017). This is based on the oxidation of nitrogen to nitrate using heat alkaline persulfate and ultraviolet radiation. Then nitrate is reduced to nitrite by a cadmium granule column. The nitrite formed is transformed into diazonium ion with diazotisation with sulfamide in acid condition. The diazonium reacts with a pink dye (N-(1-naphthyl)ethylenediamine), and the absorbance of the sample at 540 nm is related to the nitrogen total in the sample. Other methods are the measure of nitrate. After the oxidation of total nitrogen to nitrate can be determined the nitrate with the different methods that will show later. Carrying out these procedures in situ supposes a consumption of chemical substances, and their analysis could only be carried out with an analyser, because of that, some authors proposed using different variables such as pH, oxygen demand, conductivity, Turbidity, $\text{NO}_2\text{-N}$, $\text{NO}_3\text{-N}$, $\text{NH}_4\text{-N}$, and $\text{PO}_4\text{-P}$ to estimate the total nitrogen value (Lee, Han, and Kim, 2013). Another author proposed using 220 nm and 254 nm absorbance with a PARAFAC analysis. Hur and Cho (2012) studied the samples obtained for an urban river with PARAFAC analysis and detected three components. The first component (C1) is 250 nm/405 nm (excitation/emission). The second component (C2) has two peaks, 250 nm/450 nm, and 350 nm/450 nm. Finally, the third component has one peak at 280 nm/350 nm. C1 and C2 are related to humic-like organic substances, and C3 to protein. These measures can estimate the values of total nitrogen, biodegradable matter, and organic carbon matter in water. In these cases, the nitrogen and organic matter are obtained with different empirical relations in each water.

Nitrogen can be divided into TKN, nitrite, and nitrate. The TKN is the nitrogen that is not oxidised (organic nitrogen, ammonium and ammonia). Nitrite and nitrate are oxidised forms of nitrogen in water. The techniques used for detecting nitrate and nitrite are: (I) potentiometric, (II) amperometric, (III) chromatography, (IV) biosensors, (V) analysers, (VI) electromagnetic, (VII) voltammetric and (VIII) spectrophotometric (Alahi and Mukhopadhyay, 2019). The electrochemical methods (potentiometric, amperometric, and voltammetric) are based on the impedance, potential difference, or current generated between different electrodes. The different electrodes can be performed with copper, silver, platinum, gold, glassy-carbon electrode, graphite-epoxy, chitosan/bentonite, and graphene (Alahi and Mukhopadhyay, 2019). These methods need an ISE. That electrode has a membrane that allows the passage of nitrate ions. Chromatography is a method of separation of the different components of a sample. After, the element of interest (in this case, nitrate or nitrite) is analysed. Chromatography is an expensive laboratory technique that requires significant devices (Cosnier et al. 2008). Another technique is the use of electromagnetic sensors. Finally, the spectroscopic method is useful for monitoring nitrate and nitrite. These compounds have good absorption in 302 nm nitrate and 356 nm nitrite (Moo et al. 2016). The problem with using the spectrophotometric method is that (Cui, Wu and Ju, 2015) organic matter has good absorption in the ultraviolet region. It needs the determination of this interference or elimination. Another method is using the other substance that reacts with the nitrates. The use of graphene oxide mixed in water is an example. The absorption of light from graphene oxide (567 nm) changes with the presence of nitrate (Tang et al. 2016).

Organic nitrogen is determined by the Kjeldahl methods and block digestion (Rice, Eaton, and Baird, 2017). There are two variants, macro and semi-micro Kjeldahl. The election of the variant is dependent on the expected concentration. The method eliminates ammonia by adding NaOH, which reacts with ammonia at a pH of 9.5. After the digestion of the sample with H_2SO_4 , K_2SO_4 and CuSO_4 to convert the organic nitrogen to ammonia. After, the sample is heated to

remove acid fumes and distillation. Finally, a method to measure ammonia is used. In block digestion, the nitrogen organic is digested with H₂SO₄ and CuSO₄ at a temperature of 200 °C for one hour and then at 380 °C for another hour. After an analysis with the FIA instrument (explained above in the total nitrogen) is used.

To monitor ammonia, there are different methods. For in-situ measuring, the best option is the use of specific electrodes. The use of the physical sensor for measuring the ammonium and ammonia with the membrane is presented in different papers, in seawater (Ding, 2017), in wastewater (Been et al. 2014), for monitoring nitrate, nitrite, and ammonium (Nuñez et al. 2013), (Schwarz, Kaden, and Pausch, 2000). The standard methods describe the use of an ISE and present two methods, titrimetric and phenate methods (Rice, Eaton, and Baird, 2017). The two methods are based on a previous distillation of the sample and after the titration of sulfuric acid or phenol.

The other important nutrient is phosphorus. The methods to determine the concentration of this nutrient are based on (I) colourimetric, (II) electrochemical, (III) fluorescence, (IV) microfluidic, and (V) remote sensing (Islam et al. 2016), (Warwick, Guerreiro, and Soares, 2013). Colourimetric methods consist of the reaction of phosphorus with other substances. This reaction generates a change of colour in the sample. When more colour intensity, the concentration of phosphorus is higher. The electrochemical sensors are based on measuring the loss or the gain of electrons production for a reaction. The fluorescence sensors are based on a spectroscopic analysis in which the electrons of a substance are excited with electromagnetic radiation and emit different radiation. The microfluidic techniques perform the chemical reactions in a controlled environment in a set of micro-channels to reduce the number of chemicals. Finally, remote sensing analyses the multispectral radiation in aircraft or satellites (Islam et al. 2016), (Warwick, Guerreiro and Soares, 2013). The electrochemical method is presented in used in different environments. Wang et al. (2014) developed a gold microband array electrode based on reducing a molybdophosphate complex using the linear sweep voltammetric. The sensor has three electrodes, a platinum counter, a gold microband array as the working electrode, and an Ag/AgCl electrode as the reference electrode. The measurements performed in different phosphorus concentrations are in a detected solution of molybdate sodium. The sensor presents a linear range from 0.02 to 0.5 mgP/l with a R² of 0.99. Similar results are observed by Bai et al. (2014). Taylor et al. (2015) developed an in-situ analyser for orthophosphate and total phosphorus. The analyser used the chloride-molybdenum blue method following oxidative digestion with acidic peroxodisulfate. The prototype analyser ranges from 30-200µg P/L with a precision of ±4.3%. The cost of the system is \$3000 (10 times less than a commercial one). As with nitrogen, some authors use different parameters to estimate the total phosphorus concentration.

2.3.7.2 Organic matter.

Organic matter is a vast and heterogeneous group of components formed by compounds that contain carbon and hydrogen or carbon and carbon bonds. In this subsection, we analyse methods to monitor organic matter in general. We do not explore those works that seek to analyse specific organic components such as sugars, lipids, proteins, organic pesticides, etc. In wastewater, organic matter is usually divided into non-biodegradable, biodegradable, and total organic matter methods.

The methods for monitoring total organic matter (biodegradable and no-biodegradable) are based on (I) photocatalytic, (II) electrocatalytic, (III) chemiluminescence, and (IV) optical methods (Namour and Jaffrezic-Renault, 2010). The photocatalytic sensors are based on radiation with an ultraviolet lamp and the superficies of a photocatalytic compound (for example, TiO₂) to generate electron holes. This will allow the oxidation of organic matter through the oxygen present in the water. After an oxygen sensor monitors the oxygen concentration. An example of a photocatalytic sensor is presented by Kim et al. (2001). Their sensor range is 0.12 to 8 ppm of COD, and a complete analysis took about 10 min. The electrocatalytic sensor is based on the use of electrodes to oxidise organic compounds. Specific metal electrodes (catalysis) are needed to ensure the oxidation of organic compounds and not that of water. The electrons required for the

oxidation of the organic matter can be measured as an electrical current (Namour and Jaffrezic-Renault, 2010) (Ai et al. 2004), (Wang et al., 2012). Ai et al. (2004) used this method with a nano-PbO₂ electrode. Their sensor works in a range of 5 to 3000 ppm and limit detection to 2.5 ppm. Wang et al. (2012) used cobalt oxide sensing film was prepared on a glassy carbon electrode surface via constant potential oxidation. The sensor range is 1.7 to 170 ppm, with a correlation coefficient of 0.995. Other materials have been tested as copper (Silva et al. 2008), nickel (Cheng, 2011), etc. Gutiérrez-Capitán et al. (2015) tested with electrodes manufactured with Ni, NiCu alloy, CoO nanoparticles, or CuO/AgO. The best prototype manufactured was CuO/AgO. This was tested with real wastewater with good precision. Chemiluminescence is based on measuring radiation emitted by a chemical reaction (Namour and Jaffrezic-Renault, 2010). This method was used by Liu et al. (2012) to monitor the oceans' organic matter. They used ozone that reacted with the organic matter and measured the radiation emitted. The optical sensors are based on the interaction of light with the organic matter in water. Usually, these sensors use an ultraviolet lamp of 254 nm to measure the absorbance (Namour and Jaffrezic-Renault, 2010). Kim et al. (2016) used a deuterium lamp, and the light was sent into optic fibres to test samples placed in a quartz cell. The sensor has a good coefficient of determination (0.964) between potassium hydrogen phthalate (the substance used for calibration) and absorbance. As we saw earlier in the nitrogen, the optical sensor with a PARAFAC can be used for monitoring different types of organic matter (Hur and Cho, 2012). Other authors use the same technique to monitor total and biodegradable organic matter (Yang, Shin and Hur, 2014). This sensor can be used for monitoring the total organic carbon in water. The use of fluorescence has the potential to detect accidental pollution events. However, the fluorescence methods have problems with implementation as high quantities of suspended solids, temperature, fouling, etc. (Carstea et al. 2016).

The biodegradable organic matter sensors are based on oxygen consumption (when the microorganisms consume the organic matter) or microbial fuel cells (Namour, 2010). Usually, it uses sensors for monitoring the total organic matter because the biodegradable organic matter sensors need microbial growth. (Wang et al. 2010) developed a faster biosensor that can have measurements 8 times a day. (Other biosensors have similar times for measuring). In addition, the optical sensor can be used to estimate biodegradable organic matter (Yang, Shin and Hur, 2014).

2.3.7.3 pH and Oxidation Reduction Potential.

The pH is defined as the negative logarithm of the concentration of protons ($\text{pH} = -\log [\text{H}^+]$). The pH affects the growth of microorganisms, precipitation of substances, and corrosion of materials. The typical pH value in natural water is between 4 to 9, and distilled water has a pH value of 7. The standard method for measuring the pH is the electrometric method (Rice, Eaton, and Baird, 2017). The glass electrode is the most common method for measuring pH. The glass electrode has two electrodes. A reference electrode and a hydrogen electrode. The hydrogen electrode contains dilute HCl (or other substance), a wire metal, and a specific membrane to H⁺. When this glass bulb is immersed in a sample, it is generated a potential between the inter glass solution and the sample. The reference electrolyte contains a wire metal, a solution of KCl (or other salts). This electrode has an orifice that, with the dissolution of the salt, generates an electric bridge between the two electrodes (Bolan and Kandaswamy, 2005). The value of pH in the pHmeters depends on temperature. For this reason, these instruments need a temperature sensor to correct the pH value. The structure of the pH meter does not change in the last decades. However, different authors tested with different electrodes, membranes, etc. The glass electrode has a critical gap which is fragility. For this reason, different authors proposed using other materials, such as Iridium oxide (Huang et al. 2011a) (Kim and Yang, 2014), as ISE. pH sensors are the most common and are used for monitoring the pH in different environment as rivers (Chen, Guo and Shi, 2013). However, the use of membrane presents problems in the obturation of the porous, which needs clean and continuous calibration.

As some substances present significant changes in colour at different pH (pH indicator) has been used for monitoring it. The mobile camera with a pH indicator can be used to monitor the water's pH (Dutta, Sarma and Nath, 2015) (Hossain et al., 2015). Other authors propose the use of other substances. Bishnoi et al. (2006) developed an Au nanoshell with a surface-enhanced Raman scattering. They used para-mercaptobenzoic acid as an adsorbate layer that responds to infrared wavelength depending on the pH range of 5.8 to 7.6. Alvarado-Méndez et al. (2005) used an optical fibre with a blue bromophenol (pH-sensitive dye). The dye compound is immobilised in the optical fibre creating a glass-like porous structure of silica. They used the transmittance in the infrared range to measure the pH from 5 to 7. The use of chitosan is used as a pH dye with anthocyanin (Maciel, Yoshida, and Franco, 2015). As obtained from *Bauhinia blakeana* Dunn (a tree), they extracted *natural dyes containing anthocyanin* and immobilised them in chitosan (Biopolymer), whose colour changed from red to green in the pH range 2.2–9.0 (Zhang, Lu and Chen, 2014).

Similar technology is used to monitor the ORP. This sensor works with two electrodes. One reference electrode and the other electrode are manufactured of a noble metal (usually platinum or gold). The noble metal electrode does not react with the water elements but can take or give electrons. The voltage difference between the two electrodes and Nernst's equation determine the ORP. The structure of an ORP sensor is similar to a pHmeter differentiating in the presence of a selective membrane to H^+ . However, the pH is related to ORP and can be estimated empirically in controlled environments. Lin et al. (2017) developed a low cost sensor to measure pH, ORP and conductivity. Their proposal is based on three platinum electrodes (anode, cathode and sensing electrode) with an area $<1\text{ mm}^2$ and subjected to physical vapour deposition (Ti/Pt). With Labview 2011, the difference between the sensing electrode and anode, and cathode and sensing electrode to determine the ORP and the voltage difference between anode and cathode indicated pH. The sensor can measure pH from 4 to 10 with a precision of 0.5 to 1. In the ORP measure, the range is between 150 to 800 mV.

2.3.7.4 Heavy metals

Heavy metals are metals of high specific weight. The main heavy metals are mercury (Hg), cobalt (Co), copper (Cu), chromium (Cr), iron (Fe), magnesium (Mg), manganese (Mn), molybdenum (Mo), nickel (Ni), selenium (Se), zinc (Zn). Heavy metals are toxic to the environment and humans. The toxicity depends on the compound, chemical species, the exposition route, etc. (Tchounwou et al. 2012). In the WWTP, heavy metals affect the biological reactors and the toxicity of the sludge. The sludges with heavy metals need special treatment. It cannot dump in the fields. The main sensors for detecting heavy metals are electrochemical, optical, Plasmonic, and Surface Enhanced Raman Scattering (Ullah et al. 2018).

Electrochemical methods use three electrodes (a working electrode, a reference electrode, and a count electrode). The electrodes can be metals, oxide, carbon, Organic molecular ligands, organic polymers, etc. (Cui, Wu and Ju, 2015). The fabrication of electrodes has traditionally used mercury (Choi et al. 2001). They used an HgO-modified working electrode, Ag/AgCl reference electrode, and a carbon counter electrode, because of the hazards of this metal in the last years, other materials have been used to replace this metal. Morton et al. (2009) used the voltammetric method for detecting heavy metals. The electrodes are composed of an l-cysteine-functionalized carbon nanotube. The cysteine form a complex with the heavy metal. Second, the heavy metal is a reduction with negative potential produced for the electrode. Finally, the heavy metal is returned electrochemically to the solution. Other authors used Bismuth (Sahoo et al. 2013). Finally, Aragay, Pons and Merkoçi (2011) tested screen-printed electrodes without surface treatment in seawater, and the sensor was stable for 5 weeks. Ding et al. (2016) presented a review of the development of nanomaterial-based optical sensors for Hg^{2+} detection, which showed the benefits of simplicity, rapidity, high sensitivity, selectivity, and cost-effectiveness. They summarised the published innovations in nanomaterial-based optical sensors for the detection of Hg^{2+} according to different sensing strategies, including colourimetric, fluorescent, and surface-enhanced Raman

scattering detection. An example of optic sensors is presented by Forzani et al. (2005). They show a sensor based on high-resolution differential surface plasmon resonance. They use light polarised (635nm) that is focused onto a metal film that has a sensitive area able to trap heavy metals and a reference area

2.4 Discussion and future challenges on sensors.

In this section, we analyse the techniques and technologies previously presented to develop our system proposal. First, we analyse the system to detect illicit discharge in sewerage, and after, we discussed the different techniques that can be used for the different water parameters.

Different works have been developed to detect the presence of spills in storm sewerage. One research line uses trained dogs and visual recognition of the sewerage. Visual recognition is effective in detecting the illegal connections to storm sewerage and the presence of water when there should not be. Visual recognition is not enough to detect wastewater in storm sewerage. One alternative is using trained dogs. These can detect the presence of human waste in the water. This line is helpful in storm sewerage but presents an essential gap in combined sewerage. In a normal situation, only rainwater must be circulated in a storm sewer. Thus, human waste signals a spill from home, industry, or the transfer of wastewater from a combined sewer or waste sewerage to storm sewerage. Therefore, this methodology is helpful for storm sewerage but not for wastewater or combined sewerage. In addition, using dogs is not viable for continuous monitoring; thus, using e-nose is an alternative to continuous monitoring. These techniques present two important gaps that cannot detect non-volatile elements such as solids, organic matter, nutrients, heavy metals, etc. and cannot be used in combined and wastewater sewerage because, in these, the presence of human waste is expected. In water bodies, these techniques probably cannot be used, because the concentration of bacterias are low (except in exceptional cases of spills). Analysing samples obtained from the sewerage in a laboratory solves the first gap, because in a laboratory, the non-volatile substance can be monitored. In addition, in a laboratory, expensive equipment such as High Performance Liquid Chromatography (HPLC), mass spectrophotometer, thermal cycler, etc., can be used to analyse the wastewater. The use of costly analytical measures performs the detection of spills economically unfeasible. In some works, the use of specific parameters for the detection of spills has been studied. Monitor parameters such as *Escherichia coli*, ammonia, nitrate, fluoride, total chlorine, potassium, detergents, phosphorus, or turbidity, are useful to detect the presence of illicit discharge. However, the laboratory analysis does not solve the problem of continuous monitoring.

For continuous monitoring, it is necessary using sensors. The values obtained by the sensors should be transmitted to perform the decisions. In this context, the WSNs are used to monitor the sewerage and water bodies. We found that some examples included temperature and water level. In addition, the measure of pH, turbidity, conductivity, ORP, organic matter, nitrate-nitrogen, and phosphate can detect the presence of a PI. As many parameters increase the cost of the system, the number of parameters can be reduced.

To monitor the water level, there are different techniques: (I) using water electrical conductivity, (II) using the sound generated by water, (III) buoys, (IV) fibre Bragg grating and (V) acoustic or light reflectance. The electrical properties of water can be used to control the water level. The distilled water does not conduct electricity, but the freshwater has dissolved salt that converts the water into a good conductor. This can be used in conjunction with an open electrical circuit so that the water closes the circuit. This technique is useful for establishing thresholds, but it is not good to monitor the water level because it works as a digital sensor. Another use is the use of water as dielectric material in a capacitor. The air and water have different dielectric

constants. Thus, we can perform a capacitor between the water and air in a tank. This solution's main gap is that the dielectric constant of water changes with the conductivity. Ergo, it is necessary to know the conductivity. The measure of the sound is an alternative used in the environment but is hard to implement in the sewerage. In a buoy, the measure of the level is based on its movement. The wastewater has solids that can jam the buoy movement system, which makes this sensing technique not optimal. The use of optical fibre is another option. However, as we have seen previously, these fibres are affected by temperature. Finally, the sensors are based on the reflectance of light or sounds. The use of reflectance is the best option because they can measure the water level analogically without being in contact with water. The latter prevents the appearance of oxidation problems.

The technologies to monitor the temperature can be divided into (I) optical fibre, (II) infrared thermography, and (III) the change of material properties with temperature. The optical fibre allows temperature monitoring to be distributed. This technology needs the use of optical analysers to detect the backscattering. This increases the cost of the sensor and the complexity of the same compared to other technologies to monitor the temperature. Infrared thermography presents the advantage of not needing to be in contact with the water. This reduces the corrosion that can suffer the sensor. However, this technology uses infrared cameras that capture the infrared spectrum in photography. This photograph should be analysed to obtain the temperature values. This implies an increase in the computational cost of the microcontroller. An increase in this cost implies an increase in energy consumption, the use of a more powerful microcontroller, and the economic cost of the system. The better option is using technologies based on the change of material properties. These technologies are matured enough and exist in low cost commercial sensors.

Conductivity is another parameter that can signal the presence of a PI in the sewerage. We detect three technologies that can be used to control the conductivity (I) density, (II) conductivity cells and (III) inductive. The use of density methods presents significant gaps in controlling the conductivity in sewerage. (I) the vibration of the tube can cause the broken of it. (II) the change in sample density can be produced by solids that do not increase conductivity. Nowadays, this method is few used in the comparison of conductivity cells. The conductivity cells are a more matured technology than inductive sensors. The conductive cells have more precision and sensibility than inductive cells. However, it is not the best option to monitor the conductivity of the sewerage. Due to the fact that in sewerage, there may be solids that impact the electrodes and change the distance between them, and it will be out of calibration. In addition, since the sensor is in contact with water, its electrodes can oxidate or change their chemical structure over time.

Another pollutant of wastewater is total solids. Direct solids determination is performed by the drying of samples. However, this method cannot apply in a WSN because of the excessive energy used to heat the water and the time needed. The alternative is to measure turbidity because this parameter is related to solid concentration. Turbidity can be determined with (I) Secchi disk, (II) optical methods, (III) acoustic methods, and (IV) remote sensing. Secchi disk is a method that does not allow continuous monitoring. This method is easy to use and can be used by volunteers to control the turbidity in water bodies. However, it is not utility to our system because it does not allow continuous monitoring as if the optical, acoustic, and remote sensing methods permit.

Remote sensing is used on big surfaces such as rivers, lakes, seas or oceans. Thus, it is not helpful in pipes. Thus, it can be used to control water bodies that receive purified wastewater or overflows. However, remote sensing with satellite images cannot detect PI, because satellites have a temporal resolution of days, they cannot detect punctual spills but can spot the environmental degradation of the water body. In addition, the satellites are affected by clouds which impede the

direct observation of the earth's surface. Accordingly, the use of sensors is the technology that should be used to monitor the pipes and water bodies. This technology allowed continuous monitoring. Moreover, the sensors have a small size and can be deployed in different parts of the water body regardless of the dimensions of the monitored area. Finally, the sensors can be located at different depths to monitor the water column itself. We can use two techniques to monitor turbidity in water (optical and acoustic sensors). Optical sensors are a better option than acoustic sensors because acoustic sensors are a technology less matured than optical sensors to monitor turbidity. In addition, the acoustic sensors are sensitive to the size of the particle. This characteristic can help control sedimentation in WWTPs.

Eutrophication is an important pollution problem that causes the degradation of water bodies. This phenomenon does not affect the wastewater that is in pipes. The determination of a water body is in the process of eutrophication profitable to take measures to reduce the nutrient supply and detect the presence of continuous PI. To determine eutrophication, usually, the concentration of chlorophyll A is determined. Determining this compound can be done using laboratory techniques or remote sensing. The disadvantages of these techniques are the ones listed above. Thus the determination of eutrophication with different wavelengths is an alternative.

Nutrients are indispensable to living beings. However, an excess of nutrients generates an imbalance in the environment and WWTPs' bioreactors. In wastewater, the main nutrients are nitrogen and phosphorus. Nitrogen total is the summary of all nitrogen components. According to standard methods, it is measured using two methods based on converting the total nitrogen to nitrate after measuring it. These techniques require the use of reagents and the digestion of the samples. Thus, these techniques need an analyzer to be carried out continuously. This would significantly increase the maintenance costs of the proposed system. Other authors propose the use of PARAFAC analysis. The problem with this analysis is that the use of ultraviolet light in wavelengths in the range of 220 to 350 nm is needed. Deuterium and mercury lamps have traditionally been used to achieve these emission wavelengths. Nowadays, there are developed new LEDs that are capable of emitting in these wavelengths that are used as germicidal. Hsu et al. (2021) studied the perspective of ultraviolet LEDs. The LEDs based on aluminium gallium nitride AlGa_{0.3}N work in the range between 200 to 400 nm. However, the LED efficiency is reduced in wavelengths lower than 365 nm. This implicates the heating of the LEDs. These two gaps are coupled with the need to develop packaging resistant to ultraviolet light. Juarez-Leon et al. (2020) used a UVC-LED CUD5GF1B to inactivate the SARS-CoV-2 virus. This LED is powered with a voltage of 7.5V and a peak wavelength of 255 nm. The use of ultraviolet LED is an alternative to an optical sensor that needs the use of UV. However, it is not viable for our system because it needs a cooling system to prevent overheating. With the evolution of technology, it is expected that its energy efficiency will improve and, therefore, its use for future improvements to our system. Finally, the nitrogen total can be determined with an empirical equation relating to other parameters such as nitrate, phosphorus, etc. The determination of organic nitrogen is realized similar to total nitrogen but with the elimination of ammonia with NaOH. The determination of this parameter has the same inconveniences as total nitrogen. Other components of nitrogen are nitrate and ammonia. Like the previous compounds, these can be monitored through chemicals. In addition, the use of ISE is presented in the standard methods. We discard the use of ISE because the contact of the membrane in an aqueous environment provokes changes in the chemical composition of the membrane, which causes a reduction in its useful life, and changes in its operation (Maksymiuk, Stelmach and Michalska, 2020).

Organic matter is a heterogeneous group that can divide into biodegradable and non-biodegradable. To monitor the COD, there are 4 methods. The first is photocatalytic. This method

is discarded to monitor sewerage because it presents two gaps: (I) it needs dissolving oxygen to oxidize the organic matter, but wastewater usually is in an anoxic condition, and (II) to monitor dissolved oxygen with a sensor, membranes are needed. The second method is electrocatalytic. This method has been used in wastewater. Nowadays, the fabrication of these sensors needs the use of nanoparticles which implies a complexity for its application. The chemiluminescence needs reagents. Finally, there are optical methods. This has two gaps: (I) it needs a membrane with that dissolved oxygen reacts, and, (II) it needs ultraviolet light. To monitor biodegradable organic matter, it is needed the use of microorganisms. This type of sensor can take measurements every certain number of hours (every 3 hours at most), making sewage unfeasible. However, its use can become helpful in the case of bodies of water. We have decided to rule out its use since it cannot be applied in sewers.

As far as we know, there are not methodologies to measure the pH without a chemical assessment or ISE. However, using ORP sensors can estimate the pH value of water. The ORP can apport information about the presence of an illicit discharge because some substance changes the oxidation-reduction balance of water. However, we discard the use of this parameter because the measure is unstable. Finally, to monitor the heavy are analytic methods and the use of sensitive metal film. This type of sensor is delicate; therefore, its use is not recommended in sewage systems.

In conclusion, we will use the reflection of light or sound to monitor water level, a sensor based on properties material change to monitor temperature, an inductive sensor to monitor conductivity, and an optical sensor to monitor turbidity, eutrophication and oil. In addition, a rain sensor can be used to determine the presence of rain in an area to determine different scenarios in stormsewerage.

To develop our system, there are commercial sensors that accomplish our system's requirements. Regarding temperature, various temperature sensors have been developed for Arduino, raspberry and other platforms. Some examples are DHT11, LM35DZ, TMP36, and LM75. These sensors are not waterproof, and an encapsulation must be manufactured to be able to be introduced into the water. Nowadays, there are waterproof temperature sensors such as DS18B20. In the case of monitoring the water level, an option is the use of a HC-SR04 sensor. This is a sensor used to monitor the distance between the sensor and one obstacle (the wastewater, in our case).

3 Coil inductivity based sensors.

The inductive sensors that control conductivity can present interferences with other water parameters. In this chapter, the effect of solids and water level are studied to check if the inductive sensors are a good option to monitor the sewerage. This chapter is structured as follows. First, we present the general test bench. The general test bench presents information about the electric circuit and devices used. Specific information about the samples' concentration, the voltage used in the PC, frequencies tested, and prototypes are presented in each test. Then, we study the effect of solids in inductive sensors. Different solid concentrations are studied to know the effect of the induced voltage in the IC with the increase of the solids. After, we study the effect of water level in the inductive coil. In the first experiment, we study if IC presents different induced voltage in air and water. Then, we study different water amounts inside a pipe. Finally, we show the conclusions of this chapter.

3.1 General test bench.

In this subchapter, we present the general test bench of the inductive sensors. The specific information on the different tests performed is presented in the subsequent sections.

In the experiments performed, the inductive sensors are based on 2 coils. The spires are made of copper, and the coil body is made with PolyVinyl Chloride (PVC). The different prototypes are coiled against the hands of the clock, trying to make the spires as close as possible, to obtain the best results. Besides, the prototypes are powered in the same direction. In this case, upside-down of the coiled way, using the clockwise direction. This helps to maintain a similar basis for all prototypes and to obtain more relevant data. Figure 3.1 represents the winding prototypes.

One coil is the PC, and the other is the IC. The PC is powered by an alternating signal and generates an EF that induces the IC. In Figure 3.2, we show the electric circuit used. The electric circuit of the PC has a resistance placed in series. The function of the resistance is to limit the current intensity in the PC to prevent short circuits. As a power source, we use a generator AFG1022 (Tektronix, 2022a). In the circuit of the IC, we place a capacitor of 10 nF. This stabilises the signal and protects the oscilloscope from voltage peaks. The oscilloscope used to measure the induced voltage is a TBS1104 (TBS1000, 2022).

We need to know the Working Frequency (WF) in the experiments. This is the frequency that we use in the prototype. To select the WF, we need to account for different parameters such as the voltage difference between the concentration tested, the ease of mathematical model used in the calibration, the errors in the calibration and verification test, etc.

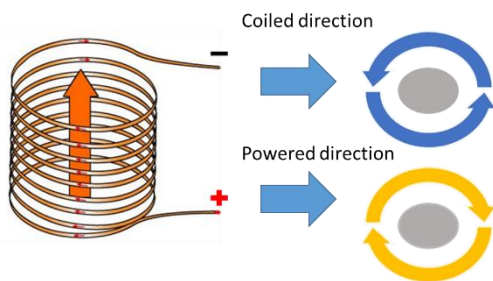


Figure 3.1. Coiled direction and powered direction.

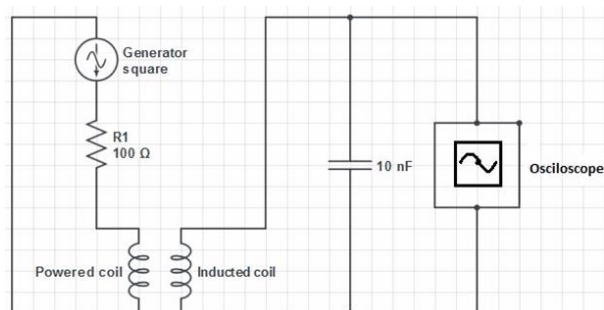


Figure 3.2 Circuit coil used in the laboratory.

3.2 Effect of solids in inductive sensors.

In this section, we analyze the possible effect of solids in the inductive sensors. It is expected that the solids have an effect in the induced voltage because the value of inductance depends on the environment surrounding the sensor. However, we check if this effect is significant in the concentration of sewerage.

We test with different prototypes of inductive sensors and solid concentrations in the then subsections. In Figure 3.3, we show the operating scheme of the prototype.

3.2.1 Material and methods.

In this subsection, we explain the methodology used in this experiment. First, we perform different samples with different solid concentrations. For the calibration of the prototypes, the concentrations tested are 0, 5, 10, 14, 17, 20, 24, 28, 32, 36 and 40 % of solids (1 % of solid concentration= 10.000 mg/L of solids or 10 g/l). To the verification test, we used the concentration of 8.8, 12.6, 13.4, 15.5, and 16 % of solids. In all cases, we prepared 750 ml of solutions and placed them in glasses with a volume of 1 L. The solids have been obtained from dehydrated sludge from a WWTP and are dried in an oven following the standard method. These ranges of concentrations are higher than the typical solid concentration in wastewater. However, do not forget that the objective of this experiment is to check the effect of solids in inductive sensors, not to monitor the concentration of solids in a sewer. To do it, we have introduced each model in a sample of tap water. The PC has been powered by a sinus wave with different frequencies from 1Hz to 500 kHz, each 25 kHz.

About to the prototypes used these are presented in Table 3.1. We test with 6 different prototypes. These prototypes are done by combining two types of coils solenoids and toroids. These prototypes are introduced in the glass with the sample, as shown in Figure 3.4.



Figure 3.3 Operating scheme.



Figure 3.4. Example of how the measurement is taken.

3.2.2 Results.

In this subsection, we present the results of the different prototypes in the calibration and the selected prototype in the verification test.

3.2.2.1 Calibration.

The results obtained by the different prototypes are represented in Figure 3.5 shows the results of detecting different concentrations of solids in water for each model. We can observe in all prototypes there is a difference in the magnitude of induced voltage between the value of 0% and 40% of solids. On the one hand, we observe that prototypes 1, 2 and 5 have the most significant difference of induced voltage between 0% to 40% of solids. These differences are 0.85 V in m1, 1.08 V in m2 and 0.93 V in m5. These prototypes have in common the presence of a toroid with 220 spires. On the other hand, if we compare the differences in the induced voltage for concentrations higher than 20%, the differences are small. The maximum voltage difference is in the prototype m5 between the concentration of 0 and 5 % of solids. The voltage difference is 0.39 V, equivalent to a difference of 0.078 V/% of solids. Considering the typical concentrations of solids in the sewer, these will not present significant interference in the conductivity readings of the sensor. So we decided to select the model m2 which is the one that presents the biggest difference between 0% and 20%. The voltage difference between 0% and 20% of concentration of solids is 0.92 V. Finally, we can model the behaviour our system by a linear equation shown in Figure 3.6. The equation is 3.1 and has a correlation coefficient of $R^2 = 0.9959$, which can be considered quite good.

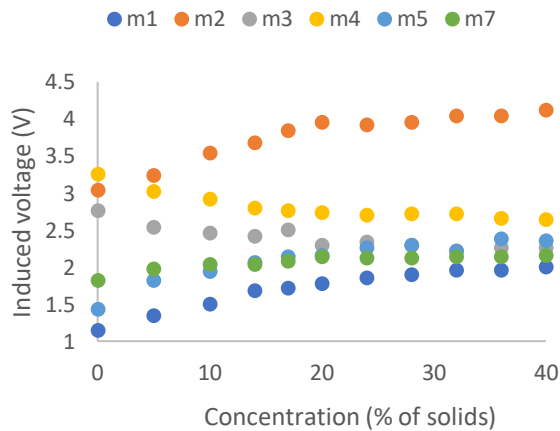


Figure 3.5 Induced voltage results

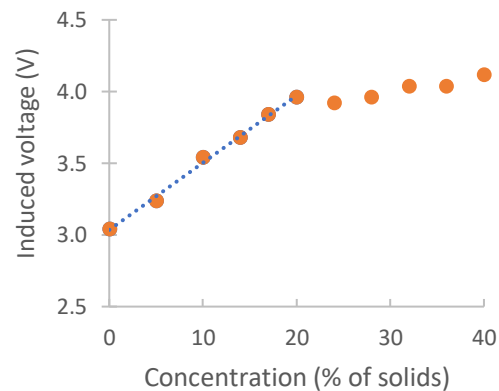


Figure 3.6 Results of model m2.

$$\text{Induced voltage (Vout)} = 0.0468 * \text{solid (\%of solids)} + 3.0349 \quad (3.1)$$

Table 3.1. Characteristics of the different coils.

Coils	Characteristics of the different coils		
	Picture	PC	IC
m1		Solenoid, N° Spires:70 High: 34 mm Diam: 25 mm	Toroid, N° Spires: 220 High: 28 mm Inner Coil Diam:25 mm, Outer Coil Diam:34 mm
m2		Toroid N° Spires: 220 High: 28 mm, Inner Coil Diam:25 mm, Outer Coil Diam:34 mm	Solenoid N° Spires:70 High: 34 mm, Diam: 25 mm
m3		Solenoid N° Spires:90 High: 42 mm Diam: 25 mm	Solenoid N° Spires:30 High: 14 mm Diam: 25 mm
m4		Solenoid N° Spires:30 High: 14 mm Diam: 25 mm	Solenoid, N° Spires:90 High: 42 mm, Diam: 25 mm
m5		Toroid N° Spires: 220 High: 28 mm, Inner Coil Diam:25 mm Outer Coil Diam:34 mm	Toroid N° Spires: 70 High: 28 mm Inner Coil Diam:25 mm Outer Coil Diam:34 mm
m6		Toroid N° Spires: 70 High: 28 mm Inner Coil Diam:25 mm Outer Coil Diam:34 mm	Toroid N° Spires: 220 High: 28 mm Inner Coil Diam:25 mm Outer Coil Diam:34 mm
m7		Toroid N° Spires: 300 High: 25 mm Inner Coil Diam:43 mm Outer Coil Diam:52 mm	Toroid N° Spires: 220 High: 28 mm Inner Coil Diam:25 mm Outer Coil Diam:34 mm

3.2.2.2 Verification.

This subsection shows the verification tests to determine the accuracy of the proposed sensor. That is, we need to ensure that after calibrating the developed sensor, it is possible to detect unknown samples and tag it accordingly to our previous analysis. To carry out this verification, we have prepared 5 unknown samples which have been monitored by our sensor to obtain the resulting induced voltage. The results are introduced in our mathematical model to estimate the concentration of solids. Finally, we compare the actual value of solids with the values calculated by our mathematical model. The results are shown in Table 3.2. The maximum error obtained is 3.18 %, and the minimum error is 0.56 %. If we compare our result with the existing sensors, we observe that our proposed sensor can operate in a larger range than turbidity sensors, presenting a detection limit of 10% of solids concentration. Our sensor can measure in a range from 0% to 20%.

Table 3.2. Errors in verification test.

% solids Real	Voltaje Measure (V)	% Solids model	Error (% solids)	RE (%)
8.8	3.44	8.52	0.28	3.18
12.6	3.62	12.36	0.24	1.87
13.4	3.68	13.66	0.26	1.98
15.5	3.76	15.41	0.09	0.56
16.0	3.80	16.30	0.30	1.84

3.2.2.3 Sensor implementation.

We check that the solids affect the induction value of the IC. However, this effect is low because it is 0.078 V/% of solids. The typical value of solid concentration in wastewater is between 350 mg/L for low pollution levels to 1200 mg/L for highly polluted wastewater (FAO, 2019).

The results showed that the prototype m2 could work in the range of 0 to 20% of solids with a maximum error of 3.2 %. Regarding to the obtained results, our sensor is able to measure higher concentrations than a turbidity sensor. A possible application is the condition monitoring of industrial processes as the treatments of sludge in water in WWTP. The design of the node to the application of our prototype is presented then.

To implement our sensor, we must integrate it in a node capable of generating the signal and gathering the data. To do it, we need a microprocessor (a NodeMCU module (NodeMcu, 2014)) and some discrete components to implement a voltage amplifier (See Figure 3.7). The NodeMCU is an open source platform specially designed to deploy IoT solutions to solve most of the requirements the society is currently demanding. The main features of this device are the following: (I) It incorporates a 32-bit MCU of low consumption (Tensilica L106), (II) IEEE 802.11 b/g/n Wifi interface, (III) 128 kB of RAM memory, (IV) 10-bit analogue input, and (V) GPIO input and output pins (general purpose).

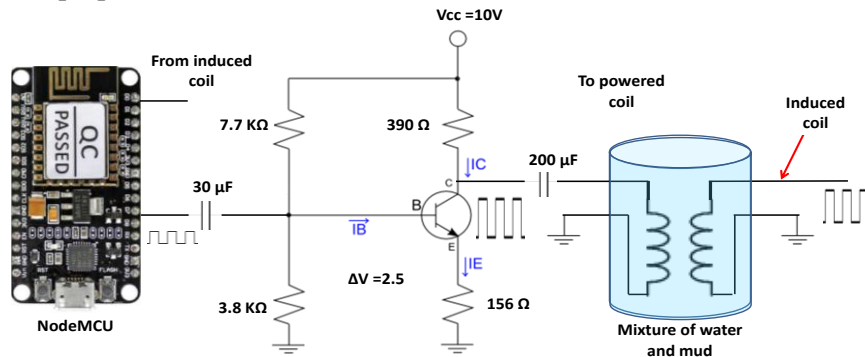


Figure 3.7. Complete circuit of our Low-cost sensor.

The power consumption of this device is typically 140 mA when transmitting with IEEE 802.11 g standard. However, it requires up to 320 mA during the start phase. Using the power save mode DTIM3, it is possible to reduce the power consumption lower than 1 mA. To power it, we

can use batteries with alternative energy sources or connecting it to the electrical network. Because this module can only generate 4.5 V output signals and our coils need at least 9 V signals, we have implemented an universal polarization network based on a bipolar junction transistor. The NodeMCU generates an alternating signal (a square or sinus signals are appropriate). This signal is amplified by the universal polarization network which is calculated to offer a voltage gain of 2.5. The output signal is driven to the PC. After that, the induced current is gathered by the NodeMCU which in charge of processing and storing the measured results. These values can be sent to a computer that acts as server. Table 3.3 shows the detailed cost of the electronic part of our proposed low cost sensor. The use of this kind of modules able to be integrated to a network permits the real-time and remote monitoring of a place or parameter since the sampling period time can be programmed according to our requirements.

Table 3.3. Prices of electronic components of our sensor.

Component	Price
Discrete components (Resistors, Capacitors, Transistors)	1.90 €
NodeMCU Module	19.82€
Coils	1.83€
Total	23.55€

3.3 Effect of water level.



As with solids in water, the amount of water in the inductive sensor can affect the values of the induced voltage. Now, we evaluate if there are significant differences between the water quantity surrounding the sensor. First, tests with air and water are performed to the effect of the induced voltage. Subsequently, carry out the experiments with different amounts of water.

3.3.1 Difference between water and air.

3.3.1.1 Test bench

The prototypes were created using different sizes of PVC material, consuming 2.2 cm long and 1.7 cm of diameter for the P1. Besides, 5.2 cm long and 2.5 cm of diameter were needed for the P2. Copper wire was used to coil the different prototypes. The P1 was coiled using 0.2 mm thickness copper. Nevertheless, a 0.4 mm copper coil was employed for the P2. Otherwise, the P1 and P2 were distinguished in two different sides, the PC and IC. The P1 was designed with ten winds for the PC part and five winds for the IC; likewise, 40 winds for PC and 80 winds for IC were used in P2. This information is represented in Table 3.4.

Table 3.4 Developed prototypes.

Prototype	P1	P2
Image		
Spires of PC	10	40
Spires of IC	5	80
Layers	1	2

We powered the coils in a clockwise direction, using the end of the coil as a negative part or ground reference. Besides, we applied 10 V to power the P1 and P2 using the generator. The experiment was done using a glass bottle where measure marks were drawn every 2.5cm, from 0 to 15 cm. The glass has a height of 16.2 cm and 8 cm of diameter. Following, the coil was placed suspended between two different marks. The P1 was located between 5 cm and 7,5 cm, and P2 between 5 cm and 10 cm. Once the coil was placed, we began to fill the bottle with water measuring the Voltage Output (V_{out}) for each mark. The water volume that we use is 1L. Finally, we test the stability of the P1 and P2. For this, we put each coil into the glass bottle, and we fill the bottle up to the mark of 15 cm. Then, we introduce the sensor between 5 cm and 7.5 cm, in the case of P1 and 5 cm and 10 cm for P2. Following, a tool was used to shake the sensor with intensity, changing the variation of movements to simulate the real environment. Figure 3.8 are represented the experiment's setup.

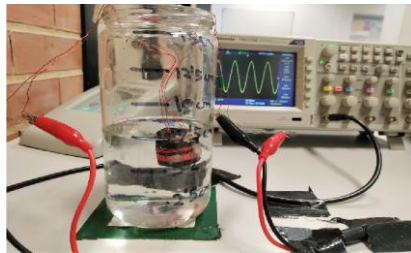


Figure 3.8. Experimental setup.

3.3.1.2 Results

In this section, we detail the results of the prototypes that we have used for the measurements. First, the test of each prototype with a different quantity of water are detailed. Successively, the prototypes are used to verify the stability of the measures that are obtained by the sensors. Finally, the best sensor is tested for different water column positions.

First of all, the WF was found. The WF for P1 was detected at 770 kHz and for P2 in 130 kHz. Following, the P1 was located between the marks 5 cm and 7.5 cm, and the glass bottle started to fill each 2.5 cm. Then, the same was done for the P2. Figure 3.9 is displayed the results of each prototype. The P1 shows an initial V_{out} of 14.18 V for 0 cm depth and a final V_{out} of 9.72 V that exposed the tendency of voltage to decrease as the water layer increases. However, the P2 represents the opposite situation, where the initial V_{out} is 23.80 V, and the final is 28.23 V. In this situation, the voltage growth with the increase of the water layer. The two prototypes behave differently from each other because the magnetic field that each one produces is not the same. Additionally, the performance of the magnetic coil is closely related to the structure of the prototypes. Looking at the results, we can see that the presence of water affects the induction of the sensor

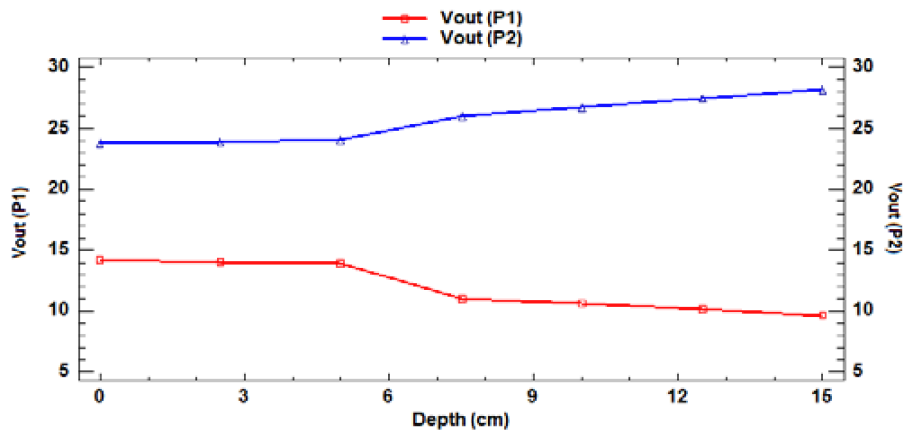


Figure 3.9. Vout in the different depths.

3.3.2 Difference between different water levels.

As we have seen previously, inductive sensors are affected by the presence of water or air in their surroundings. In this section, we analyse other inductive sensors to determine if it is possible to monitor the water volume in a pipe with this type of sensor.

We use a resistance of $100\ \Omega$ in the PC and a capacitor of 10nF in parallel of the IC (circuit represented in Figure 3.2). In Figure 3.10, we observe the assembly in the laboratory, and in Figure 3.11, we observe a recreation of the coils in the pipe. The coils are inside the pipe. The PC is connected to a signal generator and the IC is connected to an oscilloscope. The voltage of the signal is $5\ \text{V}$ peak to peak.

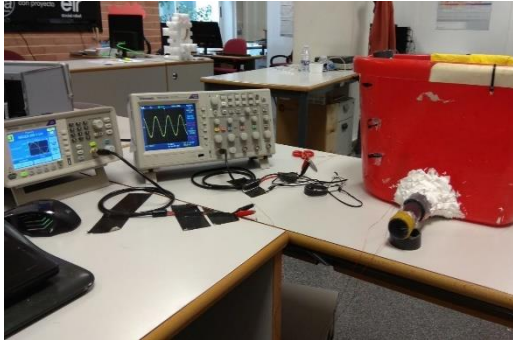


Figure 3.10 Experimental test.

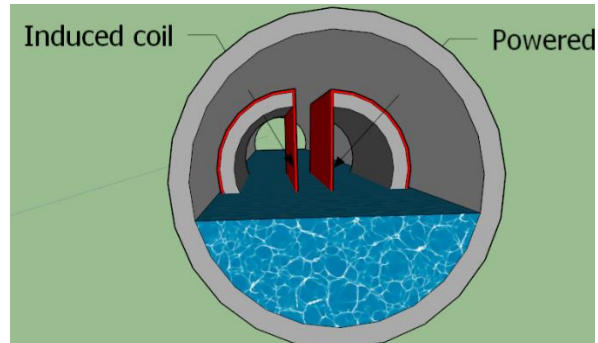


Figure 3.11 Placement of the coil inside the tube.

3.3.2.1 Test to found the WF of each prototype.

In this subsection, we are going to describe the first test that we will perform. This test will be done to find the WF.

We will introduce the different prototypes on a pipe of PVC 32 mm of diameter, 3 mm thick and length of 100 mm. The extreme of the coil will be 2 cm from the end of the large pipe. We add a transparent plastic at the end of the pipe to be able to see the inside of the pipe. The pipe will have two holes where we will pass the copper wire. The two coils will be placed on the opposite walls of the pipe that contains them. Thus, the wires that come out of the pipe will be tense to ensure that the coil stays fixed while the holes are sealed with hot-melt glue. Once the glue has dried, the cables will be untensioned since the coils will have been fixed to the pipe.

To find the WF, the PC of each prototype will be powered by a sine wave with amplitude of 3.3V peak-to-peak. We will test different frequencies from $1\ \text{kHz}$ to $25\ \text{MHz}$. In the range of $1\ \text{kHz}$ to $1,000\ \text{kHz}$, we will record the values every $20\ \text{kHz}$. However, in the range of $1\ \text{MHz}$ to $25\ \text{MHz}$, we will record the values every $0.5\ \text{MHz}$. The induced voltage will be measured with the oscilloscope. The prototypes will be tested in two conditions: empty pipe and full water pipe. The frequency that presents the greater difference between the two conditions will be set as the frequency of work.

Then, we will test the different prototypes in the same conditions used in the first test. To test the prototype, we will place the coils inside the pipe (as explained in the previous section), fill it with water, and record values of induced voltage when water reaches a height of 0%, 20%, 40%, 80% and 100% of the diameter of the pipe. Once the pipe is full, we will remove the water, and we will start the process again. This test will be done 3 times to analyze the mean values to find the best prototype. The best prototype will be the one that combines a big difference between the different percentages of water on the pipeline and that has the best adjustment equation.

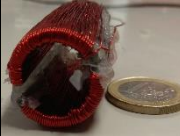

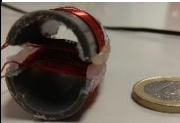
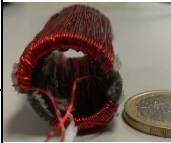


The prototypes used are composed of two copper coils. Each coil has been created with enamelled copper of $0.4\ \text{mm}$ diameter coiled over a semi-cylinder of PVC with a diameter of $20\ \text{mm}$ and $1\ \text{mm}$ thick. The prototypes are shown in

Table 3.5 includes the characteristics of the coils used in each one. We propose six different prototypes. The prototype 1 (P1) is done with copper coils forming two toroids. The two coils have the same inner diameter, outer diameter, number of spires, and height. The prototype 2 (P2) is composed of two coils in a solenoid shape. The IC has 55 spires, and the PC has 30. This prototype has the same height of PVC in both coils, but due to the IC has more spires, this coil has more

height. For this reason, the beginning of the IC is placed at the same point that the PC, but the finish not. The prototype 3 (P3) is the P2 but changing the PC by IC and vice versa. The coils of prototype 4 (P4) are in solenoidal form like the P2 and P3. In this case, the two coils have the same number of spires, 55 spired. The PCV of the P2 to P4 measures 48 mm height. The prototype 5 (P5) is formed by two coils in toroid shape. The PC has 30 spires and the IC has 55 spired. The coil with 55 spires covers all the PVC but in the case of 30 spires it does not happen. Therefore, we cover with copper the center of PVC, leaving the same PVC distance uncovered on both sides. Like the P2 and P3, the prototype 6 (P6) is the P5, but changing the powered and IC. In

Table 3.5 we can observe the parameters of different prototypes.

Table 3.5 Characteristics of the prototypes.

		PC	IC			PC	IC
P1		Type: Toroid N° Spires: 55 High: 48 mm Inner Diam: 18 mm Outer Diam 21 mm	Type: Toroid N° Spires: 55 High: 48 mm Inner Diam: 18 mm Outer Diam 21 mm	P4		Type: solenoid N° Spires:55 High: 28 mm Diam: 20 mm	Type: solenoid N° Spires:55 High: 28 mm Diam: 20 mm
P2		Type: solenoid N° Spires: 30 High: 15 mm Diam: 20 mm	Type: solenoid N° Spires:55 High: 28 mm Diam: 20 mm	P5		Type: Toroid N° Spires: 30 High: 48 mm Inner Diam: 18 mm Outer Diam 21 mm	Type: Toroid N° Spires: 55 High: 48 mm Inner Diam: 18 mm Outer Diam 21 mm
P3		Type: solenoid N° Spires:55 High: 28 mm Diam: 20 mm	Type: solenoid N° Spires:30 High: 15 mm Diam: 20 mm	P6		Type: Toroid N° Spires: 55 High: 48 mm Inner Diam: 18 mm Outer Diam 21 mm	Type: Toroid N° Spires: 30 High: 48 mm Inner Diam: 18 mm Outer Diam 21 mm

3.3.2.2 Measurement results.

In this section, we are going to detail the obtained results in the different performed tests. First, we present the results of the test done to select the WF. Next, we show the results of the test done at the WF.

3.3.2.3 Test to found the WF of each prototype.

First, we present the data from the test performed to find the WF of each prototype. Figure 3.12 presents the data gathered with P1 at different frequencies with the tube full of water and full of air. The frequencies, 300 to 340 kHz and 24.5 to 25 MHz, present higher differences between both situations and are shown in Figure 3.12. The maximum difference was found at 320 kHz. The frequencies where there are differences between both situations for P2, from 320 to 370 kHz, are shown in Figure 3.13. The maximum difference was found at 340 kHz. For P3, the frequencies with different induced voltages are between 450 and 550 kHz and at 25MHz, see Figure 3.14. The maximum difference is found at 490 kHz.

In the prototypes P4, P5 and P6, the differences in induced voltage in different environments can be seen in Figure 3.15, Figure 3.16, and Figure 3.17. Figure 3.15 shows the induced voltages of P4 at different frequencies. The frequencies shown are 300 to 360 kHz. The maximum difference was found at 340 kHz. For the P5, the values of the first test are presented in the Figure 3.16. In this case, the frequency in which we have seen differences are between 300 to 380 kHz. The highest difference was observed at 340 kHz. Finally, for P6 (Figure 3.17), the frequencies where we detect different induced voltages are between 440 to 500 kHz and at 25 MHz. The maximum difference was found at 460 kHz.

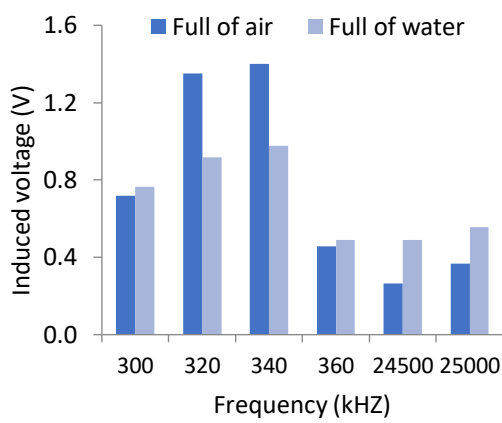


Figure 3.12 Gathered data with P1 at different frequencies.

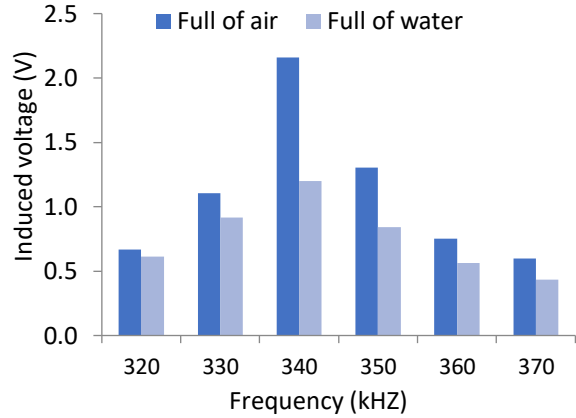


Figure 3.13. Gathered data with P2 at different frequencies.

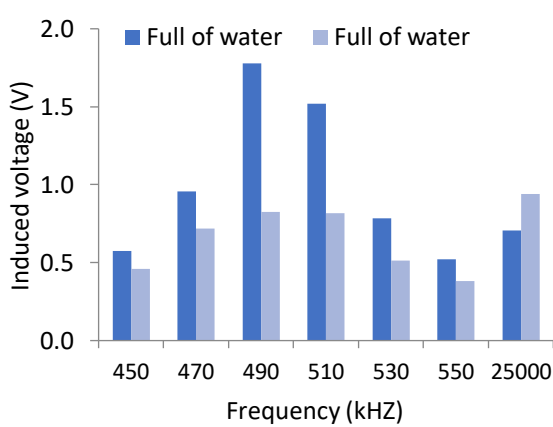


Figure 3.14. Gathered data with P3 at different frequencies

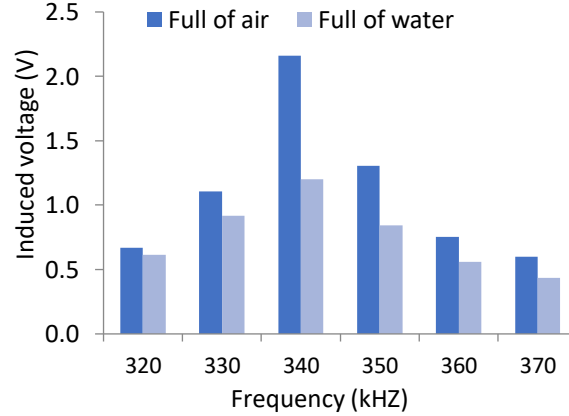


Figure 3.15. Gathered data with P4 at different frequencies

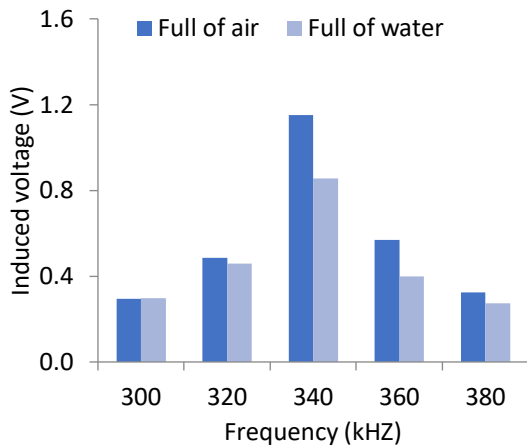


Figure 3.16. Gathered data with P5 at different frequencies.

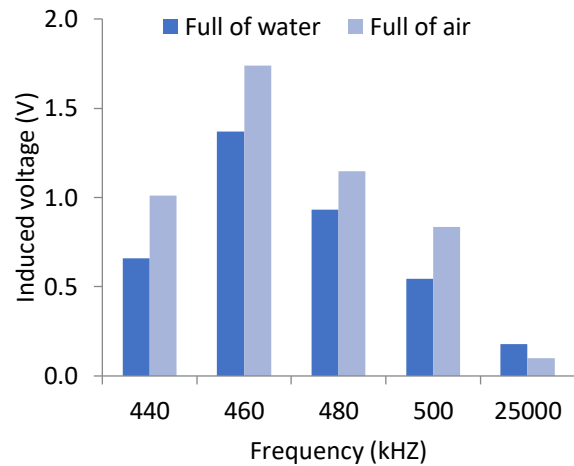


Figure 3.17. Gathered data with P6 at different frequencies

3.3.2.4 Test to determine the best prototype as a water level sensor.

In this subsection, we present the results of the different prototypes when the water level on the pipe changes. Previously, we have determined the WF of each prototype, and now we use that frequency in the corresponding prototypes.

In Figure 3.18, we can see the means of values of the induced voltages (we do three repetitions) for each prototype and different amounts of water in the pipe. We observed in almost all the prototypes (except P6) that the values of induced voltage decrease when the water level inside the pipe increases. We can observe that data from P4 present the biggest difference of all the prototypes. The difference in induced voltage between empty and full tube has a value of 1.05 V. The P2 and P3 have a similar difference, with values of 0.95 V and 0.96 V between empty and full pipe. The P1 has a difference of 0.38 V and P5 has a difference of 0.29 V. Finally, the P6 has the worst difference of the tested prototypes. The P2, P3 and P4 have a significant difference in the induced voltages compared to the other prototypes tested. These have in common that they are prototypes based on solenoidal coils. The best prototype will be selected between these.

If we observe the induced voltage when there are different amounts of water in the prototypes, they have a similar evolution. For this reason, we select the P4 as the best prototype because P4 is the one that presents the higher difference on the induced voltage.

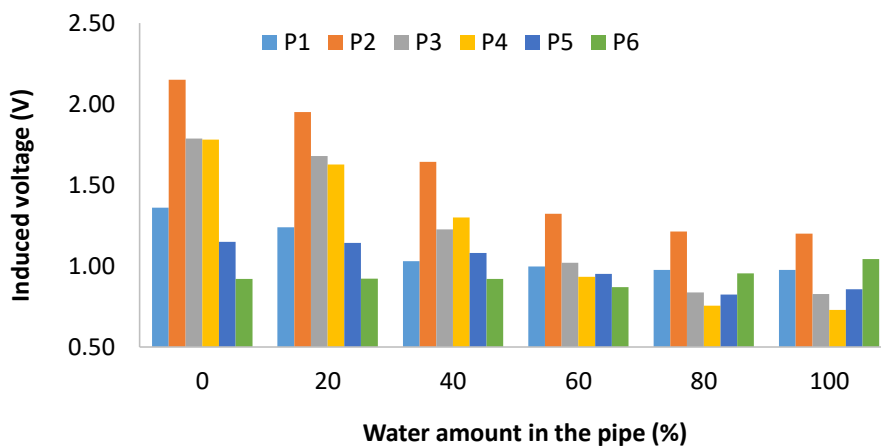


Figure 3.18. Gathered data with the different prototypes at its WF.

Subsequently, an adjustment equation is sought to explain the differences between the induced voltage and the amount of water in the pipeline. In Figure 3.19, we can see the values of induced

voltage in P4 and a representation of the adjustment equation as a mathematical model. The adjustment equation is present as equation 3.2. This equation has a correlation coefficient of -0.97, which indicates that there is a negative correlation. As this value is close to 1, it indicates that both variables have a good relation. Finally, the standard error is 0.086 V. The good relationship and the small standard error indicate that this prototype can be used to monitor the water level in pipes.

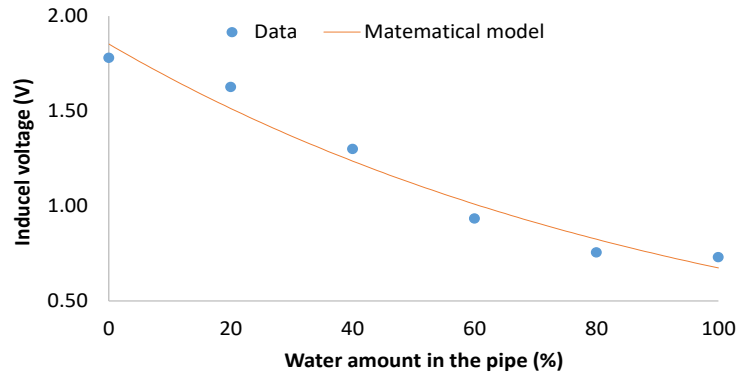


Figure 3.19. Gathered data with P4 and the mathematical model.

$$\text{Induced voltage} = e^{0.617 - 0.0101\% \text{ of water}} \quad (3.2)$$

3.4 Conclusions.

In this chapter, we studied the possible effects of the solid concentrations and water level in the inductive sensors. These two water parameters affect the inductive voltage in the IC. On the one hand, the concentration of solids in the water affects the measurement. However, the effect is low and can be depreciated. On the other hand, the water has an important impact on the induced voltage. Therefore, the sensor must be submerged in water to measure. Another parameter that can affect the measure is temperature. However, in a previous work, García et al. (2019) tested the effect of temperature in inductive sensors. They obtained a change of 0.3 V between the temperatures of 1.2 °C to 20 °C with an induced voltage of 10.9 V.

Finally, the different sections of this chapter have been published in the following references (Basterrechea, 2020b), (Rocher, 2018a), and (Rocher, 2018b)

4 Turbidity Sensor.

In this chapter, we analyze the two prototypes of turbidimeter developed. First, we presented the development of a prototype to control eutrophication in irrigation channels and water bodies affected by overflows or illicit discharges. Next, we study the effect of water level in different turbidity concentrations. Finally, we improve the use of the infrared LED.

4.1 Turbidimeter to Eutrophication in water bodies.

As we saw previously, natural water bodies can be affected by overflows of combined sewerage, stormwater sewerage, or illicit direct discharges. The overflows and illicit discharge can affect the water quality and provide nutrients. The increase of nutrients in the water increases the eutrophication problem. One solution to prevent eutrophication events is using a turbidimeter that can differentiate between the turbidity caused by sediments and turbidity caused by algae. In previous works, this idea was developed by Parra (2018b). However, they only specify whether the turbidity is of sedimentary or algae origin. We want to know the percentage of algae or sediment in the water.

4.1.1 System Description.

The prototype used in this experiment is crafted in PVC and glass. The PVC has been selected because of its robustness and watertight properties, making it suitable for high durability. The glass contains the water to be measured; it is selected because of its transparent characteristics that will allow the path of light through the sample. The developed prototype is characterized by its modularity, ensuring that damaged elements can be easily replaced. The casing is performed with a 20 cm T-shaped PVC. This external module has an internal and outer diameter of 4 cm and 5.6 cm, respectively.

The internal section, where the sensing elements are placed, is made of PVC, with a length of 18 cm and a thickness of 0.3 cm. The inner diameter of this tube is 2.6 cm, and the external diameter is 3.2 cm. A total of 12 holes to place the sensing elements have been made in the inner tube, divided into two groups of six holes placed at 180° of each other. The space between holes in each group is 1 cm. On the one hand, as a light emitter, six LEDs (blue, green, yellow, orange, red, and infrared) are inserted in one of the groups of holes. On the other hand, as light receptors, five Light-Dependent Resistors (LDRs) are used for the visible light, and a photodiode is selected for the NIR light. Although six lights are included in the prototype, we focus on the visible lights. In our prototype, we select the use of LDR for visible light. The LDRs do not present response times as fast as photodiodes. In real conditions, this is an advantage since sudden changes will less influence the sensor's response in incident light. The possible sudden changes might include the pass of fauna, rocks, or flocs across the light pass. Furthermore, eutrophication processes are slow processes concerning the response time of an LDR. Therefore, the response time of our light detectors is appropriate to evaluate the algal growth. Finally, the electronic circuit of the LDR is more straightforward than the photodiode circuit, facilitating maintenance, repair, and construction tasks. The cover of the upper part of the sensor has been modified by creating a perforation to include the glass vial. This vial has an internal diameter of 0.9 cm and a length of 1.5 cm. Waterproof silicone was used to seal the space between PVC and the glass vial. The vial is aligned between the light emitters and receptors, allowing to measure the absorption of light without direct contact between sensing elements and water.

Figure 4.1 is represented a schematic of the prototype. Figure 4.2 presents the different sections of the developed prototype. Figure 4.2a represents the encapsulation of the prototype, Figure 4.2b the core of the sensor, and Figure 4.2c the vial where the sample is deposited. Finally, Figure 4.2d displays the arrangement of the LEDs and LDRs inside the prototype. Table 4.1 summarizes the dimensions of the prototype, and Table 4.2 outlines the characteristics of selected LEDs.



Figure 4.1. Prototype of algae turbidimeter

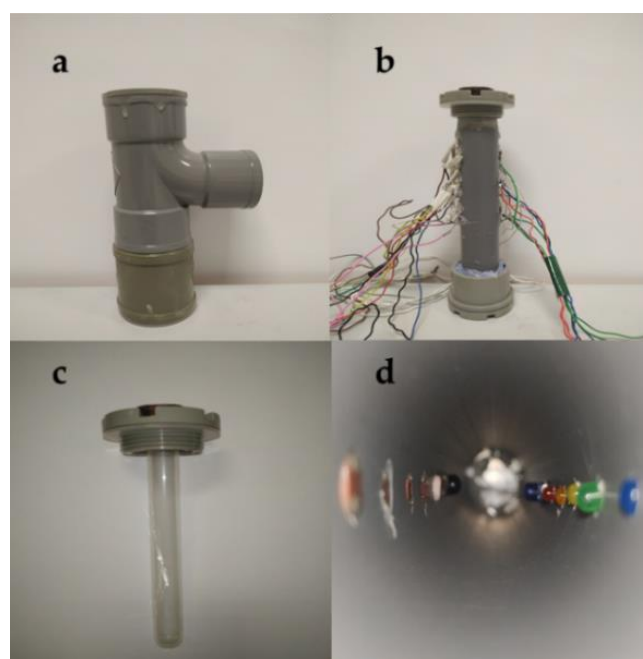


Figure 4.2. Representation of the used prototype.

(a) Casing; (b) Prototype; (c) Sample vial; and (d) Position of LEDs and LDRs.

Table 4.1. Dimensions of each section of the prototype.

	Encapsulate	Nucleus	Vial
External diameter (cm)	5.6	3.2	1.5
Internal diameter (cm)	4.0	2.6	0.9
Length (cm)	20	18	16
Thickness (mm)	80	30	5

Table 4.2. Characteristics of the LEDs of the prototype employed in these tests.

Characteristics	Blue	Green	Yellow	Orange	Red
Wavelength (nm)	467–476	562–575	581–594	581–618	612–625
Diameter (mm)	3	3	3	3	3

4.1.2 Test Bench.

This section describes the equipment used to perform the tests and the methodology selected for the entire data collection, calibration, and verification process.

4.1.2.1 Measuring Methodology.

In this subsection, the process followed for calibrating the sensor using different samples is detailed. A total of seven samples were prepared, two pure samples (one of sediment and one of *Chlorella vulgaris* (as algae)) and five mixed samples with different percentages of each turbidity source. The combinations used are: 80% sediment/20% algae; 60% sediment/40% algae; 40% sediment/60% algae; 20% sediment/80% algae. Drinking water from the tap was used to perform the samples. For these samples, sediment or algae are weighted to prepare the solution with a concentration of 7142 mg/L. The volume of the solutions is 100 mL. A serial dilution process is applied to generate the eight dilutions the each one of the solutions. The concentrations of the solutions are: 0 mg/L, 15 mg/L, 50 mg/L, 200 mg/L, 800 mg/L, 1500 mg/L, and 4000 mg/L.

Once we have obtained the different samples and their dilutions, 25 mL of each is used to take measurements with the prototype; 25 mL is the volume of the sensor vial. The aliquots are transferred to the vial, and the measurement process starts. The LEDs are powered sequentially (blue-green-yellow-orange-red), and the resistance of the associate LDR is measured to gather the data. The value of the LDR requires a short time to stabilize its measure. The data were collected once the value was stable. After each measurement, the LED is turned off, and the subsequent LEDs are powered. Using this methodology, we obtain the data as resistance values ($k\Omega$). A voltage divider has been simulated to attain the results in voltage units (V). The exact values of the voltage divider are presented in the results.

4.1.2.2 Instrumentation.

First, we describe the equipment used to power the systems and measure the light detectors' sensing elements' output signal. To power the LEDs, a FAC 662-B (Promax, 2019) generator has been used. LEDs are powered at 5 V with continuous current, and resistors of 470 Ω have been used. Regarding the light receptors, we focused on the use of visible light. Therefore, to measure the response of the LDRs, a multimeter TENMA 72-2600 (TENMA, 2022) has been used. To prepare the sample, a precision balance ENTRIS II model BCE223i-1x (Sartorius, 2022) was used to measure the weight of sediments and algae. To create the samples, tap water was used and a graduated cylinder with a volume of 100 mL and a precision of 1 mL.

4.1.3 Results.

In this section, the obtained results are presented. First, we compare the resistance values gathered in the different LDRs. Following, we transformed the resistance of the LDRs to voltage and evaluated the sensor's calibration with varying models of regression. Finally, we test the use of an artificial neural network to enhance the accuracy of the classification of samples.

4.1.3.1 Resistance of LDRs with the Use of a Combination of Turbidity Sources and Lights.

This section analyses the resistance values obtained for the different concentrations tested of sediment, *Chlorella vulgaris*, and their mixture with other lights in the LDRs used. First, we elaborated a multifactorial analysis of variance (ANOVA) to determine if there are significant differences between the type of turbidity and the concentration of solids. This information will indicate whether using the prototype to differentiate turbidity sources at different concentrations is possible. In Table 4.3, the results of the multifactorial ANOVA are shown. We observe that the p -values are below 0.05 in all the cases. Thus, we can determine that there are significant differences in the resistance values of the LDRs between the different types of turbidity sources

and the tested concentrations. This indicates that it is feasible to distinguish the turbidity concentration and its origin by using the gathered data.

Table 4.3. Multifactorial ANOVA for the LDR resistances in the different lights.

Light colour	<i>p</i> -Value for the Evaluated Factors of Turbidity	
	Turbidity source	Concentration of turbidity
Blue	0.0000	0.0000
Green	0.0004	0.0000
Yellow	0.0003	0.0000
Orange	0.0011	0.0000
Red	0.0006	0.0000

Next, we evaluated these differences. Therefore, we assess the resistance values obtained for the different turbidity sources and concentrations. The figures below represent the resistance values of the LDRs for the different light sources. Although the *X*-axis represents the tested lights, the concentration levels are represented in *Y*-axis logarithmically. In general terms, we can observe an exponential growth of the resistances with the increase in turbidity, except with the red and orange lights. In these cases, the resistance values decrease between 0 to 15 mg/L in all the samples tested and increase again until 4000 mg/L. This effect might be produced by the different reflections and refractions of light in the glass compared with other LEDs due to slight differences during the assembling.

In Figure 4.3 and Figure 4.4, measured resistance values of LDRs are represented for the different tested concentrations of sediments, see Figure 4.3; and *Chlorella vulgaris*, see Figure 4.4. Except for low concentrations, 15 and 50 mg/L, gathered resistance values are higher when *Chlorella vulgaris* is used as a turbidity source for all light sources. The observed differences are greater for the highest concentrations. For the green light, especially for the concentration of 15 mg/L, there is a big difference in the resistance values, 22.5 k Ω in algae turbidity and 27.93 k Ω in sediment. Regarding the concentration of 50 mg/L, the resistance values for algae and sediments are similar, with values of 27.5 to 28.3 k Ω , respectively. The same phenomenon occurs when the yellow, orange, and red lights are used. Resistance of LDRs presents a high difference between the algae and the sediments at 15 mg/L. Nonetheless, for the concentration of 50 mg/L, the resistance values are similar regardless of the turbidity source. This might occur due to the algae's liberation from pigments into the water, causing an increase in light absorption at specific wavelengths.

Figure 4.5 is represented the resistance obtained with the mix of 80% of sediment and 20% algae. With the blue light, there is an exponential growth of the resistance. In the three low concentrations of solids tested, the resistance values are near 8.8 k Ω . After these concentrations, the maximum resistance is measured in 4000 mg/L with a mean of 201.5 k Ω . The maximum resistance is obtained by the concentration of 4000 mg/L using green light (233.5 k Ω of mean). In contrast to blue light, there is a difference between the concentration of 0 and 15 mg/L in the green light. The resistance increases from 20.9 k Ω to 27.6 k Ω , respectively. In the other concentrations, we observe an exponential increase in the resistance. This change between the concentration of 0 to 15 mg/L is also observed in the yellow light. In this, the resistance increase is 1.2 k Ω (from 3.7 to 4.9 k Ω). In the blue, green and yellow lights, the LDR resistances increase between the concentrations 0 to 15 mg/L. However, there is a decrease in the LDR resistance between the concentrations 0 to 15 mg/L in the orange and red lights.

The same behaviours are observed in the other mixtures. Figure 4.6 are represented the values obtained in the different lights with the mixture of 60% sediment and 40% algae. Of all the mixtures made, this is the only one where the maximum resistance is obtained with blue light with a value of 347.4 k Ω compared to 323.9 k Ω obtained with the green light with a concentration of

4000 mg/L. In Figure 4.7, the mixture 40% sediment and 60% algae are shown. In this, the maximum resistance is in the use of green light and the concentration of 4000 mg/L with a value of 414.6 k Ω as the mean. Finally, the mixture of 20% sediment and 80% algae is presented in Figure 4.8. In this, the mean of maximum resistances is 492.1 k Ω . As in the rest of the samples, the same trends of resistance increase are followed. The resistance values of mixed samples are expected to be between the resistance values of sediment and algae. In general terms, resistance values are between pure sediment and algae resistance. When resistance values are out of the expected interval, the gathered values are like the values of sediment or algae. As occurred in the results of pure samples, the increase in solids concentrations in mixed samples led to an upsurge of the LRDs resistance values in all cases (except the rise from 0 to 15 mg/L in red and orange LEDs).

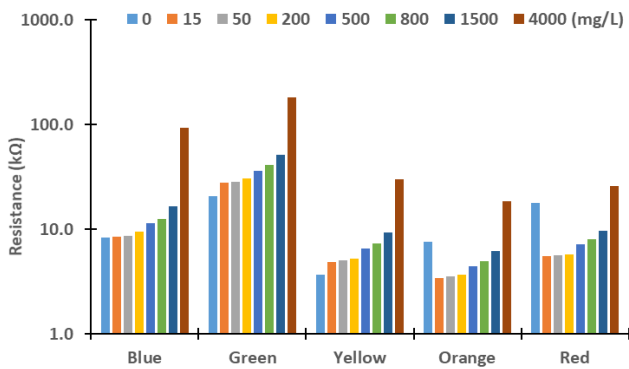


Figure 4.3. Measured resistance values for sediment.

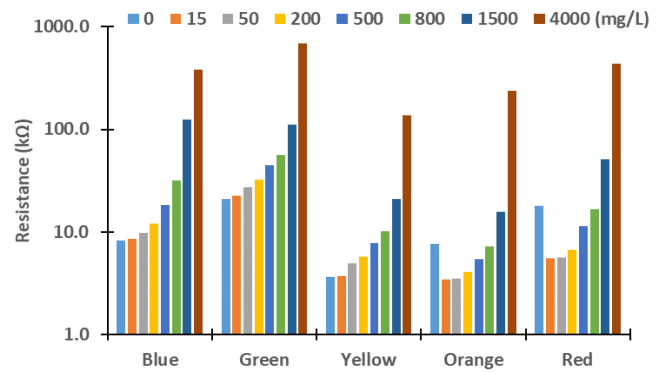


Figure 4.4. Measured resistance values for algae.

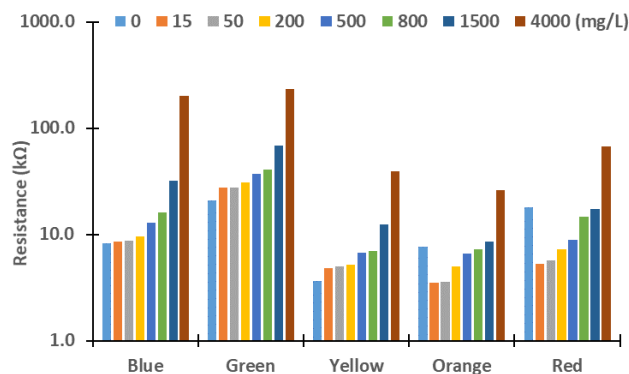


Figure 4.5. Measured resistance values for mixture 80% sediment and 20% algae.

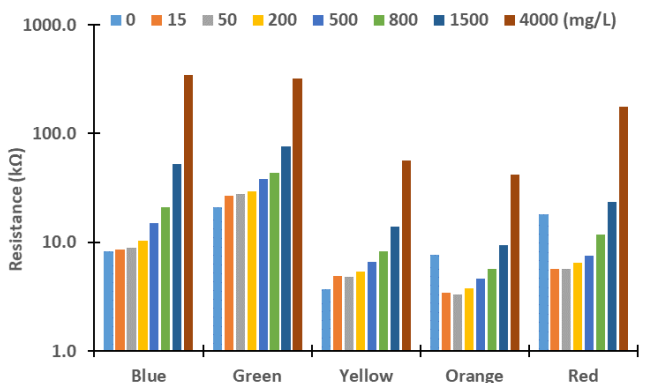


Figure 4.6. Measured resistance values for mixture 60% sediment and 40% algae.

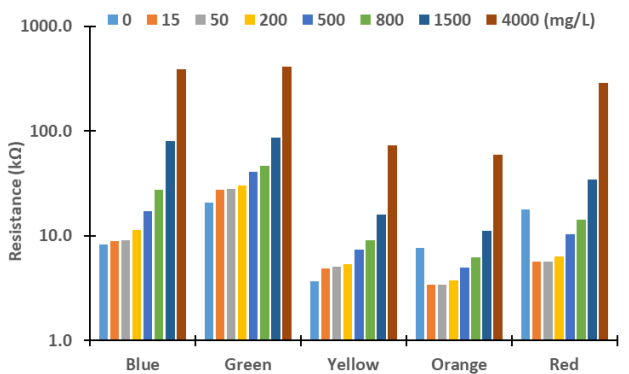


Figure 4.7. Measured resistance values for mixture 40% sediment and 60% algae.

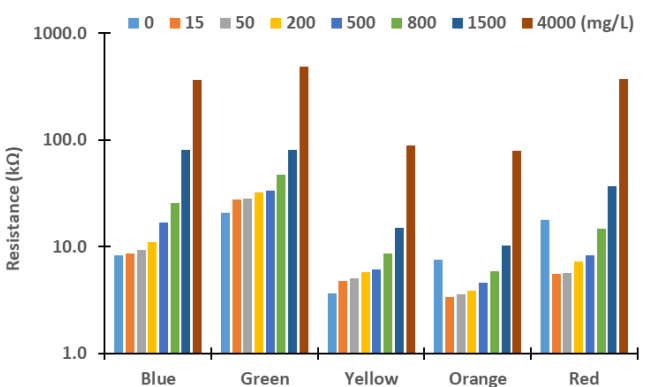


Figure 4.8. Measured resistance values for mixture 20% sediment and 80% algae.

4.1.3.2 Calibration of the Sensor for Different Sources.

In this subsection, we describe the calibration models for the different lights and turbidity sources. Firstly, resistances are converted into voltages, which are the variables measured by the node. Then, we use Statgraphics Centurion XVIII (Statgraphics, 2022) to obtain the mathematical models that correlate the solids concentration with the input voltage at the node, which is the output voltage of the voltage divider.

To simulate the operation of the node, we use a voltage divider, see Equation (4.1), to determine the change of voltage in the node input due to the differences in resistance of the LDRs. Where input voltage (IV) is the voltage provided by the node, the output voltage (V_{out}) is the voltage after the voltage divider (the input voltage for the node), the circuit resistance (CR) is the value of second resistance, the value we will adjust, and the LDR resistance (R_{LDR}) is the resistance of each one of the LDRs of the prototype. As IV, we use 3.3 V since it is the typical voltage of pins in different microcontrollers such as Arduino or Raspberry.

$$V_{out}(V) = \frac{IV(V) * R_{LDR}(\Omega)}{CR(\Omega) + R_{LDR}(\Omega)} \quad (4.1)$$

To improve the sensibility of our sensor, we select a CR that maximizes the voltage difference between 15 mg/L and 500 mg/L for a particular turbidity source. We delete the concentration equal to 0 mg/L of the calibration. Thus, we chose 15 mg/L as the minimum expected concentration. We select 500 mg/L because we do not expect the concentration of sediments to exceed 500 mg/L in normal conditions. We need to choose one of the different turbidity sources to maximize the differences. Sediment was selected as a turbidity source since it has the minor difference between the minimum and maximum resistance values. Considering that resistances calculated with Equation (4.1) are not standard resistance values and those resistances are hard to obtain, we use the most similar standard resistance. In Table 4.4, there are the values of resistance obtained by this and the standard values used.

Table 4.4. Mathematical and standard resistance to fixed resistance in the voltage divider.

Light Source	Blue	Green	Yellow	Orange	Red
Mathematical resistance (k Ω)	9.7	27.6	4.9	3.9	6.3
Standard resistance (k Ω)	10.0	27.0	5.1	3.9	6.8

Once we have established the fixed resistance values in the voltage divider, we can calculate the node's voltage values. It is important to note that the node cannot measure all values of the analogic signals. The analogic pins convert the signal from analogue to digital. For this function, the node has a limited number of values (10 bits). Therefore, we must convert the analogue values obtained with Equation (4.1) into digital values with 10 bits of resolution. First, we determine the minimum input voltage in the node when the different light sources are used. We established that the maximum voltage is 3.3 V, the maximum value V_{out} can reach. After that, we calculate the difference between the minimum and maximum voltage for each light. This value is divided into 1024 (10 bits), and we obtain the accuracy of the reading to calculate the new voltage values (Equation (4.2)). In Equation (4.2), V_{outc} is the new corrected voltage. V_{out} is the value obtained, and precision is the precision of the input for the light source used. In Table 4.5, we show the calculated precision of the analogy.

Table 4.5. The precision of the analogy entry.

	Blue	Green	Yellow	Orange	Red
Minimum Voltage (V)	1.497	1.438	1.381	1.521	1.441
Maximum Voltage (V)	3.300	3.300	3.300	3.300	3.300
Difference (V)	1.803	1.862	1.919	1.779	1.859
Precision (mV)	1.76	1.82	1.87	1.74	1.82

$$V_{outc} (V) = \text{Integer} \left(\frac{V_{out} (V)}{\text{Precision} (V)} \right) * \text{Precision} (V) \quad (4.2)$$

The following step is to have a mathematical model that correlates the concentration of both two types of solids (sediment and algae) in the water with the gathered V_{out} in the node when one or more lights are used. We use Statgraphics Centurion XVIII (Statgraphics, 2022) to generate the regression models. We search for the best model with the higher R^2 coefficient that relates them. Our objective with the models was to determine the concentration of one of the turbidity sources, alga in this case, and infer the turbidity of the second source based on the total concentration of solids in water. This is estimated using the infrared LED described in (Parra, 2018b).

With Statgraphics Centurion XVIII (Statgraphics, 2022), we performed a multiple regression analysis to determine the model that related the V_{out} obtained with the different light sources with the turbidity source or sources. In the initial model, the voltage obtained with the orange light is insignificant, with a p -value of 0.1818. We delete this parameter and the new model represented in Equation 4.3 with an R^2 of 0.7721. In Equation 4.3, V_{outB} , V_{outG} , V_{outY} , and V_{outR} represent blue, green, yellow, and red output voltage, respectively. Equation 4.3 model is modelled using all the gathered data (all turbidity sources and all tested concentrations). Figure 4.9 represents the predicted versus the observed values of the concentration of algae using Equation (4.3). We can observe many differences between the predicted and the observed values.

$$\text{Algae (mg/L)} = -1547.2 - 2654 * V_{outB} (V) - 7293.1 * V_{outG} (V) + 8523 * V_{outY} (V) + 2688 * V_{outR} (V) \quad (4.3)$$

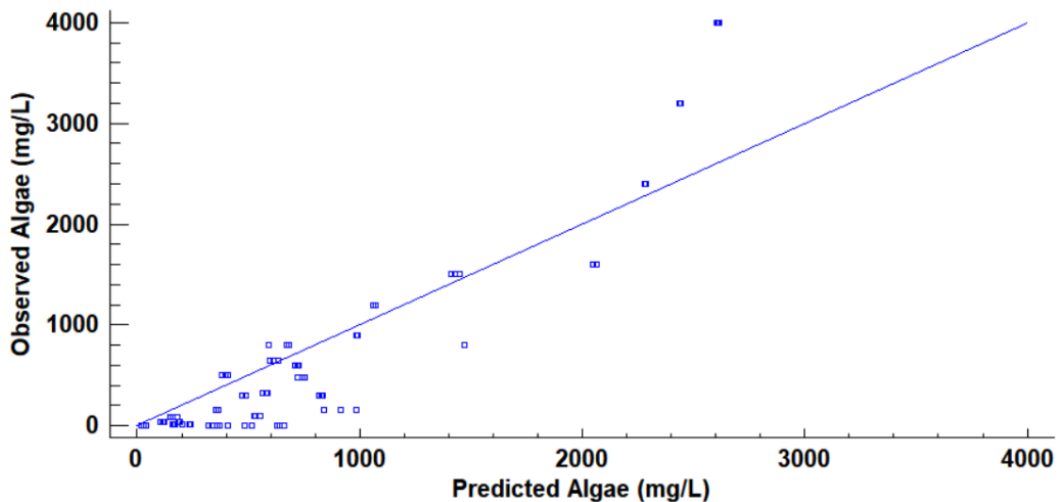


Figure 4.9. Observed versus predicted values of algae concentration with Equation 4.3.

Another option is using Eureka software (Datarobot, 2022) to obtain a mathematical model that correlates with the gathered data. Eureka is software that searches for a model that adapts the

observed values with a mathematical model. As previously, the orange light values are discarded. Thus, we do not include this variable in the Eureka model. We select a model with low complexity (16 of Eureka complexity value) and high R^2 (R^2 of 0.9542). The model used is represented in Equation (4.4). We observe that the voltage obtained with yellow light parameter is not included in this model. The predicted versus observed values of algae concentration are represented in Figure 4.10. As in the previous case, the difference between predicted and observed is high.

The problem with this type of regression is caused because of the wide range of concentrations tested and the non-linear response. For this reason, we discard the use of multiple regression with all the concentrations. Therefore, it is necessary to reduce data variability to obtain better adjustments.

$$\text{Alga} \left(\frac{\text{mg}}{\text{L}} \right) = 498.6 * V_{outB}(V) + \frac{-81.5}{V_{outB}(V) - 3.3} - 802.3 - V_{outG}(V)^2 \quad (4.4)$$

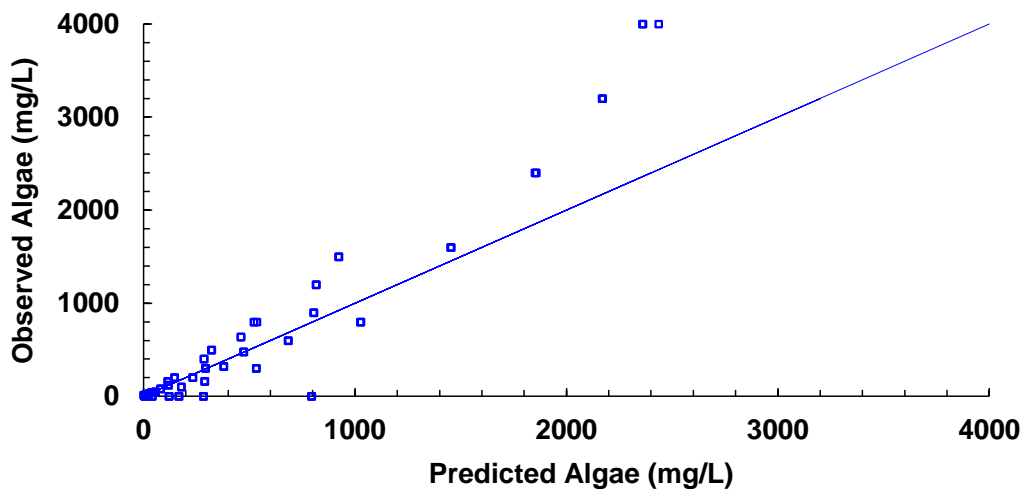


Figure 4.10. Observed vs predicted values of algae concentration with Eureka.

As the previous solution does not present a good performance, we decide to use different models according to the concentration of solids in the water. First, we determine the solids concentration with a turbidimeter. We will select a particular mathematical model according to the concentration of solids. In the case of intermediate concentrations between the studied concentrations, an interpolation is performed.

Figure 4.11, Figure 4.12, Figure 4.13, Figure 4.14, Figure 4.15, Figure 4.16, Figure 4.17, and Figure 4.18 represent each solid concentration's predictive versus observed algae concentration. In addition, we can observe the mathematical models and R^2 in Table 4.6. The lowest value of R^2 is presented in the Equation (4.5) of 15 mg/L with a value of 0.8620, see Figure 4.12. In this concentration, predicted values differ from observed more than in other concentrations. The rest of the models used present good values of R^2 . The model calculated for 15 mg/L of solids present and a relative average error of 40%. The lower errors are in the 800, 500, and 200 mg/L concentrations, with relative average errors of 4.9%, 5.2%, and 6.2%, respectively. The models for 50 and 1500 mg/L concentration are characterized by 12.1% and 10.0% of relative average error. Finally, the REs in the mix of sediment or algae are maximum in the concentration of 80% sediment and 20% algae, with a RE of 32.1%. The rest of the samples with mixed turbidity sources have REs between 4.3% to 11.1%.

Figure 4.18 illustrates the observed versus predicted voltage values for all joined models. We can observe that the combined model presents good predictability of the algae values. The average error between the predictive algae concentration and the observed is 36.52 mg/L and a RE of 12.56%.

Table 4.6. Values of R².

Concentration (mg/L)	15	50	200	500	800	1500	4000
R ²	0.8620	0.9773	0.9975	0.9854	0.9974	0.9568	0.9890
Equation	4.5	4.6	4.7	4.8	4.9	4.10	4.11

$$Alga (mg/L) = 115.46 + 292.87V_{outB}(V) - 67.919V_{outG}(V) - 288.19V_{outO}(V) \quad (4.5)$$

$$Alga (mg/L) = -1440.44 + 509.45V_{outB}(V) - 157.68V_{outO}(V) + 610.25V_{outR}(V) \quad (4.6)$$

$$Alga (mg/L) = -2032.23 + 649.97V_{outB}(V) - 424.16V_{outG}(V) + 872.32V_{outY}(V) + 173.63V_{outO}(V) \quad (4.7)$$

$$Alga (mg/L) = 1982.85 + 5819.45V_{outG}(V) - 8138.27V_{outY}(V) - 933.002V_{outO}(V) + 2205.87V_{outR}(V) \quad (4.8)$$

$$Alga (mg/L) = -4306.95 + 3180.65V_{outG}(V) - 909.23V_{outY}(V) - 1448.35V_{outO}(V) + 1342.88V_{outR}(V) \quad (4.9)$$

$$Alga (mg/L) = 4521.11 - 16788.3V_{outY}(V) + 13227.3V_{outO}(V) + 2210.21V_{outR}(V) \quad (4.10)$$

$$Alga (mg/L) = -22384.7 + 10404.0V_{outO}(V) - 2251.3V_{outR}(V) \quad (4.11)$$

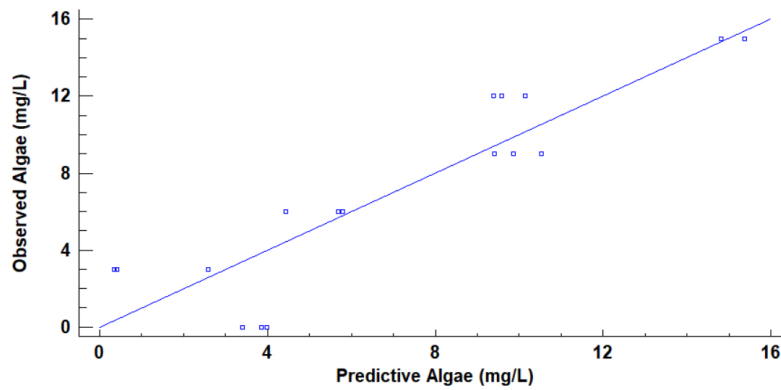


Figure 4.11. Observed vs predicted values of algae concentration with a solid concentration of 15 mg/L.

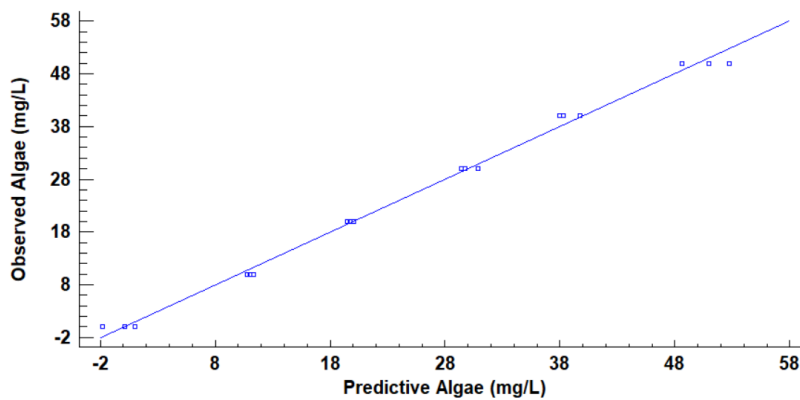


Figure 4.12. Observed vs predicted values of algae concentration with a solid concentration of 50 mg/L.

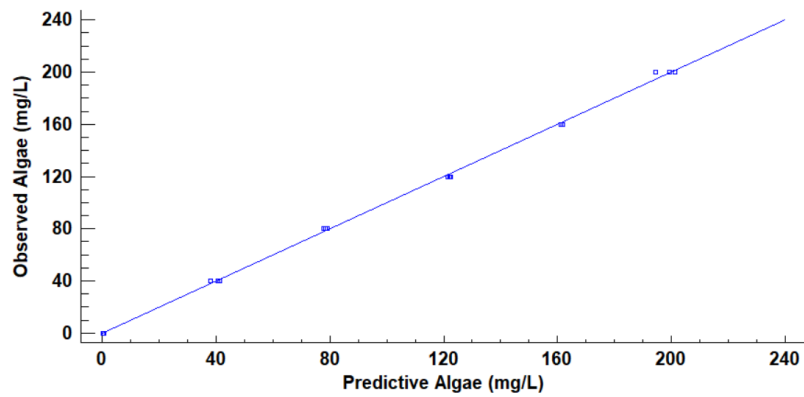


Figure 4.13. Observed vs predicted values of algae concentration with a solid concentration of 200 mg/L.

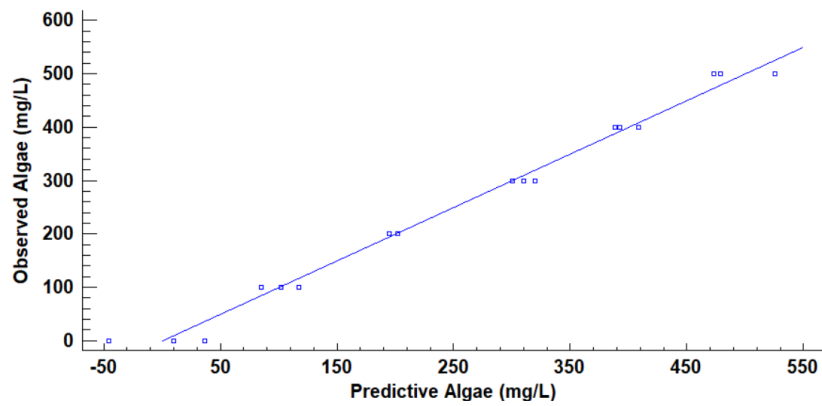


Figure 4.14. Observed vs predicted values of algae concentration with a solid concentration of 500 mg/L.

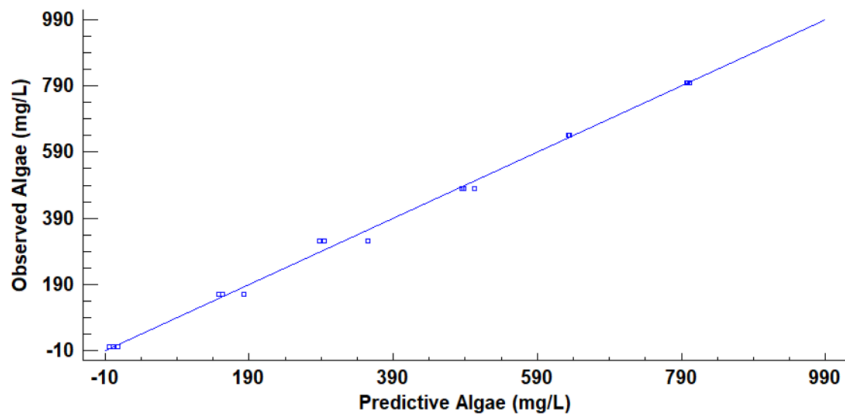


Figure 4.15. Observed vs predicted values of algae concentration with a solid concentration of 800 mg/L.

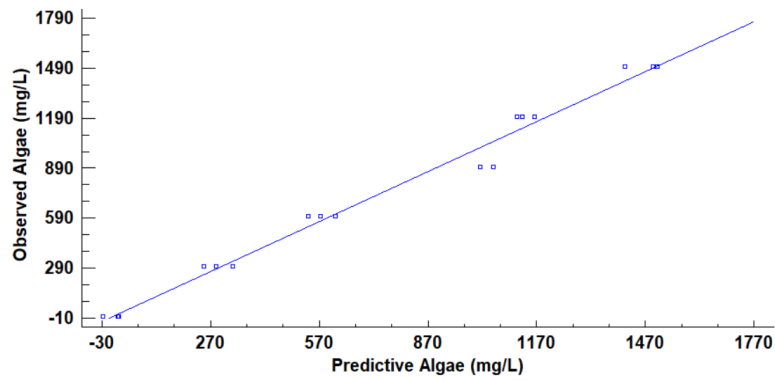


Figure 4.16. Observed vs predicted values of algae concentration with a solid concentration of 1500 mg/L.

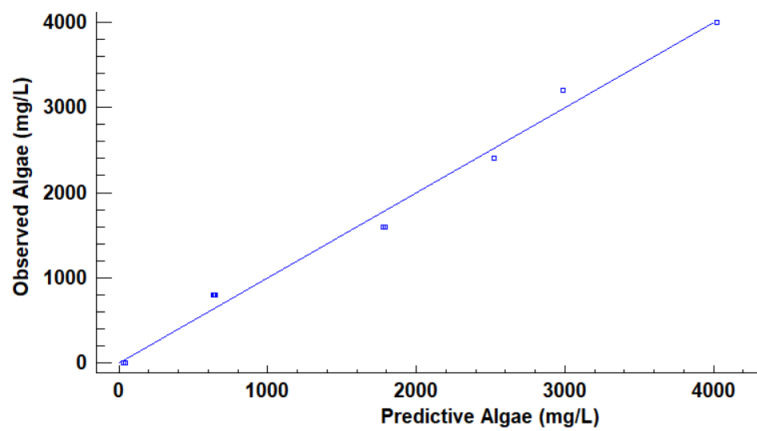


Figure 4.17. Observed vs predicted values of algae concentration with a solid concentration of 4000 mg/L.

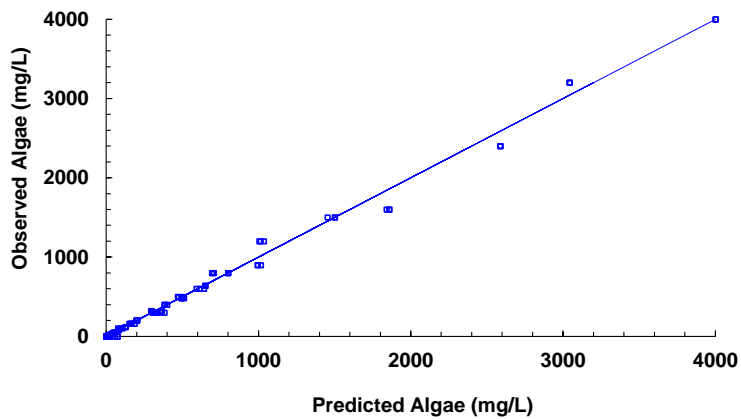


Figure 4.18. Observed vs predicted values of algae concentration with different models.

If we observe the different figures of the models presented, in some cases, we find that the concentration of algae is negative or higher than solid concentration. As this cannot happen in natural conditions, we apply two modifications to the results. On the one hand, if the result is a negative concentration, the result will be changed to 0 mg/L of Algae. On the other hand, if the result is an algae concentration higher than a solid concentration, the result will be adjusted to a solid concentration (100% algae). We reduce the Absolute Error (AE) to 31.95 mg/L with these simple modifications and the RE to 11.0%.

Finally, Figure 4.19 present the algorithm of the prototype. When the prototype starts the measure, we set different thresholds. Then, we start the function loop. First, the data of the different photoreceptors is obtained. With infrared light, we determine the concentration of solids. If the solid concentration is lower than 15 mg/L, the prototype will be on standby until the subsequent measurement. If the solid concentration is higher than 15 mg/L and lower than 4000 mg/L, the prototype will use the closest equations for the solids concentration and perform interpolation to obtain the algae concentration. Once the concentration of algae is obtained, the corrections are applied to verify that the concentration is greater than 0 and lower than or equal to the concentration of solids. Finally, this information is sent, and the prototype will rest until the subsequent measurement. If the concentration is higher than 4000 mg/L, the prototype sends an alarm. We assume that this concentration is too high for irrigation water. After sending the warning, as in the previous cases, the sensor will go into standby status.

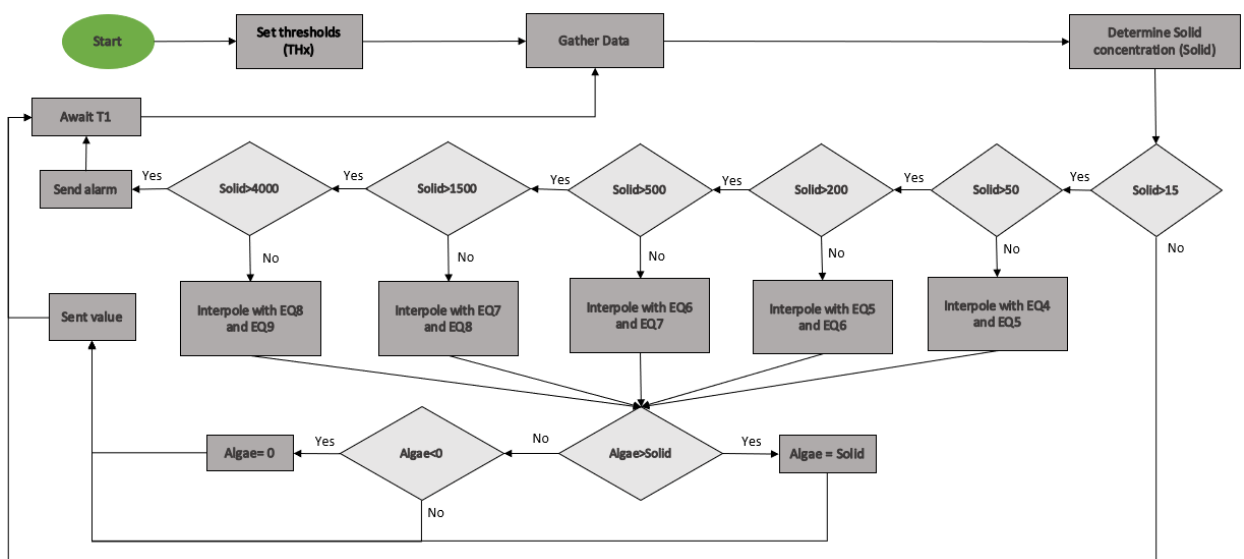


Figure 4.19. Prototype algorithm.

With the multiple regression models adjusted for every tested concentration, it was possible to reduce the error and reach a reasonable adjustment that allowed an optimal operation of the sensor. The computational requirements of including these models do not differ too much from the requirement for a single multiple regression model. The errors obtained in this calibration and the R^2 are similar to those in other papers describing low-cost sensors. For example, in (Basterrechea, 2021), another optical-based prototype for water quality monitoring, REs between 4.9% and 19.6% are related, and R^2 values are between 0.99 and 0.97. Unless R^2 between this range characterizes the model for 15 mg/L, the rest of the models and the average RE is also between the range of (Basterrechea, 2021).

4.1.3.3 Artificial Neural Network.

In the previous section, we study the use of different models to determine the concentration of algae. Now, we analyze the use of an artificial neural network to determine the percentage of algae in the different mixtures as an alternative to previous models. The aim of exploring this option is that some nodes might be able to use these systems in the short term to maintain low-cost devices and low-energy consumption. Therefore, we wish to compare the performance of existing solutions which can be included nowadays in the node with the nearby possibilities.

To develop a neural network analysis, we use Statgraphics Centurion XVIII (Statgraphics, 2022) software. 90 and 36 random values are used for the training and validation phases. The

analyses were performed five times to include the possible effect of this random selection on the success. Figure 4.20 represents the values of training and validation success for different combinations of lights. We test the use of 2, 3, 4, and 5 lights. The best percentage of success is 93% with the use of three LEDs (green, yellow, and red); another high rate of success is for the use of the 5 LEDs, with a value of 92%. In general terms, there does not seem to be a relationship between the use of a specific light source and a high success rate in the neural network. Regarding validation, the highest value is 98% with the use of 5 LEDs.

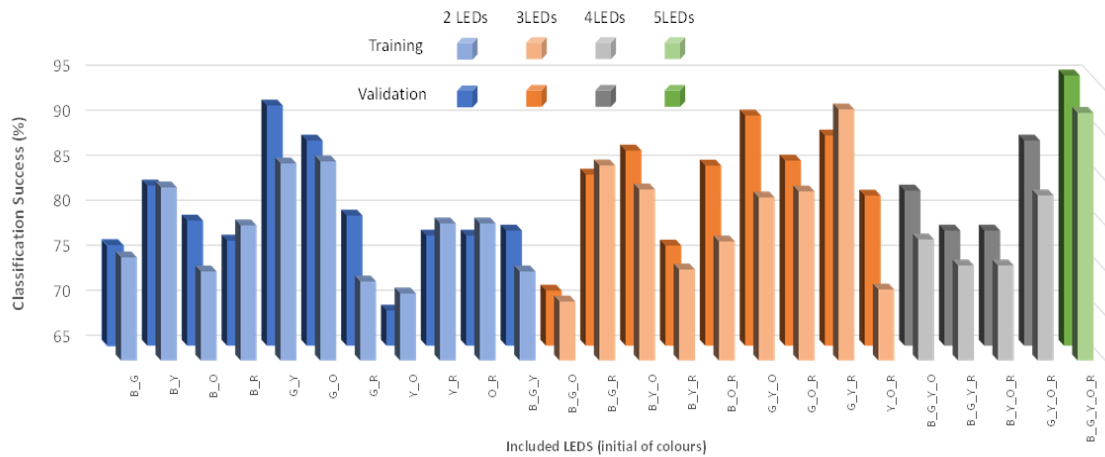


Figure 4.20. Training and validation of neural network.

We have selected 5 LEDs for our neural network since it is the one with the highest percentage of success. Table 4.7, and Table 4.8 summarize the success of training and validation, respectively. In the case of training, the values of success are high. The group with less percentage of success is 60% of algae. In this group, two points are misclassified as 0% of algae. The same occurs in the group of 40% algae, where two other values have been classified in the group without algae. Regarding the validation, we observed 100% effectiveness when classifying the values.

Table 4.7. Correctly classified cases in the training dataset.

Actual Group	Predicted Group						Correctly Classified
	0	20	40	60	80	100	
0	13	1	0	0	0	0	92.86%
20	1	16	0	0	0	0	94.12%
40	2	0	13	0	0	0	86.67%
60	2	0	0	12	0	0	85.71%
80	0	0	1	0	14	0	93.33%
100	0	0	0	0	0	15	100.00%

Table 4.8. Correctly classified cases in the validation dataset.

Actual Group	Predicted Group						Correctly Classified
	0	20	40	60	80	100	
0	7	0	0	0	0	0	100%
20	0	4	0	0	0	0	100%
40	0	0	6	0	0	0	100%
60	0	0	0	7	0	0	100%
80	0	0	0	0	6	0	100%
100	0	0	0	0	0	6	100%

The use of an artificial neural network implies a tremendous demand for calculation. Although there are different proposals for implementing artificial neural networks in microcontrollers, we consider that the best option to monitor the presence of algae or sediments and their mixtures is the proposed algorithm. Even though the algorithm can be less efficient than an artificial neural network, it requires a lower calculation power. If better precision is required, the data can be sent to a computer to perform the neural network. This solution would improve the determination of the mixing percentage at the cost of higher energy consumption.

4.2 Determine solid. Effect on algae and sediment concentrations in mg/L in the turbidity (NTU).

As we have seen previously, our prototype to determine the percentage of algae in water needs solid concentration knowledge. Thus, it is necessary the development a system to determine the solid concentration of the sample. Section 2.3.5 shows that the turbidity sensor is the better option for continuously controlling the solids in water. However, the NTU contribution of a gram of solids is different from algae's contribution. That is why we need to know the equivalence of grams of solids with grams of algae in order to be able to determine the concentration of algae and solids using turbidity. Next, the different mathematical models and algorithm used in our turbidimeter are presented.

4.2.1 Test Bench.

This section presents the materials and methodology used in the experiment. To perform the measures, we use a commercial turbidimeter model TU-2016. The samples are elaborated using two sources of turbidity. As sediment, we use a mix of silt and clay from fluvial deposits sieved with a maximum of 0.06 mm. As algae, we use a commercial pack of *Algae chlorella*. We elaborate pure samples of Algae and turbidity with a concentration of 15 g/l. Next, we perform 200 mL of five samples with the combination of the pure samples. The combinations are shown in Table 4.9. With these samples, we perform different dilutions to obtain samples with concentrations of 0, 15, 50, 200, 800, 1500, and 4000 mg/L.

Table 4.9. Samples elaborated

Sample	1	2	3	4	5	6
% Algae	100	80	60	40	20	0
%Sediment	0	20	40	60	80	100

4.2.2 Results.

In this subsection, we analyze the turbidity of different samples with a mixture of algae and sediments.

Figure 4.21 represents the NTU obtained by the different mixtures of algae and sediment in different solids concentrations. In concentrations lower than 4000 mg/L, there is an increase in turbidity with the rise of the % of sediments. Instead, in the concentration of 4000 mg/L, the turbidity is reduced with the increase in the % of sediment. In addition, in the concentration of 1500 mg/L, the turbidity in the % of sediment of 80 and 100 % is similar with 690 and 692 NTU values, respectively. If we observe Figure 4.22, we can observe that between the concentration of 0 to 1500 mg/L, the sediment samples present higher turbidity than algae samples. The opposite occurs in the concentration of 4000 mg/L. This occurs because in the sediment samples, the turbidity limit is near 917 NTU, and in the algae, samples are higher than 1039 NTU. For this

reason, in the concentration of 4000 mg/L, when we reduce the sediment concentration, the samples' turbidity increases.

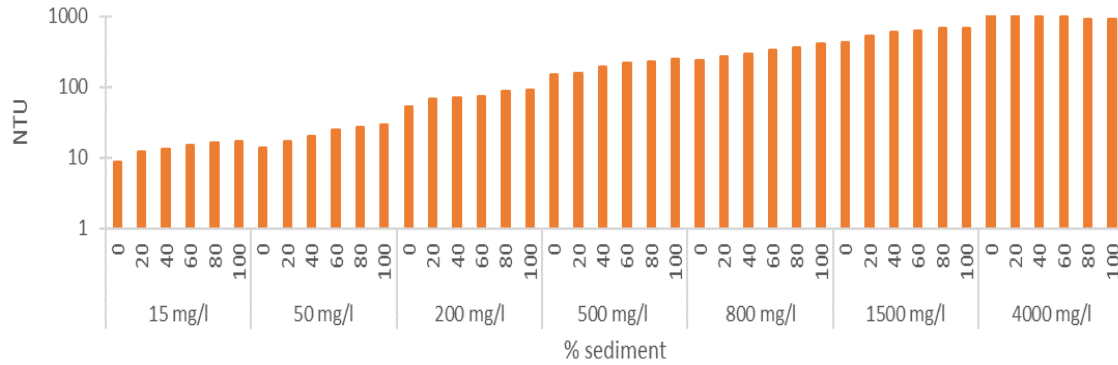


Figure 4.21. NTU in the different concentrations of solids and % of sediments.

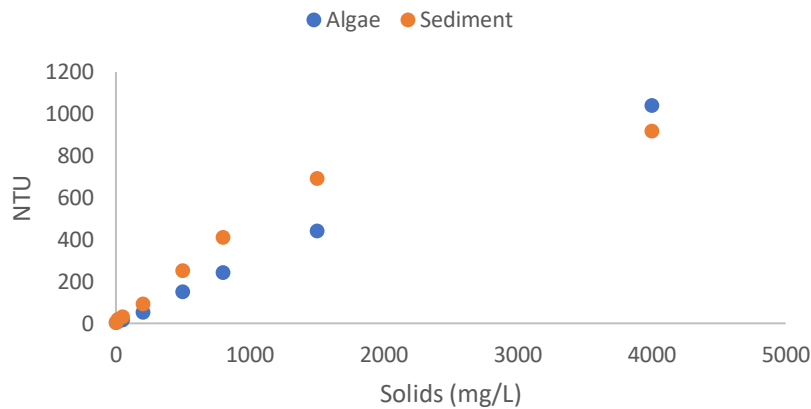


Figure 4.22. Turbidity of samples with pure Algae and Sediment

Equation 4.12 related the concentration of solids in mg/L to the NTU of algae. We use statistics to calculate this model. The best model is a double square with a R^2 of 0.9985. However, we choose the lineal model ($R^2=0.9972$) to represent turbidity's evolution with the algae solids' increase. Because the double square cannot be used in low concentrations of Algae. The R^2 of the double square is 99.85%. In the case of the sediment, we select a polynomic model represented in 4.13 with an R^2 of 0.9986.

$$\text{Solids (mg/L)} = -50.5728 + 3.82683 \cdot \text{NTU}_{\text{algae}} \quad (4.12)$$

$$\text{Solids (mg/L)} = -9E^{-5} \text{NTU}_{\text{sediment}}^2 + 0.5908 \text{NTU}_{\text{sediment}} - 4.9636 \quad (4.13)$$

First, we analyzed the correlation between sediment concentration and algae with the turbidity observed. We obtained a correlation between the turbidity values and the concentrations of sediment and algae with a P-value of 0.0000. We use the software Eureqa (Datarobot, 2022) to elaborate a model to relate turbidity with the values of concentration of algae and sediment. To elaborate on the model, we divide the data into two categories calibrations and verification. The data assigned in each category are randomly selected. For it, we located the data in an excel archive and generated a new column with random integers numbers between 1 to 3. The line with

a value of 3 is selected for verification and the other for calibration. We obtained 27 values for the calibration and 17 values for the verification. We obtained Equations (4.14), (4.15), and (4.16) that related the concentration of algae [A] and sediment [S] in mg/L with the NTU. These equations present R^2 values of 0.9991, 0.9961, and 0.9856, indicating a good correlation. The errors obtained by the equations in the calibration and verification are shown in Table 4.8 the errors of the 3 models are presented. We can check that the errors in the verification are higher than in the calibration, and with the increase in the complexity of the model, the errors decrease. The absolute minimum errors are 6.0 NTUs in the calibration and 17.8 NTUs in the verification. That supposes an AE of 10.7 NTU.

Figure 4.23 are presented the observed versus the predicted values of the three models. The three models present essential differences in the higher solids concentrations. Model 4.16 has essential differences between the observed NTUs of 592, 630, and 692 and the predicted NTUs. These NTUs correspond to the concentration of 1500 mg/L.

$$\begin{aligned} \text{NTU} = & 4.1169 + 0.4435[S] + 0.2964[A] + 1.6364E^{-4}[A][S] \\ & + 4.8604E^{-5}[S]^2 - 2.5606E^{-8}[S]^3 - 6.0049E^{-8}[S][A]^2 \\ & - 8.3739E^{-8}[A][S]^2 \end{aligned} \quad (4.14)$$

$$\text{NTU} = 0.5811[S] + 0.3025[A] - 1.0620E^{-4}[A][S] - 8.797E^{-5}[S]^2 \quad (4.15)$$

$$\text{NTU} = \frac{1421.2243[S] + 665.3329[A]}{2199.4485 + [S]} \quad (4.16)$$

In Table 4.10, the errors of the 3 models are presented. We can check that the errors in the verification are higher than in the calibration, and with the increase in the complexity of the model, the errors decrease. The absolute minimum errors are 6.0 NTUs in the calibration and 17.8 NTUs in the verification. That supposes an AE of 10.7 NTU.

Figure 4.23 are presented the observed versus the predicted values of the three models. The three models present essential differences in the higher solids concentrations. The model given in equation 4.16 has essential differences between the observed NTUs of 592, 630, and 692 and the predicted NTUs. These NTUs correspond to the concentration of 1500 mg/L.

Table 4.10. Absolute and REs of Eureka models with NTU.

Size	Error	Calibration	Verification	Total
45	Absolute (NTU)	6.0	17.8	10.7
	Relative (%)	7.4	11.4	9.0
19	Absolute (NTU)	13.0	24.3	17.5
	Relative (%)	11.3	21.0	15.1
12	Absolute (NTU)	21.2	25.2	22.8
	Relative (%)	13.0	21.4	16.3

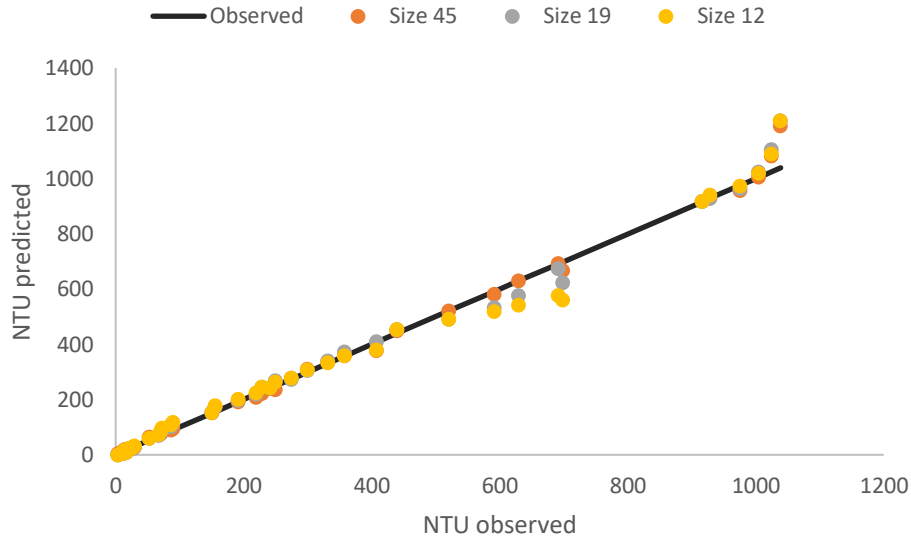


Figure 4.23. NTU predicted versus NTU observed in Eureka models

As we saw in section 4.1, it is necessary to know the total solids' concentration to determine the solids' percentage of algae and sediments. The better option to monitor the solid concentration is the use of turbidity sensor. However, algae and sediments provide different values of turbidity per gram. Therefore, we elaborated an interactive process to determine the percentage of algae and sediments. This process is represented in Figure 4.24. First, we determine the value of turbidity of the sample. For the first interaction, we assume that the percentage of algae is 100%. With this assumption, we calculate the solid concentration with equation 4.12. Knowing the amount of solids, we apply the algorithm we have seen in Figure 4.19. With this algorithm, we obtain the algae and sediment concentration and can apply equation 4.15. With this equation, we calculate NTU's theoretical value with these algae and sediment concentrations (NTUp). If the value of NTUp is different from the value of NTU that we are measuring with the sensor, we repeat the process with the new values of the concentration of algae and sediment using equation 4.18. As this process can be taken to infinity, we have decided that it is considered finished if the process reaches 20 interactions.

$$\begin{aligned} \text{Solids} \left(\frac{mg}{L} \right) = & 2.4201NTU + 0.2699Algae + 7.7682E^{-12}NTU^5 \\ & + 2.6837E^{-6}Algae * NTU^2 - 17.4815 - 4.1994E^{-6}NTU^3 \\ & - 3.8049E^{-9} * Algae * NTU^3 \end{aligned} \quad (4.17)$$

$$\begin{aligned} \text{Solids} \left(\frac{mg}{L} \right) = & 2.2321 * NTU + 3.0122E^{-12}NTU^5 - 5.4230E^{-4}NTU \\ & * Algae \end{aligned} \quad (4.18)$$

$$\text{Solids} \left(\frac{mg}{L} \right) = Algae + 4.7524E^{-3}NTU^2 - 1.3269E^{-3} * NTU * Algae \quad (4.19)$$

Table 4.11. Absolute and REs of Eureka models to determine solids.

Size	Error	Calibration	Verification	Total
47	Absolute (mg/L)	27.5	129.4	64.3
	Relative (%)	7.6	15.4	11.4
21	Absolute (mg/L)	108.8	160.5	125.2
	Relative (%)	26.8	39.8	31.7
13	Absolute (mg/L)	138.8	106.0	123.4
	Relative (%)	29.4	28.8	28.5

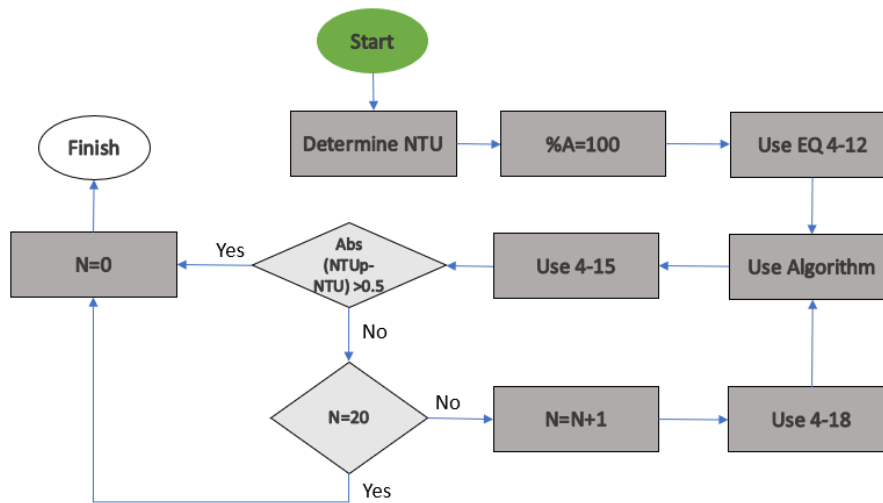


Figure 4.24. Algorithm to calculate the solid concentration.

4.3 Turbidity Levels.

In this subchapter, we study the effect of the height of the water on a turbidity sensor with the photoreceptor and light emitter located down the water column.

4.3.1 Proposal.

In this section, we present the proposed sensor for monitoring the presence of illicit/uncontrolled discharges in the sewerage. We present the physical characteristics of our sensors, the cost of the hardware components needed to develop a prototype with a microcontroller, and finally, the algorithm used to detect the measurable parameters. Although the principal aim of this sensor is to detect the presence of illicit discharges in sewerage systems continuously, we do not discard the possibility of using this sensor to detect the presence of particles in liquids for other applications such as irrigation channels industry, etc. Our sensor is based on 6 LEDs. 5 of them emit light in the visible spectrum at different frequencies, and the other is an infrared LED. An LDR and a photodiode measure the result of emitting light through the water sample. Those elements are placed at 0° and 180° concerning the LEDs position.

4.3.1.1 Proposed sensor.

In this subsection, we describe the physical characteristics of our sensor and the hardware used to implement them.

We develop two prototypes where the difference between them is the position of the LEDs. This is done to test which one works better as a sensing method to detect illicit/uncontrolled waste. In prototype 1 (P1), the position of LEDs from left to right is white, yellow, blue, green, and red.

In prototype 2 (P2), the order of position of LEDs is green, red, white, yellow, and blue. This involves changing the LEDs position: yellow in P1 by white in P2, yellow by red, blue by white, green by yellow, and finally, red by blue.

The prototypes are built using a 5cm long piece of PVC pipe with a diameter of 5 cm and a thickness of 4 mm. The LEDs measured 10 mm for colour LEDs (yellow, blue, green, red, and white) and 3 mm for infrared LEDs. The polarization voltage for the red and yellow LEDs is 1.8-2 V, while this value increases up to 3-3.4 V for the white, green, and blue LEDs. Finally, the infrared LED requires a polarization voltage of 1.5 V. The LDRs used to have 5 mm diameters, and the photodiodes have diameters of 3 mm. In the two prototypes, there is an LDR and a photodiode in the structure of the prototype (0° degrees). Besides, an LDR and a photodiode are located at 180° of the LEDs. Both prototypes share the LDR and photodiode at 180°. The photodiode model is the SFH 203 (3 mm), and the LDR used is NSL-19M51 (3 mm). In Figure 4.25-a, a picture of the two prototypes (P1 and P2) is shown.

The changes of resistance in the LDR and photodiode are transformed into voltage with a voltage divider (Figure 4.25-b). The voltage divider is based on two resistances. A fixed-resistance, and another, which is the LDR / photodiode. The value of fixed resistances is calculated to maximize the voltage difference between the maximum and minimum values for LED. This is done for all the studied solid concentrations and heights. The Equation that represents the operation of a voltage divider is Equation (4.20). In this Equation, V_{in} is the entering voltage in the voltage divider (in volts). V_{out} is the output voltage after the first resistance (in volts). and $R_{circuit}$ is the value of the fixed resistance (in ohms). Finally, R_{LDR} or $R_{Photodiode}$ is the resistance of the LDR or photodiode (in ohms).

$$V_{out}(V) = V_{in}(V) * \frac{R_{LDR}}{R_{LDR} + R_{circuit}} \quad (4.20)$$

The LDRs and photodiodes change their resistance when the light hits them. The LDR decreases its resistance when more light is received. In contrast, the photodiode increases its resistance when the light hits it. The light travels from the LED to the sample, and a part is reflected, another is absorbed, and finally, a part comes out in the upper part of the water (Figure 4.26). In the case of the photodiode and the LDR located at 0°, we measure the light reflected by the sample (in the direction of the prototype). On the contrary, for the photodiode and the LDR located at 180°, we measure the light through the water column.

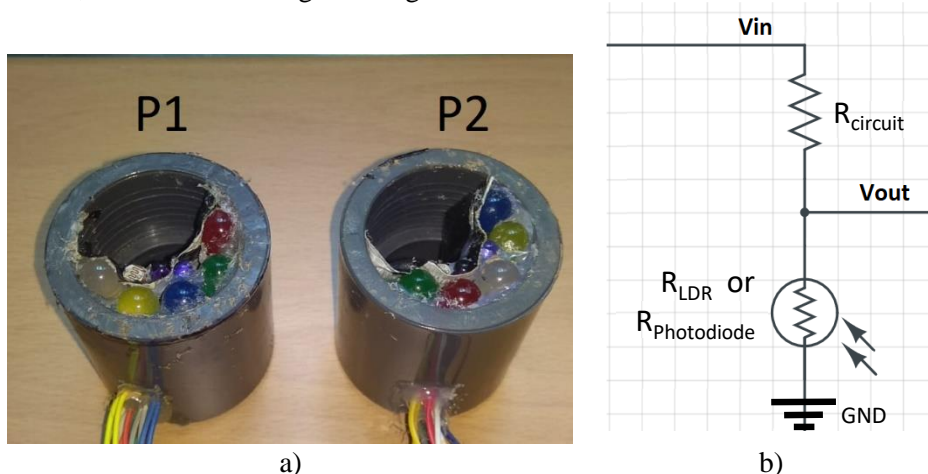


Figure 4.25. a) Picture of the prototypes; b) electronic scheme of a voltage divider.

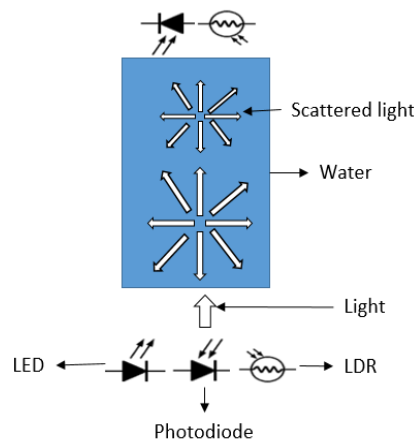


Figure 4.26. Operating principle

We locate the LDR and photodiode at 0° because this way it is easier to manufacture the sensor. In the literature, standard methods indicated that the nephelometer (instrument for monitoring turbidity) detector is located at 90° (Rice, Eaton and Baird, 2017). However, in this case, placing the photodetector at 90° is not possible due to the positioning of the sewerage pipe. Mirosław Jonasz and Fournier (2007) recollect information about the angles used in the photodetector of the nephelometer, and these angles are from 0° to 180° . In some cases, there are multiple photodetectors. We selected the 0° measurement angle to check its operation. It is expected that in real conditions, problems arise due to the solids carried by the water.

4.3.1.2 Cost of our proposal.

In order to implement a commercial device, it is also required to add additional devices to collect and process the measured data. This subsection exposes how to design and connect those elements and the cost of our proposal. This price does not consider the manufacturing cost of a chain production, i.e., we have only considered the material to develop one.

We inquired about several electronic shops to know the average price of each component. Table 4.12 shows the list of components and elements required to develop a prototype and the average price of each one. As we commented before, our prototype requires 5 LEDs of different colours and an infrared LED as light emitter sources. Two LDRs and two photodiodes are located at 0° and at 180° , taking the position of LEDs as a reference. Additionally, the sensor will be placed inside a small piece of circular PVC pipe. To limit the current thought of those elements, several resistors are required. Finally, the voltage registered as a function of the received light should be processed by a microcontroller. We can design an electronic board or use an already developed and commercial model among the range of possible solutions. In our case, we decided to use an Arduino UNO WiFi Rev. 2 based on the ATmega4809 8-bit microcontroller from Microchip and the ESP8266 WiFi module. The Arduino Uno WiFi is functionally the same as the Arduino Uno Rev3, but with the addition of WiFi/Bluetooth connectivity and some other enhancements. This module has 14 digital input/output pins, 5 of which can be used as PWM outputs and 6 analogue inputs with 10-bits Analog-to-Digital Converters (ADC). This microcontroller has output pins that provide a V_{out} of 5 V for powering the different LEDs and the LDRs or the photodiodes, respectively. The Arduino UNO WiFi Rev. 2 can be powered by batteries. So, we decided to use a 5000 mAh USB Power Bank. Finally, the entire system is placed inside a waterproof plastic box to protect it from environmental factors and possible damage from rodents. The total cost of the out prototype is 72.34 euros. Figure 4.27 shows the connection of the different elements described before and required to develop the prototype.

Table 4.12. Prices of the main components

Component	Cost (€)	Component	Cost (€)	Component	Cost (€)
2 SFH 203 (Photodiode)	1.08	1 Powerbank 5000 mah	15.00	2 NSL-19M51 (LDR)	1.88
1 Infrared LED	0.73	12 resistance	0.48	PVC	1.00
5 colour LEDs	0.75	Microcontroller	47.00	Waterproof box	5.00

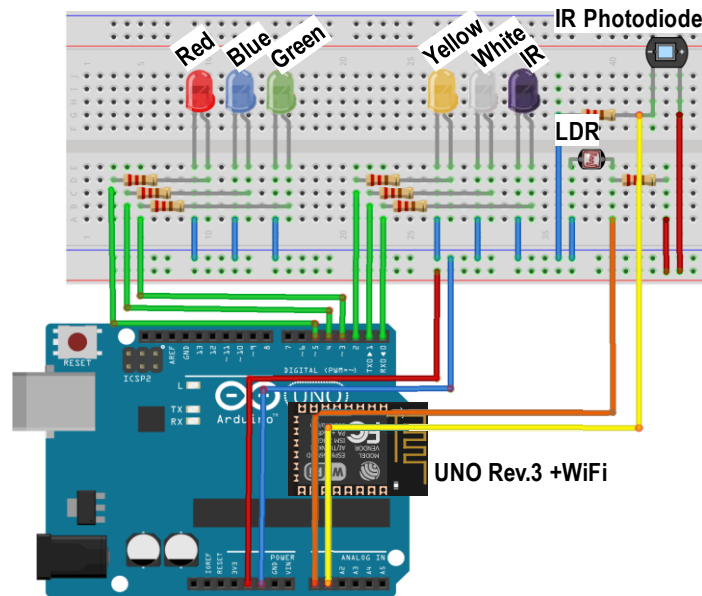


Figure 4.27. Connection diagram of our prototype.

Finally, it is important to bear in mind the effect of having a 10-bits ADC over the measures. According to the Arduino UNO specifications, the maximum voltage that an analogue input can measure is 5V, while the maximum number of levels to be considered is 1024 (2^{10} , being 10, the number of bits of the ADC). This implies that the maximum error in reading will be 5 mV due to the effect of quantization by the ADC. So, if the maximum value of turbidity or suspected solids it is expected to measure with these prototypes is 10000 mg/L, the maximum error in turbidity will be ± 9.8 mg/L.

4.3.1.3 Deployment Scheme.

In this subsection, we analyze an example of deployment for our prototype in the sewerage. Due to the wide variety of sewerage conditions, other configurations may be better. The prototype should be encapsulated to prevent damage from environmental factors (animals mostly).

In the environment, the proposed deployment is composed of two parts. One part is under the pipe. In this part, the LEDs are located on a transparent part of the pipe (methacrylate for example). The second part of our proposed deployment is a waterproof box where the microcontroller, power bank, and resistances would be. This part can be anywhere, and we propose to place it on top of the pipe in an accessible location. The two parts are connected by copper wires which would be used to power the LEDs. In Figure 4.28, we present our proposal for deployment. One problem with sensors in the environment is the damage they can cause to living beings. In this case, the sensor does not present a hazard for the species that live in the sewerage.

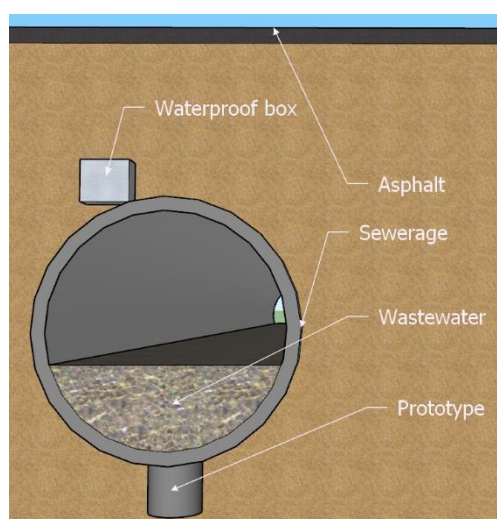


Figure 4.28 Proposal deployment

4.3.2 Test Bench.

In this section, we explain the methodology used to obtain the data. From the preparation of the samples to the usage of the prototypes. We are starting with the technological characteristics of the equipment employed for the measures.

4.3.2.1 Materials.

In this subsection, we explain the materials used in the experiment. For preparing the samples, we select clay as a source of solids and diluted it in freshwater. We select clay to prevent sedimentation problems in the glass container. We prepare different concentrations (1 mg/L, 40 mg/L, 80 mg/L, 160 mg/L, 320 mg/L, 630 mg/L, 1250 mg/L, 2500 mg/L, 5000 mg/L, 10000 mg/L of solids). The concentration of 80 mg/L, 320 mg/L, and 5000 mg/L are used to verify the mathematical model. The rest of the concentration is to build the mathematical model. We are interested in knowing the range of our sensor, for this reason, we test them in low and high concentrations of solids. The typical value of solid concentration in wastewater is between 350 mg/L for low pollution levels to 1200 mg/L for highly polluted wastewater (FAO, 2019). The concentrations tested are above and below that range. The different concentrations tested can be observed in Figure 4.29. For measuring the different samples, we use a jar inside which we put the samples. The jar's height is 25 cm, and its diameter is 13 cm, the glass of the jar has a thickness of 3 mm. The volume of the jar is 4 litres. In the jar, we locate marks for knowing the height of the water column. In Figure 4.30, the assembly can be observed.

We use two different prototypes, represented in Figure 4.25 and explained in subsection 3.1. The LEDs of the two prototypes are powered with a voltage of 5 V obtained by a power supply model FAC-662B. Between the power supply and the LED, there is a resistance of 470 Ω with a tolerance of 5 % for all LEDs.

4.3.2.2 Methodology.

In this subsection, we explain the methodology used. First, we introduce the sample in the glass beaker at the solid concentration and height that we want to measure. The heights tested are 3 cm, 5 cm, 8 cm, 10 cm, 13 cm, 15 cm, 18 cm, and 20 cm. There are not typical values for the height of the water sheet since it depends on multiple factors. Those factors include the diameter of the pipe, whether it is a separate sewer or not, the flow, etc. When the sample is introduced,

we shake it. After the shake, the glass and the prototype are covered with a box to prevent the entry of light from the outside. In sewerage, the water is in movement, which would prevent the effect of sedimentation.

Then the different LEDs are powered sequentially in the order of yellow, red, blue, green, white, and infrared. We wait 20 seconds to take the resistance measurement due to the delay that the LDRs have as standard. This process is replicated 3 times, and we note the resistance values. We measure the resistance of the LDRs with a tester (Tenma 72-2600 (TENMA, 2022)). For the photodiode, we use an oscilloscope (TBS 1104 (Tektronix, 2022b)). All measurements of P1 are carried out, and then those of P2 are started. All the measurements for the different heights for the same turbidity are carried out before moving on to the next one.

For the transformation of resistance to V_{out} in Equation (4.20), the V_{in} is 5 V. We selected 5 V because it is a typical voltage of the outputs of microcontrollers and the voltage that we power the LEDs. RLDR is the different resistances measured with the tester. Regarding $R_{circuit}$, we want to use the resistance that maximizes the difference between the minimum and maximum of V_{out} . This is done to improve the accuracy of the solid concentration measurement. In this process, we have used the Solver tool (Microsoft, 2022) in excel to search for the $R_{circuit}$ for each LED in the different heights. Once calculated, the $R_{circuit}$ s for the different heights have been averaged, and the $R_{circuit}$ for each LED has been obtained.

To determine the mathematical model, we use Statgraphics software (Statgraphics, 2022) and Eureqa software (Datarobot, 2022). We use Statgraphics for the data of LDR/photodiode in 0. This is a popular software for statistical analysis. The Eureqa software is used in the case of the LDR in 180°. This is a software to search mathematical models from a data set. The use of Statgraphics in the case of the LDR / photodiode at 0° is due to the height having a less significant effect than in the case of 180°. That is why specific software is not necessary. To calculate the best mathematical model, we look for the one that offers the highest R^2 among the different models offered by Statgraphics. This model will relate the concentration of solids to the voltage. Once the model is obtained, the data will be linearized. Afterwards, selecting the option of regression models, we will obtain the R^2 taking into account the height and the concentration of solids or only the height.

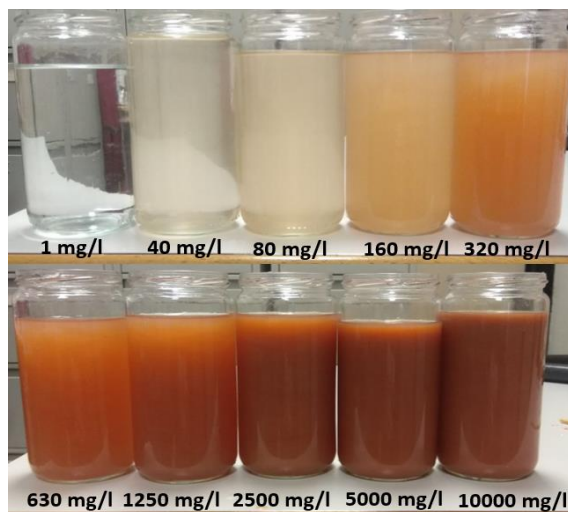


Figure 4.29. Tested samples.



Figure 4.30. Assembly.

4.3.3 Results.

In this section, we present the results of our prototypes. We tested them in different concentrations of solids and at different heights. We tested the effect of different heights due to the daily variations in the amount of water carried by the sewer system. The height of the water will affect the amount of light that the water absorbs and reflects.

4.3.3.1 Results LDR 180°.

In this subsection, we analyze when the LDR is located at the top of the glass (180°). The values of the photodiode located at 180 are analyzed in section 5.3. We calculate the R_{circuit} to obtain the maximum voltage difference (Table 4.13). Nevertheless, these resistance values are not the ones that are used as the standard resistance. We select them as those close to the theoretical value. In Figure 4.31 to Figure 4.40, we can observe the values of V_{out} obtained. In all colour cases, we can observe an exponential increase in the voltage with increasing solids and water height.

Concerning the output voltage in a concentration of 1 mg/L of solids, it is in the range of 0.63 V to 0.09 V. The output voltage is near 4.5 V when the concentration of solids or the height of water does not allow light to shine on the LDR. In these cases, the resistance of the LDR is 20 MΩ according to the datasheet of the component. The average V_{out} for P1 and P2 in the 1 mg/L concentration is 0.49 V and 0.25 V in yellow, in red, it is 0.44 V and 0.33 V, in the case of blue is 0.36 V and 0.28 V, 0.18 V and 0.20 V in the green light, and finally, 0.2 V and 0.15 V in the white LED. In the two prototypes, for a concentration of 160 mg/L of solids, the two prototypes start to fail at the highest of the heights tested. The typical concentration of solids in wastewater polluted weakly is 350 mg/L (FAO, 2019). Accordingly, the LDR in the top of the pipe presents a measuring gap in pipes with diameters longer than 20 cm. The V_{out} is related to turbidity in an exponentially increasing way. In general, we have observed that the water tends to increase (or keep stable) the V_{out} values for lower concentrations, and then they rise more abruptly from approximately 10 cm. We believe that this is because the water redirects the light at an angle that favours the illumination of the LDR from those heights. Concerning the highest concentrations, an exponential increase in the V_{out} values with height has been observed.

In Figure 4.31 and Figure 4.32, the values for the yellow LED are shown. The average V_{out} in 1 mg/L is 0.97 V and 0.62 V for P1 and P2, respectively. The resistances are 20,000 kΩ in the concentration of 10,000 mg/L and 3 cm. As well as for the concentration of 2,500 mg/L and 5 cm or 8 cm. In 10 cm and 13 cm, this happens for concentrations of 1,250 mg/L. Finally, for concentrations of 630 mg/L, it happens for the rest of the tested heights. Concerning the range, the two prototypes do not present differences. Regarding height, an exponential increase is observed in concentrations greater than or equal to 80 mg/L. For 1 mg/L and 40 mg/L, we observe that the V_{out} values remain stable up to 10 cm. From that point, they begin to increase the Voltage for P1. For P2, no pattern is observed at these concentrations.

The V_{out} values for the red LEDs are presented in Figure 4.33 and Figure 4.34. The average of V_{out} for 1 mg/L is 0.85 V for the P1 and 0.65 V for the P2. As in the previous case, the range of the two prototypes is the same. The maximum concentration that could be measured (less than 20,000 kΩ) is 5,000 mg/L for 3 cm. For the rest of the heights, the maximum has been found at 2,500 mg/L and 5 cm, 1,250 mg/L, and 8 cm, and 10 cm, 13 cm, 15 cm, and 18 cm for 630 mg/L. Finally, for 20 cm, we have not been able to measure in concentrations greater than 160 mg/L. In this case, we see that concerning the height, there is an exponential decrease starting with the 160 mg/L concentration.

Table 4.13. Resistance in voltage divider in LDR top mathematical and standard

Colour	P1_top (kΩ)	P2_top (kΩ)	P1_top standard (kΩ)	P2_top standard (kΩ)
Yellow	2177.5	1026.5	2200	1000
Red	1807.0	1432.9	1800	1500
Blue	1343.8	1308.4	1200	1500
Green	767.6	818.3	820	820
White	738.6	575.0	680	560

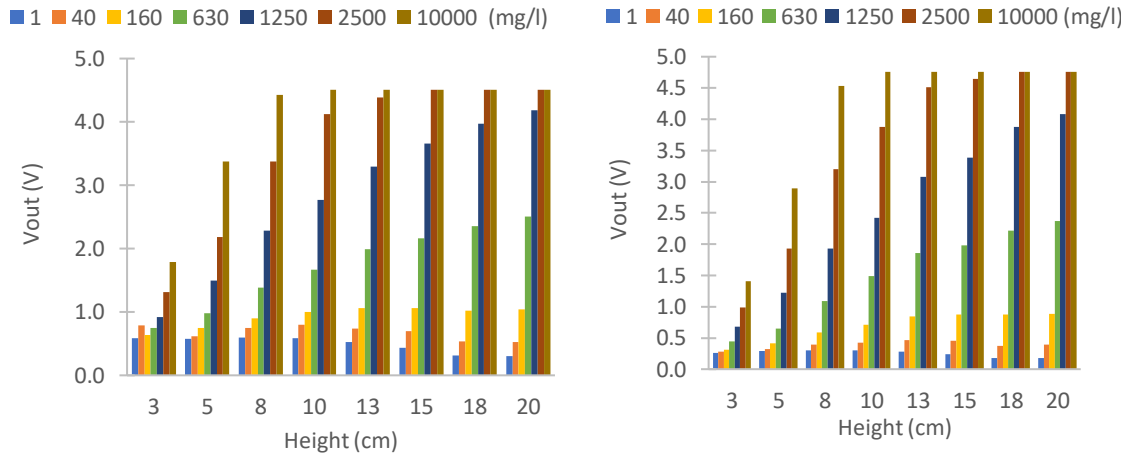


Figure 4.31. Prototype 1, yellow LED, LDR 180° Figure 4.32. Prototype 2, yellow LED, LDR 180°

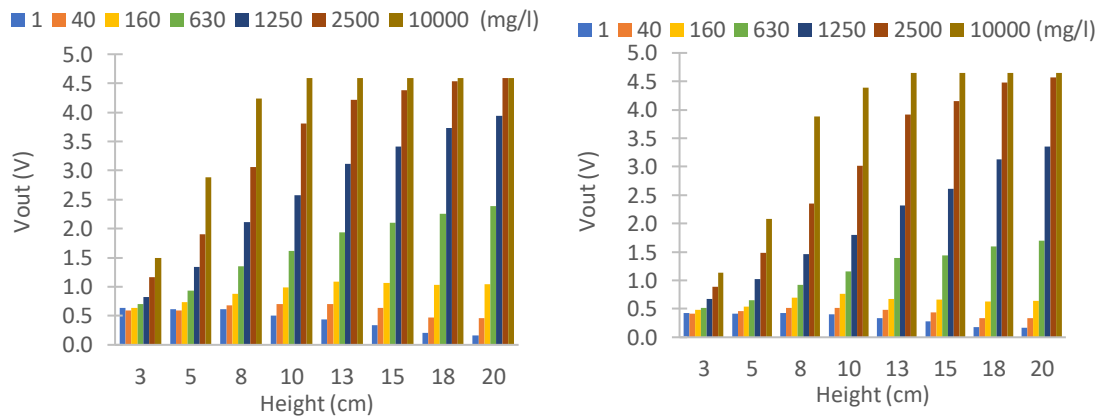


Figure 4.33. Prototype 1, red LED, LDR 180° Figure 4.34. Prototype 2, red LED, LDR 180°

Next, we analyze the blue LED (Figure 4.35 and Figure 4.36). This one, together with the green LED are the ones with the worst ranges (resistance of the LDR change). This LED has a maximum of 2,500 mg/L in 3 cm, 630 mg/L in 5 cm, 8 cm, and 10 cm the maximum is 160 mg/L. For the rest of the tested heights, the maximum is 160 mg/L. For the concentration of 1 mg/L for P1, we observed an increase in Vout. For the concentration of 1 mg/L for P2 and 40 mg/L for P1 and P2, a drop in voltage values is observed up to 10 cm. From this point on, an increase in the values is observed.

We show in Figure 4.37 and Figure 4.38 the Vout for the green LEDs. As in the previous case, its maximum measurement range is 2,500 mg/L in 3 cm. For 5 cm it is 1,250 mg/L. In 8 cm

and 10 cm, the maximum is 630 mg/L. 160 mg/L is the maximum in 13 cm, 15 cm, and 18 cm. Finally, in 20 cm, the maximum is 160 mg/L. In this case, the heights have different distributions according to solid concentration. For 1 mg/L, the P1 reduces the V_{out} from 3 cm to 8 cm. From this point, there is a linear increase in V_{out} . In 40 mg/L, the same happens but up to a height of 13 cm. For 1 mg/L in P2 increases but does not seem to follow a trend. For the same prototype, the concentration of 40 mg/L in the V_{out} remains stable.

Finally, we analyze the last LED tested, the white one. Figure 4.39 and Figure 4.40 present the values of V_{out} for them. The heights and concentration levels for which the resistance of the LDR is the highest are 5 cm at 2,500 mg/L, 8 cm, and 10 cm at 1,250 mg/L, and the rest of the heights tested at 630 mg/L. As in the previous cases, it is observed that with 1 mg/L and 40 mg/L, the values tend to decrease in the first heights tested and increase later. The concentration of 80 mg/L in P2 is observed in a cloud of points that tends to decrease. The rest of the concentrations show an exponential decrease.

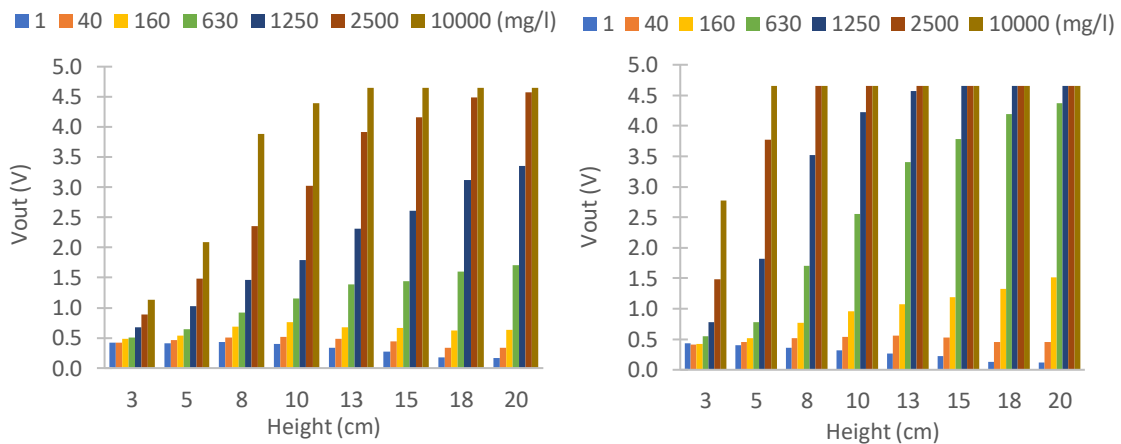


Figure 4.35. Prototype 1, blue LED, LDR 180°

Figure 4.36. Prototype 2, blue LED, LDR 180°.

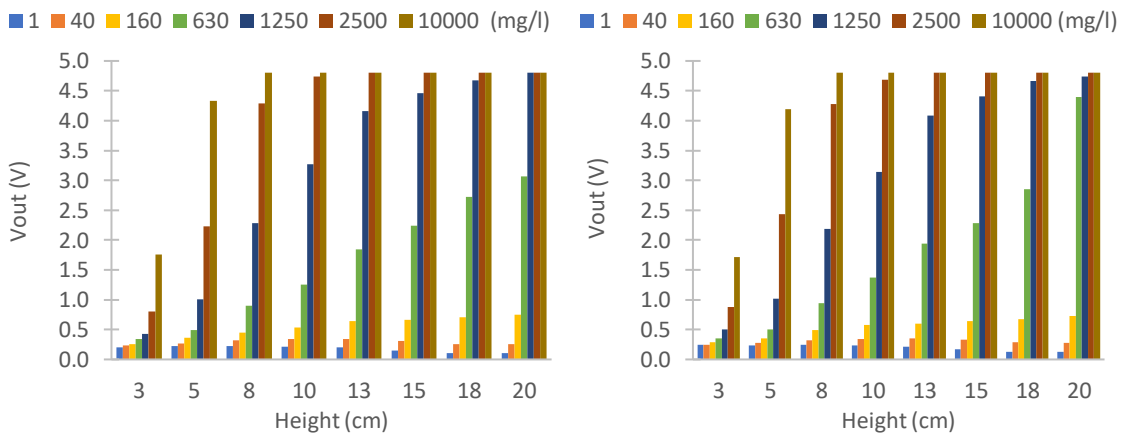


Figure 4.37. Prototype 1, green LED, LDR 180°

Figure 4.38. Prototype 2, green LED, LDR 180°

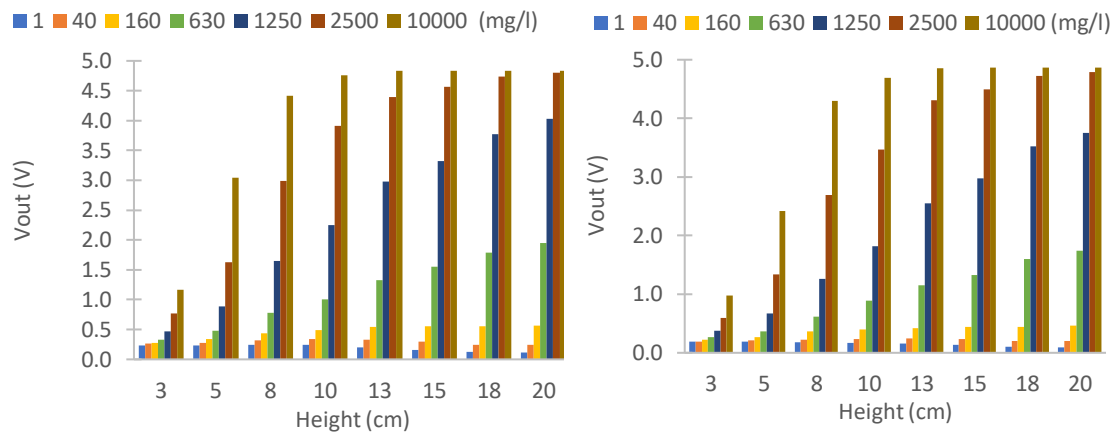


Figure 4.39. Prototype 1, white LED, LDR 180° Figure 4.40. Prototype 2, white LED, LDR 180°

For the LDR at 180°, it is obvious that the height has an important effect on the value of V_{out} . We use the Statgraphics software (Statgraphics, 2022) to determine if there are differences between the means of the different V_{out} . We obtain that there are not statistically significant differences between the means (with a p-value of 0.6874).

We have used the Eureka software (Datarobot, 2022) again to calculate the best fit mathematical model. If we use all the concentration levels tested, the values of R^2 are inferior. Therefore, we decide to eliminate the concentration with a resistance of 20,000 k Ω . With this modification, we got R^2 values of 0.993, 0.998, 0.991, 0.998, and 0.996 for yellow, red, blue, green, and white respectively in P1. In P2, the R^2 are 0.997, 0.993, 0.999, 0.999, and 0.9994 for yellow, red, blue, green, and white respectively. These models are very complex, because of this, we select those models with a complexity lower than 20 (according to the Eureka criteria) even though they have a lower R^2 . We obtain 0.990, 0.990, 0.990, 0.998, and 0.996 for yellow, red, blue, green, and white respectively in P1. 0.993, 0.92, 0.99, 0.999, and 0.9994 for yellow, red, blue, green, and white respectively in P2. This simplification of the model implies a reduction of the R^2 of 0.047, but it greatly simplifies the calculations. This sensor presents an enormous change in the V_{out} when the values of solids increase (especially in solids concentration above 40 mg/L and heights above 3 cm). These prototypes can be used to monitor areas with fast changes in the concentration of solids. For example, the clarifiers of a WWTP. In the clarifiers, the solids are accumulated in the lower part of the clarifier (Sludge), and water comes out the top. Our sensor can be located in the clarifier at the critical height of sludge to start the suction pumps so that it does not reach the critical height.

4.3.3.2 Results LDR 0°.

In this section, we present the results of our prototypes (P1 and P2). We measured the resistance of the LDR and photodiode with a tester and transformed it to output voltage with Equation (4.20). We observed that the values of the resistances are different in the two cases. These differences can be caused by the distance between the LED and the LDR/photodiode.

The values of the fixed resistance can be observed in Table 4.14.

In Figure 4.41 to Figure 4.49, we can observe the values of the two prototypes for the different colour LEDs, when the LDR is located at the same place as the LEDs. Except for the case of the blue LED in P2, the turbidity and V_{out} have a positive and logarithmic function. In the different water heights, we observe that its evolution is not constant. In the sample with 1 mg/L of solids, the V_{out} reduces until a height of 8 cm is reached in P1 and 10 cm in P2. We believe that this behaviour change is due to light reflection on the glass walls.

Now, we analyze the different LEDs. We start our analysis with the LEDs that have poor performance for solids detection. We discard the use of blue and green. In the case of blue LEDs (Figure 4.41 and Figure 4.42), the difference between the minimum and maximum concentrations tested are minimal. In P1, the difference is 0.30 V (averaged between the different heights in 1 and 10,000 mg/L of solids). The average V_{out} for 1 mg/L is 2.49 V compared to 2.19 V for 10,000 mg/L. In the P2, the average V_{out} is 2.41 V for 1 mg/L and 2.58 V for 10,000 mg/L. Regarding the form of the function, we observe that in P1, the maximum values are reached for the concentration of 2,500 mg/L. This is an unexpected result. It would be expected that once a maximum reflection of the light towards the LDR at 0° is reached, it would remain stable. Regarding P2, as we have previously stated, this one presents a strange shape. Finally, we observe a notable difference between the two prototypes, from the form of the function to the different values of V_{out} .

Table 4.14. Resistance in voltage divider in LDR down.

Colour	P1_Down (k Ω)	P2_Down (k Ω)	P1_Down standard (k Ω)	P2_Down standard (k Ω)
Yellow	112.9	139.2	120	120
Red	648.9	49.6	680	47
Blue	42.5	328.1	47	330
Green	76.3	56.9	82	56
White	10.8	19.5	12	18

There is an important difference between the green LED (Figure 4.43 and Figure 4.44) in the two prototypes. In P1, the difference is 0.22 V. The average V_{out} value for 1 mg/L is 2.51 V and for 10,000 mg/L, it is 2.29 V. Whereas in P2, the difference is 1.22 V with voltage values of 3.04 V for 1 mg/L and 1.81 V for 10,000 mg/L. This difference may be due to the change of position of the LED in the prototypes. Therefore, it is not accurate enough and should not be considered for the development of our prototype. In addition, it is important to note 2 things. (i) this is the colour with the greatest dispersion at the concentration of 1 mg/L. At first, it was believed that they would be incorrect values. But after repeating the experiment, it was confirmed that these values were correct. (ii) in prototype 2, between concentrations 1 mg/L, 40 mg/L, and 80 mg/L, there is a high dispersion between the values with 3 cm of the water column and the rest of the values.

Regarding the LEDs that have worked the best, they are the yellow, red, and white LEDs. These have a difference between 0 mg/L to 10,000 mg/L of 1.73 V, 1.76 V, and 1.13 V in P1 and 1.58 V, 1.84V, and 1.35 V in P2 for the LEDs yellow, red, and white respectively (Figure 4.45 to Figure 4.50). In all the cases we analyze, the V_{out} values between 1 mg/ l and 40 mg/ l are very similar. Therefore, we consider that the minimum concentration of solids that our sensor can measure is 40 mg/L.

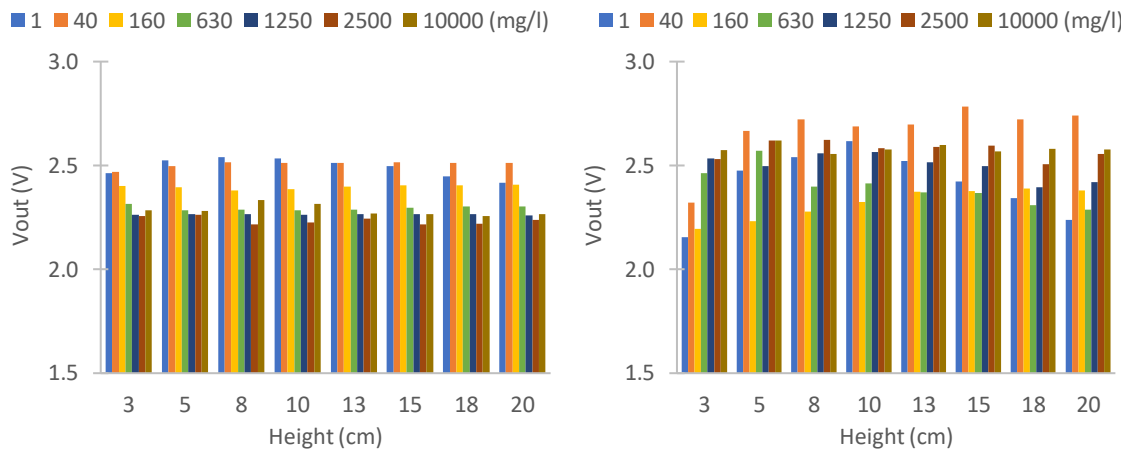


Figure 4.41. Prototype 1, blue LED, LDR 0°.

Figure 4.42. Prototype 2, blue LED, LDR 0°.

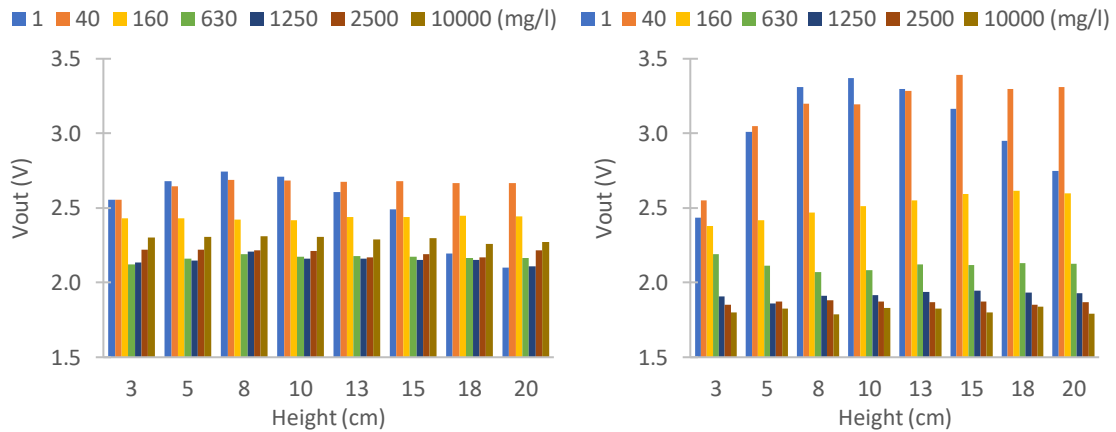


Figure 4.43. Prototype 1, green LED, LDR 0°.

Figure 4.44. Prototype 2, green LED, LDR 0°.

In Figure 4.45 and Figure 4.46, the values of the yellow LEDs in P1 and P2 are represented. The values of V_{out} are 3.27 V and 3.43 V for 1 mg/L to 1.55 V and 1.84 V for 10,000 mg/L (1.73 V and 1.58 V difference in P1 and P2 respectively). Regarding the range of higher concentrations tested, we see that in P1 the values stabilize after 2,500 mg/L and in P2 after 1,250 mg/L. Therefore, the measuring range will be from 40 mg/L to 2,500 mg/L for P1 and will be shortened to 40 mg/L to 1,250 mg/L for P2. Equations 1 and 2 represent the mathematical model of the yellow LED in P1 and P2 respectively. The ranges of these models are 40 mg/L to 2,500 mg/L in P1 and 40 mg/L to 1,250 mg/L to P2. These solids models are not a function of heights since the difference of R^2 is 0.0005 in P1 and 0.0002 in P2. These differences do not justify adding more complexity to the model. The values of R^2 are 0.9963 in P1 and 0.9830.

In Figure 4.47 and Figure 4.48, we can observe the values of V_{out} in the red LED. In P1, the first thing that stands out is the great dispersion of 1 mg/L. The minimum value (for this concentration) is 2.58 V, and the maximum is 3.82 V. This dispersion does not carry over to the other concentrations. We believe that this dispersion only occurs in very transparent waters, which does not happen in the sewer. Therefore, we do not rule out the use of this LED. In addition, in P2, there exists dispersion for 1 mg/L (between 3.25 V to 3.57 V), but the range is not as large. In addition, we observe that the maximum value of V_{out} is 1,250 mg/L. After this value, a slight drop in the values is observed. The values of V_{out} are 3.27 V and 1.51 V in P1 for 1 mg/L and 10,000 mg/L (1.76 V of difference). In P2, the values are 3.43 V and 1.59 V (1.84 V of difference). The lower threshold of these LEDs is 40 mg/L (as with the yellow LED). In the case of P1, the higher threshold is for 1,250 mg/L, and in P2, it is for 2,500 mg/L. From these concentrations on,

the voltage difference remains stable. Finally, in P2 we observe that the voltage value for 40 mg/L and 3 cm is far from the rest of the points. Furthermore, for 160 mg/L, there is a dispersion of the values in P2 and for 40 mg/L in P1.

The mathematical models for the red LED in P1 and P2 are represented in Equations 4.21 and 4.22, respectively. The ranges of these models are 40 mg/L to 1,250 mg/L in P1 and 40 mg/L to 2,500 mg/L to P2. The values of R^2 are 0.9887 in P1 and 0.9905 in P2. These solids models are not a function of heights since the difference of R^2 is 0.0002 in P1 and 0.0015 in P2. These differences do not justify adding more complexity to the model. In addition, in the case of P2, the highest R^2 is that of the model without considering the height.

The last LED analyzed is the white LED (Figure 4.49, Figure 4.50). In this case, it is striking that there does not seem to be a dispersion of the data according to the height in P1. Nevertheless, it does exist in P2. For 1 mg/L in P1, the average is 2.94 V, for 10,000 mg/L, it is 1.81 V (difference of 1.13V). The P2 has a V_{out} of 3.22 V for 1 mg/L and 1.86 V for 10,000 mg/L (a difference of 1.13 V). According to the range, both LEDs can differentiate between 40 mg/L and 2,500 mg/L. Finally, the mathematical model is represented in Equations 4.23 and 4.24. The values of R^2 are 0.9914 and 0.9794. As in the previous cases, when adding the height to the model, the difference in the R^2 when adding the height to the mathematical model is minimal.

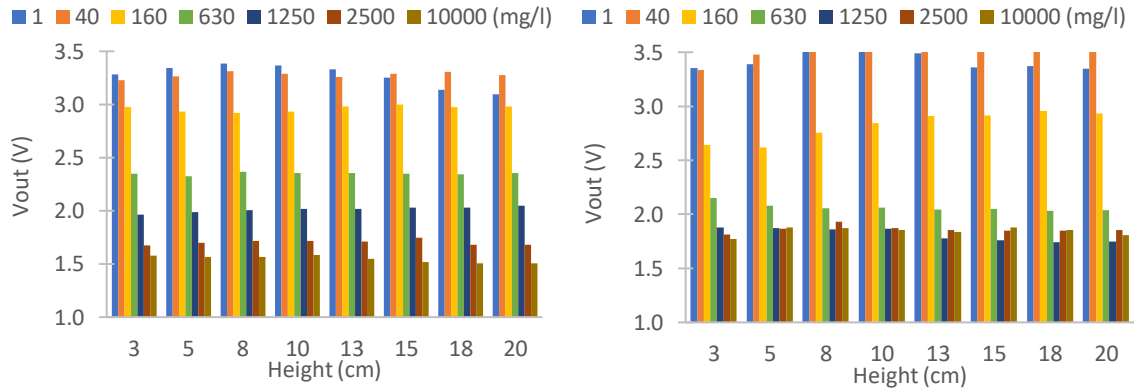


Figure 4.45. Prototype 1, yellow LED, LDR 0° Figure 4.46. Prototype 2, yellow LED, LDR 0°

$$Solids (mg/l) = \left(\frac{-39.3278 + 151.496}{V_{outyellow1}(V)} \right)^2 \quad (4.21)$$

$$Solids (mg/l) = e^{15.3912 - 6.18087\sqrt{V_{outyellow2}(V)}} \quad (4.22)$$

$$Solids (mg/l) = \left(\frac{-9.3713 + 58.8425}{V_{outred1}(V)} \right)^2 \quad (4.23)$$

$$Solids (mg/l) = \left(\frac{-40.0554 + 161.361}{V_{outred1}(V)} \right)^2 \quad (4.24)$$

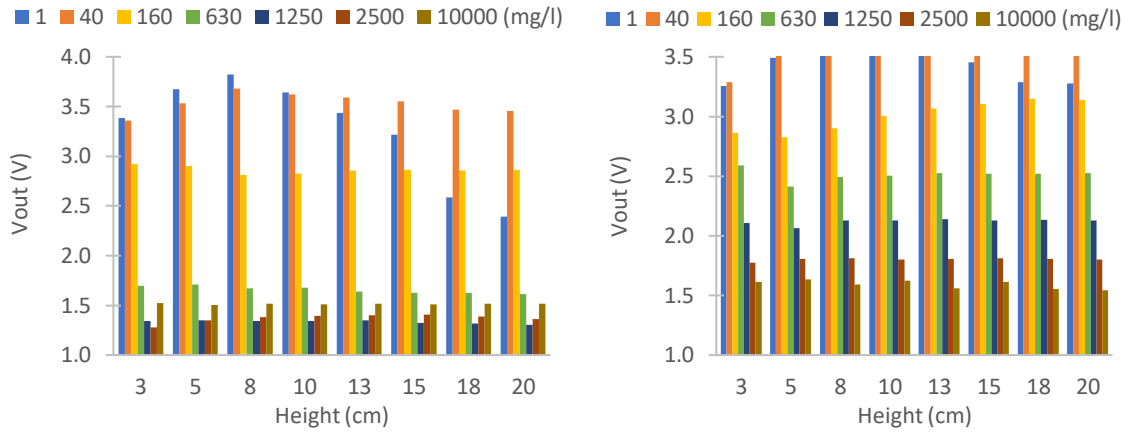


Figure 4.47. Prototype 1, red LED, LDR 0°.

Figure 4.48. Prototype 2, red LED, LDR 0°.

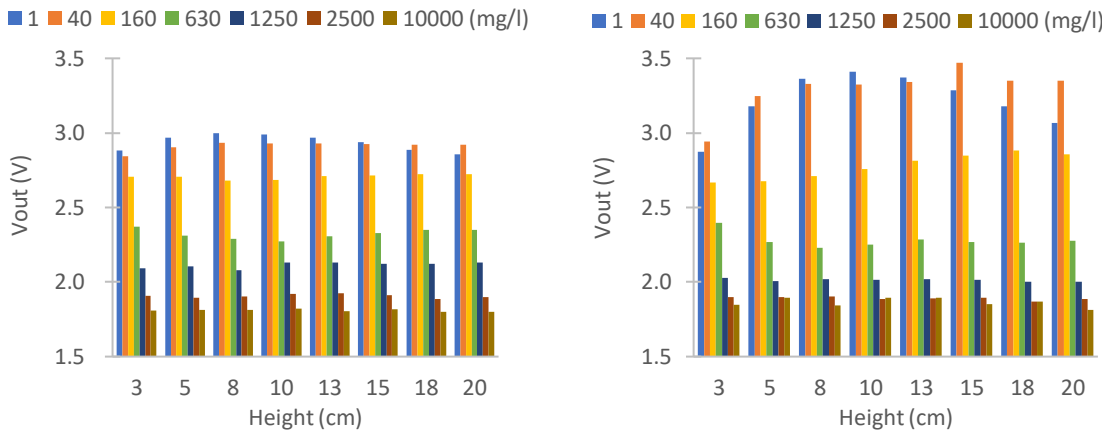


Figure 4.49. Prototype 1, white LED, LDR 0°.

Figure 4.50. Prototype 2, white LED, LDR 0°.

We have previously seen that there is no difference in the values of R^2 when the height is added to the model. Now, we proceed to study if there is a statistical difference to check if there are significant differences between the height values. For this, we performed an ANOVA multifactorial analysis (confidence interval 95%, p-value greater than 0.05 for differences to exist) with the software Statgraphics (Statgraphics, 2022). The results of the ANOVA can be checked in Table 4.15. We can conclude that in most cases, there is a statistically significant difference. Also, except for the yellow LED and red LED in P2, the p-value for the other LEDs is lower than 0.0001. In the future, we will have to study if these differences are due to the change of position of the LEDs, the agitation of the sample, or some defect in the glass. Since it is observed that although the results between the different LEDs (except for green and blue) may be similar, there are some differences.

$$\text{Solids (mg/l)} = \left(\frac{-40.0554 + 161.361}{Voutwhite2(V)} \right)^2 \quad (4.25)$$

$$\text{Solids (mg/l)} = e^{12.2156 - 7.07235 \cdot \ln(Voutwhite2(V))} \quad (4.26)$$

Table 4.15. ANOVA height in LDR 0°.

Colour	p-value P1 down	p-value P2 down
Yellow	≤0.0001	0.0002
Red	≤0.0001	0.0002
Blue	≤0.0001	≤0.0001
Green	≤0.0001	≤0.0001
White	≤0.0001	≤0.0001

For these reasons, we determine that although the height has statistically significant differences, it does not affect the general function of the sensor. Therefore, it can be used in the sewer system without having to use other sensors to determine the height and more complex models that require more than one variable. The three LEDs obtain high R^2 values. Therefore, these mathematical models are very well adapted to experimental values.

4.3.3.3 Results photodiode 0° and 180°.

In this subsection, we analyze the values of the infrared LED at 0° and 180°. First, we need to determine the best resistance in the circuit of the photodiode. In this case, we use an oscilloscope (TBS1104) to measure the resistance voltage. Because the resistance of the circuit is high, the measurement of voltage in the tester can be affected due to the tester's internal resistance not being high.

We test the maximum and minimum turbidity to determine the resistance. When the photodiode is at 180°, we test at two heights (3 cm and 18 cm). This is due to the height having an important effect on the photodiode's signal. In Figure 4.51 we can observe the voltage (V_{out}) in the resistance extremes. In the case of a water column of 3 cm, the values of 1 mg/L are upper bounded approximately in 0.167 V. The value of 0.167 V is in the resistance of 8.2 M Ω . When the solids concentration is 10000 mg/L, the values are bounded in 0.002 V. This means that the photodiode does not receive signals from the infrared LED. In the case of 18 cm, the maximum voltage is 0.004 V in the concentration of 1 mg/L and 0 in the maximum concentration tested. We discarded the use of the photodiode at 180° due to these bad results. Usually, the turbidity can measure at this angle. However, the distance between the infrared LED and photodiode is large in our case. We discarded reducing this distance due to the low distance between the emitting signal and the receptor, which can obstruct the water entry to the sensor. In the sewerage, hairs, solid materials, wipes, etc. are very common, which can cause obstructions.

When the photodiode is located at 0°, we test with a water height of 18 cm (Figure 4.52). The voltage values are upper bounded in 0.67 V in the concentration of 10,000 mg/L and 0.4 V in the concentration of 1 mg/L. From the 8.2 M Ω resistance, the bounded zone has been reached. It is chosen to place this resistance because it is the one that offers us the greatest difference between the two concentration levels with the least resistance. Placing a higher resistor can cause problems in the current sensor development.

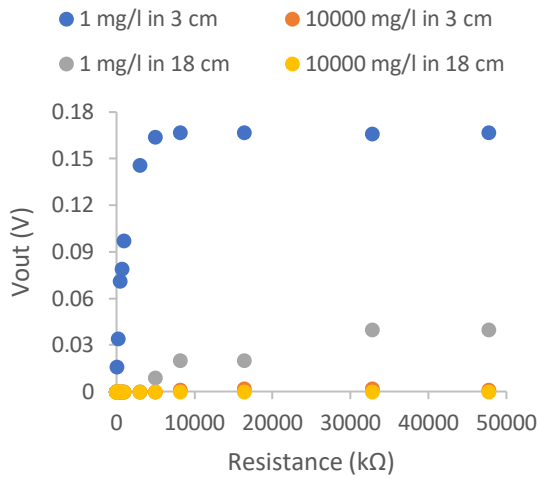


Figure 4.51. Voltage in resistance photodiode at 180°

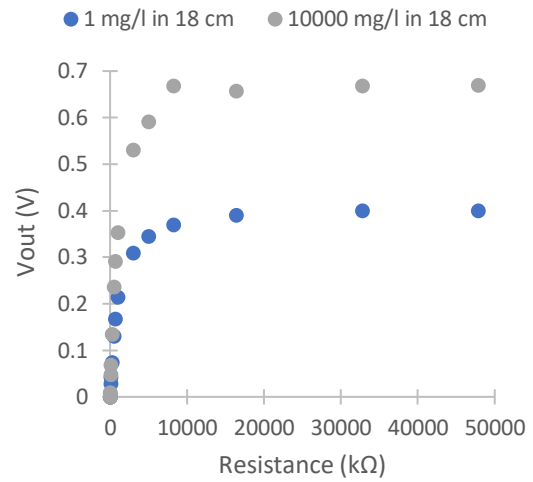


Figure 4.52. Voltage in resistance photodiode at 0°

The photodiode results are shown in Figure 4.53 for P1 and Figure 4.54 for P2. In P1, the voltage is between 0.402 V in 1 mg/L to 0.68 V in 10,000 mg/L. In P2, the voltage is between 0.10 V in 1 mg/L to 0.34 V. The voltage difference is 0.28V in P1 and 0.24 in P2. The two prototypes have the same traits. We think that these differences in voltage are due to the manufacturing process that is done by hand. We observe in the two prototypes that the increase of voltage increases with the concentration of solids. However, for the first points, the variation is low. The increase in voltage is produced from the concentration of 630 mg/L. For this reason, we think that with the current circuit, this LED cannot be used for monitoring the concentration of solids. However, it could be used to verify the presence of an illicit dumping. If a coloured LED detected a high concentration of solids, the infrared LED could light to confirm the possible presence of a spill.

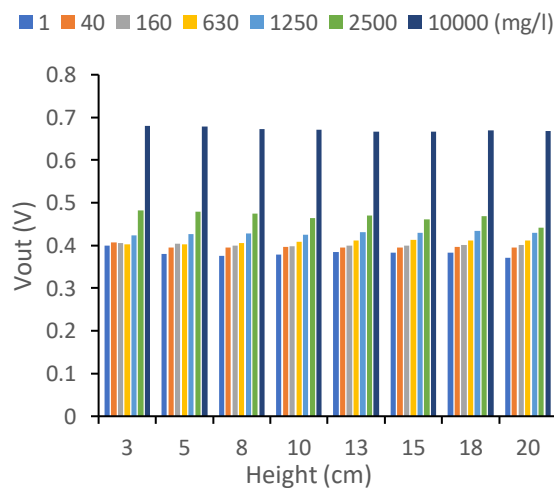


Figure 4.53. Prototype 1 infrared LED

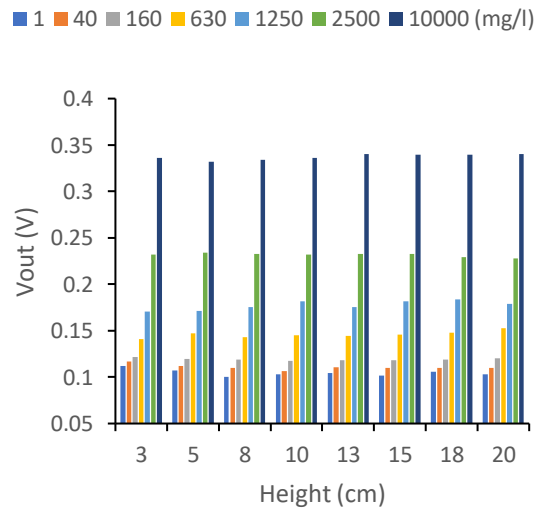


Figure 4.54. Prototype 2 infrared LED

4.3.3.4 Verification.

In this section, we analyze the mathematical models of our prototypes with verification concentration levels of 80 mg/L, 320 mg/L, and 5,000 mg/L.

When the LDR is 180° , errors are present, especially in the low concentrations and low heights, which is unacceptable for the sensor we are developing. Moreover, the errors in low concentration levels (1 and 40 mg/L) and 3 cm of height are high. Other turbidity and solids sensors work with a photosensor at 180° . Our sensor possibly presents these bad errors compared to the other sensors because the light pierces through two environments (water and air). When the light changes from water to air, a refraction of light has negatively affected the results obtained.

Regarding the LDR when at 0° , in Table 4.16, the relative and AEs of the models are shown. Previously, we determined that our prototypes could measure in a maximum concentration of 2,500 mg/L. For this reason, the concentration of 5,000 mg/L is not used to verify the functioning of the prototypes. The greatest error is in red LED of P2 with a relative value of 49.2% and an absolute value of 174.8 mg/L. Generally, the red LEDs are the ones that have greater errors. Regarding yellow LED, P1 presents fewer errors than P2. Finally, for the white LEDs, P1 presents a RE of 8.3% and 8.9 % for concentration levels of 80 mg/L and 320 mg/L, and P2 presents values of 19.6% and 18.5% for the same concentrations.

The two prototypes for the different LEDs (yellow, red, and white) have similar values of R^2 and operating ranges. As seen in Table 4.16, the errors in the verification of red LEDs are greater than for the other LEDs. Moreover, their V_{out} values are similar to those of yellow LEDs. Red LEDs have a V_{out} difference of 1.16 V and 1.21 V in P1 and P2 respectively, compared to the difference of 1.14 V and 1.05 V in yellow LEDs. Therefore, we discard the use of red LEDs. White LEDs present values of less than 1 V. Even though the white LEDs have lower REs than the yellow ones, we consider that the best LED is yellow. Since it has a greater voltage difference (greater sensitivity) and similar errors. A commercial sensor for measuring turbidity is CUS50D. This sensor has a maximum error for monitoring the solids of 5% with a specified range of 0 mg/L to 25,000 mg/L (Endress+Hauser, 2018). Another commercial sensor is the OBS501, with a range of 0 NTU to 4,000 NTU and an accuracy of $\pm 2\%$ or 0.5 NTU (which is greater) (Campbell, 2022). Although these sensors are more precise, their cost is higher than that of our prototype. This prevents a large number of sensors from being located in the sewer, which is possible with our sensor. An example of a low-cost sensor is presented by (Wang et al. 2018). The sensor has a 20% difference between the lecture from their prototype and the reference turbidity (HI 93703) in the range of 0–1000 NTU. This value is similar to the maximum error that we have obtained.

Table 4.16. Errors in the LDR 0°

	Solids (mg/L)	Yellow P1	Yellow P2	Red P1	Red P2	White P1	White P2
RE (%)	80	9.2	19.3	17.2	19.5	8.3	19.6
	320	13.5	4.9	15.4	54.6	8.9	18.5
AE (mg/L)	80	7.4	15.5	13.8	15.6	6.6	15.7
	320	43.4	15.7	49.2	174.8	28.6	59.1

4.4 Improve the infrared sensor.

4.4.1 Test Bench.

In this subsection, we explain the materials and methodology used in the experiment.

4.4.1.1 Material.

The different samples have been elaborated with clay using the concentrations shown in Table 4.17. Figure 4.55 includes a photograph with the tested concentrations. We decided to use a wide range of concentrations to know the range of the prototype in order to evaluate other applications in the future.

The prototype is located below a glass that contains the sample. The diameter of the glass used to perform tests has 8 cm, its thickness is 4 mm, and its height is 16.5 cm. We elaborated 200 ml of sample, equivalent to the height of a water sheet of 4.5 cm in the glass. Figure 4.56 shows our prototype. We located the infrared LED and the photodiode below the glass. Between the infrared LED and the photodiode, we put a wall to prevent the infrared LED light reaches the photodiode without going through the glass with the sample.

On the one hand, we used an infrared LED (TSUS5400 model), which features are: a peak wavelength of 950 nm, a diameter of 5 mm, a forward current of 150 mA, and an angle of half intensity of 22° (RS online, 2022). On the other hand, we used an OSRAM photodiode (SFH 203 model), which features are: diameter of 5 mm, a package in clear epoxy, and a switching time of 5 ns (RS online, 2018).

Table 4.17. Solid concentrations of the samples used in the experiment.

Calibration (mg/L)	0	15	50	80	200	300	500	800
	1500	2500	4000	5000	7000	8000	9000	10000
Verification(mg/L)	30	100	400	1000	3000	6000		

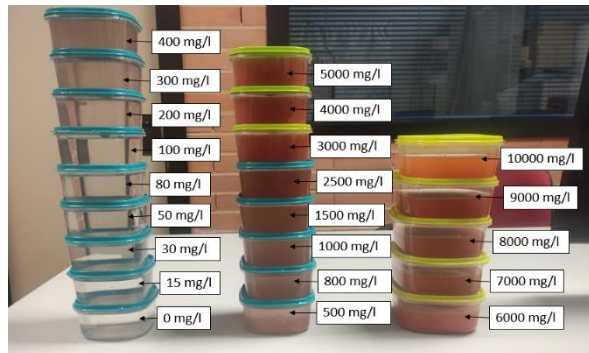


Figure 4.55. Picture of the used samples.

4.4.1.2 Methodology.

First, we measure the turbidity of the samples with the commercial turbidimeter (TU-2016). The turbidimeter has been calibrated with 0 and 100 NTU calibrations.

We power the LED and photodiode in our prototype with a power supply (FAC-662B). This power supply has two channels, one is used to power the LED, and the other is to power the photodiode with a voltage of 5 V. The LED and the photodiode are firstly powered for 5 seconds before taking measurements in order to ensure the correct measurement. The measurement is taken three times for each concentration in the calibration and verification. The different combinations of intensity in infrared LED and resistance are represented in Table 4.18.

The glass with the sample and prototype is located within to opaque container to prevent the

natural light effect in the measurements. Once a measurement is performed, the container is removed, the sample is shaken, and the opaque container is replaced. In order to select the best combination of resistances in the LED and the photodiode circuit, we test the different combinations of resistance with concentrations of 0, 500, and 5000 mg/L. Then, we search the maximum difference of V_{out} between the three concentrations tested. When the best combinations are selected, we test the samples using the same procedure explained previously, but this time with the concentrations shown in Table 4.17.

With the data gathered, we use Statgraphics program to find a mathematical model that relates the concentration of solids with the V_{out} .

Table 4.18. Values of resistance and intensity used in the led and the resistance in the photodiode.

Resistance LED (Ω)	560	270	220	150	100	68	33	22
Intensity LED (mA)	7.09	14.50	17.73	24.14	35.29	53	100	150
Resistance ($k\Omega$)	10	47	100	220	6800	1000	2200	8200

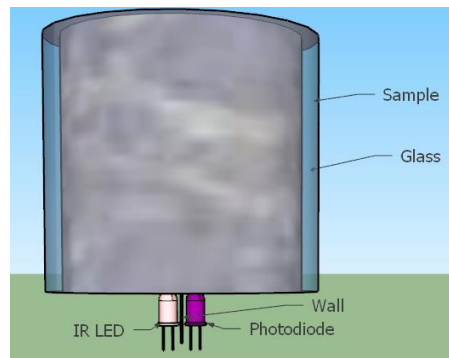


Figure 4.56. Prototype drawing.

4.4.2 Results.

In this section, we present the results obtained with infrared LED. First, we analyze the relation between turbidity and solids in the elaborated samples. Secondly, we select the best combination of resistances in the photodiode circuit and the intensity of the infrared LED. Finally, we present the calibration and verification of our prototype.

4.4.3 Relation between turbidity and solids.

First, we analyze the relation of solids with the NTU. It is an empirical relation that depends on the type of solids.

In Figure 4.57, the NTU values for each concentration of solids are shown. We observe a linear relation between the turbidity (expressed as NTU) and the solid concentrations in the range of 0 mg/L to 1500 mg/L. In addition, it can be observed an upper limit (with a value of 900 NTU) when there are concentrations higher than 1500 mg/L.

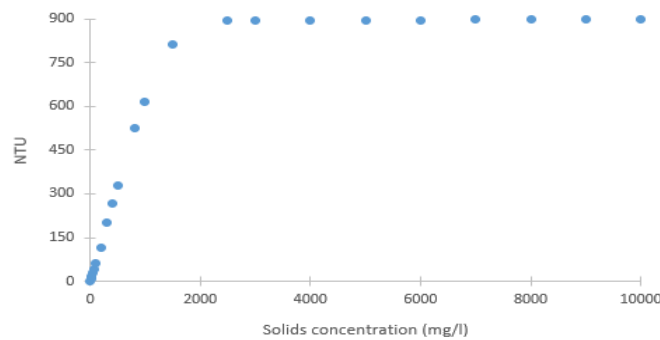


Figure 4.57. Relation between solids and turbidity.

4.4.4 Selection of best combination of resistances.

In this subsection, we perform the test with different currents to power the infrared LED and different resistances in the voltage divider of the photodiode. To determine the best combinations of resistance and intensities, we perform the test with three concentrations: 0, 500, and 5000 mg/L. Figure 4.58 and Figure 4.59 shows the data obtained. We observe that when the current in the infrared LED increases, the V_{out} increases. The same occurs when we increase the resistance in the voltage divider.

Figure 4.58 shows the V_{out} obtained when we fix the resistance at 10, 47, 100, and 220 k Ω . When the resistances are 10, 47, and 100 k Ω , we observe that the difference of V_{out} between the concentrations of 0 to 500 mg/L is near 0 V, with a maximum difference of 0.061 V, in the current of 150 mA and 100 k Ω of resistance. In the range of 0 to 5000 mg/L, the maximum difference is produced in the same current and resistance. The V_{out} is 0.732 V in 0 mg/L and 1.221 V in 5000 mg/L (difference of 0.489 V). When the resistance is 220 k Ω , the voltage differences increase concerning the other resistances shown in Figure 4.58. The differences are 0.131 V between the concentration from 0 to 500 mg/L and 1.036 V between the concentration from 0 to 5000 mg/L for the maximum currents tested.

Continuing with the test of different fixed resistances, in Figure 4.59, we show the values of 680, 1000, 2200, and 8200 k Ω of fixed resistances for different currents. In this case, we observe higher differences than the ones shown in Figure 4.58 for different concentrations using a current of 53 mA when 1000 k Ω is used as fixed resistance. In this case, the currents higher than 53 mA present a value of V_{out} near 5.3 V for the three concentrations. Finally, we tested what happens when the fixed resistance is 2.2 and 8.2 M Ω . In those cases, we observed very similar V_{out} for the tested currents in those concentrations. On the one hand, when we used the resistance of 2.2 M Ω , the maximum difference was obtained with a current 24.1 mA, with values of 4.021, 4.282, and 5.045 V in the concentration of 0, 500, and 5000 mg/L respectively. On the other hand, when we used 8.2 M Ω , the difference was 0.251 and 1.202 V for the concentration of 0 to 500 mg/L and 0 to 5000 mg/L, respectively.

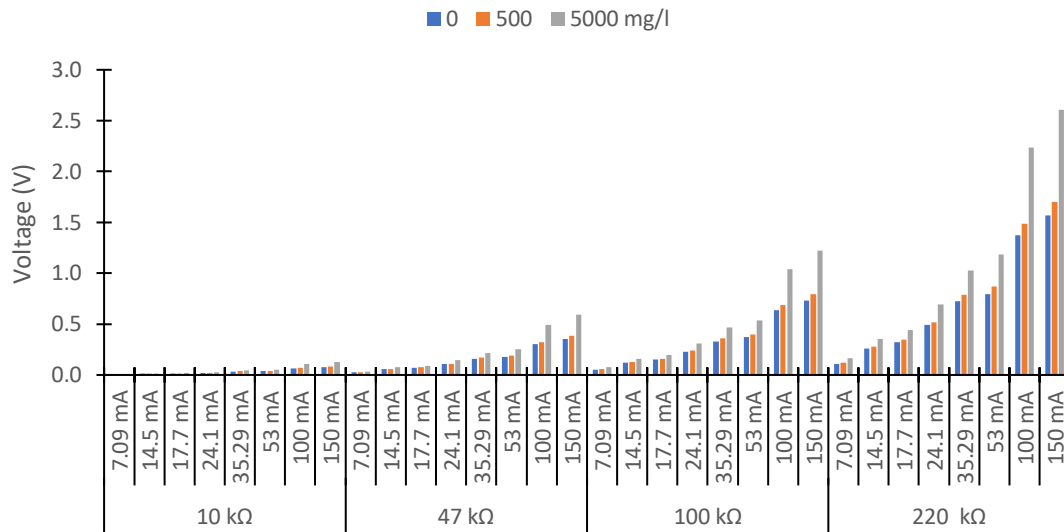


Figure 4.58. Data obtained for different currents tested for the resistances from 10 to 220 kΩ.

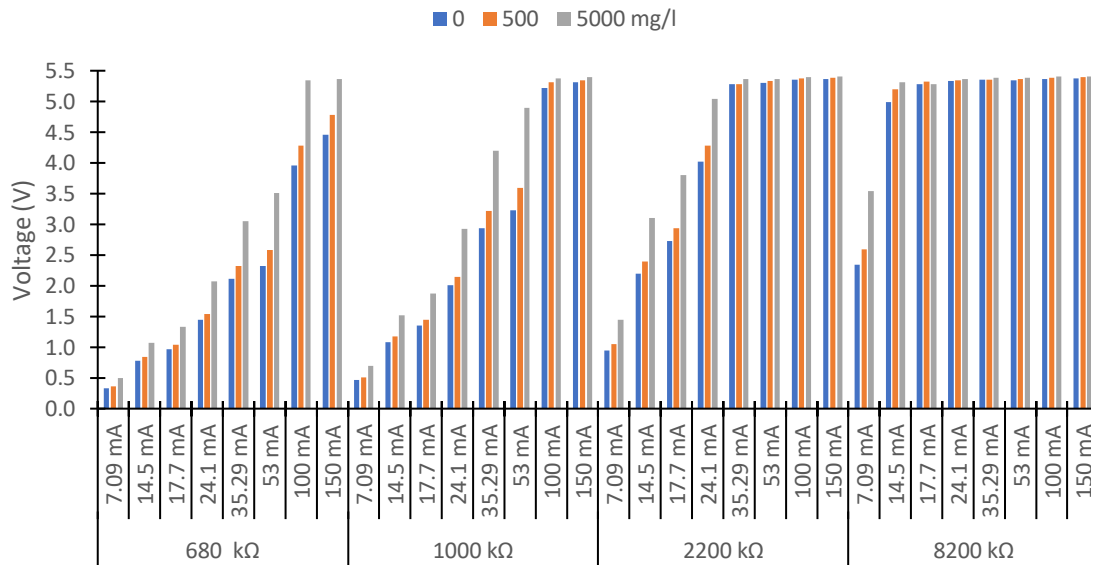


Figure 4.59. Data obtained for different currents tested for the resistances from 680 to 8200 kΩ.

Considering the previous experiments, we select the combination of 7.09 mA and 8200 kΩ, 35.29 mA and 1000 kΩ, 53 mA and 680 kΩ, 53 mA and 1000 kΩ, and 100 mA and 680 kΩ, because this combination produces the maximum difference between the concentration of 0, 500, and 5000 mg/L.

4.4.5 Calibration and verification.

In this subsection, we show the results obtained in the calibration and verification of the previously selected configuration.

Figure 4.60 shows the V_{out} values for the configurations previously selected. In all cases, we observe that V_{out} increases with the concentration of the solids increases. As we will analyze

below, in some of the studied cases, there are changes in the V_{out} increase trend.

The configurations of 7.09 mA and 8200 k Ω , and 53 mA and 680 k Ω have similar trends. In both cases, the V_{out} of solid concentrations 0, 15, and 50 mg/L have similar voltage values. In solid concentrations from 50 to 4000 mg/L, V_{out} increases when the concentration of solids increases. But in the concentration of 5000 mg/L, in the current of 7.09 mA, and 4000 mg/L, in the current of 35.29 mA, there is a change in the slope up to the concentration of 7000 mg/L. From this concentration, the voltage values remain similar. In the configuration of 35.29 mA and 1000 k Ω , we observe that the values from 80 to 200 mg/L increase very few, in the range from 200 to 7000 mg/L there is an exponential increase of the V_{out} , and finally, when there are concentrations higher than 7000 mg/L, the V_{out} is constant. We discard the use of these last configurations because there are changes in the slope V_{out} vs the concentration of solids. It makes more difficult to create a mathematical model relating both parameters.

Finally, we analyze configuration 1 (current of 53 mA and resistance 1000 k Ω , and configuration 2 (current of 100 mA and resistance 680 k Ω). In configuration 1, the V_{out} of the solid concentrations 0, 15, 50, and 80 mg/L are similar. In the case of configuration 2, this occurs in the concentration of 0, 15, and 50 mg/L. In both configurations, we observe an upper limit of 5.33 V. This limit occurs in the concentration of 7000 mg/L in configuration 1 (however, in the verification step, we are going to observe that this limit occurs in 6000 mg/L). In configuration 2, the limit occurs to 4000 mg/L. In configuration 1, the working range is 200 to 5000 mg/L with an increase of the V_{out} of 1.66 V, and in configuration 2, the working range is 80 to 4000 mg/L with an increase of the V_{out} of 1.2 V (the upper limit starts in the concentration of 4000 mg/L). According to FAO, the values of solids in wastewater are between 350 mg/L in low polluted and 1200 mg/L in strongly polluted wastewater (FAO, 2019). Therefore, the typical range of solids in the sewer is within the operating range of our sensor. In configurations 1 and 2, we observe that the working range has a higher concentration than 1500 mg/L. If we observe Figure 4.57, in the range higher than 1500 mg/L, the turbidity is within the upper limit. This tells us that the proposed sensor does not respond to the turbidity but to the concentration of solids. Figure 4.61 are represented V_{out} values versus turbidity expressed as NTU in the range of 1.78 to 894 NTU (solid concentrations of 0 and 2500 mg/L, respectively). In solid concentrations higher than 2500 mg/L, the turbidity has an upper limit (Figure 4.57). However, the V_{out} increase (Figure 4.58). In all cases, there is an increase of the V_{out} with the turbidity increase. The difference in V_{out} between the minimum and the maximum turbidity is near 0.57 V in the configurations 7.09 mA, 8200 k Ω , 35.29 mA, 1000 k Ω , and 53 mA, 680 k Ω . In the other configuration, the differences are near 1.1 V.

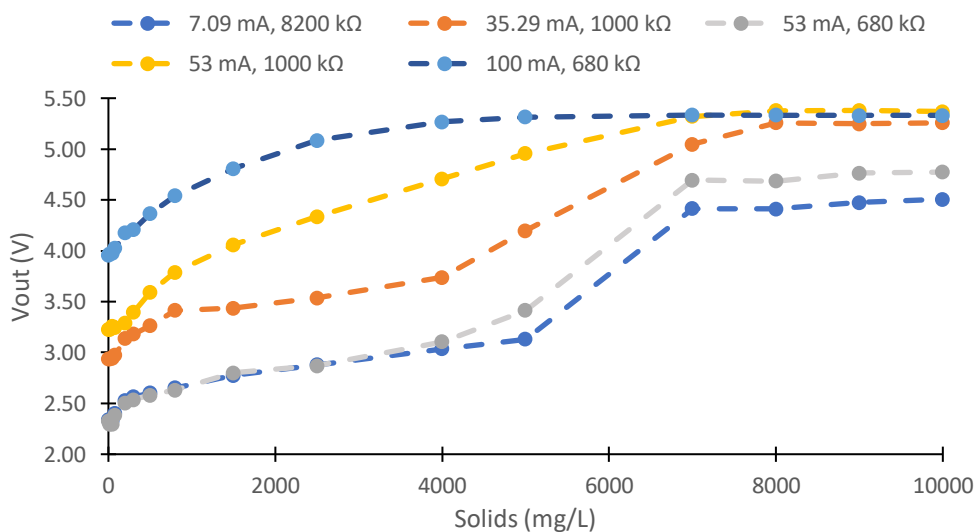


Figure 4.60. Calibration values of the tested configurations (Solids).

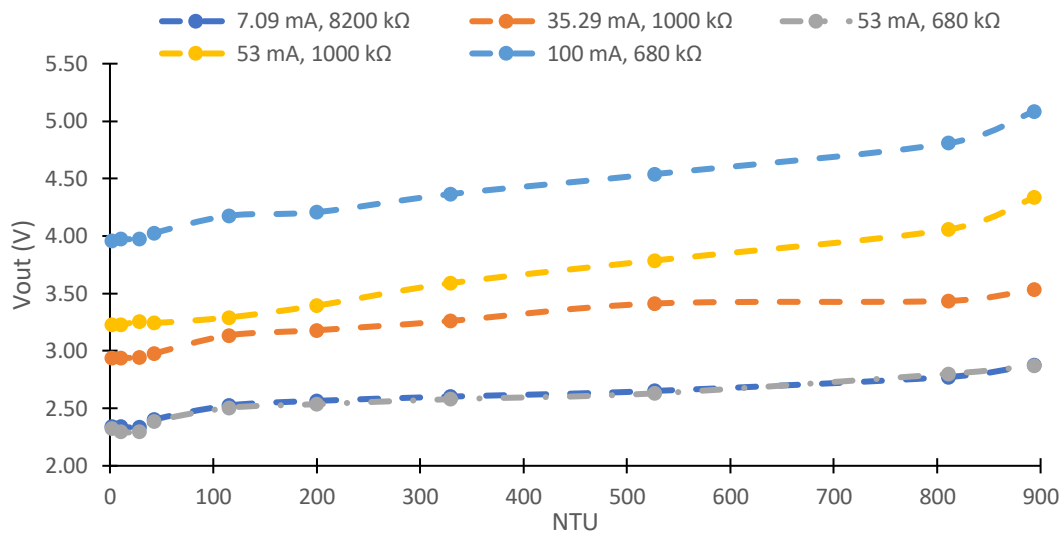


Figure 4.61. Calibration values of the tested configurations (NTU)

Now, we calculate the absolute and REs of the calibration and verification tests. The models have been obtained using Statgraphics (Statgraphics, 2022). Between the models calculated by Statgraphics, we selected the 4 models with the highest R^2 mean of both configurations.

First, we analyze the models that related the turbidity and the V_{out} . The absolute and REs are less in configuration 1 than in configuration 2. The minimum RE in the calibration is in the square root of X with a value of 7.0 %. Similar to the error with a linear model with an error of 7.1 % and a logarithm of X model with a RE of 7.5 %. In the verification, the REs of the four models tested are between 4.4 to 4.8%.

Then we analyze the models that related the solid concentration and V_{out} . The AEs are shown in Table 4.19. In Table 4.20, the REs are presented.

On the one hand, we can observe that in the calibration, the minimum errors are given in configuration 1, with values of 68 and 72 mg/L in the Square Root of Y model and Double Square Root model, respectively. On the other hand, in configuration 2, the minimum error in calibration is 99 mg/L in the model Square Root-Y Square-X. Regarding the verification, in general, the AEs are lower in configuration 1 than in configuration 2. However, the absolute minimum error is 83 mg/L in the Square Root-Y Log-X model. If we calculate the mean of all errors (calibration and verification), configuration 1 presents lower AEs than configuration 2. The minimum error is given in the model Square Root of Y with a value of 72 mg/L. In Table 4.20, we observe the REs. As in the AEs, the calibration of configuration 1 presents lower error than configuration 2. In configuration 1, the lower REs are shown in the model Square Root-Y Square-X instead of in the model square root of Y as occurs in the AE. We select configuration 2 because the errors in the calibration are higher than in configuration 1. In the verification, there are lower errors. This is indicative that configuration 2 presents better performance in the points between the calibrations of the 4 models analyzed. We select the model based on the Square Root of Y. Although it presents higher total errors than those based on Square Root-Y Square-X, it presents fewer calculation difficulty and minor verification errors. Equation 4-27 represents the model of configuration 1, and Equation 4-28 represents the model of configuration 2.

Table 4.19. AEs statgraphics.

Configuration	Data	Square Square-X (mg/L)	Root-Y of Y (mg/L)	Double Root (mg/L)	Square Square Log-X (mg/L)	Root-Y of Y (mg/L)
1	Calibration		100	68	72	97
2	Calibration		99	125	139	153
1	Verification		121	84	85	94
2	Verification		129	97	90	83
1	Total		106	72	76	96
2	Total		109	116	123	130

Table 4.20. REs statgraphics.

Configuration	Data	Square Square-X (%)	Root-Y of Y (%)	Double Square Root (%)	Square Root Log-X (%)	Root-Y of Y (%)
1	Calibration		7.1	7.7	10.7	14.4
2	Calibration		8.0	10.7	12.6	14.4
1	Verification		4.9	5.5	7.3	9.2
2	Verification		11.5	6.6	7.4	8.4
1	Total		6.5	7.1	9.7	13.0
2	Total		9.1	9.3	10.8	12.4

$$\text{Solids } \left(\frac{mg}{L}\right) = (-29.1892 + 4.07327 * Vout (V))^2 \quad (4.27)$$

$$\text{Solids } \left(\frac{mg}{L}\right) = (-158.696 + 41.4702 * Vout (V))^2 \quad (4.28)$$

Finally, we use Eureka software (Datarobot, 2022) to calculate a model that relates the $Vout$ with the solid concentration. Table 4.21 shows the AEs of the models estimated by Eureka. Eureka classifies the models that are calculated by the size of the model. In our case, we compare 4 models, which sizes are 9, 20, 22 and the maximum size (max size). When we used Statgraphics, the minimum AEs were presented in configuration 1, with a value of 9 mg/L in the model with a size of 20. In the verification, configuration 1 presents lower errors than in the use of Statgraphics (except in the model with the size of 22). This does not occur in configuration 2. Finally, if we compare the total errors, the models proposed by Statgraphics present higher values than the Eureka models. In Table 4.22, the REs of the models are shown. As it was in the case with AEs, the REs have lower values than in Statgraphics (except in the verification of configuration 2). For this reason, we consider that configuration 1 is the best configuration. With the increase of the size of the model, the RE decreases but the calculation difficulty increases. The model with a maximum size has a complexity of 118 versus the complexity of 22 of the select model, according to Eureka. In addition, the select model has 5 coefficients versus the 12 coefficients of the model with a maximum size. We select the model with a size of 22 (represented in Equation 4-29). This model presents a RE in the calibration of 2.8 % and 5.3 % in the verification. We consider that the improvement of the REs with the use of the model with a maximum size does not compensate for the increase in calculation costs.

Table 4.21. AEs Eureka

Configuration	Data	Size 9 (mg/L)	Size 20 (mg/L)	Size 22 (mg/L)	Max (mg/L)	size
1	Calibration	21	9	111		42
2	Calibration	50	28	77		50
1	Verification	58	50	140		63
2	Verification	157	156	123		143
1	Total	31	20	118		48
2	Total	86	70	92		81

Table 4.22. REs Eureka

Configuration	Data	Size 9 (%)	Size 20 (%)	Size 22 (%)	Max size (%)
1	Calibration	7.0	3.6	2.8	1.8
2	Calibration	8.0	6.3	6.5	5.3
1	Verification	6.2	5.6	5.3	3.3
2	Verification	10.3	11.7	12.3	11.7
1	Total	6.8	4.1	3.4	2.2
2	Total	8.7	8.1	8.4	7.5

$$\text{Solids } \left(\frac{\text{mg}}{\text{l}}\right) = 5783.8 + 139.0 * e^{V_{out}(V)} - 2753.7 * V_{out}(V) - 0.342 * e^{2V_{out}(V)} \quad (4.29)$$

4.5 Conclusions

In this chapter, we studied the use of two different turbidimeters in sewerage and water bodies. On the one hand, in water bodies, the measurement of water turbidity might not be enough in many cases since different turbidity sources might require other actions. For the same level of solids concentration, if turbidity is caused by sediment, it can indicate a high water runoff. In contrast, the algae might indicate a pollution event linked to eutrophication. Therefore, the characterization of turbidity is essential. We have developed and calibrated a low-cost sensor based on light absorption capable of quantifying the concentration of algae and sediment in mg/L independently. The prototype is based on the light absorption of 5 LEDs with different light colours. Two operational methodologies for the prototype operation are given and compared. On the one hand, the use of multiple regression models adjusted for different solids concentrations is proposed. The combined model (a combination of seven multiple regression models) is characterized by low absolute and RE, similar to those of other low-cost sensors, which possibilities its use. On the other hand, for a more powerful node, using an artificial neural network ensures a drastic reduction in errors with a correct classification of 100% of the cases in the validation phase. This turbidimeter needs to know the concentration of solids to determine the % of alga. For this reason, we developed an algorithm that used of turbidity to obtain the solid concentration and, through an iterative process, obtain the % of algae.

On the other hand, for sewerage, we developed two prototypes for monitoring the concentration of solids in sewerage. This was done to create a system capable of detecting illegal discharges in the sewerage. We studied two situations: when the LDR/photodiodes are at 0° and when they are at 180°. The infrared LED presented a voltage difference that was accentuated in high concentrations for the sewer system.

In the case of the 180° LDR, a significant voltage difference between the minimum and the maximum was achieved. For the concentration of 1 mg/L, the V_{out} is approximately 3 V, which changed until reaching 0 V for the highest concentrations and heights. We consider that due to this limitation, this sensor would not be suitable for sewer monitoring. Nevertheless, it could be used to detect possible excesses in already treated wastewater.

In the case of the LDR at 0°, the LEDs yellow, red, and white presented voltage differences between the minimum value of V_{out} and the maximum. The blue LEDs presented low voltage differences. Regarding the green LEDs, P2 offered a significant difference between the minimum and the maximum, which does not happen for P1. Therefore, we have ruled out the use of this LED for future prototypes. The yellow, red, and white LEDs presented the biggest voltage differences, which are 1.14 V, 1.16 V, and 0.74 V in P1 and 1.05 V, 1.21 V, and 0.89 V in P2 respectively. In this case, a greater dispersion of the results was observed for low concentrations of solids. Since these concentrations are unlikely to occur in wastewater, we believe this will not have a significant effect on our sensor. Finally, mathematical models that relate the V_{out} with the concentration of solids were developed. It was seen that although height had a statistically significant effect, good R^2 was achieved with models that do not include it. Taking into account the errors in the verification phase, we concluded that the best LED is the yellow one. To improve the development of the infrared LED, we use different combinations of resistance in the photodiode circuit and intensities in the infrared LED. We obtained an improvement in the precision of the sensor due to the voltage difference between the minimum and maximum has been increased. However, we have seen that it does not respond satisfactorily to the NTU but rather to the concentration of solids. Therefore, in future works, we will test with other configurations in order to be able to detect the concentration of algae in the water.

Finally, the work presented in this chapter has been published in the following references (Rocher et al. 2021a), (Rocher et al. 2021b), (Rocher et al. 2022)

5 Oil sensor.

5.1 Proposal.

In this section, we summarise the included elements in our proposal. First, we show the characteristics of the proposed prototype. Our prototype is based on photoreceptors and colour LEDs. Finally, an operational algorithm that integrates the sensor on a WSN is displayed. The algorithm sends an alarm to the people responsible for water control to inform them that oil is detected. The control of oil presence in water is critical to prevent the contamination of soils. The proposed sensor is part of the SMARTWATIR project. This project aims to develop and deploy a WSN to detect and purify irrigation water in the Mediterranean area.

5.1.1 Description of the Optical System.

In our prototype, the light source is activated using five colour LEDs: blue, yellow, red, green, and white. Besides, photodetectors are selected to receive the amount of light absorbed, dispersed, reflected or passed through the water column. For this purpose, two photodetectors (LDRs) are located at 0° and 180° from the LEDs. We assume that the amount of the oil modifies the percentages of dispersed, reflected, absorbed or passed light, causing different lectures of the LDRs. The light radiated by the LEDs crosses the water column and hits the oil layer (if there is oil pollution). In cases where there is an oil layer, part of the light is reflected in the oil layer, going back to the LDR located at 0° , and another part crosses it, reaching the LDR located at 180° . The physical operating principle related to light dispersion and the location of LDRs and LEDs of the proposed sensor can be seen in Figure 5.1.

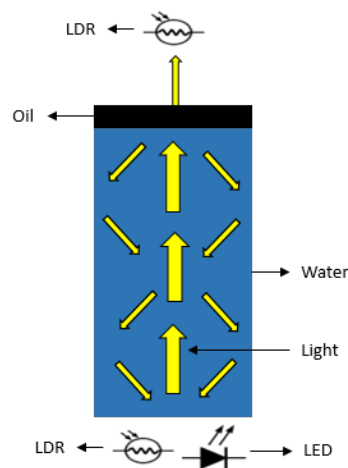


Figure 5.1. Sensor working diagram.

The selected LEDs for our prototype are diffused LEDs with different function voltages. The function voltages are 1.8–2 V for yellow and red and 3–3.4 V for white, blue, and green LEDs. The vision angle is 20° , and the maximum recommended intensity is 20 mA for all of them. As a photodetector, the NSL-19M51 (5 mm) was selected. Finally, the prototype is crafted with a PVC pipe characterized by an external and internal diameter of 5 cm and 4 cm, with a thickness of 5 mm. Figure 5.2 depicts the preliminary design of the proposed prototype. To test this prototype's usability and obtain a calibration, we placed the prototype below a glass tank with water and added different amounts of oil.

5.1.2 Operational Algorithm.

The operational algorithm of the proposed sensor is outlined in Figure 5.3. First, the threshold values are set (TH_x). Then, the sensor determines the presence of oil in the water (by turning on the LEDs and gathering the data with the LDR). Since the height of the water column might affect the measurement of oil concentration, we use the sensor level presented previously (Basterrechea, 2020). If the sensor detects oil presence, the turbidity sensor (Rocher, 2021) is activated. The turbidity sensor is used to impede false positives of oil presence caused by the presence of particles in the water. To properly control the presence of oil, the measured turbidity value has to be below the pre-established threshold. If turbidity values are below the threshold, the system determines that there is pollution by oil, sends an alarm, and the concentration and type of oil data are stored in the SD card of the node. If the turbidity value is above the threshold, it can be a false positive. In this case, data are stored, but no alarm is triggered. We have limited the number of records that the node can store to 3600. When new data is saved, the algorithm adds +1 to a variable (clock). If the “clock” is full (3600 records stored), the system sends all the stored data and erases the SD to release the internal memory. Then, for starting a new measure, the system waits for a time (t_2).

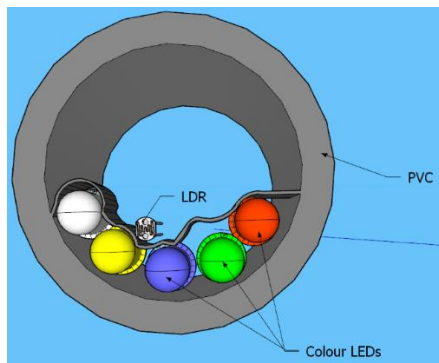


Figure 5.2. Design prototype.

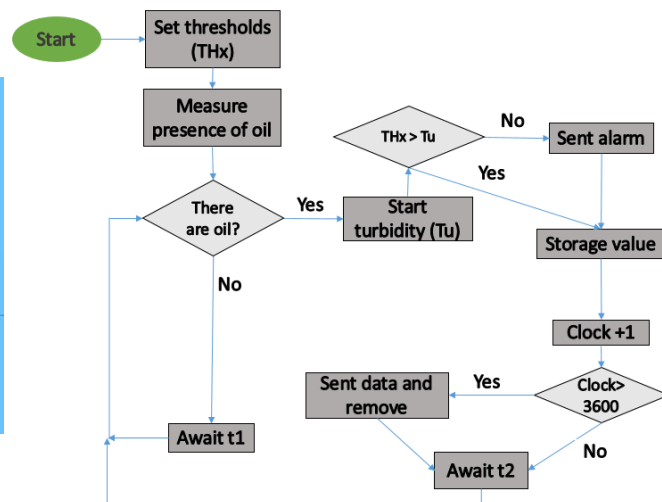


Figure 5.3. Algorithm of oil detection.

5.2 Test Bench.

This section shows the methodology used to power the sensor, the obtention of oil, and prepare the samples for calibration and verification tests.

5.2.1 Electronic Operation.

An AC power supply model FAC-662B is used to power the LEDs with a voltage of 5 V. The required resistors for each LED are calculated using the voltage drop of the LEDs. We calculated the resistance for an intensity of 15 mA. We selected resistors based on the most similar available standard electronic components. The following resistors, 220 k Ω , 220 k Ω , 150 k Ω , 150 k Ω , and 100 k Ω , were selected for yellow, red, blue, green, and white LEDs respectively. Due to the differences in resistance between the calculated and used resistors, we had different intensities for the LEDs. The intensities were 13.48 mA, 13.00 mA, 12.33 mA, 13.60 mA, and 12.39 mA for the yellow, red, blue, green, and white LEDs. To gather the data, we measured the resistance of the LDRs with a tester (Tenma 72-2600 (TENMA, 2022)). As the LDRs have a delay, we waited for 20 s to gather the data for each LED. We repeated the measurements three times in order to

work with mean values. Once we gathered the data, we turned off the LED. Then, we turned on the subsequent LED. The sequential order to power the LEDs was yellow, red, blue, green, and white.

5.2.2 Sources of Oil.

The industrial fuels that we used were obtained from a mechanical workshop. Two types of oil were used for the experiment, oil used by a gasoline engine and oil used by a diesel. The oil used was 0w/30, characterised by an SAE (Society of Automotive Engineers) viscosity of 0 in cold conditions and an SAE viscosity of 30 at working temperature. The used oil is from a mechanical workshop of Valencia province (Spain). The oil is INEO FIRST 0W-30 manufactured by TOTAL QUARTZ (Madrid (Spain)). The two oils have similar values of kinematic viscosity with a value of 25.4 mm²/s at 25 °C. Furthermore, the oils used belong to different types of engines. The first was used in a diesel engine with 77,000 km and three years of use. A gasoline engine with 31,000 km and two years of use was selected for the second oil source. This type of oil is one of the most common oils used in vehicles and machines. In general, the oil of diesel engines is dirtier than the oil of gasoline engines. Diesel engines generate more particles than gasoline engines, and some end up in engine oil. For this reason, used oils in diesel engines tend to be darker than used oils in gasoline engines. In addition, the used oil of diesel or gasoline engines might present some differences in the additives, neutralization number, oxidation, and nitration (Agocs et al. 2020).

5.2.3 Samples for Calibration and Verification.

The experiment was performed at static conditions introducing the samples in a glass tank of approximately 17 L, measuring 35 cm long, 21 cm wide, and 23 cm high. Although the conditions were static, we noticed that the oil stains had some movement on the water's surface due to small performances, such as vibrations, that occurred during the measurement. The glass tank was marked with red tape at water heights of 0 cm, 5 cm, 10 cm, 15 cm, and 20 cm to carry out the measurements. We gathered the data with water at each one of the different heights. In addition, we obtained the data by setting the LDR to 0° and 180°. Figure 5.4 illustrates the used tank, with water up to 20 cm and 0.03 mL_{oil}/cm² (used by a gasoline engine). In the first round, different amounts of oil were used: 0, 7.1, 21.2, 28.3, 35.4, 56.6, 70.7, 106.1, and 141.5 mL. The used volumes correspond to concentrations of 0, 0.01, 0.03, 0.05, 0.08, 0.1, 0.15, and 0.2 mL on the surface of the water. Each of these oil quantities was measured at different water heights. The data obtained was then used to obtain a calibration. Once the calibration had been obtained, four new samples were used to verify the models obtained. The samples for the verification had the following characteristics: 0.02, 0.06, 0.12, and 0.18 mL_{oil}/cm².



Figure 5.4. Experimental tank with $0.03 \text{ mL}_{\text{oil}}/\text{cm}^2$ from gasoline engine at 20 cm height.

5.3 Results.

In this section, the results obtained by our sensor are described. First, we analyze the performance of the developed sensor with industrial oil from a diesel engine. Then, we display the results with the industrial oil from a gasoline engine. Finally, the verification of the obtained mathematical models is analyzed.

5.3.1 Industrial Oil of Diesel Engine.

This subsection shows the sensor's performance when the pollution comes from industrial oil used by a diesel engine.

Figure 5.5 to Figure 5.9 represent the data of the LDR's resistance at 0° for the different light sources tested. We verify that the resistances of the LDR at 180° are not stable due to oil stains moving on the water surface, which causes shadows on the 180° LDR. It is expected that in real conditions, this situation will get worse. Therefore, we decided not to use this LDR. In general terms, and before analyzing case per case, we can identify two different behaviours according to the gathered data. On the one hand, we can see that the resistance of the LDR increases when the concentration of samples increases. This phenomenon indicates that the oil in the water layer absorbs more photons than the same portion of the interface water/air (in the samples without oil). Thus, fewer photons are reflected and reach the LDR, increasing its resistance value compared with the samples without oil. On the other hand, we can find that the oil layer reflects more photons than the interface water/air. Thus, more photons will reach the LDR, decreasing its resistance. The chemical compounds' optical behaviour explains the different tendencies in the oil and the wavelength of the different light sources.

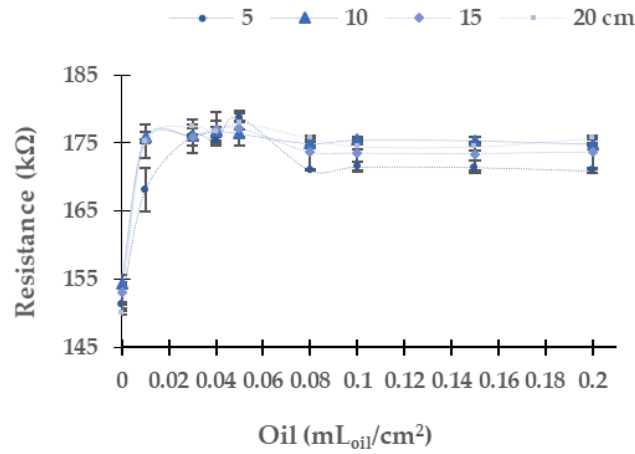


Figure 5.5. Resistance of LDR at 0° in diesel oil in the yellow LED.

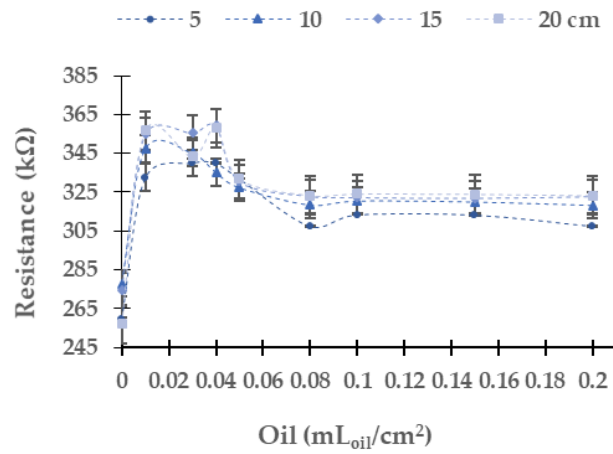


Figure 5.6. Resistance of the LDR at 0° in diesel oil in the red LED.

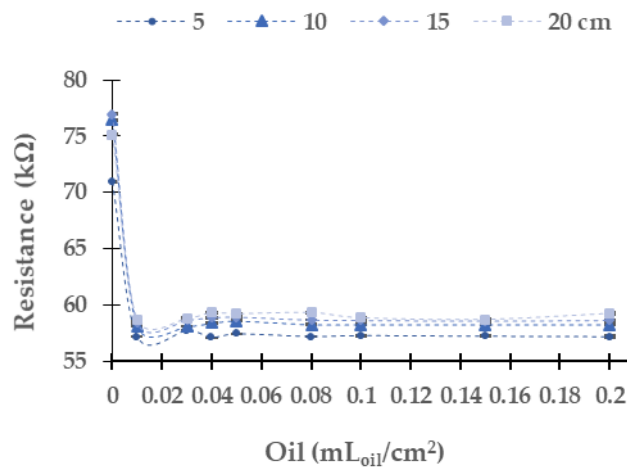


Figure 5.7. Resistance of the LDR at 0° in diesel oil in the blue LED.

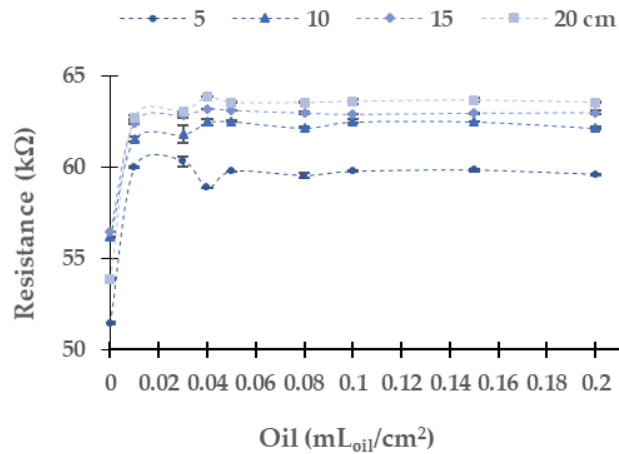


Figure 5.8. Resistance of the LDR at 0° in diesel oil in green LED.

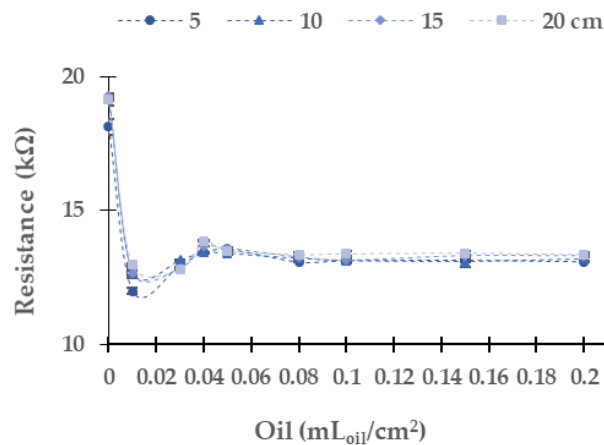


Figure 5.9. Resistance of the LDR at 0° in diesel oil in white LED.

In the following, we analyze the resistance values of the LDR with different light sources and water column heights. The LDR resistance values for the different concentrations of oil used by a diesel engine when the yellow light source is used are displayed in Figure 5.5. The resistance values of LDR of the four tested heights in the concentration of 0 mL_{oil}/cm² are around 151 kΩ. The resistance of the LDR increases when the oil concentration rises. The absolute (and relative) differences between the water without oil and the maximum oil concentration tested are 19.6 kΩ (12.94%) at 5 cm, 20.5 kΩ (13.26%) at 10 cm, 20.6 kΩ (13.44%) at 15 cm, and 25.7 kΩ (17.15%) at 20 cm. For the four tested heights, the maximum value of resistance is found at 0.05 mL_{oil}/cm². From this concentration, the resistance values decrease slightly (except for 5 cm height, where there is a significant decrease in resistance of the LDR between concentrations of 0.05 and 0.08 mL_{oil}/cm²). The resistance values obtained with a water column of 5 cm are slightly away from the rest of the heights for an identical oil concentration. Meanwhile, the values of 10, 15, and 20 cm are relatively similar. Regarding the dispersion of the results in general, this is low. The relative average of standard dispersion is 0.30%, and the maximum standard dispersion occurs in the case of 0.01 mL_{oil}/cm² at 5 cm of water with a value of 3.23 kΩ.

The data gathered using the red LED as a light source is represented in Figure 5.6. The red light has the maximum absolute resistance difference in the LDR between the water without oil and the maximum concentration tested among all tested lights. The absolute (and relative) resistance difference between the minimum and maximum oil tested is 48.1 kΩ (18.5%) at 5 cm,

40.3 k Ω (14.5%) at 10 cm, 48.2 k Ω (17.6%) at 15 cm, and 66.3 k Ω (25.8%) at 20 cm. As in the yellow light source, at all tested heights, LDR resistance values present a great change between 0 to 0.01 mL_{oil}/cm². The resistance values are similar in each height between the concentration of 0.01 and 0.4 mL_{oil}/cm². At all heights, when the oil concentration increases to 0.05 mL_{oil}/cm², the resistance data upsurges. At 5 cm, we observe a significant decrease of the resistance value of the LDR for the samples with concentrations from 0.05 to 0.08 mL_{oil}/cm². At this height, with the increase of oil concentration, the values are stable. The samples with a concentration above 0.05 mL_{oil}/cm² present similar values in the other heights.

In this light source, there is a significant dispersion of the resistance values in the LDR. The maximum standard deviation is 6.99 k Ω . The average standard deviation is 0.84 k Ω , and the relative average standard deviation is 0.25%.

Figure 5.7 presents the results gathered when the blue light is used. The absolute (and relative) resistance difference in the LDR between the concentrations of 0.00 to 0.20 mL_{oil}/cm² is 13.8 k Ω (19.4%) at 5 cm, 18.2 k Ω (23.8%) at 10 cm, 18.3 k Ω (23.8%) at 15 cm, and 15.9 k Ω (21.2%) at 20 cm. In contradistinction to the results above, the resistance values of LDR decrease with increasing oil concentration. In this light, the dispersion of resistance values is low; both maximum and average values are low. The maximum standard deviation is 0.16 in 0.01 mL_{oil}/cm² at 15 cm, and the relative average standard deviation is 0.091%. As in the other light sources previously studied, the values gathered at 5 cm differ from the other resistance values gathered at different water column heights. In this case, we do not observe a tendency such as in yellow and red LEDs. The main change of resistance is between 0 to 0.01 mL_{oil}/cm². Then, from 0.03 mL_{oil}/cm² to 0.20 mL_{oil}/cm², the resistance values are similar, tending to 57 k Ω .

Figure 5.8 displays the data gathered (LDR at 0°) when the green light is used. The absolute (and relative) differences between the first and last samples are 8.1 k Ω (15.8%) at 5 cm, 6.0 k Ω (10.6%) at 10 cm, 6.5 k Ω (18.0%) at 15 cm, and 9.7 k Ω (18.0%) at 20 cm. The values of resistance tend to an upper bound of 60 k Ω at 5 cm, 62.13 k Ω at 10 cm, 62.93 k Ω at 15 cm, and 63.53 k Ω . The maximum dispersion is 0.49 k Ω in the concentration of 0.15 mL_{oil}/cm², and the average dispersion is 0.07 k Ω .

The resistance values measured with the LDR when the white LED is selected as a light source are presented in Figure 5.9. In this case, the absolute (and relative) differences are 5.0 k Ω (27.8%) at 5 cm, 5.9 k Ω (31.1%) at 10 cm, 6.0 k Ω (31.1%) at 15 cm, and 5.8 k Ω (30.3%) at 20 cm. Except in the concentration of 0 and 0.01 mL_{oil}/cm², the rest of the resistance values for the different heights are similar. In this case, the maximum standard deviation and the average for the concentration of 0.01 mL_{oil}/cm² at 20 cm are 0.34 k Ω and 0.06 k Ω , respectively.

Subsequently, we apply a multifactorial Multivariate Analysis of Variance (ANOVA) using Statgraphics Centurion XVI (Statgraphics, 2022) to analyze if the observed differences between resistance values at different concentrations and different heights are significant or not. The results for the analyses are outlined in Table 5.1. In all the cases, the *p*-value is lower than 0.05. Thus, we can state with a probability of 95% that there are statistical differences in the different heights. We do the same for the oil used by an engine and verify that the value of *p* is lower than 0.0001.

Table 5.1. Multivariate analysis of variance for the height and concentration of diesel oil.
Significance levels: *** *p* < 0.05.

	<i>p</i> -Value for Height	<i>p</i> -Value for Concentration
Yellow	0.0031	<0.0001
Red	0.0006	<0.0001
Blue	<0.0001	<0.0001
Green	<0.0001	<0.0001
White	0.0107	<0.0001

Although there is a statistical difference among the LDR resistance values for all the used light sources, the lack of a homogeneous trend along the tested samples precludes determining the sample's concentration. Thus, it is impossible to have a calibration for detecting industrial oil used by diesel engines. The sole option is to determine the presence or absence of oil.

5.3.2 Industrial Oil of Gasoline Engine.

In this subsection, we analyze the resistance values of the LDRs obtained with different light sources and using the industrial oil used in the gasoline engine. As in the case of oil used by a diesel engine, we discard the use of LDR at 180° due to the oil stains generated shadows in the LDR. Now, we focus on the change of resistance of LDR with the different colour light sources and oil concentrations. First, we analyze the results gathered using the yellow light, which is displayed in Figure 5.10. The absolute (and relative) difference in resistance values between the maximum and minimum concentration of oil is $3.5 \text{ k}\Omega$ (3.5%) at 10 cm, $7.2 \text{ k}\Omega$ (7.2%) at 15 cm, and $10.9 \text{ k}\Omega$ (10.9%) at 20 cm. At the height of 5 cm, the resistance values do not have a homogeneous and defined trend. The most probable explanation for the gathered data is the non-homogeneous distribution of the oil over the water. This phenomenon is observed to a lesser extent in industrial diesel engine oil. At 10 cm of the water column, there is no evident trend in the LDR's resistance values for concentrations from 0 to $0.08 \text{ mL}_{\text{oil}}/\text{cm}^2$. Instead, we detect continuous growth at 15 cm and 20 cm until reaching an upper limit, approximately $161 \text{ k}\Omega$. When the yellow light is used, we observe few dispersion data. The maximum standard deviation is $2.38 \text{ k}\Omega$, with an average of $0.48 \text{ k}\Omega$, and a relative standard deviation of 0.31%.

Figure 5.11 represents the LDR resistance values for the red light using the oil of the gasoline engine. The absolute (and relative) difference in resistances values are $26.3 \text{ k}\Omega$ (9.5%) at 10 cm, $36.1 \text{ k}\Omega$ (13.2%) at 15 cm, and $56.5 \text{ k}\Omega$ (56.5%) at 20 cm between the water without oil and the maximum concentration of oil. For 5 cm of the water column, the resistance values do not have a defined trend. We observe that the values measured at 10 cm, 15 cm, and 20 cm tend to grow when oil concentration increases. The maximum standard deviation is found for the height of 5 cm. The standard deviation is generally low, with an average standard deviation of $0.67 \text{ k}\Omega$ with all data gathered. Since data follow a homogeneous trend (except for the last two samples) and the standard deviation is low, we can use these values for calibration.

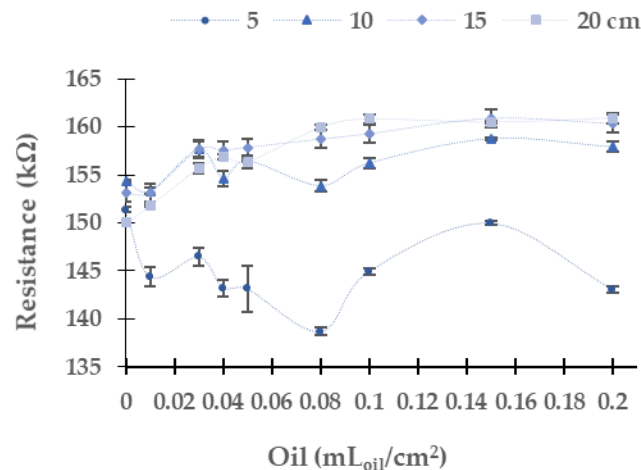


Figure 5.10. Resistance of the LDR at 0° in gasoline oil in the yellow LED.

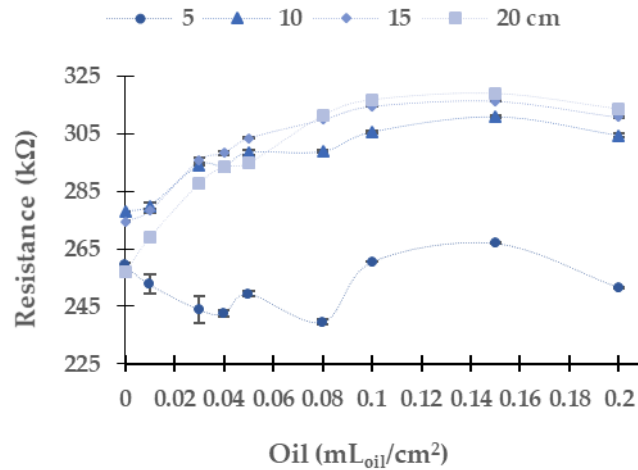


Figure 5.11. Resistance of the LDR at 0° in gasoline oil in red LED.

The calibration models, including the confidence and prediction limits obtained for the red light at 10, 15, and 20 cm, are presented in Figure 5.12, Figure 5.13, and Figure 5.14. Note that the data gathered with the two samples with the highest concentrations are not used for the calibration since they do not follow the same trend as the rest of the data. Mathematical models for the heights at 10 cm, 15 cm, and 20 cm are calculated with Statgraphics Centurion XVI, obtaining the following correlations R^2 0.9138, 0.9560, and 0.9784. The mathematical models are presented in Equations 5.1, 5.2 and 5.3 for 10 cm, 15 cm, and 20 cm. The average AEs are 0.0074 $\text{mL}_{\text{oil}}/\text{cm}^2$ for 10 cm, 0.0031 $\text{mL}_{\text{oil}}/\text{cm}^2$ for 15 cm and 0.0023 $\text{mL}_{\text{oil}}/\text{cm}^2$ for 20 cm. The REs (REs) are 25.9% for 10 cm, 15.8 % for 15 cm and 10.2% for 20 cm.

$$\text{Oil} \left(\frac{\text{mL}_{\text{oil}}}{\text{cm}^2} \right) = (-2.78924 + 0.0101666 \times \text{Resistance (k}\Omega))^2 \quad (5.1)$$

$$\text{Oil} \left(\frac{\text{mL}_{\text{oil}}}{\text{cm}^2} \right) = (-1.88586 + 0.00698826 \times \text{Resistance (k}\Omega))^2 \quad (5.2)$$

$$\text{Oil} \left(\frac{\text{mL}_{\text{oil}}}{\text{cm}^2} \right) = (-1.26118 + 0.00497868 \times \text{Resistance (k}\Omega))^2 \quad (5.3)$$

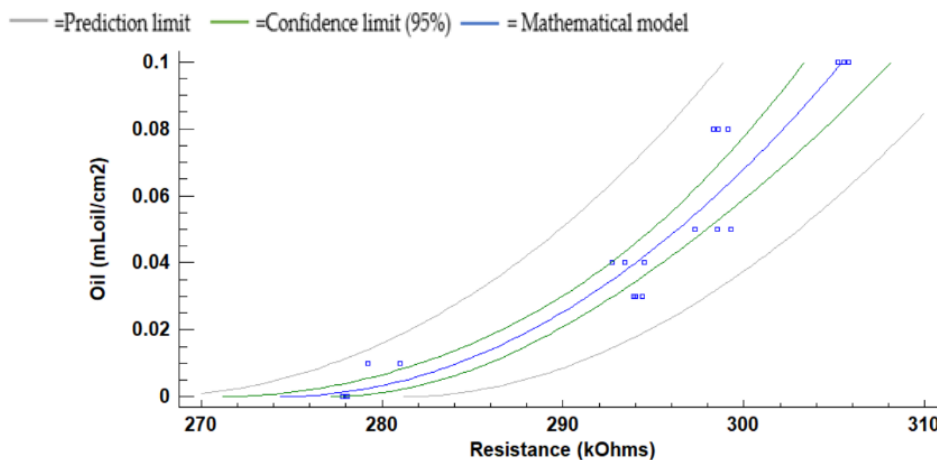


Figure 5.12 The mathematical model for the red light at 10 cm to oil using the gasoline engine.

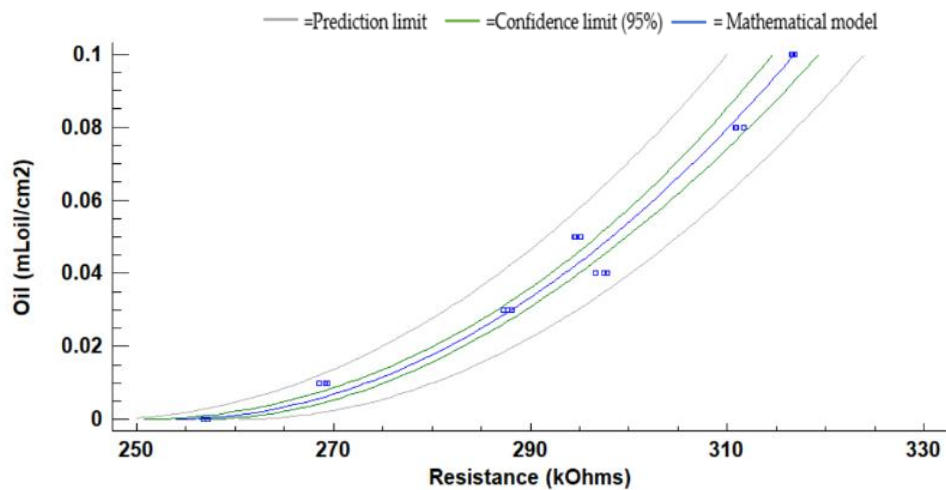


Figure 5.13. The mathematical model for the red LED at 15 cm to oil using the gasoline engine.

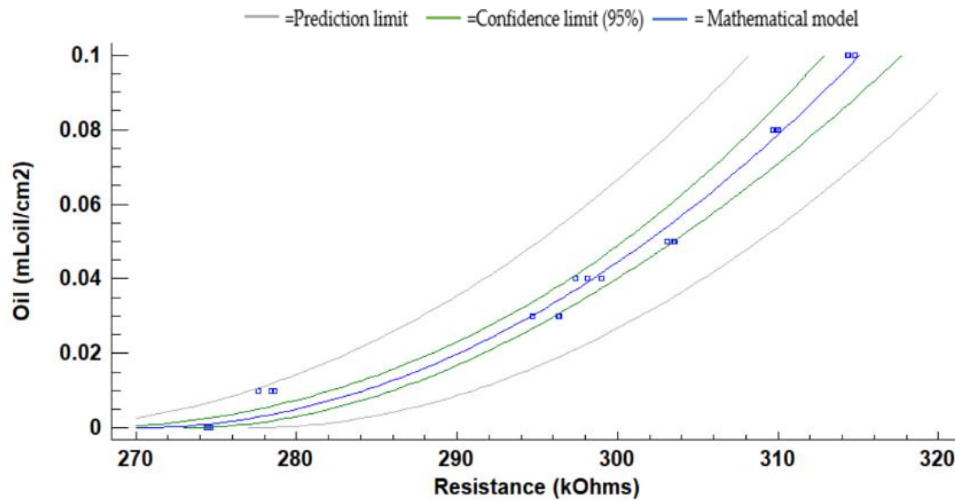


Figure 5.14. The mathematical model for the red LED at 20 cm to oil using the gasoline engine.

In the following, we present in Figure 5.15 the measured resistances in the LDR using blue light. The absolute (and relative) differences in resistances between the samples are 1.1 k Ω (1.4 %) at 10 cm, 1.0 k Ω (1.3 %) at 15 cm, and 1.0 k Ω (4.6%) at 20 cm. These low differences preclude using this LED to monitor the presence of oil in a gasoline engine. As in the previous cases for oil used by a gasoline engine, the height of 5 cm does not have a defined tendency. The rest of the water column heights present an increase of the resistance values between 0 to 0.01 mL_{oil}/cm². From this point, a general reduction of resistance is produced. The resistance values at 10 cm are lower than at 15 cm and 20 cm of water column heights. The average standard deviation is 0.25 k Ω .

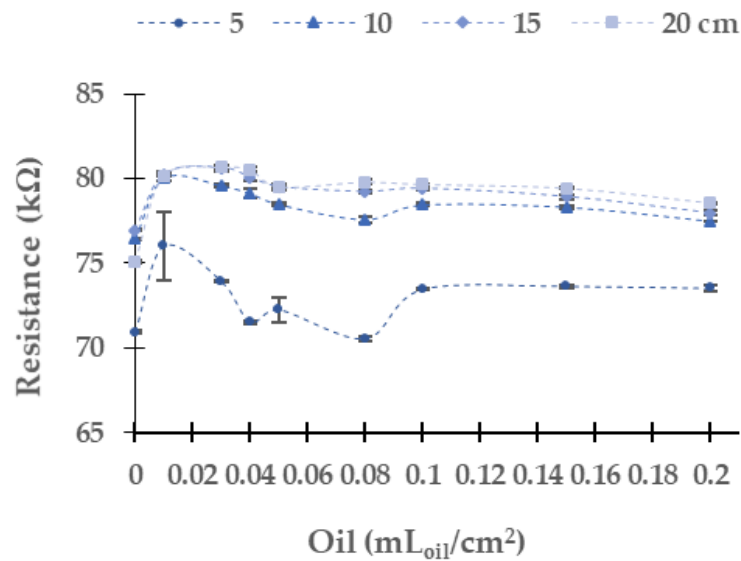


Figure 5.15. Resistance in LDR at 0° in gasoline oil in blue LED.

Figure 5.16 represents the results of the LDR using the green light. The absolute (and relative) differences in resistance values are 6.9 kΩ (12.3 %) at 10 cm, 7.9 kΩ (14.1 %) at 15 cm, and 10.6 kΩ (19.7 %) at 20 cm. In this case, the values tend to grow between 0 and 0.04 mL_{oil}/cm². From this concentration, resistance values are close to an upper limit. The average deviation standard is 0.19 kΩ with a maximum value of 1.20 kΩ.

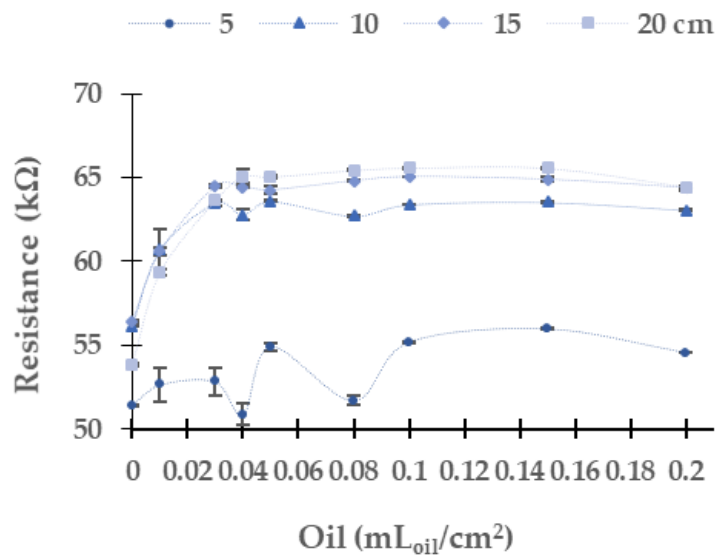


Figure 5.16. Resistance in LDR at 0° in gasoline oil in green LED.

Finally, Figure 5.17 displays the resistance values of the LDR obtained using white light. In this case, we identify a similar trend than in the blue LED with the diesel oil. The tendency, opposed to the observed ones in the rest of the LEDs, is a decreasing resistance when the concentration increases. The absolute (and relative resistances) differences in resistances between the samples are 6.9 kΩ (38.6%), 7.9 kΩ (38.9%), and 10.6 kΩ (38.5%) at 10 cm, 15 cm, and 20 cm respectively. The change in the resistance occurs between the concentrations of 0 and

0.01 mL_{oil}/cm². However, at 0.03 mL_{oil}/cm², there is a slight increase in resistance values. At 0.04 mL_{oil}/cm², there is a decrease in the LDR resistance at all the measured heights. Then from 0.05 mL_{oil}/cm², there is a gradual decrease in resistance values. The average standard deviation is 0.06 k Ω . This deviation is the lowest one among all the LEDs used for monitoring the presence of oil used by a gasoline engine.

We apply a multifactorial ANOVA to analyze if the observed differences between resistance values at different concentrations and different heights are significant or not, as in the previous subsection. The results for the analyses are outlined in Table 5.2. The results indicate that both the height and oil concentration have statistically significant effects on the value of LDR resistance. There is an exception in the case of the yellow LED, for which the concentration of oil has no effect.

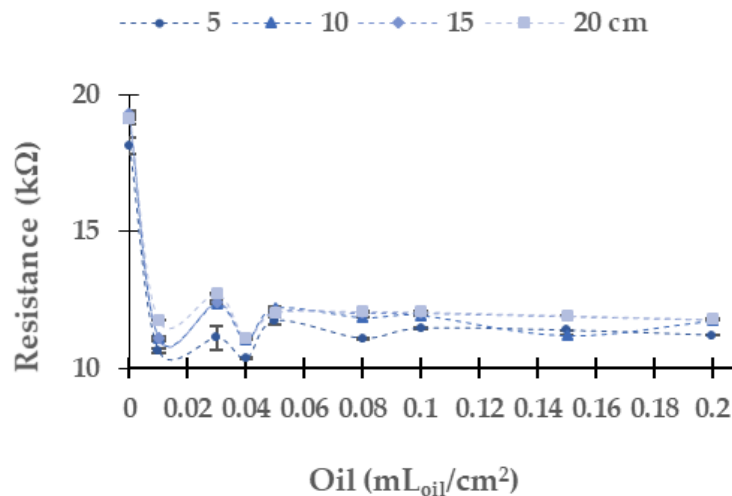


Figure 5.17. Resistance in LDR at 0° in gasoline oil in white LED.

Table 5.2. Multivariate analysis of variance for the height and concentration of gasoline oil. Significance levels: *** $p < 0.05$.

	p -Value for Height	p -Value for Concentration
Yellow	<0.0001 ***	0.0977
Red	0.0003 ***	<0.0001 ***
Blue	<0.0001 ***	<0.0001 ***
Green	<0.0001 ***	<0.0001 ***
White	<0.0001 ***	<0.0001 ***

5.3.3 Verification.

In this subsection, we verify the function of our prototype by measuring four samples, the concentrations of which are different to the ones used in the calibration.

As we said before, concerning the oil from diesel engines, we can differentiate between the presence or absence of an oil layer but not quantify it. Thus, a verification of a proper mathematical model is not possible.

Concerning oil used in a gasoline engine, the red light is the one that presents an optimal behaviour to determine the concentration of oil used by a gasoline engine. Previously, in the red light, we discarded the height of 5 cm of the water column due to its high dispersion of data and its non-regular trend. We verify the mathematical models of the heights 10, 15, and 20 cm (Equations 5.1, 5.2, and 5.3). The results obtained are shown in Table 5.3. Previously, we decided

to use 4 verification points. Nonetheless, the concentration of $0.18 \text{ mL}_{\text{oil}}/\text{cm}^2$ was discarded because this concentration was higher than the ones used for the calibration of the mathematical model. Moreover, the point $0.12 \text{ mL}_{\text{oil}}/\text{cm}^2$ is a higher oil concentration than the calibration points. However, it is a value close to those used to calibrate the model and is included.

Table 5.3. Verification for the red LED.

Height (cm)	Concentration ($\text{mL}_{\text{oil}}/\text{cm}^2$)	Calculated Concentration ($\text{mL}_{\text{oil}}/\text{cm}^2$)	AE ($\text{mL}_{\text{oil}}/\text{cm}^2$)	RE (%)
10	0.02	0.025	0.005	27.1
10	0.06	0.073	0.013	21.1
10	0.12	0.134	0.014	11.5
15	0.02	0.020	0.000	2.3
15	0.06	0.079	0.019	30.9
15	0.12	0.111	0.009	7.9
20	0.02	0.019	0.001	2.7
20	0.06	0.073	0.013	22.0
20	0.12	0.110	0.010	8.5

Regarding the verification results, the average RE is 19.9 % at 10 cm, 13.7 % at 15 cm and 11.1 % at 20 cm. At the 15 cm and 20 cm heights, the maximum RE is found in the concentration of $0.06 \text{ mL}_{\text{oil}}/\text{cm}^2$ with values of 30.9% at 15 cm and 21.3 % at 20 cm. Regarding the verification, at 10 cm, the maximum RE is 27.1% at $0.02 \text{ mL}_{\text{oil}}/\text{cm}^2$.

5.3.4 Discussion.

This section discusses the obtained results. First, we analyze the results obtained for the two sources of pollution. Next, we present the algorithm to calculate oil concentration in water. Finally, we discuss the lessons learned and the limitations of our study. Finally, the relevance of this sensor for smart irrigation is argued for.

5.3.4.1 Differences among Oils.

In this subsection, we analyze the differences among the obtained results with the different pollutants. Table 5.4 outlines the minimum and maximum resistance values gathered with the two oils (gasoline and diesel engine). LDR combined with green and white lights present similar minimum and maximum resistance values. Meanwhile, when combined with yellow, red, and blue lights, they present higher resistance differences with the two tested oils.

Table 5.4. Maximum and minimum resistance measured when the two oils.

Colour	Gasoline		Diesel	
	Minimum (k Ω)	Maximum (k Ω)	Minimum (k Ω)	Maximum (k Ω)
Yellow	138.68	160.91	150.01	178.81
Red	239.50	318.83	256.97	359.19
Blue	70.56	80.66	57.09	76.94
Green	50.88	65.57	51.44	63.85
White	10.35	19.29	11.98	19.29

Summarizing the obtained values of the two experiments, we can identify some differences, which can be used to create our sensor. For example, the red LED can be used as a light source to quantify the volume of contamination in the oil used by gasoline engines, while no one LED can be used to quantify the oil used by diesel engines. We observe an important difference in the

trends by comparing the resistance values with oil from a gasoline engine with the same oil from a diesel engine using the blue LED. There is a rapid reduction of the resistance values in diesel oil, which is not identified with the oil used by a gasoline engine. This fact can be used for determining the presence of oil used by gasoline or diesel engines. Thus, we can affirm that there is an option to combine different LEDs to create a sensor for industrial oil detection and quantification in certain cases.

5.3.4.2 Selection of LEDs.

In this subsection, we present in detail the best configuration of LEDs and the operation algorithm for the developed sensor.

After checking the results, we can affirm that quantifying the oil concentration used in diesel engines in water is not possible with our prototype. Nonetheless, it is possible to determine the presence or absence of oil used in diesel engines. The green, white, and blue LEDs can be used for that purpose. They all present a great difference of resistance between the concentration of 0 to 0.01 mL_{oil}/cm², and have similar resistance values in concentrations higher than 0.01 mL_{oil}/cm². Since the white LED has the highest relative difference between water with and without oil, it is the best option to determine the presence of oil. To determine the source of oil, we use the blue LED. The resistance value of the LDR is different according to the origin of the oil present in the water. If the oil is from a gasoline engine, the red LED can be used to determine the concentration. Next, we are going to detail the steps followed to determine the presence of oil in water followed by our prototype.

The first step in our operational algorithm is to determine if there is oil in the water and to identify if the oil comes from a diesel or gasoline engine. We use the white LED to determine the presence or absence of oil in water. The minimum resistance of the LDR with the white LED when there is no oil is 18.2 kΩ. Meanwhile, when oil concentration is 0.01 mL_{oil}/cm² or higher, the resistance value decreases to 12 kΩ or 11 kΩ, according to the origin of the oil, diesel, or gasoline engine. Therefore, if the measured resistance value on the LDR is lower than 18 kΩ, we can assume that there is oil pollution in the water. Once the presence of oil in the water has been determined, the next step is to ascertain whether the oil comes from a diesel or gasoline engine. We use the blue LED to recognize the origin of the oil. In gasoline oil, the resistance of the LDR increases with the concentration of oil. On the contrary, if the oil was used by a diesel engine, the resistance decreases with the concentration of oil. On the one hand, with the blue light, the resistance values of LDR when the origin of oil is a diesel engine are below 60 kΩ. On the other hand, the resistance values are close to 75 kΩ (or higher) when the oil was used by a gasoline engine. Thus, we set a threshold of 70 kΩ to determine the origin of the oil.

Regarding the oil of a gasoline engine, it is possible to quantify its concentration using the red LED. Nevertheless, in this case, the height has a significant impact on the gathered data. Therefore, the water height must be measured in order to select which calibration model must be applied (see Equations 5.1, 5.2, and 5.3). If the water column height is lower than 7.5 cm, we cannot apply any of the equations since we are reaching the scenario with a water column equal to 5 cm and our results indicate that it is not possible to have a calibration. If the water column is higher than 22.5 cm, we cannot use any equation because the height of the water is far away from the highest tested water height and no information about the expected results is obtained. In these two cases, the algorithm can indicate the origin of the oil but not its concentration. For water column heights between 7.5 and 22.5 cm, interpolation will be carried out between Equations 5.1, 5.2, and 5.3, depending on the case.

To sum up, we use a combination of LEDs in our prototype. The white LED is for determining the presence of oil, and the blue LED is for identifying the source of the oil. The red LED is used to quantify the oil concentration if it comes from a gasoline engine in water heights between 10 to 22.5 cm. The whole process with the thresholds can be seen in Figure 5.18.

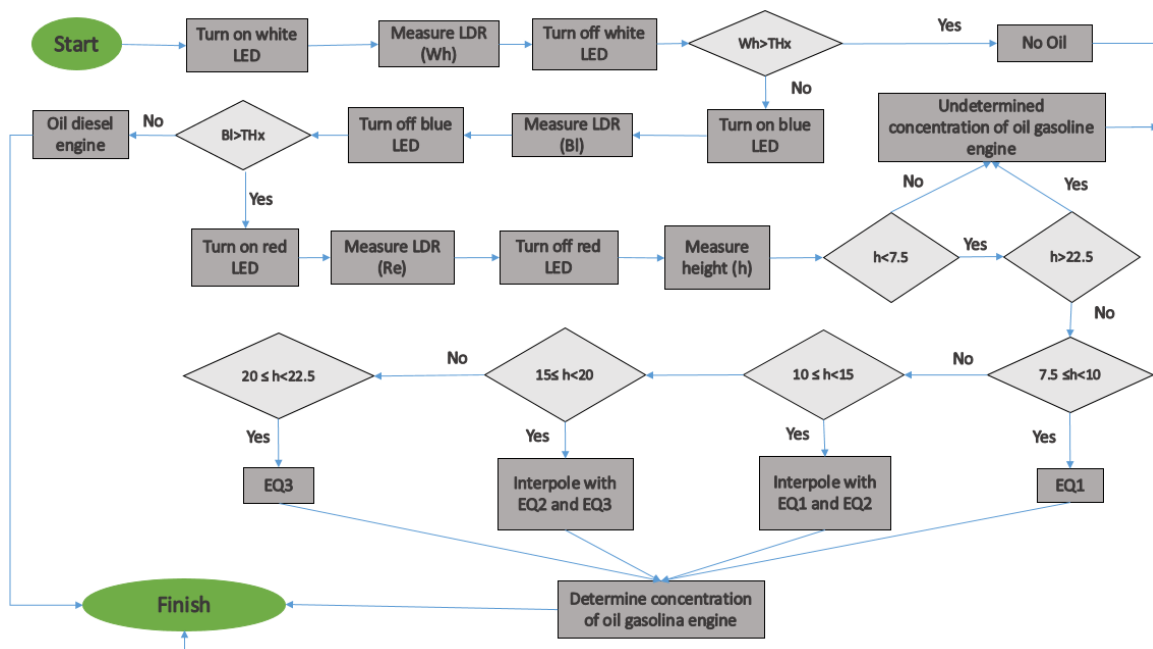


Figure 5.18. Algorithm of the function of our sensor.

5.3.4.3 Lessons Learned and Limitations of the Present Study.

Along with this study, we have identified some interesting issues which must be considered for future sensors for water quality designs. First and foremost, the irregular dispersion of oils in the water surface causes a series of shadows and irregularities in the light distribution, which precludes the use of the light receptor at 180° from the light source. Moreover, this dispersion also causes many difficulties when the sensor (at 0° from the light source) is placed too close to the water surface, at 5 cm or less. Thus, in future designs and test benches, we will establish the sensors farther from the water surface. We tested the sensor in static conditions. In the future, we will test in a real irrigation channel. Sloshing from the oil and water interface can lead to problems for oil determination. To solve this problem, the sensor will be located in areas with a laminar water regime. Moreover, the inclusion and the most appropriate orientation and materials for measuring conduct to avoid bubbles, voluminous suspended solids, and fouling will be studied.

Regarding some possible interferences with other pollution sources, the combination of the turbidity sensor with the proposed prototype reduces the range of pollutants, which can produce a false negative. Despite this, other organic compounds with density values lower than the water might interfere with our sensor. Some examples are gasoline and diesel. The water velocity might also reduce the accuracy of our sensor. If the water current is too high, it will move and disperse the pollution very fast, which will make reading the resistance of the LRD or precluding the competition of the entire operational algorithm before the water characteristics change difficult.

5.3.4.4 Relevance of the Present Study for Smart Irrigation and SMARTWATIR Project.

Although the pollution of industrial oil from irrigation channels is a relatively controlled issue in developed countries, it is not a controlled issue in developing countries. As far as we know, there is no evidence in papers or reports that reviews the periodicity of pollution events linked to industrial oil of agricultural machinery. Nonetheless, the impact of this pollution is very high, affecting the soils, the aquifers and even the yield, as set out in the introduction. One of the principal reasons for this lack of information is the fast dispersion and local incidence jointly to the vast surface of irrigation channels, which causes difficulties data sampling and monitoring.

Therefore, the inclusion of this low-cost sensor will be crucial in monitoring pollution in irrigation channels. This is particularly important in scenarios where smart irrigation is being applied since the industrial oil can produce interferences in other sensors (such as conductivity sensors) or foul other optical sensors placed on the water surface.

Focusing on the SMARTWATIR project and the phytodepuration, the detection of pollutants such as industrial oil must be accomplished before the phytodepuration in order to determine if the water can be regenerated or not. Moreover, some pollutants might be toxic to the plants, jeopardizing the entire ecosystem.

In this subchapter, we evaluated the application of an optical sensor to measure industrial oil concentration in irrigation water. For this purpose, we used an assay which included two types of industrial oil (from a diesel engine and a gasoline engine). We evaluated the sensor's performance at four different water heights (5, 10, 15, and 20 cm). As a light source, we used yellow, red, blue, green, and white LEDs.

5.4 Conclusions.

We evaluated the application of an optical sensor to measure industrial oil concentration in irrigation water. For this purpose, we used an assay which included two types of industrial oil (from a diesel engine and a gasoline engine). We evaluated the sensor's performance at four different water heights (5, 10, 15, and 20 cm). As a light source, we used yellow, red, blue, green, and white LEDs.

The white LED can be used to detect the absence or presence of industrial oil. Meanwhile, the blue LED can determine the source of this industrial oil. For pollution coming from the oil used by a diesel engine, at all light sources and water column heights, the LDR resistance has an abrupt change between 0 to 0.01 mL oil/cm², allowing the detection of pollution. At higher concentrations, the values approached an upper limit or decreased slightly, precluding the determination of oil concentration. For the oil used by a gasoline engine, the red light is the unique one that presents homogeneous changes in the LDR's resistance values at all tested concentrations, allowing us to measure the concentration of the industrial oil. The calibration verification provided an average RE of 19.9%, 13.7%, and 11.1% for 10, 15, and 20 cm, respectively. Thus, our prototype will combine different light sources for monitoring oil in irrigation water.

Finally, the work presented in this chapter has been published in the following reference (Basterrechea et al., 2020c) and (Basterrechea et al., 2021a).

6 Practical deployment analysis.

In this chapter, we analyze the use of sensors in a pipeline. First, we study the different scenarios that can occur in storm sewerage according to the water level and rain. Then, we test the oil and conductivity sensor in a pipeline to check its operation. In addition, we use simulation software to determine if it is possible to detect blockages and illicit discharges in the sewerage.

6.1 Scenarios in storm sewerage.

In this subchapter, we propose a system based on level sensors and rain sensors for monitoring the water level in separated sewerage. First, we present the algorithm that uses our proposal and after the results.

6.1.1 Algorithm.

In this section, we show the algorithm of decision of our system.

The algorithm is represented in Figure 6.1. In the first place, the water level sensor measures the level of water in the sewerage. The system compares the water level now (W_n) with a water level critical (W_c). The W_c is a level defined by the user for indicating from which point the water level is not in a normal situation. After, the system checks if it is raining or not. Finally, the system compares the water level in a point (W_u) with the water level of the next control point downstream (W_d). This algorithm is used when the pipes have the same diameter. In the case of different diameters between two points, it must compare the volume of water in the two points with the use of the mathematical equation to calculate the volume in a cylinder. With this information can be calculated the water level which corresponds to the pipe diameter.

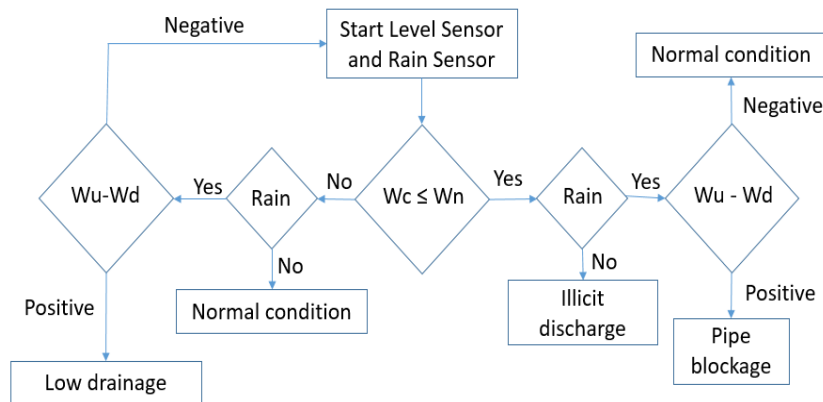


Figure 6.1. Algorithm for data processing

The definition of a W_c is important for discharged false positives. The value of W_c should be determined by the person responsible in order to prevent small amounts of water arising from the irrigation of gardens, private vehicles, etc., and setting of alarms that are not related to the illicit dumping.

6.1.2 Results.

In this section, we study the different scenarios that can be analyzed in section 6.1.1. These different scenarios presented are simulated. We simulate the behaviour of a stretch of sewerage that has two acoustic sensors at its ends when the rain starts and when it finishes.

The first scenario is the normal condition. This condition happens in two situations. When it is not raining, and the sewerage does not transport water. The other normal situation is when it is raining and the sewerage has water. This situation is represented in Figure 6.2. In this situation,

the rain starts at 25 minutes and finishes at 150 minutes. The two water level sensors are located upstream and downstream. The downstream will register a value of water level higher because at this point, more water will accumulate. If we subtract the height value of the two sensors, we will obtain a difference that will be less than what we will obtain in the other cases.

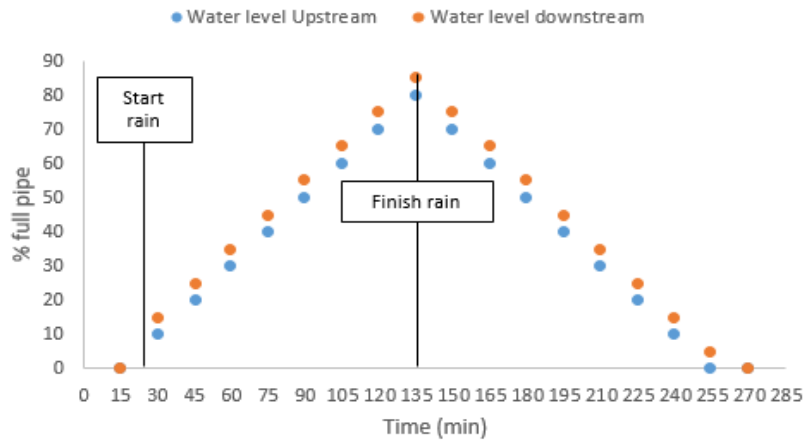


Figure 6.2. Normal scenario.

Another scenario is when the pipe is stuck. In this situation, the rainwater is accumulated in the sewerage during the rain before the blockage. When this happens there is much more water in the upper area compared to the lower area because of this the drainage will occur very slowly. This situation is represented in the Figure 6.3. In this case, an unlocking device should be sent to the pipe in order to eliminate the jam.

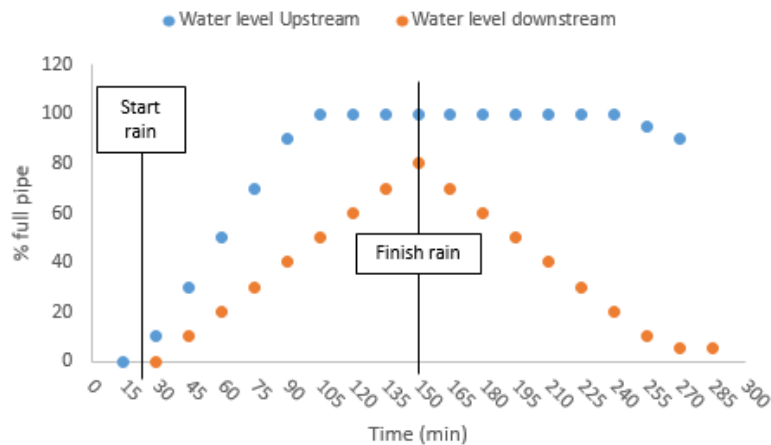


Figure 6.3. Blockage scenario

When a problem in the drainage of the runoff occurs, we can observe that the value of the water level upstream is much smaller than the value of the water level downstream. This occurs because upstream water is not entering the sewer while downstream will be entering. In this case the system generates an alarm so that drains are monitored at street level. If the problem is not solved in a short space of time floods can occur in lower areas of the city. Figure 6.4, it is represented this situation.

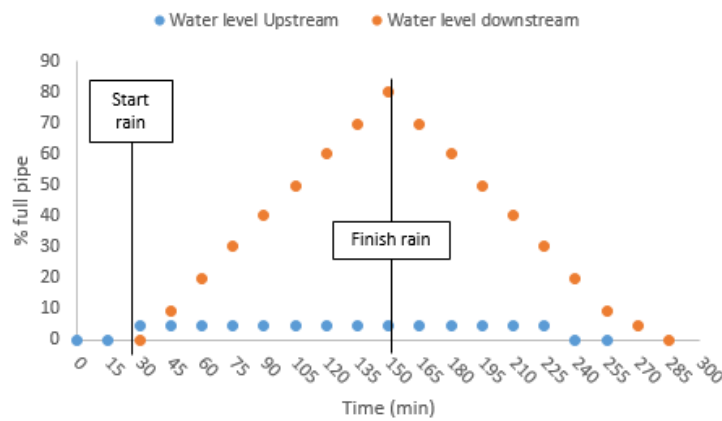


Figure 6.4. Low drainage

Finally, in the case, we detect there is no rain, and the water level is larger than the critical water level this is a sign of illicit discharge. In this case, we assume that the discharge is made somewhere between the two measurement points. The critical water level is defined by the user, and it is used to discard possible positives due to the irrigation of parks, washing of private vehicles, etc., that use water and could end up in the sewer system. This situation is represented in Figure 6.5.

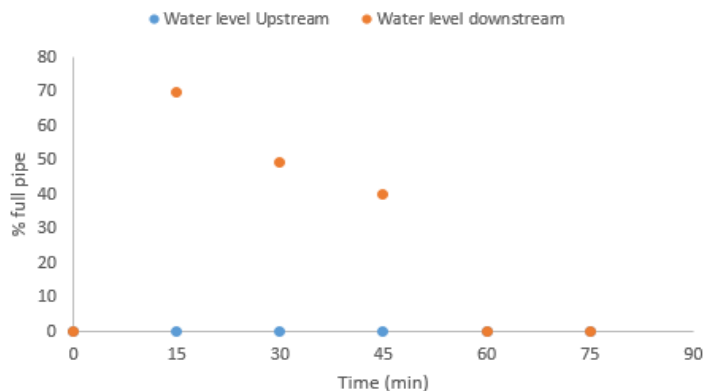


Figure 6.5. Illicit discharge

6.2 Water level, conductivity, and oil sensor.

One time the different scenarios were studied. We analyze the use of conductivity, distance and oil sensors to detect the presence of illicit spills and blockages in the storm sewerage in this subsection. Our proposal uses rain, water level, oil, turbidity, and conductivity sensors to determine the presence of illicit spills in the sewerage and blockages in the storm sewerage networks. We use the rain sensor to control the presence and amount of rain in the monitoring area and the level sensor to monitor the presence of water in the pipes. We establish 4 different scenarios according to the rain and water level in the sewer. The perfect scenario for an illicit discharge is when it is raining and there is water in the storm pipes. In this scenario, the rain and level sensors cannot monitor the presence of illicit spills. We use turbidity, oil, and conductivity sensors to solve this problem.

6.2.1 Test bench.

In this section, we explain the methodology used. First, we explain the methodology used to calibrate oil and conductivity sensors. After, we show the methodology used to check the use of level sensors in sewerage.

6.2.1.1 Conductivity and oil sensor.

In this subsection, we explain the methodology used to obtain the data of the oil and conductivity sensors.

We performed a closed hydraulic circuit with PVC pipes represented in Figure 6.6. The circuit starts in a water tank with a pump for pumping water. The pump has a power of 400 W, providing a flow of 1.7 L/s. The pumped water is impulsed to the circuit through an impulse pipe. The pump pumps the water from the base of the water tank to the circuit through an impulse pipe. The impulsion pipe has a height of 25 cm. Next, an elbow connects the impulse pipe and the transport pipe. The transport pipe has a length of 2 m. Then, two elbows are connected from the transport pipe to the return pipe. The return pipe returns the water to the tank. The return pipe has a slope of 2 %. The conductivity and oil sensors are placed in the middle of this pipe. The pipes used have an external diameter of 50 mm, and a thickness of 3 mm. In the two tests, we used 20 litres of freshwater, and each measurement is performed by triplicate.

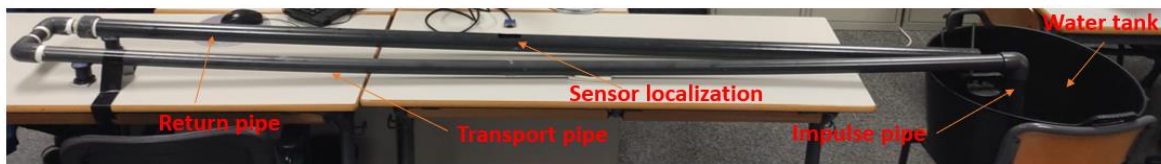


Figure 6.6. Hydraulic circuit.

Conductivity and oil sensor calibration are carried out separately. First, we perform the conductivity test, adding table salt to the water to perform the different samples. The concentration of samples used for the calibration and verification is represented in Table 6.1. We use a conductivity sensor presented previously in (Parra, 2015). We add an epoxy layer to the sensor to increase its protection. On the one hand, the epoxy layer protects the insulating layer of copper from the chemicals that can be present in the storm sewerage. On the other hand, the epoxy helps keep the spires in the same position by keeping them glued together. The conductivity sensor is based on 2 coils with 40 and 80 spires of copper with a diameter of 0.4 mm. The PC is the coil with 40 spires and the other is the IC. The function generator model AFG1022 (Tektronix, 2022a) is used to power the coil. We use an oscilloscope model TBS1104 (Tektronix, 2022b) to measure the voltage induced. The PC has a current of 3.3 V peak to peak with a series resistance of 47 ohms. We use a metalized polyester film capacitor of 10 nF parallel to the coil in the IC. We test the frequencies between 150 to 180 kHz, each 1 kHz. We select these frequencies due to the frequency peak is between 160 to 170 kHz, and we want to know the behaviour of the sensor in the frequencies nearby to select the best WF.

Table 6.1. Salt concentration used in calibration and verification.

Calibration	Salt (g/L)	0.0	1.0	3.0	4.0	5.0	7.0	10.0	12.0
	Conductivity (mS/cm)	0.53	2.66	6.68	8.59	10.64	14.34	19.7	23.2
	Salt (g/L)	15.0	18.0	20.0	22.0	25.0	28.0	35.0	
	Conductivity (mS/cm)	28.2	32.9	36.2	39.6	44.2	48.8	58.4	
Verification	Salt (g/L)	2.0	4.5	8.0	13.0	19.0	23.0	30.0	
	Conductivity (mS/cm)	4.73	9.58	16.1	24.9	34.5	41.1	51.9	

About the oil sensor, it is presented in (Basterrechea, 2021) and in chapter 5. However, we added an infrared LED and photodiode to improve the prototype. We use the same hydraulic circuit explained previously. As the sensor can be affected by the external light, we cover it with an opaque bag. When we start the measurements for each concentration, we clean the sensor. We use a multimeter model Tenma 72-2600 (TENMA, 2022) to measure the resistance of the LDR and the output voltage (V_{out}) of the photodiode. In our design, we use a voltage divider formed by a fixed resistance and, after the circuit, the photodiode or LDR.

A power supply model FAC-662B is used to power the LEDs and photodiode. The LEDs are powered sequentially with a voltage of 5 V, and each is powered for 20 seconds. We want the intensity current for the colour LEDs to be close to 15 mA. We select this value because the colour LEDs are not recommended to have an intensity current higher than 20 mA. However, as we use standard resistance, the real intensity of the colour LEDs are 13.48, 13, 12.33, 13.6, and 12.39 mA to yellow, red, blue, green, and white, respectively. In the infrared LED, we test with different intensities. These are 13.2, 17.4, 23.2, 34.4, 49.6 and 90 mA. The maximum intensity recommended in the infrared LED by the manufacturer is 150 mA.

The values of resistance of the LDR must be changed to voltage to allow the microcontroller to read it. We use a voltage divider for signal conditioning. To select a fixed resistance value, we find a value to maximise the difference between the water without oil and the maximum concentration of oil tested. In the case of the photodiode, we measure the V_{out} directly. For this, we need to determine previously the resistance that we will be using. To determine it, we tested with different current intensities in the infrared LED and changed the fixed resistance. In the fixed resistance, we test with different resistances between 1 k Ω to 8.2 M Ω . To perform this test, we used the pipe with water and a black object that simulated the presence of oil. We do not use oil to determine the fixed resistance to prevent water pollution.

For elaborating the different oil samples, we use the same water to reduce the quantity of polluted water. In the water, we add different volumes of oil to elaborate the sample. Once the sample is elaborated, we measure with the sensor and repeat the process for each sample. The concentrations used in the calibration and verification are represented in Table 6.2. We use used oil provided by a local car workshop in Valencia (Spain). The oil was used by a gasoline car for 31,000 km and 15,526 km.

Table 6.2. Oil concentration used in calibration and verification.

Calibration (mLoil/ Lwater)	0.0	0.2	0.4	0.6	0.8	1.0	1.2	1.4	1.6	1.8	2.0	2.2
	2.4	2.6	5.0	10.0	15.0	20.0	25.0	30.0	35.0	40.0	45.0	
Verification (mLoil/ Lwater)	0.1	0.7	1.3	1.9	2.5	17.0	32.0	47.0				

6.2.1.2 Blockage detection in sewerage.

In this subsection, we explain how the simulations are performed to determine the possibility of using level sensors to monitor the sewerage.

The software used to perform the simulation is the EPA Storm Water Management Model SWMM 5.1 (EPA, 2014) to simulate a subsection of a storm sewerage network. The software offers different models for simulating storm sewerage. We select the dynamic wave model because this model calculates the water that accumulates in the sewer in the case of excess water. The model needs the rain values to calculate the water entering the sewerage. We create artificial rain represented in Table 6.3.

Table 6.3. Values of the artificial rain.

Time simulation (h)	1	2	3	4	5	6	7	8	9
Rain (mm)	0	7	6	8	20	7	5	2	0

The measurements of the basins and pipes used in the simulation have been obtained following an industrial park's typical distribution. This distribution is large plots occupied by industrial buildings and streets for access. The storm sewerage is distributed in accordance to the streets, and the different buildings dump the pluvial water into the street. In our simulation, we have 4 plots of 4.5 ha each. Each plot is subdivided into 6 parts (sub-basins) that dump the stormwater into a node. We estimate that 90 % of the area is impervious as it is an industrial zone. The rest of the parameters are the default values of the program. The pipe diameter used is 0.5 m diameter for all pipes with a pending of 2 %. These are the minimum values recommended in the storm sewerage. The simulation concept is represented in Figure 6.7, and Table 6.4 shows the values of length and heights of the different pipes.

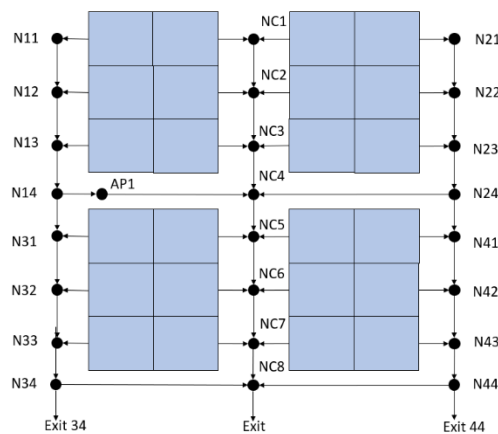


Figure 6.7. Map of the simulation section.

Table 6.4. Values of length and heights of the different pipes.

Pipe	Length (m)	Start Height (m)	Finish Height (m)	Pipe	Length (m)	Start Height (m)	Finish height (m)
NC1-NC2	93.3	11.4	9.5	N22-N23	93.3	12.7	10.9
NC2-NC3	93.3	9.5	7.7	N23-N24	93.3	10.9	9.0
NC3-NC4	93.3	7.7	5.8	N24-N41	5.0	9.0	8.9
NC4-NC5	5.0	5.8	5.7	N24-NC4	160.0	9.0	5.8
NC5-NC6	93.3	5.7	3.8	N31-N32	93.3	8.9	7.0
NC6-NC7	93.3	3.8	2.0	N32-N33	93.3	7.0	5.2
NC7-NC8	93.3	2.0	0.1	N33-N34	93.3	5.2	3.3
NC8-Exit	5.0	0.1	0.0	N34_Exit34	5.0	3.3	3.2
N11-N12	93.3	14.6	12.7	N34-NC8	160.0	3.3	0.1
N12-N13	93.3	12.7	10.9	N41-N42	93.3	8.9	7.0
N13-N14	93.3	10.9	9.0	N42-N43	93.3	7.0	5.2
N14-NC4	160.0	9.0	5.8	N43-N44	93.3	5.2	3.3
N14_N41	5.0	9.0	8.9	N44-NC8	160.0	3.3	0.1
N21-N22	93.3	14.6	12.7	N44-Exit44	5.0	3.3	3.2

6.2.2 Results.

In this section, first, we analyse the results obtained in the oil sensor. Then, we present the results obtained in the water level simulation. Finally, we show the results of the conductivity sensor.

6.2.2.1 Oil sensor.

In this section, we show the results obtained with the oil sensor. First, we need to determine the fixed resistance in the photodiode circuit and the current intensity of the infrared LED. After, we analyse the results obtained by the photodiode of the prototype. Finally, we study the results obtained with the LDR.

Concerning photodiode, we test with the intensity current of the infrared LED and the fixed resistance of the voltage divider. The V_{out} difference between water and the black object is represented in Figure 6.8. In this figure, we observe that the V_{out} difference is near 0 V in the lower fixed resistances in all intensities tested. The V_{out} difference between the water and the black object increases with the increase in resistance up until a maximum. To the intensities of 49.6 and 90 mA, the maximum difference occurs at 2.2 M Ω . With the increase of the fixed resistance, we observe a reduction of the V_{out} difference in these two current intensities. Which would indicate a parabolic behaviour with the increase of fixed resistance. In the other intensities tested, we do not observe a maximum. We think that these intensities, with the increase of the resistance in the circuit, probably have the same behaviour as the intensities 49.6 and 90 mA. However, we did not test higher resistance values because these are not standard values, and we discarded the idea to use more than one resistance to facilitate the use of the sensor. In the resistance of 2.2 M Ω , the V_{out} difference is 0.21, 0.39, 0.43, 0.39, 0.87 and 0.89 V to an infrared intensity current of 13.2, 17.4, 23.2, 34.4, 49.6 and 90 mA respectively. In the same intensity currents and the change to fixed resistance to 8.2 M Ω , the difference of V_{out} is 0.52, 1.03, 1.06, 0.98, 0.76, and 0.00 V, respectively. The maximum difference is produced at the infrared LED intensity of 23.2 mA with a resistance of 8.2 M Ω . We determine that is the best option because it is the option with a greater V_{out} difference and the intensity current is not high.

With the intensity of the infrared LED and the fixed resistance determined in the photodiode's voltage divider, we start the test in the different oil samples. In Figure 6.9, we can observe the V_{out} obtained in the different lights used with a photodiode as photoreceptor. The V_{out} obtained

is low in the green, blue, yellow, and red lights. We discard these lights to monitor the oil in the sewerage with the configuration tested. In the case of white light, we observe a few increases of the V_{out} with the increase of oil concentration. This increase is 0.29 V between 0 to 45 mL oil/L water. The increase of V_{out} is produced mainly between the concentration of 0 to 2.6 mL oil/L water. In this range, the difference of V_{out} is 0.13 V. This difference is too little, and we must rule out white light with the photodiode as photoreceptor. Finally, there is a difference of V_{out} of 2.17 V in the use of infrared light between the water without oil and the maximum mix of water and oil tested. With the use of the infrared LED, we observe three trends. The first trend, the V_{out} increase in the range of 0 to 1 mL oil/L water. The second trend is detected in 1 to 5 mL oil/L water, where the V_{out} is constant. Finally, there is another trend in 5 to 45 mL oil/L water, where the V_{out} increases. The infrared LED is the only one that we can use to monitor the presence of oil with a photodiode in our prototype.

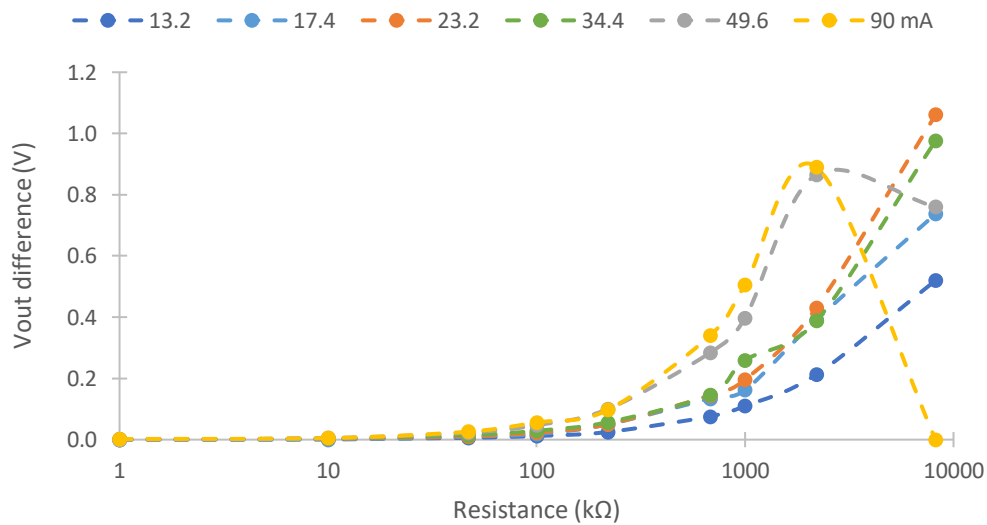


Figure 6.8. Effect of the intensity and fixed resistance in the voltage divider in V_{out} differentiate.

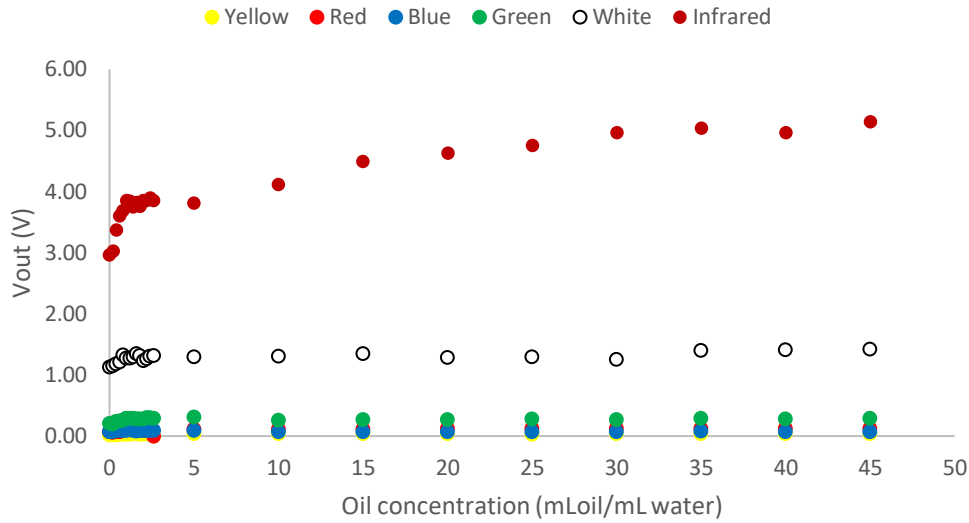


Figure 6.9. V_{out} with the use of photodiode in the different oil concentrations.

Now, we analyse the mathematical models that relate the V_{out} with the oil concentration. We use Statgraphics software (Statgraphics, 2022) to calculate the models. We use one model for all oil concentrations tested represented in Equation 6.1, and two models for the low oil concentration and the other for the high oil concentrations represented in Equations 6.2 and 6.3. The values of R^2 , AE and RE of these models can be observed in Table 6.5. Using one model for all the oil concentrations, the AE is 1.5 mLoil/Lwater with a RE of 47.7%. In this model (equation 6.1), the maximum REs are produced in the range of 0 to 10 mLoil/Lwater. In this range, the mean of RE is 66.73%. We consider these REs too high for our sensor. For this motive, we decided to use two models. On the one hand, a model in the concentrations between 0 to 2.6 mLoil/Lwater. The AE of this model is 0.3 mLoil/Lwater, and the RE is 31.3%. On the other hand, the second model (5 to 45 mLoil/Lwater) has an AE of 2.1 mLoil/Lwater and a 9.8% of RE. The use of two models reduces the errors. However, the errors in the low oil concentrations are too elevated. In Figure 6.10, we represented the observed versus predicted values using the model in the range of 0 to 2.6 and 5 to 45 mLoil/Lwater. In Figure 6.10 a), we observe the low concentration of oil values. In general, we confirm that the mathematical model is ineffective in predicting oil concentration. Nevertheless, in the high concentration of oil tested (Figure 6.10 b)), we can regard that the model predicted well the concentration of oil.

$$\text{Oil concentration} \left(\frac{\text{mL oil}}{\text{L water}} \right) = (-4.20311 + 0.400849 * V_{out}^2)^2 \quad (6.1)$$

$$\text{Oil concentration} \left(\frac{\text{mL oil}}{\text{L water}} \right) = (-1.62013 + 0.198401 * V_{out}^2)^2 \quad (6.2)$$

$$\text{Oil concentration} \left(\frac{\text{mL oil}}{\text{L water}} \right) = (-3.18522 + 0.3644 * V_{out}^2)^2 \quad (6.3)$$

Table 6.5 Values of R^2 , errors and range of the different equations.

Equation	Range	R^2	AE (mLoil/Lwater)	RE (%)
2	0-45	0.9549	1.5	47.7
3	0-2.6	0.8353	0.3	31.3
4	5-45	0.9643	2.1	9.8

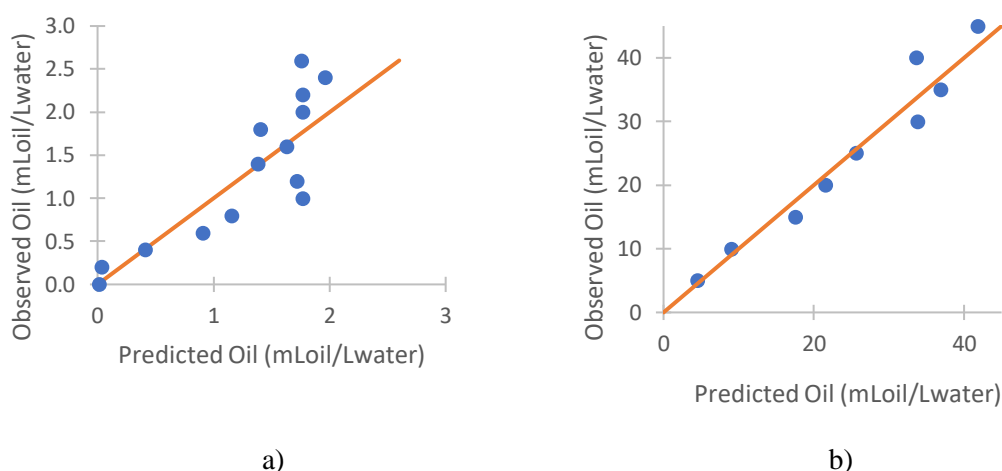


Figure 6.10 Two models.

Finally, we perform a verification of the sensor. In the range of 0 to 2.6 mLoil/Lwater, the AE is 0.77 mLoil/Lwater, and the RE is 63.39%. With the errors observed in the calibration and verification, we can affirm that the sensor cannot be used to determine the oil concentration in this range. However, we think that the sensor can be used to determine the presence of oil. In the range of 5 to 45 mL oil / L water, the average AE is 3.16 mLoil/Lwater, and the RE is 11.23%. The RE is 12.84, 16.77, and 4.08 % in the concentration of 17, 32, and 47 mLoil/Lwater, respectively. In this case, we can affirm that the sensor can be used to monitor the oil concentration in the range of 5 to 45 mLoil/Lwater. Thus, we can use infrared light with a photodiode as photoreceptor to detect the presence of oil in low concentrations and quantify the concentration in higher concentrations. Now, we study the values obtained with the LDR. The resistance values of the LDR in the use of the different lights are transformed to voltage using Equation (4.20). First, we search for the fixed resistance value that maximises the difference between the minimum and maximum V_{out} values. Usually, the resistance values obtained with this method are not standard. Thus, we select the standard resistance value nearest to it. Table 6.6 represents the calculated resistance value and the standard resistance value used.

Table 6.6. Values of resistance in the fixed resistance.

Colour	Yellow	Red	Blue	Green	White	Infrared
Model resistance (k Ω)	81.55	21.57	94.03	7.87	5.52	9716.02
Standard resistance (k Ω)	82.0	22.0	100.0	8.2	5.6	10,000

Once the resistance values are transformed to V_{out} , we obtained Figure 6.11 and Figure 6.12. Figure 6.11 represents the values of V_{out} with the use of the light colours yellow, red and blue. With the use of yellow and red lights, there is a decrease in the V_{out} with the increase of the oil concentration. The decrease of V_{out} with the yellow light is 0.36 V between the minimum and maximum oil concentration tested. The decrease is produced between 0 to 1.8 mLoil/Lwater. In the higher concentration tested, the V_{out} has similar values with a trend to a limit inferior of 1.46 V. With red light, the V_{out} decrease is 0.3 V between the water without oil and the water with the maximum oil concentration. In this light, the V_{out} decrease is produced mostly in the concentration between 0.6 to 0.8 mLoil/Lwater. Thus, we discard the use of this light to monitor oil concentration. However, this light can be used to differentiate between water with oil and water without oil. Another light tested is the blue light. The evolution of V_{out} with the oil concentration is not consistent. First, there is a V_{out} reduction up until 1.4 mLoil/Lwater concentration. From this concentration up until the concentration of 15 mLoil/Lwater, there is an increase of the V_{out} with the increase of oil concentration. In higher concentrations than 15

mLoil/mLwater, the V_{out} trends to an upper limit of 1.73 V. The other lights tested (green, white and infrared) are represented in Figure 12. About these lights, we discard the use of green and white lights. Because the difference of V_{out} is little when considering the increase of oil. In the use of green light, the V_{out} has values between 1.58 V to 1.65 V. With the use of white light, the V_{out} without oil is 1.55 V, and the V_{out} with the maximum tested oil is 1.73 V. This is a decrease of 0.28 V that is produced mainly between the concentrations of 0 to 0.8 mL oil/mL water. In higher concentrations, we observe a low limit of 1.55 V. Finally, we analyse the use of infrared light. With this light, there is a decrease of the V_{out} of 1.03 V between the water without oil and the maximum oil concentration tested. As in the previous cases, the values of V_{out} have a lower limit of 1.12 V as of 20 mL oil/L water. The reduction of the V_{out} is indicative of the increase of light that hits the LDR. This can increase the light reflected by the water of oil or fluorescence produced by one or more substances present in the oil.

Given the previous results, white and red light can be used to detect the presence of oil but not for monitoring. The yellow and infrared light are useful for monitoring the oil concentration in different ranges. The yellow light can be used in 0 to 2.2 mL oil/L water, and infrared light in the range of 0 to 20 mL oil/L water. First, we analysed the results obtained with the yellow LED. Equation 6.4 represents the mathematical model that related the oil concentration with the V_{out} in this light. The value of R^2 of the model is 0.97293, and in Figure 6.13, the predicted values versus the observed values of the model are represented. In general, the values obtained from the model predicted the observed values well. We do not observe an important difference between the observed and predicted oil concentrations.

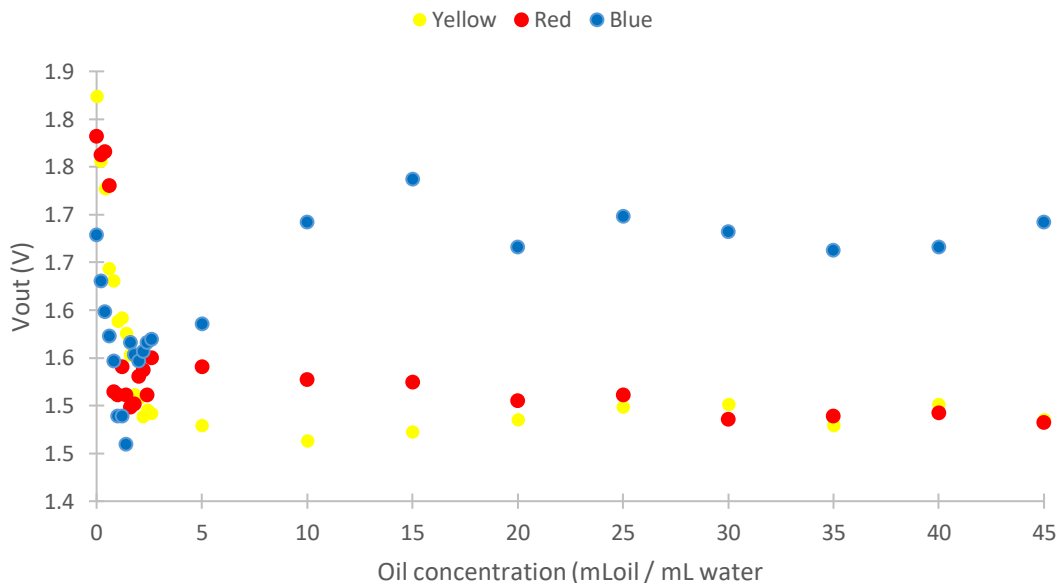


Figure 6.11 V_{out} in the different oil concentrations with the use of yellow, red, and blue lights.

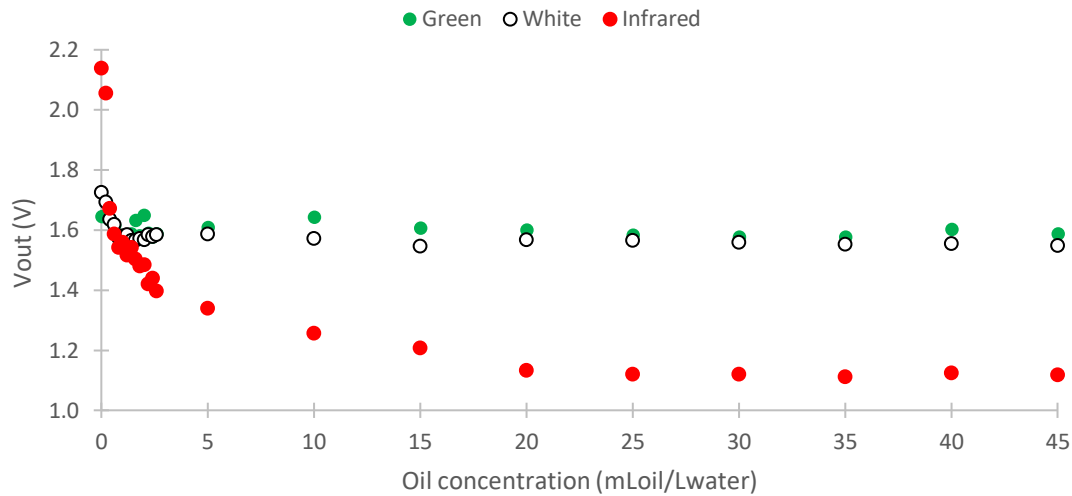


Figure 6.12 Vout in the different oil concentrations whit the use of green, white, and infrared lights.

$$\text{Oil concentration} \left(\frac{\text{mLoil}}{\text{Lwater}} \right) = (4.23337 - 1.24727 * V_{out\text{yellow}})^2 \quad (6.4)$$

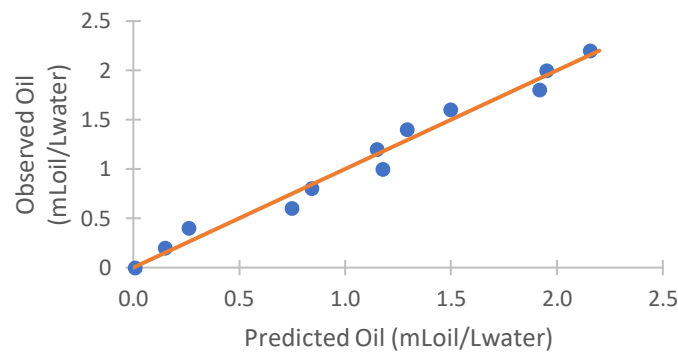


Figure 6.13. Observed versus predicted concentration of oil in yellow light.

Now, we analyse the models of Vout with infrared light. First, we calculate the mathematical model with Statgraphics (Statgraphics, 2022) with the Vout values between 0 to 20 mLoil/Lwater. We obtain Equation 6.5, which has an R^2 value of 0.8665. This low value of R^2 implies a short ability to predict the values of oil concentration. This is observed in Figure 6.14 a) and b), we can see that the predicted values are far from the observed. It can be seen that the predicted value except in 0.2 and 5 mLoil/Lwater concentrations are far from the observed. In addition, in Table 6.7, the errors in the calibration and verification of that model are represented. The AE in the calibration is 1.2 mLoil/Lwater, and the RE is 42.3 %. In the verification, the RE is similar, with 45.95 %. These errors are not good for our sensor to know the oil concentration. Thus, we test with the elimination of values of the calibration. By eliminating the calibration of the value without oil, we obtained an R^2 value of 0.8764. This is still a low value of R^2 . With which we continue to eliminate the next value of the calibration. In this case, we obtain Equation 6.6 with an R^2 value of 0.9710 in the range of 0.4 to 20 mLoil/Lwater a. We obtained a reduction in the errors. The absolute and REs are 0.54 mLoil/Lwater and 21.25 %, respectively, in the calibration and the verification are 1.75 mLoil/Lwater and 18.41 %.

In summary, the use of a photodiode is only effective with the use of infrared light to detect the oil concentration in the range of 5 to 45 mLoil/Lwater. With the use of a LDR as

photoreceptor, red light can be used to determine the presence of oil, but not to determine the concentration. Regarding the yellow and infrared light, these can be used for monitoring the oil concentration. Yellow light can be used in the range of 0 to 2.2 mL oil/L water and infrared light in the range of 0.4 to 20 mL oil/L water. Infrared light is also used in the determination of turbidity. We determine that the maximum concentration that our sensor can measure is 20 mL oil/Water, using infrared light

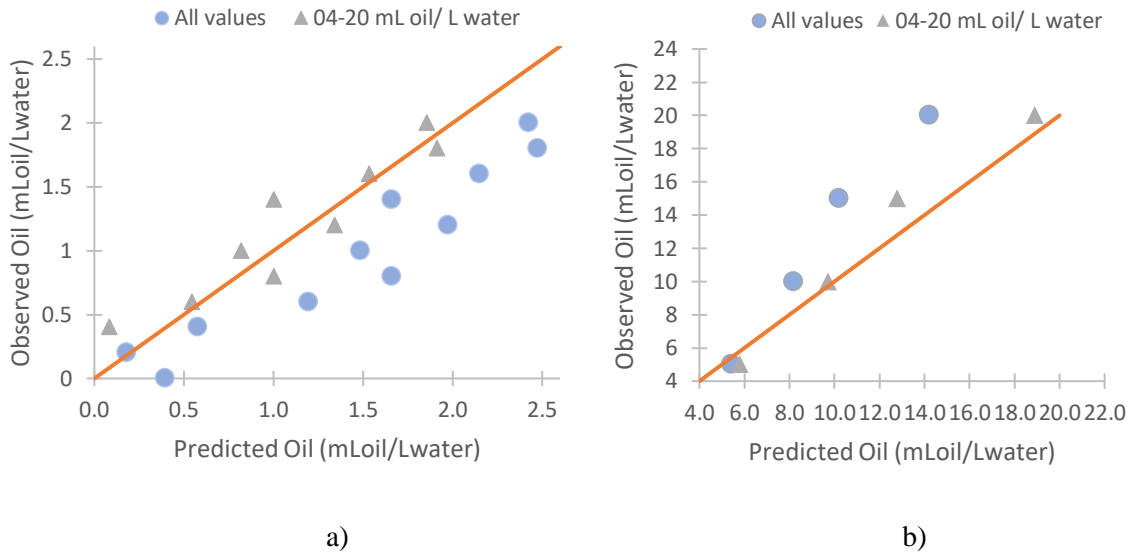


Figure 6.14. Observed versus predicted concentration of oil in infrared light in the two models.

$$Oil\ concentration\ \left(\frac{mLoil}{Lwater}\right) = \left(-5.58178 + \frac{10.605}{v_{outinfrared}}\right)^2 \quad (6.5)$$

$$Oil\ concentration\ \left(\frac{mLoil}{Lwater}\right) = \left(-8.27867 + \frac{14.3223}{v_{outinfrared}}\right)^2 \quad (6.6)$$

Table 6.7. Range and errors.

Colour light	Range (mL oil / L water)	Calibration		Verification	
		AE (mLoil/Lwater)	RE (%)	AE (mLoil/Lwater)	RE (%)
Yellow	0-2.2	0.09	12.42	0.21	28.65
Infrared	0-20	1.20	42.30	0.68	45.95
Infrared	0.4-20	0.54	21.25	1.75	18.41

6.2.2.2 Level sensor.

In this subsection, we analyse the effect of the presence of a blockage or illegal spills on the water level of storm sewerage.

First, we check if it is possible to detect the presence of dumping with the use of the level sensor. Nevertheless, we do not observe a significant difference in the sewerage between the rain with a spill and no spill. This is because if we calculated the water that enters the sewerage with the first value of rain (7 mm), we obtained 52.5 m³/h in each node. We consider that such high

volumes would not be reached in the event of an illegal discharge. Therefore, it is impossible to detect a spill with the use of level sensors at the time that rain occurs.

Now, we analyse the use of the level sensors to detect blockage in the pipes. Figure 6.15 represents the pipes that presented differences between a blockage and no blockage with the different percentages of blockage levels. In Figure 6.15 a), we represent a blockage effect between one of the lateral pipes and the central pipes. If the blockage is located in the lateral pipe, we obtain the results observed in Figure 6.15 b). We show similar pipes affected (except pipe N34 to NC8). Figure 6.15 c) and Figure 6.15 d) represent what occurs if the blockage is located at the end of the simulated section. In the case of the blockage located in the lateral pipe, we observe that the pipes near the blockage are affected. However, many pipes are affected if the blockage is in the central pipe. We can affirm that the use of a level sensor can be a tool to detect the presence of a blockage.

In sewerage, the blockage can be produced by the deposit of solids (wet wipes, rocks, trash, branches, etc.). The presence of these elements will affect the velocity of the water. Therefore, there will be an increase in water level upstream and a decrease downstream. However, a water level sensor could not detect the damage to the pipes at the top of it by the roots of trees.

6.2.2.3 Conductivity sensor.

In this section, we analyse the results obtained with the conductivity sensor.

We observe that the frequency peak changes with the increase of conductivity. The peak frequency in freshwater is 164 kHz, and the conductivity of 58.4 mS/cm is at 162 kHz. In Figure 6.16, Figure 6.17, , and Figure 6.19, the values of induced voltage are represented in the different frequencies tested. We identify 4 types of trends that are represented in the different figures. The first trend is represented in Figure 6.16. This trend is produced between the frequencies of 150 to 158 kHz. First, with the increase of the conductivity, there is an increase of the induced voltage until a certain conductivity. After this conductivity, the value of induced voltage is reduced with the increase of the conductivity. In addition, we observe that the conductivity value where the change occurs between the increase and decrease of the induced voltage is reduced. Until the frequency of 159 kHz, where the voltage increases between the first and second concentration tested and then decreases with the increase in conductivity. We can see this trend in the frequencies 159 to 165 kHz, and the induced voltage of these frequencies is shown in Figure 6.17. In these frequencies, some induced voltage values can be associated with two conductivity values of water. For this reason, we discard the use of frequencies between 150 to 165 kHz. represents the frequencies between 166 to 176 kHz. In these frequencies, we observe an induced voltage decrease with increasing conductivity. These frequencies can be used to monitor the conductivity of the water. Finally, in Figure 6.19, there is a decrease in induced voltage with the conductivity increase. Except in the case of 2.66 to 6.68 mS/cm, where there is an increase in the induced voltage.

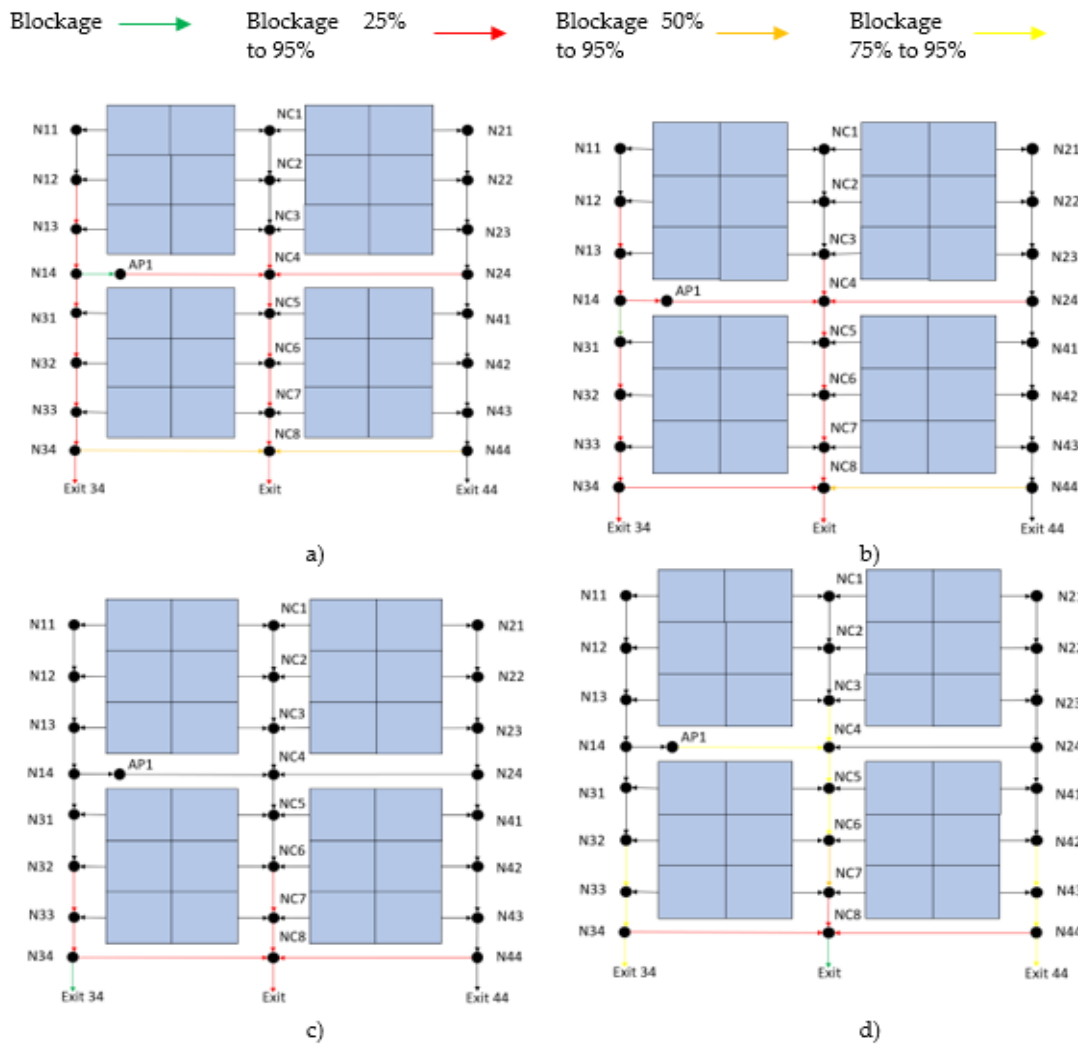


Figure 6.15. Pipes affected by the different % of blockages and blockage positions.

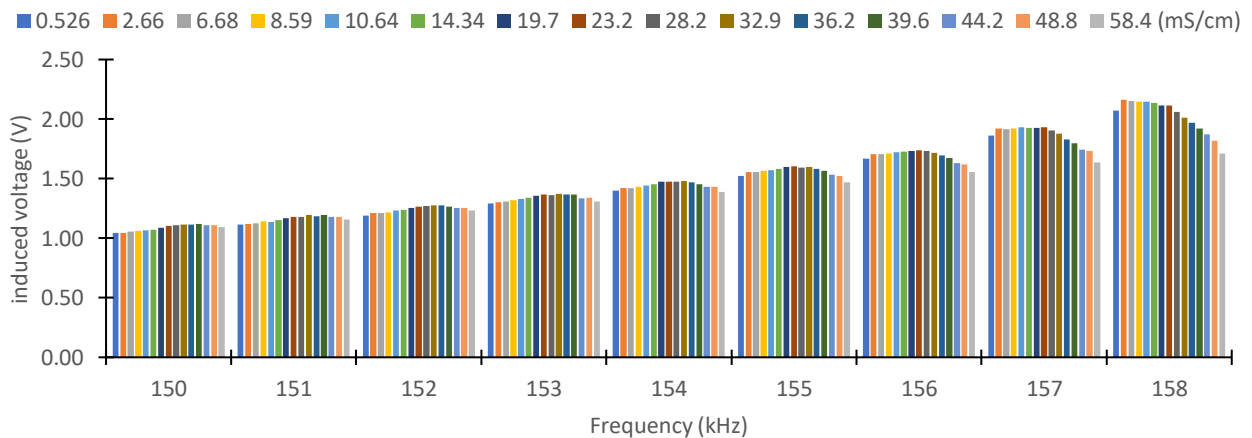


Figure 6.16. Induced voltage in the different conductivities in the frequencies between 150 to 158 kHz.

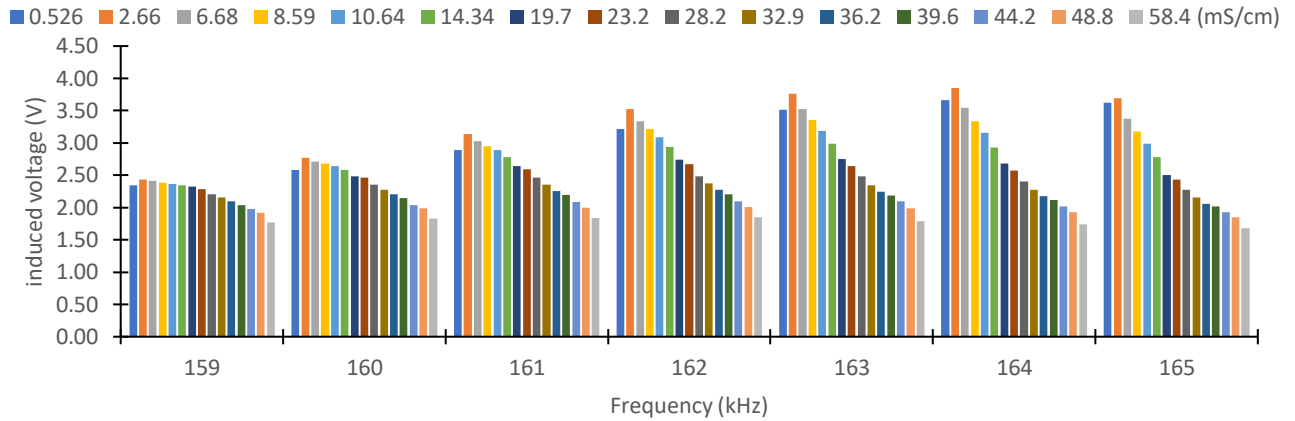


Figure 6.17. Induced voltage in the different conductivities in the frequencies between 159 to 165 kHz.

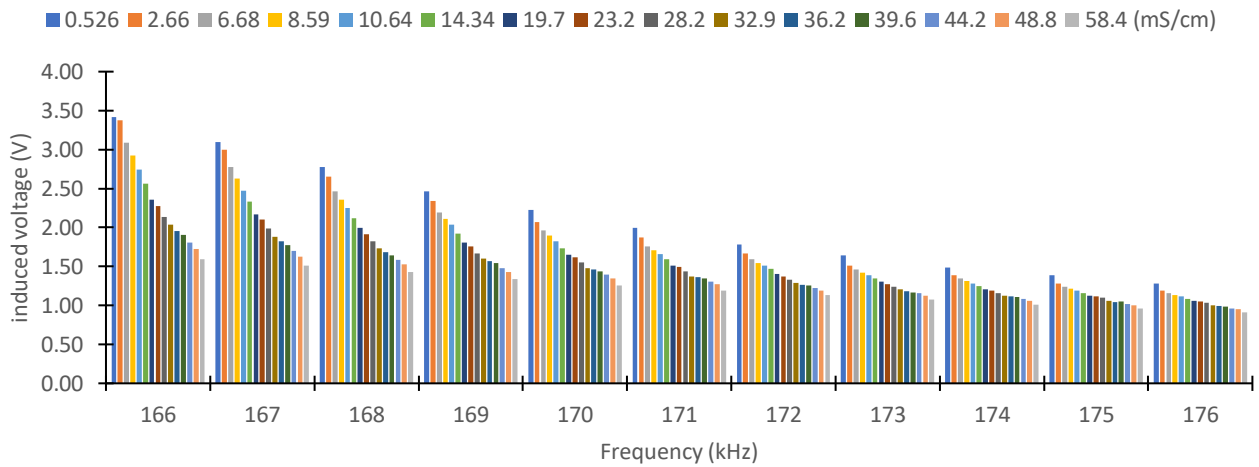


Figure 6.18. Induced voltage in the different conductivities in the frequencies between 166 to 176 kHz.

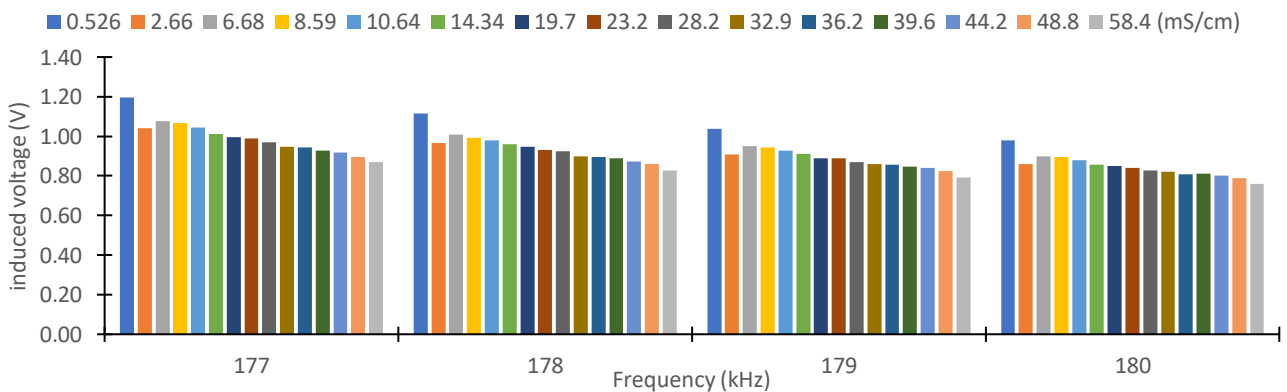


Figure 6.19. Induced voltage in the different conductivities in the frequencies between 177 to 180 kHz.

The frequencies between 166 to 176 kHz are utilised to perform a calibration model. The other frequencies present changes in the trend of the induced voltage with the conductivity. This creates difficulty in the implementation of the system. Since an induced voltage value would be associated with more than one conductivity value. In addition, we discard the use of the frequencies 174, 175, and 176 kHz due to presenting a low induced voltage difference with the increase of conductivity.

With the data gathered of the induced voltage of the frequencies between 166 to 173 kHz, we perform mathematical models that relate the induced voltage and the water conductivity. First, we obtained the values of R^2 for all models that Statgraphics (Statgraphics, 2022) calculated. Second, we calculate the mean of R^2 for the different models in the different frequencies. Finally, we use the six models with the higher R^2 mean value to relate the induced voltage with the conductivity. The models used are Square Root-Y Log-X, Square Root of Y, Inverse Y-Square Root of X, In-verse of X, Square Root-X Square-Y, and Logarithm of X. Of the six models used, the minimum error in calibration, verification or mean of calibration and verification are produced in the three first models for the RE. The model with the least absolute error is Square Root-Y Log-X in all cases. In Figure 6.20, we represent the RE with the use of the mathematical models obtained with Statgraphics software (Statgraphics, 2022). In general, we observe that the increase of frequency reduces the REs (except in the case of 173 kHz).

In Figure 6.21, we represent the distribution of the REs for the different conductivity tests and frequencies selected. The model used in each frequency has fewer REs for that frequency. In general, the maximum REs are in the lower concentrations tested. The minimum RE in the concentration of 0.526 mS/cm is in the frequency of 172 kHz with a RE of 2.1%. The maximum error in this concentration is in the frequency of 127.3 mS/cm. In the 2.66 mS/cm concentration, the mean RE is 22.6%, with a minimum value of 0.3 % to the concentration of 171 kHz. In Figure 6.22, the RE of the verification in the frequencies between 166 to 170 kHz, the REs are higher than the 13.1% in the other frequencies, the REs are less than 5.3% are represented. In the other concentrations, the values are less than 9.1 % of REs.

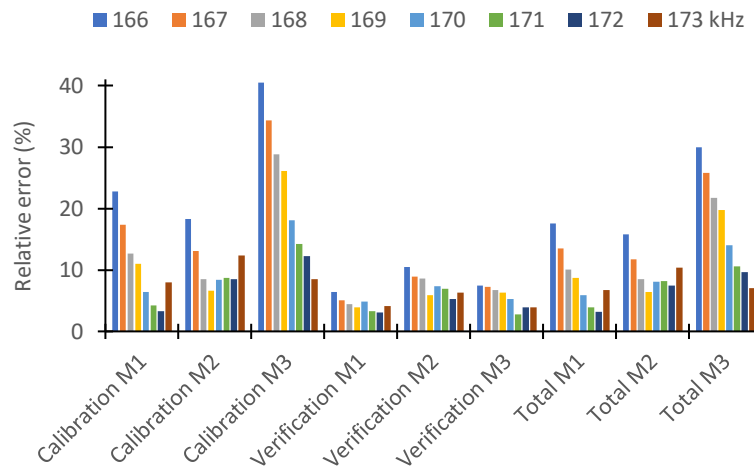


Figure 6.20. REs of models

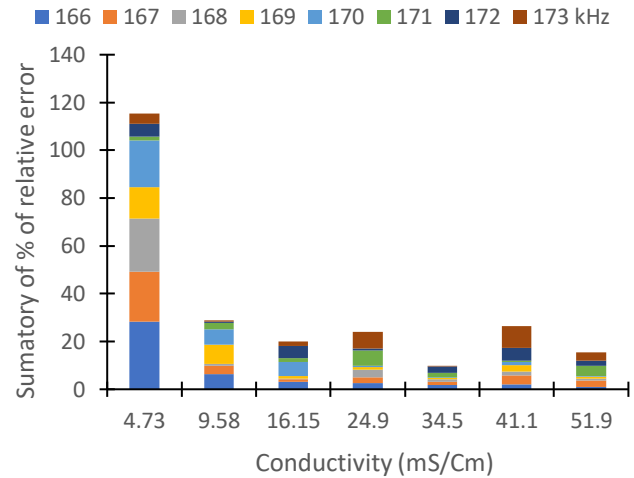
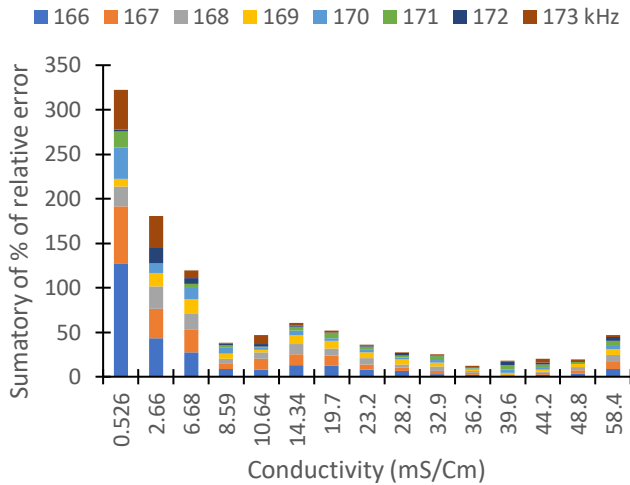


Figure 6.21. Summary of the % of RE in the calibration.

Figure 6.22. Summary of the % of RE in the verification.

As we saw previously, the absolute Voltage difference and the total RE are reduced with the increase of frequency. In our case, the best option is the frequency of 171 kHz. Because it is the frequency with smaller REs at lower conductivity concentrations. Which will be the most typical concentrations in a sewer. At higher concentrations, the errors will be higher than at other frequencies, but our goal is to detect the presence of a spill. The thing that would be fulfilled in that frequency. Equation 6.7 related the value of voltage with the oil concentration of the frequency 171 kHz.

$$\text{Conductivity } mS/cm = (10.1752 - 13.6081 * \text{LN}(V_{out}))^2 \quad (6.7)$$

6.2.3 Conclusions.

We presented a system to monitor the storm sewerage to prevent illicit discharges and detect blockages. With rain and water level sensors, we established 4 scenarios possible. There are two options when there is water in the sewerage, but it is not raining. (I) A stormwater tank is being emptied, or (II) There has been a spill in the sewerage. In this scenario, our system checks if the stormwater tank is emptying. If the answer is negative, the sensors are used to detect who is responsible. Another scenario is when it is raining, but there is no water in the sewerage. This is a signal of the presence of a blockage in the sewer manhole. The third scenario is when there is no water in the storm sewerage and it is not raining. That is a normal situation. Finally, if it is raining and there is water in the sewerage, a spill is produced. However, only using a level sensor will not be enough to detect it. For this reason, the use of oil, turbidity, and conductivity sensors is needed. In addition, the use of the level sensor can help detect blockage in the sewerage. We tested that there are significant differences in the water level in one sewerage depending on the presence or not of a blockage.

We improve the design of two sensors previously developed. The conductivity sensor and the oil sensor. In this last one, we include infrared light and a photodiode in the design previously developed. On the one hand, we obtained that infrared light and the use of a photodiode present an AE of 2.1 mL oil/L water in the range of 5 to 45 mL oil/L water and a RE of 9.8%. The RE is 11.23 % in this range and 0.77 mL oil/L water of AE. With the use of the photodiode, the other colours of light are not useful for detecting the oil. On the other hand, with the use of an LDR as a photoreceptor. Red light can differentiate between water with oil and without. Regarding the yellow light, it can be used in the range of 0 to 2.2 mL oil/L water with an AE of 0.09 mL oil/L water. With this photoreceptor, the infrared light presents an AE of 0.54 mL oil/L water in the range of 0.4 to 20 mL oil/L water.

Also, we improve the design of the conductivity sensor previously developed. We detect 4 different trends of induced voltage with the increase of conductivity. The frequencies that are utilized for monitoring the conductivity are included in the range of 166 to 173 kHz. In general, we detect that the REs decrease with the increase of conductivity. In addition, the REs decrease with the increase of the frequency. We select 171 kHz as the better option of measurement in this sensor. Due to presenting an absolute difference of 0.81 V in (alternative current), a 0.57 V in a continuous current. In this, the RE is 3.9%.

Finally, work presented in this chapter has been published in the following references (Rocher et al. 2019b), (Rocher et al. 2022).

7 Application in sewerage.

In this chapter, we develop our proposal. First, we select the technology used to the communication of the different nodes and topology network.

7.1 Selection and Definition of Communication Technology.

One of the most critical capabilities that must be considered when selecting and implementing sensor nodes is the communication system or protocol that will be used to transmit the monitored information through the nodes. The nodes will be installed in irrigation ponds, as these ponds are generally located at a great distance from the points from which it is possible to connect to Internet Service Providers. Therefore, this connection becomes very complicated, and to solve it, it will be necessary to use communication through wireless technologies.

Among the wireless technologies most used in IoT are viewer by (García et al. 2018). We can high light the following ones (I) Wi-Fi (IEEE 802.11) (IEEE, 2014), (II) Radio-frequency identification (RFID) (ISO, 2011), (III) Bluetooth Low Energy (BLE) (IEEE 802.15) (IEEE, 2020), (IV) ZigBee (IEEE 802.1.4) (IEEE, 2018), (V) Sigfox (Sigfox, 2017), (VI) LoRa (Lora-alliance, 2019), and (VII) mobile technologies, such as WiMAX (IEEE802.16) (IEEE, 2001), LTE Cat-M1 (3GPP, 2016) or NB-IoT (5G) (GSMA, 2019).

In our case, we can discard technologies with a more limited scope, such as RFID, BLE, or Zigbee. Moreover, we can discard those with a higher maintenance cost since, although they can operate at a greater distance, which has an additional cost of connection to an Internet Service Providers, such as WiMAX, LTE Cat-M1, or NB-IoT. For all the reasons previously described, the most appropriate technologies to carry out our implementation are LoRa.

7.2 Topology.

The topology of a network is the design as the different nodes are connected. Different topologies exist (I) Ring, (II) Mesh, (III) Star, (IV) Fully connected, (V) Line, cascading (VI) Tree and (VII) Bus (Mamat, Ibrahim and Sulong, 2020). These topologies are represented in Figure 7.1. The star and tree topologies are the most reliable and stable in the context of smart cities (Mamat, Ibrahim and Sulong, 2020).

In the ring topology, the different nodes are connected to other 2 nodes forming a circle. Therefore, communication can be produced in two ways. Thus, the data is sent from one node to another until reaching the destination node. We obtained a mesh topology if we increased the number of nodes so that one node could be connected directly. It is a fully connected topology if all nodes are connected with all nodes. In another topology, the different nodes are connected to a cable (bus). In Star topology, the different nodes are connected to a central node. Any communication you want to carry out between the different nodes must go through the central node. If different stars connect between them, we get a tree network. The different topologies can be combined to form other topologies.

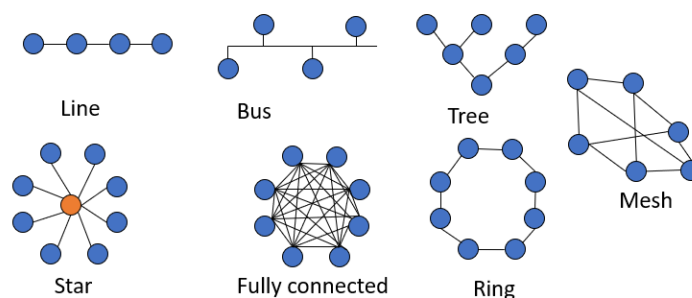


Figure 7.1. Network topologies.

To develop our proposal, we have three scenarios, water bodies, separate sewerage and combined sewerage. The topology of the three scenarios is similar. Different sensor nodes are located in the sewerage or water body. The number of nodes will depend on the size of the area to control, the presence of the possibilities of PIs or overflows occurring, and the budget available for the system. The different sensor nodes will connect to a Cluster Head (CH). The CH will send the data to a central computer through the internet. The connection of the sensor nodes and CH will occur through Wi-Fi or LoRa technology. As in the urban areas, there are buildings that can avoid the connection of the nodes with the CH; we will use signal repeaters, and wireless sensors self-location systems (Garcia, 2009).

7.3 Algorithms.

In our system, we must differentiate between the nodes in a storm sewer and those in a wastewater sewer, combined or in a body of water.

In storm sewerage, we analyse the 4 scenarios that may happen in the combination of rain and level sensors.

(I) The first scenario is when it rains and there is water in the pipe. In this condition, we use the level sensors to detect blockages in the pipes. In addition, we use turbidity, conductivity, and oil sensor to detect the presence of possible spills. (II) The second scenario is produced when it is raining and there is no water in the pipes. This is an indication that the rainwater is not entering the sewerage. This can occur by a blockage in the storm drain. (III) The third scenario is when it is not raining, but there is water in the pipes. The presence of water in the storm sewerage can be produced by an illicit spill or due to a discharge of a stormwater tank. (IV) Finally, the last scenario is when it is not raining and there is no water in the pipes. In this situation, there are no more things to analyse.

The process of measurement is constantly executed every fixed period of time, and it starts reading the level of the water. When the level is higher than a threshold, the node should start checking possible spills. This threshold could be fixed but, to allow the proposal to adapt to different pipes and scenario conditions, is statistically calculated using a p-value of 0.9. When the node starts checking the spills, the turbidity, conductivity, and oil sensors will start measuring to detect problems. In addition, the water level will be used to check if there are any clogs in the sewerage. Finally, if there is a high level in some of the measurements, these measurements will be sent to the MH along with the level measurement.

Figure 7.2 shows the process of the CH. The first action is to check the level of the water. If the node has sent a level that is lower than a specific threshold, the value of the raining sensor should be checked. A positive value of that sensor shows that there is a clog, since the level of water should be higher. Otherwise, there is no mismatch. If the level is higher than the threshold, the state of the water tank must be checked. If it is open or if it is closed, but it is raining, it could be a normal situation. However, if it is not, there is an illicit discharge. That could be possible even if the tank is open or if it is raining. That is the reason why the measurements are also checked in that case. When one of these problems is detected, the MH sends a message to the user. After all the checking, the MH awaits for the next message to be received.

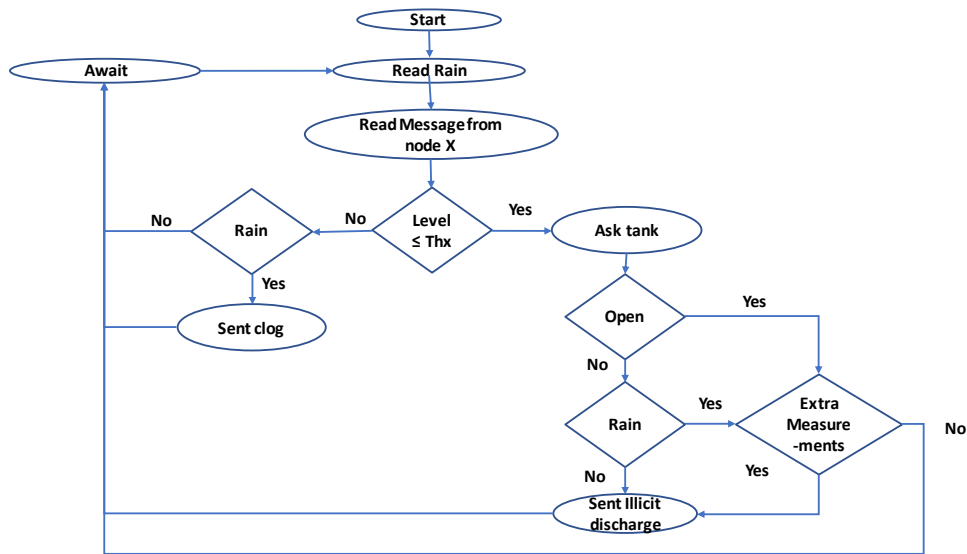


Figure 7.2. Master Head algorithm.

Figure 7.3. In our system, the maximum and minimum threshold values for contaminant concentration must be defined first. These thresholds are defined in Table 7.1. Once the thresholds have been defined, the measure of the different sensors is performed. The value of the different sensors is compared whit the TH maximum and minimum for each parameter. In the case that a parameter measured is outside the thresholds, a tag different to 00 is generated. As a parameter's value can only be at a low or a high level, we use the same tag for the same pollutant, changing the value. With this, we reduced the amount of data that needed to be sent. The different tags are represented in Table 7.1. When all the sensors have been checked, the information is sent from the sensor node to the CH. Once the information is sent, the values of the different tags are converted to 00.

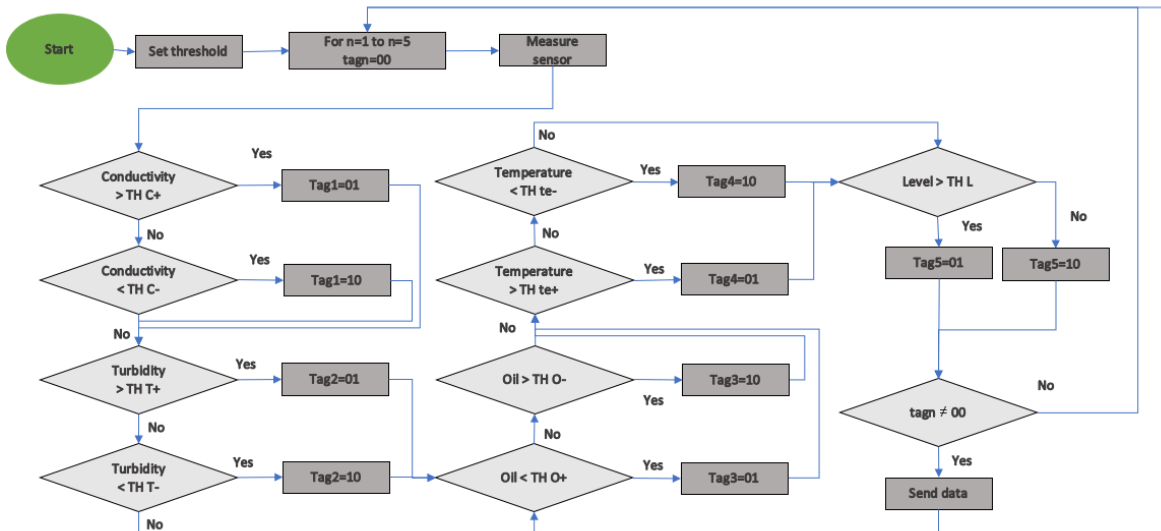


Figure 7.3. Algorithm to wastewater sewerage.

Table 7.1. Parameter algorithm is represented in Figure 7.3.

Thresholds	Meaning	Tag number
TH C+	High conductivity	Tag1=01
TH C-	Low conductivity	Tag1=10
TH T+	High Turbidity	Tag2=01
TH T-	Low Conductivity	Tag2=10
TH O+	High Oil	Tag3=01
TH O-	Low Oil	Tag3=10
TH te+	High temperature	Tag4=01
TH te-	Low temperature	Tag4=10
TH L	High Level	Tag5=01
TH L	Normal Level	Tag5=10

7.4 Cost of a sensor node.

The cost of our sensor node is represented in Table 7.2. As a microcontroller, we select node B-L072Z-LRWAN1. This node has enough analogue and digital inputs and outputs for our sensors and LoRa communication. This device must connect an SD card reader and an SD card to save the data. We use a power bank with a solar panel to power the system. However, as the sensor node is in smart cities in some cases, it will be possible to connect to public lighting. In turbidity and oil sensors, we use a RGB LED for visible lights. This allows the generation of visible light waves, saving on the number of LEDs to use and, therefore, the number of outputs to power them from the microcontroller .current. Since microcontrollers are generally incapable of generating this type of current (except for the PMW output), we will use a 555 integrated circuit. To read the sensor's response, it is necessary to go from alternating current to direct current. For that, we will use a diode bridge circuit. Finally, we use the temperature sensor DS18B20 and distance sensor HC-SR04 to monitor the water level and temperature of the water. The cost of the system is 120 euros, which can be reduced when making a purchase of more than one component.

Table 7.2. Cost of our sensor node.

Purpose		Item	Unitary cost (€)	Units	Cost	
Turbidity		RGB LED	L-154A4SUREQBFZGEW	1.43	1	1.43
		LDR	NSL- 19M51	1.88	3	5.64
		IR LED	TSUS5400	0.73	1	0.73
		Photodiode	SFH 203	1.08	1	1.08
		Resistances		0.27	6	1.62
Oil		RGB LED	L-154A4SUREQBFZGEW	1.43	1	1.43
		LDR	NSL- 19M51	1.88	3	5.64
		Resistances		0.27	6	1.62
Conductivity		Copper	Copper 0.4 mm	0.5	1	0.5
		555 timer IC	TLC555IP	1.05	1	1.05
		Discrete components (Resistors, Capacitors, Transistors)		3.00	1	3.00
Water level	Ultrasonic distance sensor	HC-SR04	2.93	1	2.93	
Temperature	Temperature	DS18B20	6.15	1	6.15	
Node		Node LoRa	B-L072Z-LRWAN1	61.34	1	61.34
		Micro SD Card reader		2.19	1	2.19
		Micro SD Card 4Gb		0.82	1	0.82
Energy system		Power bank 20,000 mAh		20.99	1	20.99
		Solar panel	CN3163	2.07	1	2.07
				Total	120.23	

8 Application to other environments.

8.1 Design and Calibration of Moisture Sensor-based on Electro-magnetic Field Measurement for Irrigation Monitoring.

Soil moisture control is crucial to assess irrigation efficiency in green areas and agriculture. We propose the design and calibration of a sensor based on inductive coils and EFs. The proposed prototypes should meet a series of requirements such as low power consumption, low RE, and a high voltage difference between the minimum and maximum moisture. The aim of this work is to design and calibrate an moisture sensor based on EFs, which identifies the water scarcity and can be applied in gardens, urban lawns, agriculture fields, etc. We can estimate soil moisture based on the induced voltage. The sensor's signal is affected by the variation of the generated EF; the changes in water content modifies the dielectric constant of the environment. The final sensor might consist of one or several prototypes in one housing to cover the widest possible range of soil moisture. Although the use of solenoid coils have been proved for monitoring other environments, their use to monitor soil moisture is yet to be tested to its full potential.

8.1.1 Test bench

In a previous job, Parra Boronat (2019) tested 15 prototypes based on coils to monitor the soil's moisture. They determined that the better prototype is composed by 5 spires in PC and 10 spires in IC. These sensors (NP1 to NP4) exploited the best windings ratio. All of the new sensors had their spires in one layer. Furthermore, to minimize the error when connecting the sensors, they had all the elements necessary for the circuit already connected to the sensor, turning them into a fully functional sensor. Their characteristics can be seen in Table 8.1.

Table 8.1. Features of the prototypes NP1 to NP4.

Prototype	ØW (mm)	ØPC & ØIC (mm)	NS PC	NS IC	Windings Ratio
NP1	0.4	25	5	10	1:2
NP2	0.4	50	5	10	1:2
NP3	0.4	25	15	10	1:0.67
NP4	0.4	50	15	10	1:0.67

A power generator was the source of the power for the PC (a sinus-wave), the AFG1022 from Tektronix was selected. The range of frequencies it can generate, and it is user-friendly handling fostered the selection of this generator. The voltage chosen was 3.3 V. This is the standard voltage at which Arduino works. For both sets of tests, the selected oscilloscope to register the Vout was the TBS1104 from Tektronix. Furthermore, a resistance of 47 Ω on the positive wire of the PC was added to protect the oscilloscope and reduce peaks, as well as a capacitor of 10nF, which was connected to both wires on the IC.

It is to be noted that each datum for this experiment in the results section corresponds to the mean of three repetitions. The Vout reading was taken in triplicate, thus making the results more rigorous. To simplify the analyses, standard deviation data will only be presented when calibration tests were performed.

Next, the measurement protocols for each set of tests are described. The frequencies used for this set of tests were those close to the peak. The peak frequencies are determined in the different samples when the soil has the maximum moisture tested. In these conditions we search the peak frequency in the range of 0 to 1 MHz. Once the peak frequency is found, we measure at the frequencies of ± 10 , 20, 30 and 40 kHz of peak frequency. This range was chosen because it represents the frequencies where the sensor shows a higher sensitivity to changes in the environment and displays a higher output voltage. These experiences allowed us to check the effectiveness of the sensors for a different soil type.

The sensors were left inside the pots along the entire experiment. Measurements were taken daily for as long as the tests were conducted. The objective of these experiments was to prove the usefulness of keeping the sensors buried, to minimize the errors from extracting and inserting them. Furthermore, since the soil was different, these experiments wanted to test the efficiency of the prototypes for a crop during harvest.

The different soils have been obtained in summer in the La Safor region (Valencia, Spain). The soils are a representation of typical farmer soils of this region. Considering that collected cannot be classified as unaltered samples since they are sifted and water was added to the soil, the specific ambient conditions in which samples are collected are not relevant. The soil screening was carried out to avoid creating preferential water channels that could affect the measurements and homogenize the samples. A sole type of soil was used. Nevertheless, it was different from the previous types, and four repetitions were used (C1 to C4). The soil was a sandy type extracted from an orchard field. The pots used for these tests were smaller, with a maximum radius of 6.65 cm. A total of 1 kg of each soil was inserted in each pot. A sample was taken from the original soil and dried in order to obtain the moisture percentage to calculate the dry soil. In Figure 8.1, the pots of soils C1, C2, C3, and C4 are depicted. Regarding the procedure of soil moisturizing, we followed the aforementioned moisturizing process, which consists of adding small quantities of soil and let water saturate all the gaps of soil.

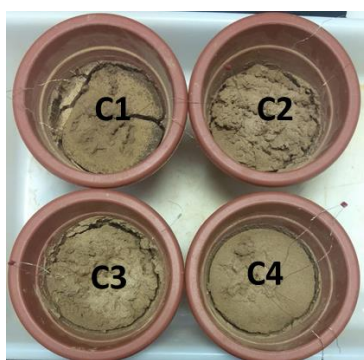


Figure 8.1. Soils C1 to C4

The soil weight characteristics, the original % of dry soil, and the derived weight values for the soil moisture estimation by weight are presented in Table 4. The measures of the pots, as well as their volume, are presented in Table 5. Furthermore, the results for the soil moisture measures are presented in Table 6; this information will help understand the results. It presents the soil volume, the initial and final water volume and their variation.

Table 4. Soil characteristics.

	C1-4
% Dry soil	97.6
Total weight of the dry soil (g)	976
Weight of the pot and filter paper (g)	87
Weight of dry soil+pot+filter paper (g)	1063
Sand (%)	80
Silt (%)	15
Clay (%)	5

Table 5. Pots characteristics.

	C1-4
Minor radius (cm)	4.55
Major radius (cm)	6.65
Height (cm)	7.04
Volume (cm ³)	697.7

Table 6. Summary of the soil moisture variations.

	C1	C2	C3	C4
Initial water percentage (%)	57.2	56.6	63.1	59.3
Final water percentage (%)	7.0	6.4	8.5	7.5
Soil moisture variation (%)	50.2	50.2	54.6	51.8

The behaviour of C1-4 is similar since they come from the same lot. All of them started at around 55-65 % soil moisture and ended close to 6-9 %. The target range was studied because sandy soils have their FC at around 24 % and their WP at around 7 % (Datta, Taghvaeian and Stivers, 2017).

8.1.2 Results.

The results of the 4 prototypes are analyzed in this subsection. Furthermore, the values of V_{out} for the different soil moisture and prototypes are shown.

In the representation of data gathered in prototypes NP1, NP2, NP3, and NP4, we include only 1/3 of the obtained values to ensure a proper visualization of data and trends; in the calibration, we will use the whole dataset. In general, we can observe that increasing the diameter of coils reduces the peak frequency. A reduction of peak frequency entails a more reliable circuit. Except in NP3, the higher voltage differences are in the frequencies beyond the peak frequency.

In Figure 8.2, we show the results of the different frequencies tested for NP1. In this prototype, the peak frequency is displaced when the soil moisture decreases, as seen in previous tests. In the frequencies of 700 kHz, 710 kHz, 720 kHz, and 730 kHz, the first values of V_{out} decrease from 57.2 % to 39.1 %, from which V_{out} remains almost constant. In agriculture, these high soil moisture values are unusual, too high. Meanwhile, in urban lawns, these values are more typical. However, the low difference of V_{out} discards the use of these frequencies in NP1. In the frequency of 740 kHz, there is a low difference in the V_{out} with soil moisture change (except for anomaly values). We observe absolute (and relative) differences between the maximum and minimum V_{out} of 0.6 V (16.63 %) at 750 kHz, 0.8 V (26.67 %) at 760 kHz, 0.7 V (27.66 %) at 770 kHz, and 0.5 V (23.97 %) at 780 kHz. If we study the change of V_{out} with the soil moisture in this prototype, the only frequency useful is 750 kHz.

The values of the V_{out} for frequency 750 kHz are shown in Figure 8.3. The V_{out} of prototype NP1 frequency 750 kHz. In this case, we observe that there are not a great dispersion of the values (except abnormal values). We use Statgraphics Centurion XVI (Statgraphics, 2022) to calculate mathematical models, which are presented in Table 8.2 (Equation (8.1) and (8.2)). The value of V_{out} for the 7.3 % of soil moisture is eliminated since the model cannot calculate the soil moisture with the values of V_{out} observed. For the first, we use all data obtained, and the model has an R^2 of 0.8093 and a RE of 6.23 %. We observe 4 atypical residuals (difference between the observed value and predicted value). These are the data for 48.9 %, 39.1 %, 29.1 %, and 15.6 % soil moisture. We eliminated these values and obtained a new mathematical model, see it in Table 8.2.

$$\text{Soil moisture (\%)} = \sqrt{41296.7 - 20667.9 * \sqrt{V_{out} (V)}} \quad (8.1)$$

$$\text{Soil moisture (\%)} = \sqrt{12472.5 - 786.904 * V_{out} (V)^2} \quad (8.2)$$

Table 8.2. Mathematical models to prototype NP1 frequency 750 kHz.

Equation number	Atypical residuals	RE (%)	R ²
8.1	Yes	6.23	0.8092
8.2	No	3.63	0.9443

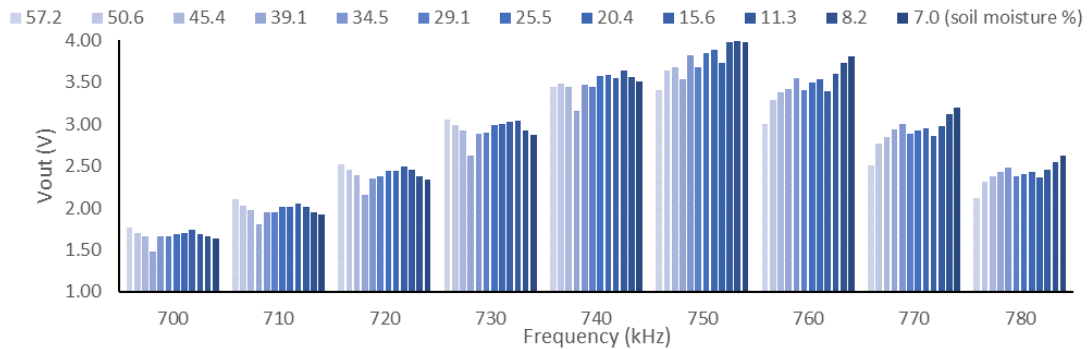


Figure 8.2. The V_{out} in the different frequencies tested in the prototype NP1.

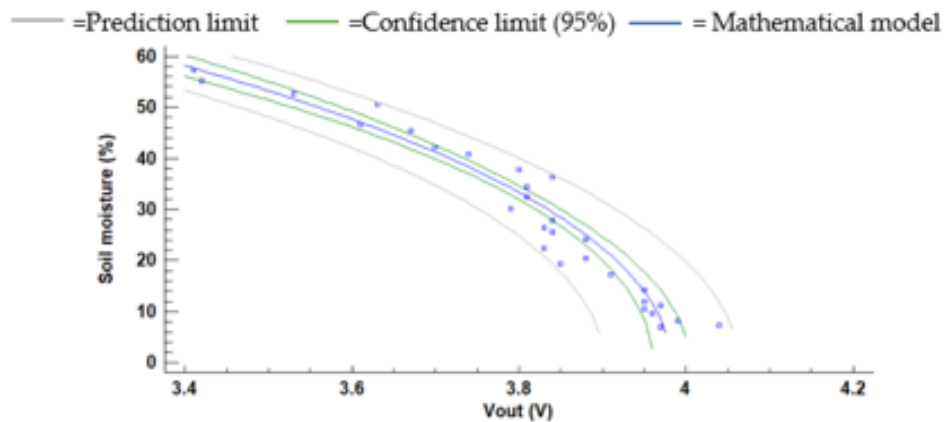


Figure 8.3. The V_{out} of prototype NP1 frequency 750 kHz.

The results for NP2 are presented in Figure 8.4. The V_{out} in the different frequencies tested in prototype NP2.. Like the previous case, the frequency peak is displaced from 480 kHz to 490 kHz. Although in this case, the change occurs in the last measurement of soil moisture. In frequencies before the peak, the differences of V_{out} are minimal. In these frequencies, the highest difference is 0.33 V in 460 kHz, and we discard the use of them. The more significant differences of V_{out} are in the peak frequency and the subsequent tested frequencies. These frequencies are 480 kHz, 490 kHz, 500 kHz, 510 kHz, and 520 kHz, and the absolute (and relative) differences between the maximum and minimum V_{out} are 1.4 V (29.36 %), 2.2 V (52.69 %), 1.8 V (52.38 %), 1.1 V (41.26 %), and 0.7 V (31.59 %) respectively. The V_{out} decreases rapidly in the first and last datum obtained concerning the evolution of V_{out} with the soil moisture in those frequencies.

We use Statgraphics to compare the value of the R² with a unique model for each frequency and all collected data. The values of R² are 0.8458, 0.9291, 0.9309, 0.9303, and 0.9381 for 480

kHz, 490 kHz, 500 kHz, 510 kHz and 520 kHz respectively. Despite these values of R^2 , we observe graphically that the models do not represent well enough the values we have obtained. We test two possibilities: (I) We eliminate the initial moisture values before the trend reversal occurs (until 45.3 % of soil moisture); and (II) we use two models. Table 8.3 represents the equation of the models (Equations 8-3 to 8-7), the values of R^2 and RE for (I). Meanwhile, Table 8.4 presents the same information for (II) (Equations 8-8 to 8-17). In (I), the values of R^2 are slightly lower than the second model of the previous case. In (II), we observe that the first model has a reduction in the value of R^2 , and the second model has an increase of R^2 . In (I), we lose the upper values in the range of use. However, we will get minor errors, and the loosed values are in conditions where irrigation should not be managed in most agricultural fields. If we observe the values of the REs in Tables Table 8.3 and Table 8.4, the highest is in 480 kHz for the two cases, (I) and (II). In (II), the RE is similar between the two models, with values over 5 % higher between one model and the other. However, in (I), the lowest REs are in frequencies 490 kHz and 500 kHz. As the absolute difference and relative difference of V_{out} are in the frequencies of 490 kHz and 500 kHz, we will use these frequencies in the verification test. The mathematical models (I) and (II) of the frequencies 490 kHz and 500 kHz are shown in Figures 26 to 29. Figure 8.5, Figure 8.6, Figure 8.7, and Figure 8.8

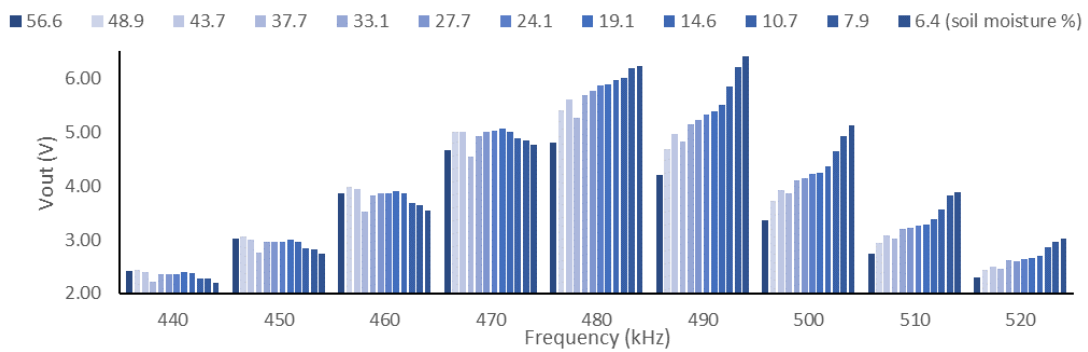


Figure 8.4. The V_{out} in the different frequencies tested in prototype NP2.

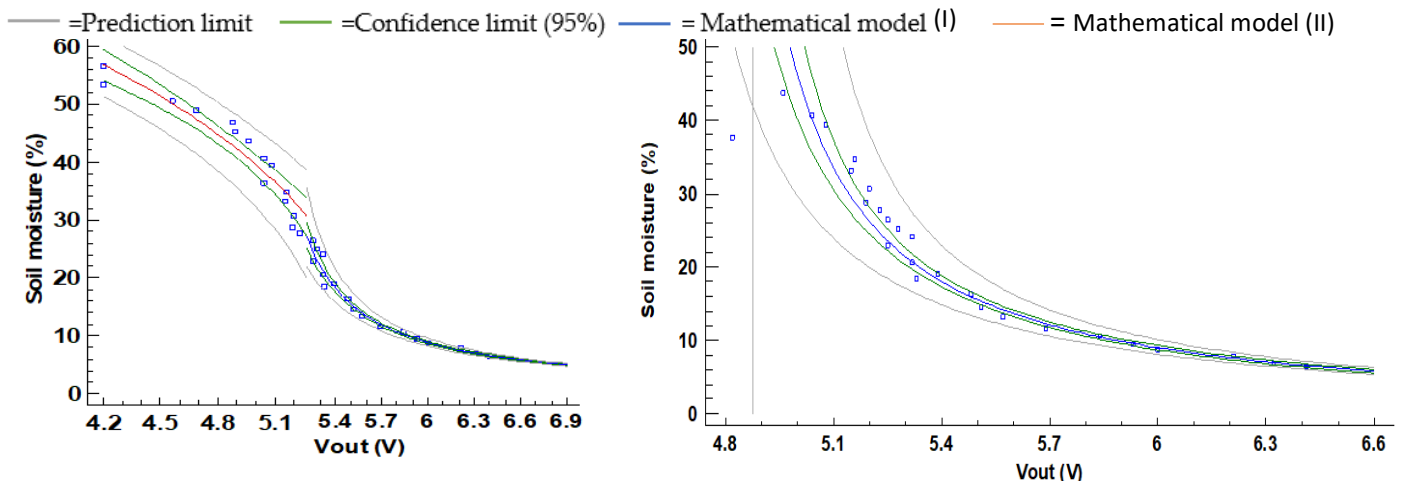


Figure 8.5. V_{out} NP2, 490 kHz, two models (II) Equation 8.11 and 8.12 as the mathematical model I and II, respectively.

Figure 8.6. V_{out} NP2, 490 kHz, one model (I) Equation 8.4.

$$\text{Soil moisture (\%)} = e^{10.3148 - 0.214189 * V_{out} (V)^2} \quad (8.3)$$

$$\text{Soil moisture (\%)} = \frac{1}{-0.181988 + 0.00814101 * V_{out} (V)^2} \quad (8.4)$$

$$\text{Soil moisture (\%)} = \frac{1}{-0.176427 + 0.0126477 * V_{out} (V)^2} \quad (8.5)$$

$$\text{Soil moisture (\%)} = \frac{1}{-0.200654 + 0.0232309 * V_{out} (V)^2} \quad (8.6)$$

$$\text{Soil moisture (\%)} = \frac{1}{-0.263374 + 0.0445901 * V_{out} (V)^2} \quad (8.7)$$

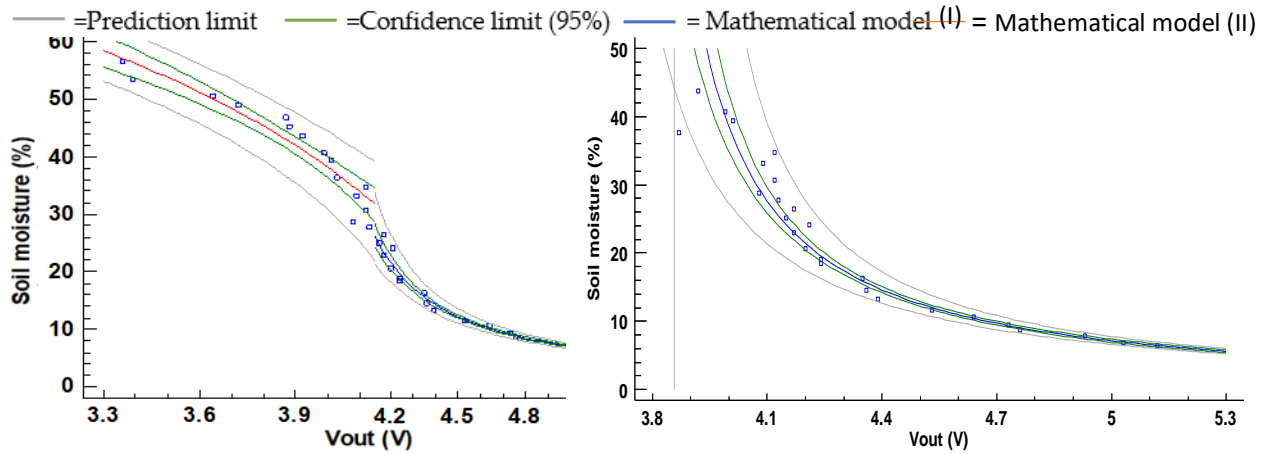


Figure 8.7. Vout NP2, 500 kHz, two models (II) Equation 8.13 and 8.14 as the mathematical models I and II, respectively.

Figure 8.8. Vout NP2, 500 kHz one model (I) Equation 8.5.

Table 8.3. Values of R² and REs in NP2 (I) Without the first values before the trend reversal occurs.

Frequency (kHz)	480	490	500	510	520
Equation number	8-3	8-4	8-5	8-6	8-7
R ²	0.862	0.98	0.984	0.974	0.969
RE (%)	13.1	7.5	7.1	8.0	9.3

$$\text{Soil moisture (\%)} = \sqrt{7901.29 - 202.249 * V_{out} (V)^2} \quad (8.8)$$

$$\text{Soil moisture (\%)} = \frac{1}{-0.63484 + 0.0200203 * V_{out} (V)^2} \quad (8.9)$$

$$\text{Soil moisture (\%)} = \sqrt{7202.71 - 225.536 * V_{out} (V)^2} \quad (8.10)$$

$$\text{Soil moisture (\%)} = \frac{1}{-0.467387 + 0.0967319 * V_{out} (V)^2} \quad (8.11)$$

$$\text{Soil moisture (\%)} = \sqrt{7545.65 - 380.326 * V_{out} (V)^2} \quad (8.12)$$

$$\text{Soil moisture (\%)} = \frac{1}{-0.445713 + 0.117128 * V_{out} (V)} \quad (8.13)$$

$$\text{Soil moisture (\%)} = \sqrt{8957.26 - 764.546 * V_{out} (V)^2} \quad (8.14)$$

$$\text{Soil moisture (\%)} = \frac{1}{-0.646451 + 0.585493 * \ln (V_{out} (V))} \quad (8.15)$$

$$\text{Soil moisture (\%)} = \sqrt{10373.8 - 1368.73 * V_{out} (V)^2} \quad (8.16)$$

$$\text{Soil moisture (\%)} = \frac{1}{-0.276662 + 0.0463475 * V_{out} (V)^2} \quad (8.17)$$

Table 8.4. Values of R² and REs in NP2 (II) Using two models.

Frequency (kHz)	480		490		500		500		510	
Equation number	8-8	8-9	8-10	8-11	8-12	8-13	8-14	8-15	8-16	8-17
R ²	0.7797	0.9493	0.9112	0.9112	0.9907	0.9908	0.9308	0.9811	0.9327	0.9867
RE model (%)	10.8	11.2	6.4	6.4	4.8	4.2	5.2	4.7	5.3	4.6
Mean RE (%)	10.8		4.8		5.4		5.2		5.1	

Now, we analyze the values of the NP3, and we show them in Figure 8.9. This prototype presents in all tested frequencies significant differences between the maximum and minimum soil moisture tested. The absolute (and relative) differences between the maximum and minimum V_{out} are 1.0 V (19.83 %) at 750 kHz, 1.1 V (21.6 %) at 760 kHz, and 1.0 V (19.83 %) at 770 kHz. The frequency peak is changing between 760 kHz and 770 kHz in the different soil moisture. According to the values, except in 760 kHz, the rest of the frequencies present great dispersions of the V_{out} values for similar soil moisture measures. The frequency of 760 kHz is the only frequency for which our prototype can be used.

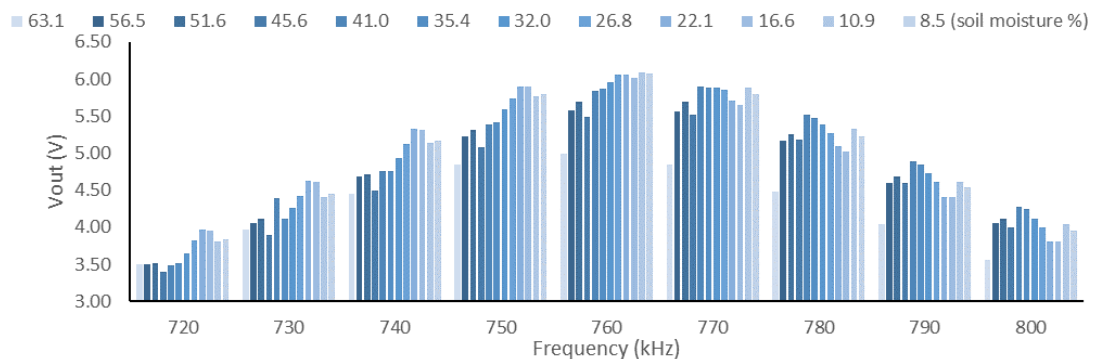


Figure 8.9. The V_{out} in the different frequencies tested in prototype NP3.

Figure 8.10 shows the V_{out} in the frequency of 760 kHz. If we use all data to develop the model, we obtained an R² of 0.6916. However, we consider that values of the V_{out} in the points of 33.0 % and 45.6 % soil moisture (5.16 V and 5.49 V, respectively) are aberrant. In the case that we build our model without these values, the value of R² is 0.8471. We consider that R² is lower than the previous prototypes. In addition, the frequency with which the prototype works is high, and the voltage difference is less than for prototype NP2. For these reasons, we discard the use of this prototype for monitoring the presence of water in the soil.

Finally, Figure 8.11 represents the values of NP4. In this prototype, the peak frequency is 490 kHz when the soil is wet and 500 kHz when the soil is dry. The change of peak frequency happens at 38.0 % soil moisture. As in the previous prototypes (except NP3), the greater differences are in frequencies higher to the frequency peak (490 kHz). The absolute (and relative) differences between the maximum and minimum V_{out} are 0.5 V (7.8 %), 1.0 V (15.43 %), 1.2 V (20.17 %), 1.3 V (23.89 %), and 1.1 V (23.53 %) for 490 kHz, 500 kHz, 510 kHz, 520 kHz, and 530 kHz, respectively. However, these differences (except in the case of 490 kHz) mean that the

voltage difference is higher at very low moisture. For this reason, NP4 is not suitable for monitoring irrigation; it might have other uses when very low soil moistures (less than 10 %) must be measured.

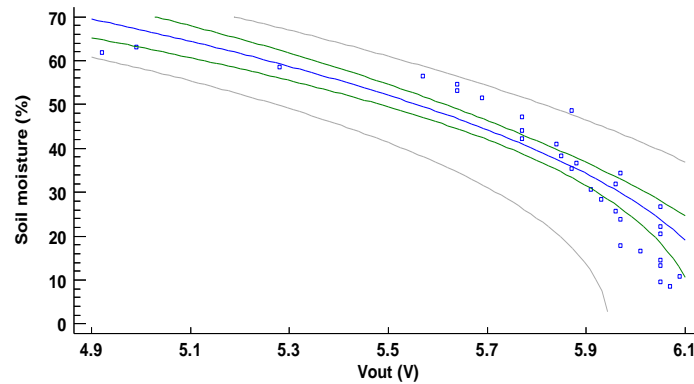


Figure 8.10. The V_{out} in the frequency of 760 kHz in prototype NP3.

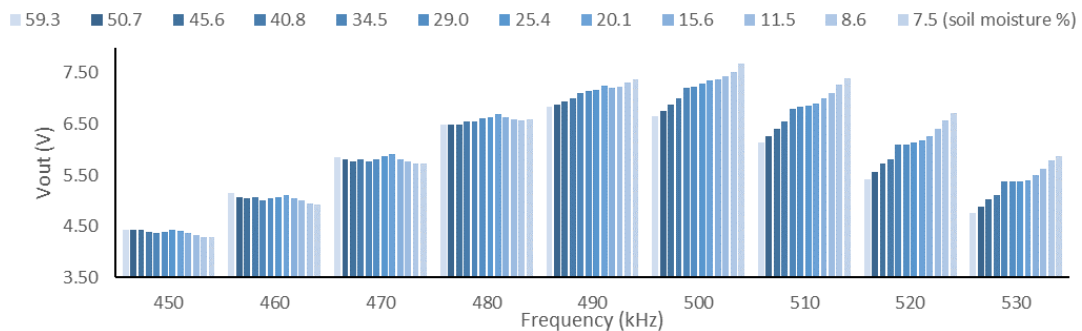


Figure 8.11. The V_{out} in the different frequencies tested in the prototype NP4.

8.1.3 Verification.

In this subsection, we analyze the values of the verification test for NP1 and NP2. In Table 8.5, the results of the verification of NP1 for the frequency of 750 kHz are shown. We can see as the maximum RE is 48.0 % when the soil moisture is at 13.2 %. With this high error, the sensor cannot work in a low concentration of soil moisture. For the other moisture levels used in the verification, the errors are lower. For the central values, the errors are 13.8 %, 17.0 %, and 9.3 % for the moistures of 23.4 %, 33.8 %, and 43.9 %, respectively. Finally, the RE is minimal (0.6 %) in the moisture value of 53.9 %.

In Table 8.6, we show the verification of prototype NP2 and one model. In this case, we do not use the value of 51.7 % soil moisture because it is outside the model range. In general, with a frequency of 500 kHz, the REs are lower than the REs at 490 kHz. The higher errors are in soil moisture levels of 31.8 % and 42.3 %. The maximum RE is 25.5 % in soil moisture and 31.8 % at 490 kHz. In Table 8.7, we show the values of verification of the prototype NP2 using two models. In this case, we can observe that the maximum error occurs with the soil moisture of 31.8 %, as it happened with a single model. Regarding the other RE values, these are small. In the two frequencies, the mean of the RE is 6.5 % for 490 kHz and 6.2 % for 500 kHz.

Table 8.5. Verification NP1, 750 kHz.

Moisture (%)	Vout (V)	Estimated moisture (%)	AE (%)	RE (%)
53.9	3.49	53.6	0.3	0.6
43.9	3.72	39.8	4.1	9.3
33.8	3.85	28.1	5.7	17.0
23.4	3.87	26.6	3.2	13.8
13.2	3.92	19.5	6.3	48.0
Average			3.9	17.7

Table 8.6 Verification NP2, 490 kHz, and 500 kHz one model.

490 kHz		500 kHz						
Moisture (%)	Vout (V)	Estimated moisture (%)	AE (%)	RE (%)	Vout (V)	Estimated moisture (%)	AE (%)	RE (%)
42.3	4.97	49.2	7.0	16.4	3.95	47.4	5.1	12.0
31.8	5.24	23.7	8.1	25.5	4.13	25.0	6.8	21.5
22.1	5.29	21.4	0.7	3.0	4.19	21.9	0.1	0.7
12.3	5.68	12.4	0.0	0.4	4.52	12.2	0.1	1.1
Average			3.9	11.3			3.1	8.8

Table 8.7. Verification NP2, 490 kHz, and 500 kHz two models.

490 kHz		500 kHz						
Moisture (%)	Vout (V)	Estimated moisture (%)	AE (%)	RE (%)	Vout (V)	Estimated moisture (%)	AE (%)	RE (%)
51.7	4.35	54.2	2.5	4.8	3.51	53.6	1.8	3.5
42.3	4.97	40.3	2.0	4.7	3.95	40.3	2.0	4.8
31.8	5.24	25.3	6.5	20.4	4.13	26.0	5.8	18.2
22.1	5.29	22.4	0.3	1.5	4.19	22.4	0.3	1.4
12.3	5.68	12.2	0.1	1.1	4.52	11.9	0.4	3.1
Average			2.3	6.5			2.1	6.2

8.1.4 Overview and general discussion.

NP2 and NP1 exhibit good results. The main reason behind the erratic trends observed in several cases is that soil is a more complex substratum than water. It has a higher heterogeneity, and within the soil, different environments coexist (such as organic matter, soil particles of different granulation, air, water, etc.). Therefore, the behaviour of the EF is modified by the different environments it crosses. This fact causes slight variations in the location of the sensor, can involve changes in the Vout, and can cause difficulting in the correct calibration of the prototypes.

To monitor the crops, mainly citrus with soils similar to the one used in the last set of tests, we select the prototype NP2 with a powering frequency of 500 kHz, with two models. Due to it accomplishing all the features that we determined previously. The NP2 presents greater voltage differences between the minimum and the maximum Vout values than the other prototypes. Furthermore, its REs and AEs are lower when two models are used.

During these tests, we have confirmed some of the observed trends in (Basterrechea, 2020a). We confirm that the peak frequency, the frequency at which the IC presents the highest V_{out} , is modified by the properties of the environment in coreless inductive coils. Moreover, the modification in the decreasing/increasing trend before and after the peak frequency, reported in (Basterrechea, 2020a) is confirmed for inductive coils with a soil core.

Regarding the results of keeping the sensor buried during the tests or using the sensor as a probe (introducing it every time that a measure must be done), we can conclude that less abnormal data is gathered when the sensor is kept buried.

Even though some sensors are buried over one month, more test which durations reaches 12 months should be conducted to verify this issue. Notwithstanding the aforementioned information, some of the prototypes shown in this chapter, have been used in previous experiments in different conditions of temperature, conductivity and are immersed in water for several days without noticing any fault in their operation (Kleinberg, Chew and Griffin, 1989). Considering that the sensing element, the copper wire, is isolated from the environment by a thin layer of enamel, it prevents many damages caused by the environment. Nonetheless, a test to evaluate the degradation of enamel must be planned before the final deployment of these prototypes.

8.2 IoT Sensor to Detect Fraudulent use of Dyed Fuels in Smart Cities.

Currently, fossil fuels are the main source of energy for vehicles, which have associated with different taxes. Certain activities use fuels with lower taxes and have a different colour. There is the possibility of commit fraud by using the low taxes fuel for private vehicles. In this subchapter, we present an IoT system to detect the presence of low-taxed fuels in the deposit of cars. Moreover, the system can send a message to the police to proceed with the denunciation if it is required. The sensor is based on the differences in light absorption by the different fuels, the normal fuel, and the low-taxed fuel. As a light source, we use seven LEDs: white, green, yellow, orange, blue, red and infrared. We measure the changes in the resistance values with different LEDs with non-dyed diesel and dyed diesel.

8.2.1 System description.

In this section, we present the description of our proposal. First, the structure of the system is detailed. Then, the operation algorithm is shown. Finally, we describe the message flow protocol.

8.2.1.1 Structure of the system.

The general structure of the system includes an IoT device, which is used by the police. In addition, it is able to send data to the police server, as shown in Figure 8.12. The IoT device is composed of the physical sensor and the node that process the data gathered by the sensor and forwards the data to the main server. The sensor is based on light absorption and it has a LED that emits a certain wavelength and a detector that measures the light absorption where the sensor is introduced in the fuel deposit. The sensor connects to a wireless device, which can be a mobile device, a LoRa, etc. The device is able to transmit the alert message to the main server. Hint, the alert message is sent to the server when it is necessary. Thus, the system can automate showing the results to the police and forward the data to the server. The police can use the information to inform of the fraud or proceed to report the owner of the vehicle.

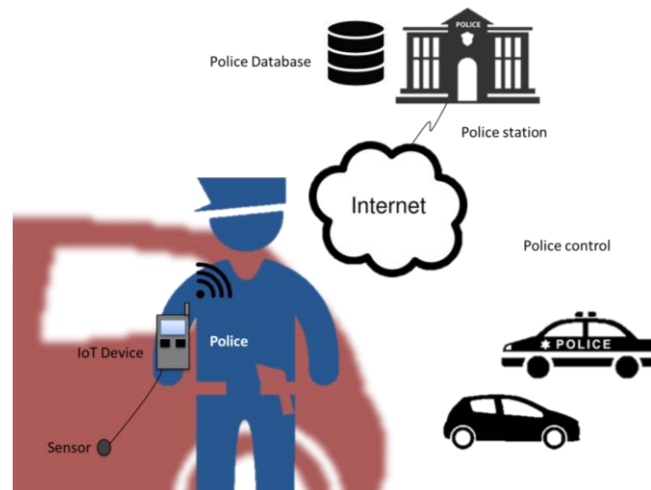


Figure 8.12. General structure of the system.

8.2.1.2 Proposed algorithm.

In this subsection, we show the proposed algorithm to detect the fraudulent use of low-taxed fuel. In order to detect a measurement of the regularity and irregularity of combustibles, we propose an algorithm. The operation algorithm of the IoT devices is shown in Figure 8.13. The IoT device gathers data from the LEDs sensor, the measurement results specifies the type of the fuel and all information is extracted. Two parameters are considered in the algorithm, a parameter for the regular case when the system detects normal value and other for the irregular case the sensor reads abnormal value.

Whether the system detects regular fuel, it means there is no issue in the gasoline and the car can continue. Otherwise, when the sensor depicts irregularities in the measurement of fuel, the system shows the irregularity in the IoT device (identity by code 1). Then the police can report to the driver. In addition, the data is wirelessly sent to the police station in order to save the information. Moreover, when the IoT device is not sent information to the police server the device provides code 2, which means that there is no connection between the two devices.

8.2.1.3 Message flow protocol.

In this subsection, we present the message flow protocol between the IoT device and the police server. The message flow topology between IoT device and Police server is presented in Figure 8.14. Flow message conversation.. At first, the IoT device, which collects data from the connected LED sensor, connects to the police server by establishing a connection on the Internet using HTTP protocol. In the scheme, the IoT device initiates the conversation that includes: the source host identity, the measure of fuel from the LED sensor, and destination server. The server is a police server that holds information. After the establishment is done, the police server asks for authentication for both device and the user in the system. Then the server asks for registering plate of car and query driver information such as full name and license number. The policy server has SQL database, which contains registered information of fuel measurement, car, and driver. The system will check the information and it will reply to the IoT device. Furthermore, all messages are based on HTTP/TCP in order to reliable delivery of the data between IoT devices. After the process of conversation is finished, the IoT device sends a terminate message to the police server to close the session.

8.2.1.4 System description.

In this subsection, we are going to describe the system of the sensor.

To develop the measurements, we use a glass tube with a diameter of 18 mm and a thickness of 1 mm. The tube is completely covered with an opaque material. Thus, the exterior light does not interfere with the measurements, only the light from the LEDs reaches the inner part of the tube. The LEDs are placed on the outside part of the tube. We use seven LEDs with different coloration including red, blue, yellow, orange, green, white and infrared LEDs.

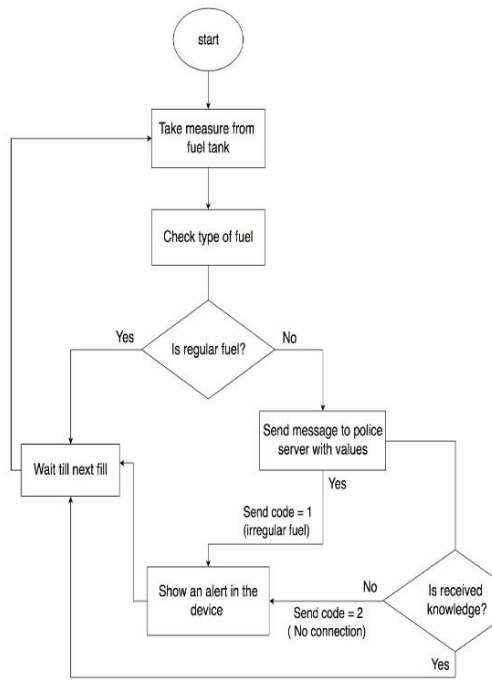


Figure 8.13. Proposed algorithm.

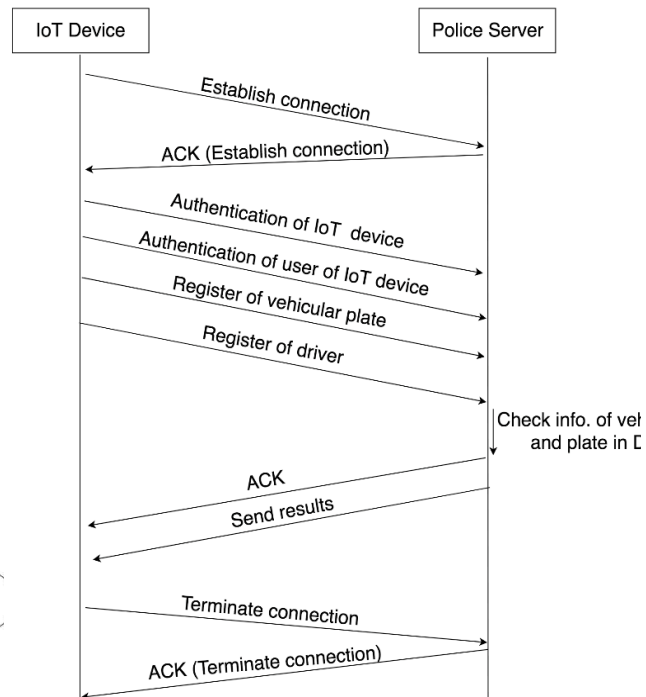


Figure 8.14. Flow message conversation.

The coloured LEDs are 3 mm of diameter while the infrared LED is 5mm of diameter. To measure the absorbance of the fuel to the different lights, we measure the incident light on the opposite side of the tube (see Figure 8.15). This sensor is based on the one presented in (Parra, (2018), (Sendra et al. 2013)). We measure the incident light as the resistance of an LDR and a photodiode in the case of the infrared LED. The resistance of LDR and photodiode change when the light strikes it. More light less the resistance. The environment that is between the LED and the LDR/photodiode, the non-dyed fuel or the dyed fuel, absorb more or less light depending on the wavelength of the emitted light.

The resistance measurements were done in a tester (model Fluke 110). The LEDs are powered by a power supply (model FAC-662B) with a voltage of 5 V and an intensity of 300 milliamps. At the positive pole of the power supply, there is a resistance with a value of 470 Ω.

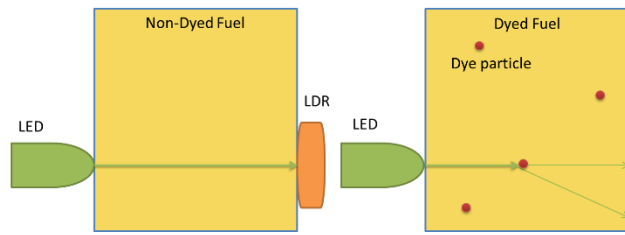


Figure 8.15. Light absorption by the samples.

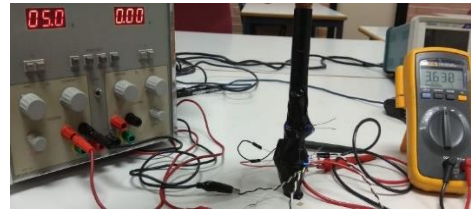


Figure 8.16. Experimental test.

8.2.2 Measurement and Results.

In this section, we describe the experiments performed and the obtained results that show how the sensor is able to differentiate between normal dyed and non-dyed fuel.

For the measurements, the LEDs are powered sequentially. The measurement of the incident light is taken as the resistance of the LDR or the photodiode. Once the measurement has been recorded, the LED is turned off and turned on to take the measurement again. This is done to obtain three replicas of each measurement. In Fig 5 we can see the assembly in the laboratory to measure the light abortion.

We measure the resistance of the LDR/photodiode with the empty tube, the tube full of dye diesel and normal and premium diesel of four gas stations from four different brands. The petrol stations are located in Valencia (Spain). The St1 sample was taken from a small town gas station, the St2 was taken from a gas station associated with a supermarket, the St3 from a large oil company, and finally, the St4 was taken from a low-cost gas station. The dyed diesel was only taken from the St1 because the other gas stations did not sell dyed diesel.

Once we have described how the measurements are obtained, we are going to analyze the obtained data. In Figure 8.17,

Figure 8.18. The resistance of LDR with white light.

, and Figure 8.19 can be seen the resistance of the LDR/photodiode in the tubes with the different diesel testing. We can be observed that there is not a high difference between the values of resistance with the normal and premium diesel of the different gas stations. These small differences can be explained by the presence of additives that gas stations put to their fuels. In the dyed diesel, the differences are observed in the white, green, blue and yellow LEDs.

In Figure 8.17, shows the value of resistance with different colour LEDs. The resistance values with the green LED are much higher than with the other LEDs. In contrast, the orange LED has lower values of resistance. The green LED has a mean value of 7.05 k Ω in normal and premium diesel while the orange has values of 0.87 k Ω . The Yellow and Red LEDs have very similar values with an average value of 2.10 k Ω and 2.11 k Ω respectively for normal and premium diesel. Finally, the red LED has an average value of 1.56 k Ω .

In

Figure 8.18. The resistance of LDR with white light.

, we can be observed values of resistance much lower than those observed in the other LEDs. We can see how the average of the resistance values is 335.5 Ω for normal and premium diesel. The normal and premium diesel has an important difference with empty tube and dyed diesel.

In Figure 8.19, we observe the highest Resistance values we have observed. The average value for non- coloured diesel is 3.80 M Ω . The value of St1 normal is the highest resistance with a value of 3.9 M Ω . The values of St1_premium, St2_normal and dyed diesel have similar values (close to 3.83 M Ω). The St2_normal, St3 normal, and premium fuel present different values. The St4 normal and the premium fuels presents are similar values.

Now, we are going to compare the differences between the values of normal and premium diesel with the dyed diesel. The observed difference are 188.93 Ω in white, 3.11 k Ω in blue, 0.76 k Ω in the yellow and 1.72 k Ω in the green, which supposes a variation on the resistance of 36%

for the white light, 59.7% for the blue light, 26.3% for the yellow light, and 32.3% for the green light. For the other LEDs, the variations of the resistance are 6.2% for red light, 4.4% for orange light, and 0.1% for infrared light. Thus, we are going to analyze in detail the response of the sensor for the aforementioned lights.

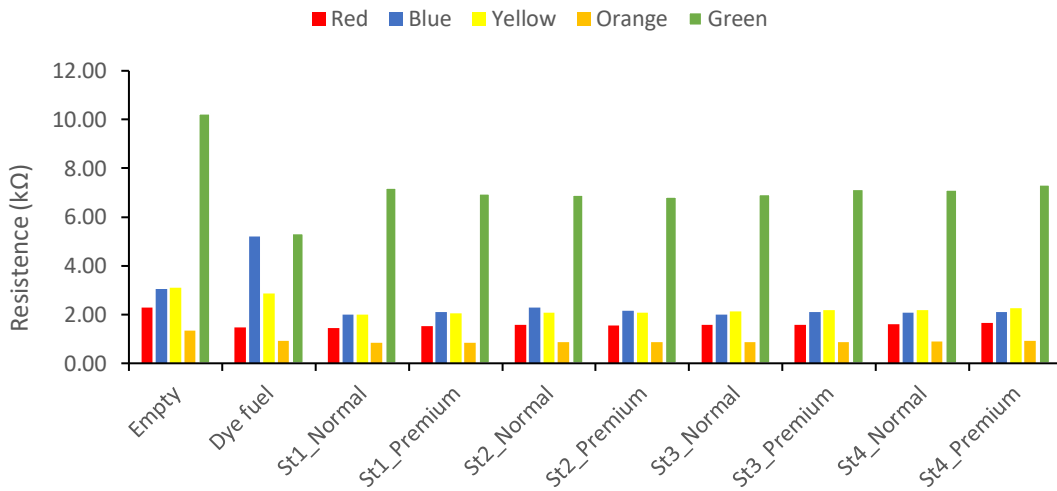


Figure 8.17. The resistance of LDR with different lights.

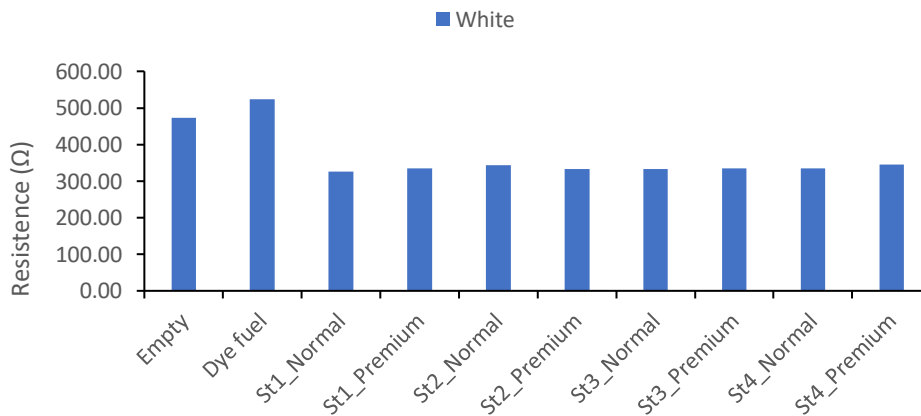


Figure 8.18. The resistance of LDR with white light.

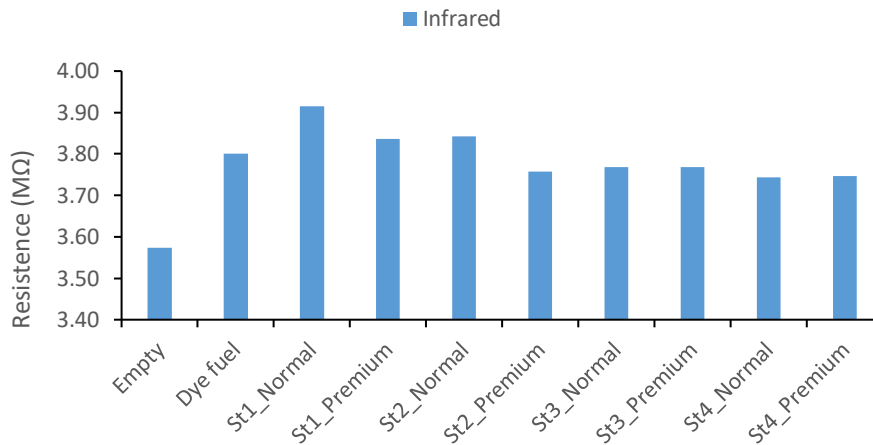


Figure 8.19. The resistance of a photodiode with infrared light.

In Figure 8.20, Figure 8.21, Figure 8.22, and Figure 8.23, we observe the box plot of the resistance of the LDR/photodiode in the 3 replicas. As previously mentioned, in these graphs can be observed that there are differences between the normal and premium diesel according to the gas station from which the sample is obtained. These differences are due to the different additives that are added by the manufacturer. It is possible to observe that the values of dispersion are low and that in no case these come close to the values of the coloured diesel.

In Figure 8.20, it can be seen the values of resistance when the blue LED is used. The values for the normal and premium diesel are in the range of 2.00 kΩ to 2.30 kΩ. The lowest value is St1_normal and the highest is St2_normal. Regarding to the dispersion of the measurements, we can see that in all cases the values are not dispersed among them. There is a big difference between the dyed diesel, the empty tube, and the normal and Premium diesel.

The resistance values for the green LED can be seen in Figure 8.21. In this case, we can note that there is a greater dispersion in the data of the coloured diesel and the St2_Normal in regard to the other values. In St2_normal the values are from 6.81 kΩ to 7.00 kΩ and in the coloured diesel are in a range of 5.43 kΩ to 5.21 kΩ.

In Figure 8.22, we observe that the dispersion between the values is small. The resistance values in the different types of normal and premium diesel are different. Therefore, it is possible that the sensor can identify the type of diesel with the yellow LED..

In Figure 8.23, it can be observed the resistance values for the white LED. The values of St1_premium, St2_premium, St3 normal and premium, and St4_Normal have very similar values, around 330 Ω. The other values of non-dyed diesel are in a range between 325 Ω. and 345 Ω. The values of the non-the dyed diesel are much lower than dyed diesel. In addition, it is observed that the values of the different replicas are not dispersed.

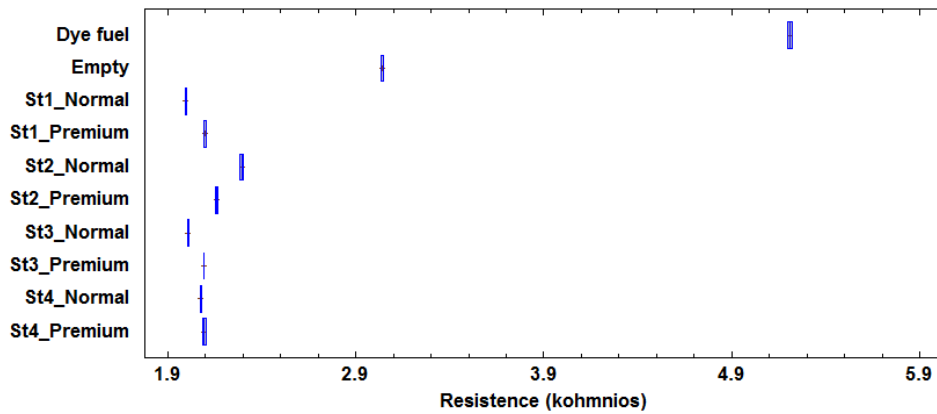


Figure 8.20. Box plot resistance of LDR with blue light.

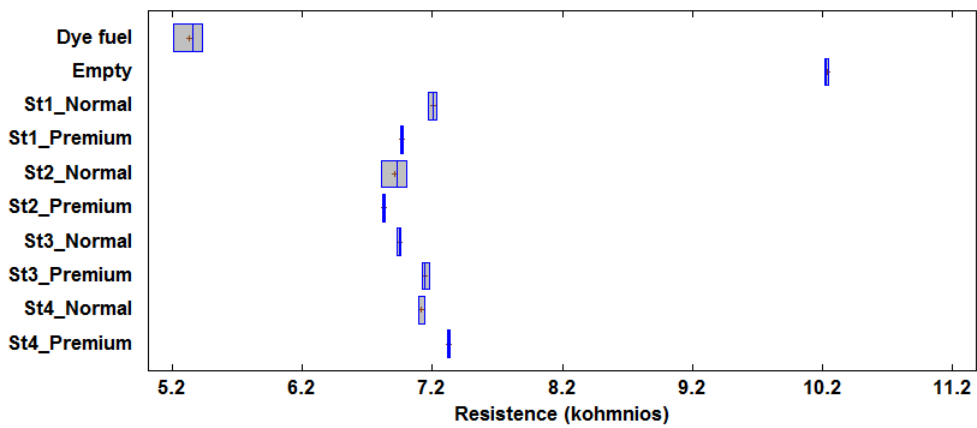


Figure 8.21. Box plot resistance of LDR with a green light.

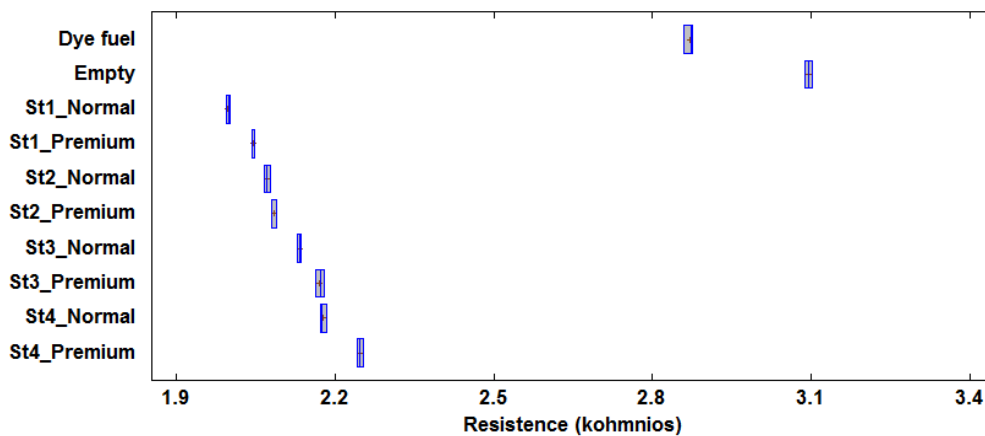


Figure 8.22. Box plot resistance of LDR with yellow light.

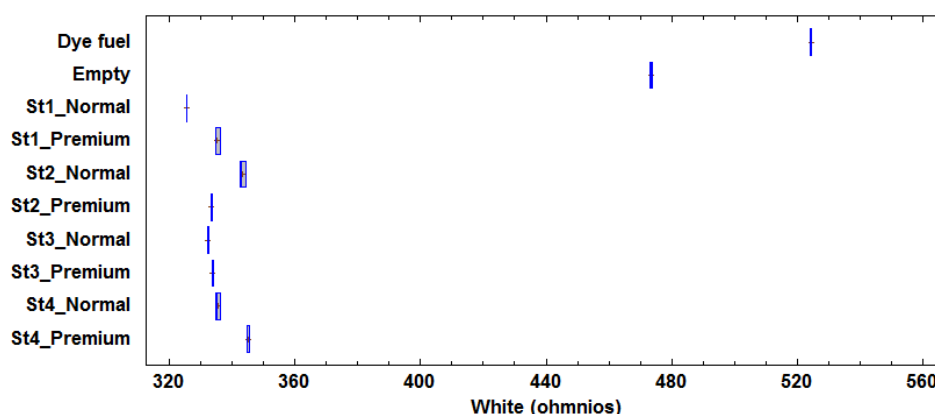


Figure 8.23. Box plot resistance of LDR with white light.

We selected the blue, green and yellow LEDs because they produce the highest difference between non-dyed diesel and dyed diesel in the resistance of the photodetectors. We used three LEDs in order to augment the security of the detection. If only two LEDs detect a dyed diesel the test will be repeated. If a solely LED detects a dyed diesel will is considered a false positive.

8.3. Sensors and Biosorption for Better Reuse of Wastewater

One of the objectives of the project SMARTWATIR is the use of WSN to ensure the quality of water in irrigation. In the event that the quality of the water is not sufficient, bioadsorption technology will be used. Bioadsorption process is based on physical and chemical processes by adsorption, where the particles come together and precipitate. Biosorption can be used in all types of sources of pollutants, from non-point sources such as runoff caused by heavy rains through localized focus such as industrial wastewater (Gupta and Rastogi, 2008). Likewise, biosorption is a technique with great aptitude to eliminate the heavy metals of these waters, considering themselves sustainable with the environment and differentiated from the others by their minimum cost of investment (Vieira and Volesky, 2000).

In the current research, we are going to highlight the possibility of using biosorption for water reuse. Different sensor after and before biosorption process are supposed to be used to check its operation and whether we find optimal water.

In Mediterranean region especially, the design and operation of competitive and cost effective wastewater treatment systems for irrigation is a real challenge. Within this context an innovative system of wastewater treatment has been proposed that is based on biosorption technology and sensors. The biosorption system that we are going to develop could be used for augmenting the reuse of wastewater. It comprises sensors for monitoring water quality in the entry and exit. Sensors in the entry are used for detecting if the water needs treatment. Sensors in the exit are used to assess released water quality and to explore the efficiency of biosorption system. Biosorption technique is used for eliminating wastewater pollutants that are not removed by both primary and secondary WWTP. In Figure 8.24, we show the scheme of the proposed system.

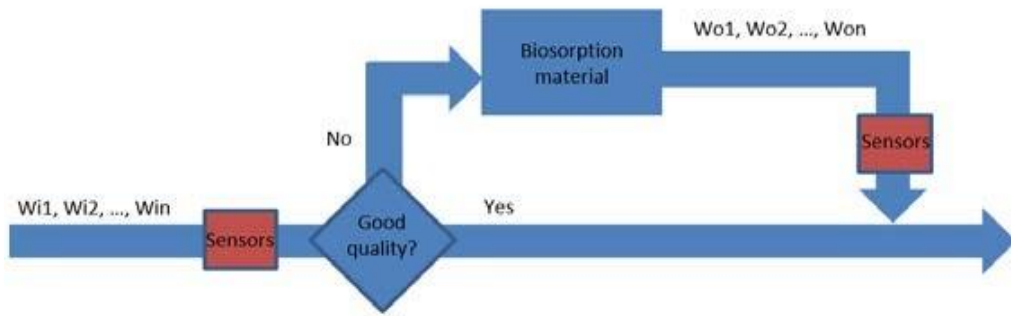


Figure 8.24. Scheme of the proposed wastewater treatment system.

For our proposal, the sensors need to comply with different characteristics: (I) Low cost, because the sensors will be used in many areas especially developing countries. (II) Physical sensors. The use of chemical sensors caused an increase in maintaining cost. (III) Low electrical demand. The sensors are located in the countryside when the supply can be a problem. (IV) The sensors should be able to detect values in long periods. (V) The sensors should not need a daily calibration.

In the wastewater, the main pollutants are: (I) Heavy metals, (II) Nitrogen, (III) Phosphorus, and (IV) microorganisms. Microorganisms are relatively easy to eliminate by means of disinfection processes that usually occur in conventional WWTPs. In addition, pollutants can be removed in wastewater if the way of operating the plant is changed. Finally, heavy metals are a group of chemical elements. The main are Mercury, Nickel, Copper, Lead, and Chromium. These pollutants can be eliminated in WWTP with chemical precipitation, carbon adsorption, ion exchange, evaporation and membrane processes. However, the typical concentration is low and does not compensate economically. Also, these techniques have certain disadvantages such as incomplete metal removal, high reagent and energy consumption and generation of toxic sludge that require disposal. Another problem is the high conductivity. This is usually due to marine intrusion and represents a huge cost for its purification. That is why in the presence of high concentrations of salinity is advisable not to use that water for irrigation.

Our system can be defined with equation (8.18). W_{i0} are the concentration of the different pollutants that we measure with our sensors before the biosorption. W_{o0} is the same pollutants of W_{i0} but after the biosorption. Finally, A_{0000} is the % of absorption of the pollutant by the biosorption material. So each output value can be expressed as given by equation 8.19:

$$\begin{bmatrix} W_{W001} \\ W_{W002} \\ W_{W003} \\ \dots \\ W_{W00n} \end{bmatrix} = \begin{bmatrix} A_{0001} & 0 & 0 & 0 & 0 \\ 0 & A_{0002} & 0 & 0 & 0 \\ 0 & 0 & A_{0003} & 0 & 0 \\ \dots & \dots & \dots & \dots & \dots \\ 0 & 0 & 0 & 0 & A_{000n} \end{bmatrix} \begin{bmatrix} W_{Wii1} \\ W_{Wii2} \\ W_{Wii3} \\ \dots \\ W_{Wii0} \end{bmatrix} \quad (8.18)$$

$$W_{W000} = \sum_{i=1}^n A_{000i} \cdot W_{Wii0} \quad (8.19)$$

8.4. Development of Optical Sensor to detect Industrial Oil in Agricultural Irrigation System.

Nonetheless, the incorporation of new types of machinery can cause problems in the environment. One of these problems is the use of oil for their operation. Due to accidents or negligence, the oil from the engine can reach the irrigation channel. The industry is another source

of pollution; some industries can incorporate used oil into the water by illegal dumping. These discharges often end up in different water bodies, such as channels or ditches, whose water can be used for irrigation purposes. The polluted water used for irrigation can infiltrate and pollute the soil, the crops, or the groundwater or can be diluted into larger water bodies (rivers, reservoirs, sea, etc.) The most common water sources used in irrigation are groundwater and irrigation ditches (Wu et al. 2016).

8.4.1. Proposal

In this section, we show the proposed sensor and the microcontroller that we propose to use to control its operation. In addition, we outline a possible scheme to locate the sensor into the irrigation channels, and an operation algorithm if the sensor is integrated into a WSN for precision agriculture. The sensor is based on different LEDs to measure oil presence in irrigation water. The objective of this prototype is to detect the presence of oils in the water and send alarms to the different water agents to inform them about detected illegal dumping. Furthermore, this information can be used to avoid irrigating the fields with polluted water.

This sensor will be part of the Smart WSN to detect and purification water salinity and pollution for agriculture irrigation (SMARTWATIR) final monitoring system.

8.4.1.1. WiFi node.

In this subsection, we show the wireless node that we propose to use with the prototype in the future deployments. The functions of the node will be read the Vout of LDR and photodiode, sent data, and powered the LEDs.

We propose to use a microcontroller ATmega328p with a module ESP8266 to WiFi. ATmega328p is a low-cost and easy to program node, compatible with Arduino IDE. This node has outputs of 5V and 3.3 V. We can use the 5 V output to power the LEDs and the 3.3 V output for feed the LDRs and photodiodes in the future. The antenna and microcontroller are located in a waterproof box out of the water due to the WiFi is attenuated in the water.

8.4.1.2. Future deployment.

In this subsection, we show a proposal for the future deployment of the tested prototype in the environment.

The prototype must be encapsulated for preventing damage from animals, obstructions due to solids in water, etc. The encapsulation might decrease the light input and can affect the measurement. The prototype has openings at the top of the encapsulation to allow the entrance of the water with oil. Our prototype can be hooked on the wall of the channel. The microcontroller, batteries, and WiFi antennas are in a waterproof box above the water level to ensure the WiFi connectivity. In Figure 8.25, we can observe the proposed scheme for the deployment of our prototype in the irrigation channel.

8.4.1.3. Algorithm.

In this subsection, we explain the function of the algorithm of our sensor.

The algorithm is summarised in Figure 8.26. First, the threshold values of used industrial oil and turbidity are set (THx). Next, the sensor determines the presence of oil in the water (on the LEDs and read the LDR/photodiode). If the value of oil is lower than THx, the sensor waits a specified period (t1) to get back into operation. On the other hand, if the presence of oil is higher than the THx, turbidity sensor started working. The turbidity sensor is starting to prevent false positive of oil presence. If the turbidity level is below the set value, it indicates the presence of

oil in monitored water. If the systems determine the presence of oil, the node sends an alarm using the WiFi antenna, and stores the data in its memory. Instead, if the value of turbidity is higher than the value set, it can indicate a false positive and data is stored. We have established the limit of 3600 record stores in the node. When data is stored, the system adds +1 to a variable (clock). If the variable clock is 3600, the system sent data and removes internal memory. Finally, the system waits for a time (t_2) for starting a new measure.

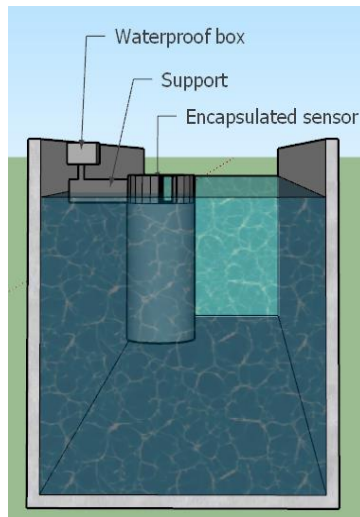


Figure 8.25. Deployment of the sensors in the Irrigation channels for agriculture.

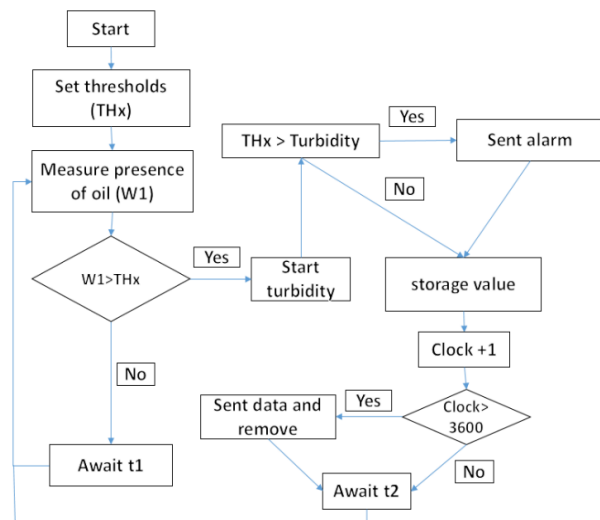


Figure 8.26. Developed Algorithm.

8.4.2. Test Bench.

In this section, we show the used methodology to obtain the data required to evaluate the performance and calibrate our prototype. In addition, we display the characteristics and functioning of the proposed prototype.

We use an AC power supply model FAC-662B to power the LEDs with a current of 5 V and 0.3 A. Each LED has a resistance of 470Ω with a tolerance of 5% between the power supply and the LED. We carry out the measurements by turning the LEDs sequentially. The sequential order to light the LEDs is yellow, red, blue, green, white, and infrared. As the LDRs have a delay, we wait 5 seconds to take the measurement. The measurements are taken in triplicate. Once we have already gathered the resistance values, we turn off the LED. Then, we turn on the following LED.

We measure the resistance of the LDRs and photodiodes with a tester (Tenma 72-2600 (TENMA, 2022)). The resistance of the LDR decreases when the light exposure increases and the resistance increases when the light intensity decrease. Otherwise, the photodiode works oppositely to LDR. The industrial oil used has been obtained from a mechanical workshop. The oil is a 0W-30 used for a fuel car during 10.000 km, which can be one of the possible oil sources in the farms. We use this sample to recreate a similar scenario of dumping in an agricultural irrigation system. Notably, the oils, which have remained for a long time in vehicles, are the more pollutant ones.

The samples are introduced in a glass cylinder with a diameter of 8 cm and 16 cm in height. We introduce the water sample up to a height of 12 cm (approximately 600 ml). After each measurement, we add a small amount of oil to the sample of water. We test with a volume of 1, 2.5, 5, 7.5, and 10 ml of oil in the sample of water. Since the oil is not mixed with the water in the irrigation channels, due to the different densities and polarities, these volumes correspond to the concentration of 0.02, 0.05, 0.1, 0.15, and 0.2 ml oil/cm² on the surface of the water.

8.4.3. Results.

In this section, we analyse the results of our prototype for detecting the presence of industrial oil in water.

After gathering data and analysing the results, we observe that the values of the resistance in the LDR and photodiode placed at 180° of the light source are not constant. Since we recreate the water movement expected in the irrigation channel, the oil stains do not remain quiet over the surface water. Due to this movement, oil spots cover the light of the LDR and the photodiode intermittently. Due to this effect, the resistance values are not constant.

Furthermore, in the case of infrared LED, the value of the resistance of the photodiode at 360° varies from 7980 to 7907 kΩ in the concentrations of 0 and 0.2 ml Oil/cm² respectively (in the rest samples, the resistance is between these two values). With these resistance values, the voltage difference after the voltage divider is almost null. For this reason, we discard the use of infrared LED.

Therefore, we are going to focus on the values of resistance in the LDR at 0° for the different colour lights. With the values of resistance of LDR and Eq. 1, we can obtain the most appropriate resistances to be used for the voltage divider (Table 8.8).

The calculated values of V_{out} for the different LEDs can be observed in Figure 8.27. The obtained V_{out} with the 5 LEDs included in Figure 8.27 presents a similar behaviour linked to the changes in the pollution presence. When the pollution level increases, the V_{out} of the LDR rises. It is caused by the higher light reflection on the oil surface compared with the water surface. If we study the different LEDs independently, we can see that the white LED has the lowest V_{out} difference between maximum and minimum oil quantity (0.025 V). This reduced voltage difference implies a low resolution of the future sensor. The difference with the white LED is much lower than with the other light sources. The yellow and blue LEDs present a difference in the V_{out} between the most and the less polluted samples of 0.089 and 0.075 V, respectively. On the other hand, the green and red LEDs have a higher difference with 0.29 and 0.39 V.

As the red and green LEDs have the highest voltage difference, and they can differentiate between 0 to 0.1 ml oil/cm of industry oil, we select them. Now, we detail the mathematical equations that model the concentration of oil (cm²/l) and V_{out} . The mathematical model between the V_{out} and the presence of industry oil is presented in 8.20 and 8.21. Equation 8.20 is the mathematical model for the red LED, and 8.21 is the mathematical model for the green LED. The value of R^2 (Coefficient of determination) is 0.9604 for 8.20 and 0.8647 for 8.21.

$$V_{out \text{ Red LED}}(V) = 1/(0.553557 + 0.357183 * \sqrt{(Oil ((cm)^2/l)))} \quad (8.20)$$

$$V_{out \text{ Green LED}}(V) = 1/(0.574694 + 0.245706 * \sqrt{(Oil ((cm)^2/l)))} \quad (8.21)$$

To obtain more reliable data from our prototype, we applied a Single ANOVA statistical procedure to the gathered data. Moreover, we reach two indicators: Reason-F and Value- P. The first one is used to determine whether from among a group of independent variables, at least one ability to explain a significant part of the variation of the dependent variable. Otherwise, Value-P is required to know if the obtained results are produced by random sampling, or they are statistically significant. When the Value-P is lower than 0.05, we can affirm that the observed differences are caused by differences in the samples and not to the randomness of the data. In this context, Table 8.9 presented the results of these two indicators for the five different wavelengths. Basing on the results shown in Table 8.9, we can confirm that all the tested light are capable of distinguishing and quantifying the amount of oil. Nevertheless, further analyses are required to evaluate if it is possible to distinguish between all tested concentrations of pollutant.

Table 8.8. Value of selected resistance for the different LEDs.

LED	Yellow	Red	Blue	Green	White
Resistance (k Ω)	75.5	429.6	49.6	70.8	11.1

Table 8.9. Results of statistical ANOVA tests to analyse measured values.

LED	Yellow	Red	Blue	Green	White
Reason- F	354.28	1745975.11	5732.62	175727.47	7110.87
Value-P	0.0000	0.0000	0.0000	0.0000	0.0000

We performed a multirange analysis with the values of the different LEDs. In Figure 8.28, we classify the different range of industrial oil according to the different groups with an interval of confidence of 95%. The value of the blue bar is the average of the three measurements taken. The values of the black lines are the standard deviation for each sample. Finally, the letter indicates the group in which they are classifying with a 95% confidence interval. The groups are performed according to the Least significant difference of Fisher. With the obtained data of V_{out} with the yellow LED, it is possible to differentiate all the tested oil concentrations. Nevertheless, we can see that the value of V_{out} in 0.15 ml oil/cm² does not follow the same trend that the other gathered data (this value increases instead of decreasing). This trend is also observed in the other series of data. In addition, the yellow LED has lower voltage changes between the different concentrations than the red and green LEDs. In the case of the blue and white LEDs, the gathered V_{out} cannot be used to differentiate in concentrations higher than 5 ml of industry oil. With regards to the data gathered with the blue light only 0.1 and 0.2 ml oil cm² are in the same group. With respect to the white light except for the 0.1 and 0.15 ml oil cm², all concentrations are in different groups. Finally, in the case of the data obtained with the red and green light, all concentrations tested are classified as different groups. Nonetheless, in concentrations higher than 0.1 ml oil/cm², the V_{out} values remain similar for the green and red LEDs. The V_{out} obtained with the red and green LEDs have a difference between the maximum and minimum tested pollution levels up to 0.27 V. Though, the red light has a higher correlation than green light. Moreover, with the data gathered with the red LED can difference between 1 and 2.5 ml of industry oil, while the data from the green LED cannot do it.

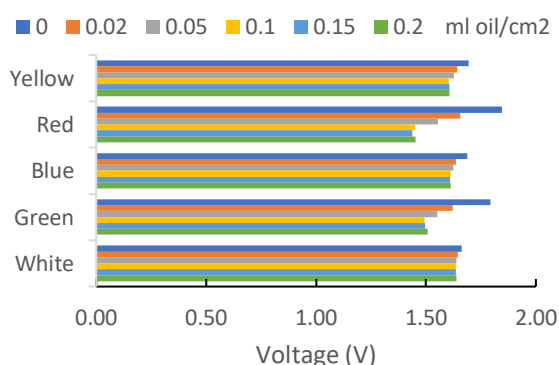


Figure 8.27. Values of V_{out} of the LDR in the different LED colours.

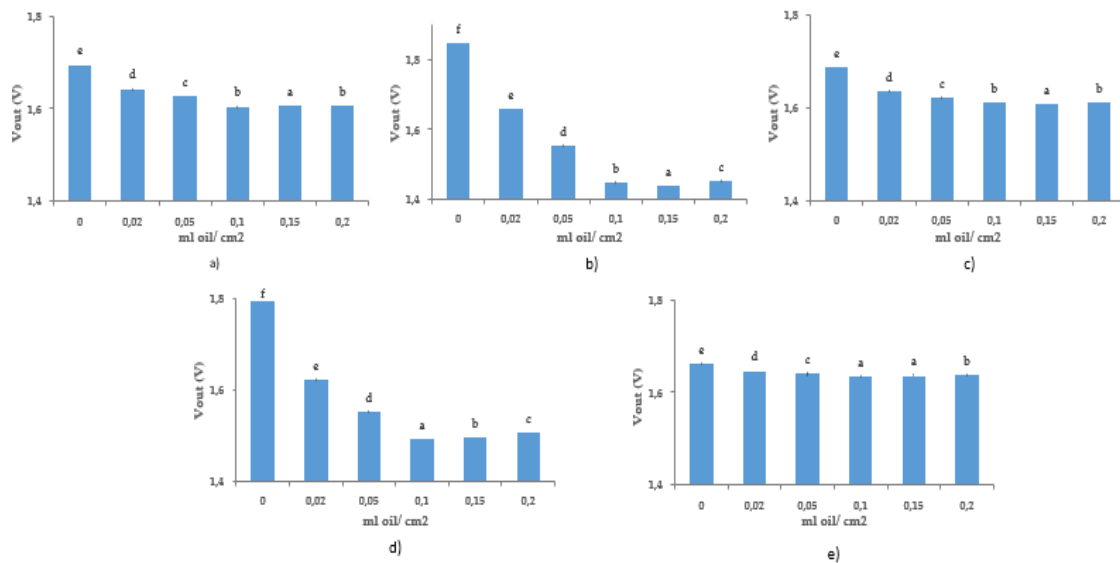


Figure 8.28. Voltage out of the different LEDs, groups classification with a confidence interval of 95% and standard deviation. (a) Yellow (b) Red (c) Blue (d) Green (e) White.

8.5. Conclusions

We have studied the use of inductive sensors to monitor the soil moisture, the use of optical sensor to detect dyed fuels in vehicles, the use of biosoption and sensors to control the irrigation water, and the use of oil sensor in an irrigation channel.

The use of inductive sensor is an option to monitor the soil moisture. The need for soil moisture monitoring is crucial in achieving sustainability in water usage. Many systems were developed for minimizing the water waste in irrigation. However, the high cost of the commercial sensors is curbing their implementation in the urban lawns and agriculture fields. Those smart irrigation systems are only used nowadays in some greenhouses and other specific places where precision agriculture is applied. We presented a solution based on the use of EFs generated by inductive coils to measure the water content of the soil. The sensor is based on the mutual inductance effect and is composed of two solenoids. A total of 15 different prototypes were tested in the first test to find a prototype with a high V_{out} , high Δ of V_{out} between different moisture levels, different V_{out} for all the tested moisture samples, and a low WF. The prototypes chosen for enhancement were P5, P8, and P9. Then, we tested prototypes P5, P8, and P9 in 5 types of soils. P5 exhibited good results for S1 and S2. However, it was not suitable for the other soil types. P8 was the optimal one for S3, S4, and S5. Unfortunately, P9 seemed to perform well only for S1. Finally, based on P8, we developed four new prototypes (NP1-NP4) used in the second set of tests. The best prototypes were NP1 (at frequency 750 kHz) and NP2 (at frequencies 490 kHz and 500 kHz). Therefore, we performed the verification with these prototypes. The verification tests indicate a minimal error in the moisture value of 53.9 %, with a RE of 0.6 % for NP1. In the case of NP2, two verifications were carried out, one using a single model and the second with two models. In the first case, the maximum error is 25.5 % and 21.5 % in soil moisture in 490 kHz, 500 kHz, respectively. In the two frequencies, the mean of the RE is 6.5 % for 490 kHz and 6.2 % for 500 kHz. The results indicate that NP2 with the two mathematical models is the most suitable one for monitoring irrigation.

The use of dyed fuels in particular vehicles is a crime. Nowadays, the hydrocarbons are the main source of energy for the transport of freight and people. These have taxes associated. Though some activities are exempt from paying these taxes or these are not so high. For these activities, there are dyed fuels with low taxes. The use of these fuels in an illegitimate way supposes a cost for the governments. Therefore, in this paper, we showed an IoT sensor for use in smart cities to avoid the fraudulent use of coloured diesel. The sensor proposed in this paper is based on a new methodology to detect dyed fuels. The main advantages of the proposed sensors are its low cost and the ease of use of the sensor. The main disadvantage is that the sensor is only tested with the dyed used in Europe. Thus, the sensor can be used only in Europe. The sensor is based on light absorption effect with different colours (green, white, yellow and blue). This sensor is inserted into the tank of the car to check if the gasoline contains this coloured or not. If it is a message is sent to the server of the police to take the appropriate measures.

The irrigation channels can receive the wastewater and treated wastewater with insufficient quality for use in agriculture. Therefore, the use of tertiary treatments such as bioabsorption is a solution to reduce the load of pollutants. To prevent overuse of bioabsorption, a system is proposed that, through the use of WSN, is capable of monitoring the load of contaminants and thus subjecting that water to tertiary treatment.

The detection and quantification of oil pollution in water of irrigation channels is vital to ensure proper water quality in PA. The physical sensors based on the optical phenomenon (such as light absorption, reflection, refraction, etc.) are the most appropriated method for water monitoring. In this paper, we developed and calibrated a sensor for monitoring the presence of industrial oil in the irrigation system. Our prototype is based on LEDs as a light source and LDRs and photodiode as light detectors. We discard the use of LDR at 180° to the light source. The presence of oil stains on the surface causes considerable changes in the light that affects the light detectors at 180°. Nonetheless, the data gathered with light detectors placed at 360° from the light source offers reliable information. The infrared light sources were discarded due to its low interaction with the tested samples. Among the different LEDs tested, the best results are gathered with the red LED.

Finally, work presented in this chapter has been published in the following references (Basterrechea, 2021), (Rocher, 2018), (Rocher, 2018).

9 Conclusions.

9.1 Conclusions.

Throughout this dissertation, we have presented the development of a WSN to monitor sewerage and water bodies to detect the presence of illicit discharges.

First, we analyse WSN systems that are now used in sewerage. We determined that the parameters easier to monitor are turbidity, conductivity, presence of oil, and temperature. In addition, we use a rain sensor and distance sensor (determine water level) to detect the presence of rain to determine the different scenarios of storm sewerage and the presence of overflow or blockage. Nowadays, there are low cost sensors to monitor temperature, rain and distance. For this reason, these sensors are not developed. However, the other parameters do not have a commercial low cost solution that can be applied to our system.

First, we study the effect of solids and water level in the inductive sensors used to determine the conductivity. Our results show that the two parameters studied affect the induced voltage in the IC. However, in the case of solids, this effect is low because, in the prototype with more difference between the concentration of 0 mg/L and 5000 mg/L, the increase of induced voltage is approximately 0.078 V/gram. It is not expected to find concentrations of solids that significantly change the induced voltage. Secondly, the water level presents an important change in the induced voltage of the IC. For this reason, this type of sensor must permanently be submerged in water to obtain reliable conductivity values.

Another studied sensor is the turbidimeter. We developed two turbidimeters, one for water bodies and another for sewerage. On the one hand, turbidimeters developed for water bodies can quantify the % of algae or sediment in the sample. On the other hand, we studied a turbidimeter with the photoreceptor at 0°. Our results suggest that the water height does not significantly affect the sensor.

For the oil sensor, we developed an optical sensor. We located the sensor down the sample with water. We test with different colour LEDs and observe that depending on the oil source, we can quantify it. In the case of oil used in a diesel engine, we cannot quantify the concentration. However, the oil concentration can be quantified in the case of used oil in a gasoline engine. In addition, we can differentiate between the used oil by a gasoline engine and the diesel engine.

We test the conductivity and oil sensor in a pipe. In addition, we simulated the water levels in sewerage. Our results suggested that we can monitor the presence of oil and conductivity in the pipe. In the case of water levels, the presence of PIs cannot be detected by the quantity of water in the pipe. However, the presence of blockage can be detected.

Finally, we presented the characteristics of our proposal. We used a star topology with a CH with a LoRa as technology for communication. The cost of our proposal is 120 euros per sensor node.

In the time that I developed this dissertation, I developed other works with the use of sensors. The first one was to monitor the moisture in soil using inductive sensors, the second one allowed to detect the presence of dyed diesel in the cars and the last one was used jointly with bioabsorption to control the irrigation water.

9.2 Future Work.

In this PhD thesis, we developed a proposal to monitor the sewerage and water bodies to detect PIs in sewerage. The main future work will test the different sensors and the proposal in real conditions. The idea is to increase the Technology Readiness Level (TRL) from level 4 to level 7. A TRL 4 implies that the technology is validated at the laboratory, TRL 5 is that they are

tested in a relevant environment, TRL 6 means that it is demonstrated in relevant environments, and TRL 7 implies that technology is demonstrated in an operational environment.

We want to improve the turbidity sensor so that it responds better to the NTU, for this, we will test other positions of the photoreceptor and other configurations of resistances, distance, etc.

Some of the sensors developed in this dissertation can be applied in other environments. It is the case of the inductive sensors to monitor the concentration of solids in mechanical dehydration. In the dehydration, there are two effluents, one with a high solid concentration (between 15 to 30% of solid concentration), and another with a low solid concentration. The value of induction is in the function of the solid concentration and conductivity. Probably, we can determine the solid concentration in the sludge.

Another future work is in the secondary clarifier in WWTP. In secondary clarifiers, the sludge sedimented as hindered settling. Therefore, there is an interface between water with a low concentration of solids and water with a high concentration of solids. With the use of low-cost turbidity sensors, such as the one developed, a sensor can be developed that determines if the sludge has reached a certain level to control internal recirculation from the clarifier and to detect sedimentation problems in the sludge.

9.3 Problems Faced and Personal Contributions.

In the development of this PhD thesis, I have encountered a series of problems. The first is the global pandemic. It forced me to be locked up in my home without being able to develop my PhD thesis. Another problem was my background. I studied environmental science and a master in environmental engineering. Before starting the dissertation, my background in electronics or computer networks was non-existent.

Another problem is developing a sensor to detect leaks in a pipe. We used an accelerometer to detect the presence of leaks, but our results were unsuccessful, so I wasted much time on it.

9.4 Publications derived from the PhD.

Journal Papers:

Basterrechea, D.A., **Rocher**, J., Parra, L. and Lloret, J. (2021). Low-Cost System Based on Optical Sensor to Monitor Discharge of Industrial Oil in Irrigation Ditches. *Sensors*, 21(16), p.5449. doi:10.3390/s21165449.

Rocher, J., Parra, L., Jimenez, J.M., Lloret, J. and Basterrechea, D.A. (2021a). Development of a Low-Cost Optical Sensor to Detect Eutrophication in Irrigation Reservoirs. *Sensors*, 21(22). doi:10.3390/s21227637.

Basterrechea, D.A., **Rocher**, J., Parra, M., Parra, L., Marin, J.F., Mauri, P.V. and Lloret, J. (2021b). Design and Calibration of Moisture Sensor Based on Electromagnetic Field Measurement for Irrigation Monitoring. *Chemosensors*, 9(9), p.251. doi:10.3390/chemosensors9090251.

Rocher, J., Parra, M., Parra, L., Sendra, S., Lloret, J. and Mengual, J. (2021b). A Low-Cost Sensor for Detecting Illicit Discharge in Sewerage. *Journal of Sensors*, 2021, pp.1–16. doi:10.1155/2021/6650157.

Rocher, J., Rego, A., Lloret, J. and Oliveira, L.M.L. (2022). Use of wireless sensor network system based on water level, rain, conductivity, oil and turbidity sensors to monitor the storm sewerage. *IET Wireless Sensor Systems*, 12((3-4)), pp.103–121. doi:10.1049/wss2.12040.

Rocher, J., Aldegheishem, A., Alrajeh, N. and Lloret, J. (2022). Develop an Optical Sensor to Detect Pollution Incidents in Sewerage. *IEEE Sensors Journal*, doi: 10.1109/JSEN.2022.3219931. (Early acces)

Conference papers:

Rocher, J., Sendra, S., Parra, L., Lloret, J. and Shu, L. (2018). Low Cost Sensor to Measure Solid Concentrations in Wastewater. In: *IECON 2018 - 44th Annual Conference of the IEEE Industrial Electronics Society*. IEEE. doi:10.1109/iecon.2018.8591149.

Rocher, J., Parra, L., Lloret, J. and Mengual, J. (2018a). An Inductive Sensor for Water Level Monitoring in Tubes for Water Grids. In: *2018 IEEE/ACS 15th International Conference on Computer Systems and Applications (AICCSA)*. 2018 IEEE/ACS 15th International Conference on Computer Systems and Applications (AICCSA). IEEE. doi:10.1109/aiccsa.2018.8612845.

Rocher, J., Taha, M., Parra, L. and Lloret, J. (2018c). IoT Sensor to Detect Fraudulent Use of Dyed Fuels in Smart Cities. In: *2018 Fifth International Conference on Internet of Things: Systems, Management and Security*. 2018 Fifth International Conference on Internet of Things: Systems, Management and Security. IEEE. doi:10.1109/iotsms.2018.8554631.

Rocher, J., Garcia-Navas, J.L., Romero, O. and Lloret, J. (2019b). A WSN-based Monitoring System to Control Sewerage. In: *2019 Sixth International Conference on Internet of Things: Systems, Management and Security (IOTSMS)*. 2019 Sixth International Conference on Internet of Things: Systems, Management and Security (IOTSMS). IEEE. doi:10.1109/iotsms48152.2019.8939269.

Basterrechea, D.A., **Rocher, J.**, Parra, L. and Lloret, J. (2020c). Development of Optical Sensor to detect Industrial Oil in Agricultural Irrigation System. In: *2020 Global Congress on Electrical Engineering (GC-ElecEng)*. 2020 Global Congress on Electrical Engineering (GC-ElecEng). IEEE. doi:10.23919/gc-eleceng48342.2020.9285981.

Basterrechea, D.A., **Rocher, J.**, Parra, L. and Lloret, J. (2020b). Development of Inductive Sensor for Control Gate Opening of an Agricultural Irrigation System. In: *2020 Fifth International Conference on Fog and Mobile Edge Computing (FMEC)*. 2020 Fifth International Conference on Fog and Mobile Edge Computing (FMEC). IEEE. doi:10.1109/fmec49853.2020.9144810.

Rocher, J., Basterrechea, D. A., Fawzy, M., Lloret, J., & Omar, M. Y. (2020). Sensors and Biosorption for Better Reuse of Wastewater. In E. M. (Ed.), *Advances in Intelligent Systems and Computing* (pp. 321–330). Springer. https://doi.org/10.1007/978-3-030-36664-3_36

Basterrechea, D.A., **Rocher**, J., Parra, L. and Lloret, J. (2020c). Development of Optical Sensor to detect Industrial Oil in Agricultural Irrigation System. In: *2020 Global Congress on Electrical Engineering (GC-ElecEng)*. IEEE. doi:10.23919/gc-eleceng48342.2020.9285981

Reference

- 3GPP (2016). *Standards for the IoT*. [online] 3GPP. Available at: https://www.3gpp.org/news-events/1805-iot_r14 [Accessed 30 Sep. 2021].
- Abbas, O., Abou Rjeily, Y., Sadek, M. and Shahrour, I. (2017). A large-scale experimentation of the smart sewage system. *Water and Environment Journal*, 31(4), pp.515–521. doi:10.1111/wej.12273.
- Agocs, A., Budnyk, S., Frauscher, M., Ronai, B., Besser, C. and Dörr, N. (2020). Comparing oil condition in diesel and gasoline engines. *Industrial Lubrication and Tribology*, 72(8), pp.1033–1039. doi:10.1108/ilt-10-2019-0457.
- Ai, S., Gao, M., Yang, Y., Li, J. and Jin, L. (2004). Electrochemical Sensor for the Determination of Chemical Oxygen Demand Using a Lead Dioxide Modified Electrode. *Electroanalysis*, 16(5), pp.404–409. doi:10.1002/elan.200302839.
- Alahi, M.E.E. and Mukhopadhyay, S.C. (2019). Literature Review. In: *Preparation and Characterization of the Selectivity Material of Nitrate Sensor*. Springer, pp.7–41. doi:10.1007/978-3-030-20095-4_2.
- Albuquerque, J.S., Pimentel, M.F., Silva, V.L., Raimundo, I.M., Rohwedder, J.J.R. and Pasquini, C. (2004). Silicone Sensing Phase for Detection of Aromatic Hydrocarbons in Water Employing Near-Infrared Spectroscopy. *Analytical Chemistry*, 77(1), pp.72–77. doi:10.1021/ac0495788.
- Alsan, M. and Goldin, C. (2019). Watersheds in Child Mortality: The Role of Effective Water and Sewerage Infrastructure, 1880–1920. *Journal of Political Economy*, 127(2), pp.586–638. doi:10.1086/700766.
- Alvarado-Méndez, E., Rojas-Laguna, R., Andrade-Lucio, J.A., Hernández-Cruz, D., Lessard, R.A. and Avina-Cervantes, J.G. (2005). Design and characterization of pH sensor based on sol-gel silica layer on plastic optical fiber. *Sensors and Actuators B: Chemical*, 106(2), pp.518–522. doi:10.1016/j.snb.2004.07.020.
- Antonio-Lopez, J.E., Sanchez-Mondragon, J.J., LiKamWa, P. and May-Arrijoja, D.A. (2011). Fiber-optic sensor for liquid level measurement. *Optics Letters*, 36(17), pp.3425–3427. doi:10.1364/ol.36.003425.
- Aragay, G., Pons, J. and Merkoçi, A. (2011). Enhanced electrochemical detection of heavy metals at heated graphite nanoparticle-based screen-printed electrodes. *Journal of Materials Chemistry*, 21(12), p.4326. doi:10.1039/c0jm03751f.
- Arman Kuzubasoglu, B. and Kursun Bahadır, S. (2020). Flexible temperature sensors: A review. *Sensors and Actuators A: Physical*, 315(1), p.112282. doi:10.1016/j.sna.2020.112282.

- Arslan, N. (2018). Assessment of oil spills using Sentinel 1 C-band SAR and Landsat 8 multispectral sensors. *Environmental Monitoring and Assessment*, 190(11). doi:10.1007/s10661-018-7017-4.
- Aulinas, M., Tolchinsky, P., Turon, C., Poch, M. and Cortés, U. (2012). Argumentation-based framework for industrial wastewater discharges management. *Engineering Applications of Artificial Intelligence*, 25(2), pp.317–325. doi:10.1016/j.engappai.2011.09.016.
- Bai, Y., Bian, C., Xia, S., Tong, J. and Wang, J. (2014). Electrochemical microsensor based on gold nanoparticles modified electrode for total phosphorus determinations in water. In: *The 8th Annual IEEE International Conference on Nano/Micro Engineered and Molecular Systems*. IEEE, pp.31–36. doi:10.1049/iet-nbt.2013.0041.
- Barnstable County (2015). *Components of Waste Water : Barnstable County Department of Health and Environment*. [online] Barnstable county health. Available at: <https://www.barnstablecountyhealth.org/health-topics/wastewater/components-of-wastewater> [Accessed 7 Mar. 2022].
- Basterrechea, D.A., Parra, L., Botella-Campos, M., Lloret, J. and Mauri, P.V. (2020a). New Sensor Based on Magnetic Fields for Monitoring the Concentration of Organic Fertilisers in Fertigation Systems. *Applied Sciences*, 10(20), p.7222. doi:10.3390/app10207222.
- Basterrechea, D.A., Rocher, J., Parra, L. and Lloret, J. (2020b). Development of Inductive Sensor for Control Gate Opening of an Agricultural Irrigation System. In: *Proceedings of the 2020 Fifth International Conference on Fog and Mobile Edge Computing (FMEC)*. 2020 Fifth International Conference on Fog and Mobile Edge Computing (FMEC). IEEE, pp.250–255. Available at: <https://doi.org/10.1109/FMEC49853.2020.9144810>.
- Basterrechea, D.A., Rocher, J., Parra, L. and Lloret, J. (2020c). Development of Optical Sensor to detect Industrial Oil in Agricultural Irrigation System. In: *2020 Global Congress on Electrical Engineering (GC-ElecEng)*. 2020 Global Congress on Electrical Engineering (GC-ElecEng). IEEE. doi:10.23919/gc-eleceng48342.2020.9285981.
- Basterrechea, D.A., Rocher, J., Parra, L. and Lloret, J. (2021a). Low-Cost System Based on Optical Sensor to Monitor Discharge of Industrial Oil in Irrigation Ditches. *Sensors*, 21(16), p.5449. doi:10.3390/s21165449.
- Basterrechea, D.A., Rocher, J., Parra, M., Parra, L., Marin, J.F., Mauri, P.V. and Lloret, J. (2021b). Design and Calibration of Moisture Sensor Based on Electromagnetic Field Measurement for Irrigation Monitoring. *Chemosensors*, 9(9), p.251. doi:10.3390/chemosensors9090251.
- Been, F., Rossi, L., Ort, C., Rudaz, S., Delémont, O. and Esseiva, P. (2014). Population Normalization with Ammonium in Wastewater-Based Epidemiology: Application to Illicit

- Drug Monitoring. *Environmental Science & Technology*, 48(14), pp.8162–8169.
doi:10.1021/es5008388.
- Berounsky, V.M., Travers, H. and Reynolds, K. (2018). Canine Detection of Fecal Coliform Bacteria from Human Sources in the Pettaquamscutt Estuary, RI - Preliminary Results. In: *OCEANS 2018 MTS/IEEE Charleston*. OCEANS 2018 MTS/IEEE Charleston. IEEE, pp.1–10. doi:10.1109/OCEANS.2018.8604706.
- Berte, D.-R. (2018). Defining the IoT. In: *Proceedings of the International Conference on Business Excellence*. 12th International Conference on Business Excellence. Sciendo, pp.118–128. doi:10.2478/picbe-2018-0013.
- Bigham Stephens, D.L., Carlson, R.E., Horsburgh, C.A., Hoyer, M.V., Bachmann, R.W. and Canfield, D.E. (2015). Regional distribution of Secchi disk transparency in waters of the United States. *Lake and Reservoir Management*, 31(1), pp.55–63.
doi:10.1080/10402381.2014.1001539.
- Bilro, L., Prats, S.A., Pinto, J.L., Keizer, J.J. and Nogueira, R.N. (2010). Design and performance assessment of a plastic optical fibre-based sensor for measuring water turbidity. *Measurement Science and Technology*, 21(10). doi:10.1088/0957-0233/21/10/107001.
- Bishnoi, S.W., Rozell, C.J., Levin, C.S., Gheith, M.K., Johnson, B.R., Johnson, D.H. and Halas, N.J. (2006). All-Optical Nanoscale pH Meter. *Nano Letters*, 6(8), pp.1687–1692.
doi:10.1021/nl060865w.
- Bolan, N.S. and Kandaswamy, K. (2005). pH. In: *Encyclopedia of Soils in the Environment*. Elsevier, pp.196–202. doi:10.1016/b0-12-348530-4/00210-1.
- Brown, E., Caraco, D. and Pitt, R. (2004). *Illicit discharge detection and elimination : a guidance manual for program development and technical assessments*. [online] Washington, D.C.: Water Permits Division, Office Of Water And Wastewater, U.S. Environmental Protection Agency. Available at:
https://www3.epa.gov/npdes/pubs/idde_manualwithappendices.pdf [Accessed 21 Feb. 2022].
- Buras, M.P. and Solano Donado, F. (2021). Identifying and Estimating the Location of Sources of Industrial Pollution in the Sewage Network. *Sensors*, 21(10). doi:10.3390/s21103426.
- Cambridge University Press (2022). *Cambridge Dictionary | English Dictionary, Translations & Thesaurus*. [online] Cambridge.org. Available at: <https://dictionary.cambridge.org/> [Accessed 22 Oct. 2022].

- Campbell (2022). *OBS501 - Smart Turbidity Meter with Antifouling Features*. [online] www.campbellsci.es. Available at: <https://www.campbellsci.es/obs501> [Accessed 18 Feb. 2022].
- Cao, Y.-H., You, J.-X. and Liu, H.-C. (2017). Optimal Environmental Regulation Intensity of Manufacturing Technology Innovation in View of Pollution Heterogeneity. *Sustainability*, 9(7), p.1240. doi:10.3390/su9071240.
- Carlson, D.F., Pavalko, W.J., Petersen, D., Olsen, M. and Hass, A.E. (2020). Maker Buoy Variants for Water Level Monitoring and Tracking Drifting Objects in Remote Areas of Greenland. *Sensors*, 20(5), p.1254. doi:10.3390/s20051254.
- Carminati, M. and Luzzatto-Fegiz, P. (2017). Conduino: Affordable and high-resolution multichannel water conductivity sensor using micro USB connectors. *Sensors and Actuators B: Chemical*, 251, pp.1034–1041. doi:10.1016/j.snb.2017.05.184.
- Carstea, E.M., Bridgeman, J., Baker, A. and Reynolds, D.M. (2016). Fluorescence spectroscopy for wastewater monitoring: A review. *Water Research*, 95, pp.205–219. doi:10.1016/j.watres.2016.03.021.
- CDC (2019). *Agricultural Water*. Available at: <https://www.cdc.gov/healthywater/other/agricultural/index.html> [Accessed 21 Feb. 2022].
- Chachuła, K., Nowak, R. and Solano, F. (2021). Pollution Source Localization in Wastewater Networks. *Sensors*, 21. doi:10.3390/s21030826.
- Chanson, H., Takeuchi, M. and Trevethan, M. (2008). Using turbidity and acoustic backscatter intensity as surrogate measures of suspended sediment concentration in a small subtropical estuary. *Journal of Environmental Management*, 88(4), pp.1406–1416. doi:10.1016/j.jenvman.2007.07.009.
- Chen, Z., Guo, Q. and Shi, Z. (2013). Design of WSN node for water pollution remote monitoring. *Telecommunication Systems*, 53(1), pp.155–162. doi:10.1007/s11235-013-9689-y.
- Cheng, Q., Wu, C., Chen, J., Zhou, Y. and Wu, K. (2011). Electrochemical Tuning the Activity of Nickel Nanoparticle and Application in Sensitive Detection of Chemical Oxygen Demand. *The Journal of Physical Chemistry C*, 115(46), pp.22845–22850. doi:10.1021/jp207442u.
- Chetpattananondh, K., Tapoanoi, T., Phukpattaranont, P. and Jindapetch, N. (2014). A self-calibration water level measurement using an interdigital capacitive sensor. *Sensors and Actuators A: Physical*, 209, pp.175–182. doi:10.1016/j.sna.2014.01.040.

- Choi, J.-Y., Seo, K., Cho, S.-R., Oh, J.-R., Kahng, S.-H. and Park, J. (2001). Screen-printed anodic stripping voltammetric sensor containing HgO for heavy metal analysis. *Analytica Chimica Acta*, 443(2), pp.241–247. doi:10.1016/s0003-2670(01)01219-3.
- Chourabi, H., Nam, T., Walker, S., Gil-Garcia, J.R., Mellouli, S., Nahon, K., Pardo, T.A. and Jochen Scholl, H. (2012). Understanding smart cities: An integrative framework. In: *2012 45th Hawaii International Conference on System Sciences*. 45th Hawaii International Conference on System Sciences. IEEE. <https://doi.org/10.1109/HICSS.2012.615>.
- Clean Water Act (1972). Chapter 26—Water Pollution Prevention And Control. US EPA. [online] Available at: <https://www.epa.gov/laws-regulations/summary-clean-water-act>.
- Cole-Parmer (2021). *Wastewater Treatment Process Steps from Cole-Parmer*. [online] Coleparmer.com. Available at: <https://www.coleparmer.com/tech-article/eight-stages-of-wastewater-treatment-process> [Accessed 1 Mar. 2022].
- Congaree riverkeeper (2020). *Congaree Riverkeeper / About Us*. [online] www.congareeriverkeeper.org. Available at: <https://www.congareeriverkeeper.org/about-congaree-riverkeeper-south-carolina> [Accessed 7 Mar. 2022].
- Cosnier, S., Da Silva, S., Shan, D. and Gorgy, K. (2008). Electrochemical nitrate biosensor based on poly(pyrrole–viologen) film–nitrate reductase–clay composite. *Bioelectrochemistry*, 74(1), pp.47–51. doi:10.1016/j.bioelechem.2008.04.011.
- Cui, L., Wu, J. and Ju, H. (2015). Electrochemical sensing of heavy metal ions with inorganic, organic and bio-materials. *Biosensors and Bioelectronics*, 63, pp.276–286. doi:10.1016/j.bios.2014.07.052.
- Datarobot (2022). *Nutonian*. [online] DataRobot AI Cloud. Available at: <https://www.datarobot.com/nutonian/> [Accessed 18 Feb. 2022].
- Datta, S., Taghvaeian, S. and Stivers, J. (2017). *Understanding Soil Water Content and Thresholds for Irrigation Management*. [online] Oklahoma, USA: Oklahoma State University. Available at: <https://extension.okstate.edu/fact-sheets/understanding-soil-water-content-and-thresholds-for-irrigation-management.html> [Accessed 31 May 2019].
- Deblonde, T., Cossu-Leguille, C. and Hartemann, P. (2011). Emerging pollutants in wastewater: A review of the literature. *International Journal of Hygiene and Environmental Health*, 214(6), pp.442–448. doi:10.1016/j.ijheh.2011.08.002.
- Ding, L. (2017). Solid-contact Potentiometric Sensor for the Determination of Total Ammonia Nitrogen in Seawater. *International Journal of Electrochemical Science*, 12, pp.3296–3308. doi:10.20964/2017.04.01.

- Ding, Y., Wang, S., Li, J. and Chen, L. (2016). Nanomaterial-based optical sensors for mercury ions. *TrAC Trends in Analytical Chemistry*, 82, pp.175–190.
doi:10.1016/j.trac.2016.05.015.
- Directive 91/271/EEC of 21 May 1991 concerning urban waste-water treatment.*[online] Available at: <https://eur-lex.europa.eu/legal-content/EN/TXT/?uri=CELEX%3A31991L0271> [Accessed 10 Feb. 2022].
- Downing, J. (2006). Twenty-five years with OBS sensors: The good, the bad, and the ugly. *Continental Shelf Research*, 26(17-18), pp.2299–2318. doi:10.1016/j.csr.2006.07.018.
- Dutta, S., Sarma, D. and Nath, P. (2015). Ground and river water quality monitoring using a smartphone-based pH sensor. *AIP Advances*, 5(5), p.057151. doi:10.1063/1.4921835.
- Endress+Hauser (2018). *Turbimax CUS50D*. [online] Turbimax CUS50D. Available at: https://portal.endress.com/wa001/dla/5001112/2043/000/00/TI01395CEN_0118.pdf [Accessed 18 Feb. 2022].
- EPA (2003). *Licensing guidelines for sewage treatment systems*. [online] Sydney, (Australia): Environment Protection Authority. Available at: <https://www.epa.nsw.gov.au/-/media/epa/corporate-site/resources/epa/stslicensingguidelines.pdf> [Accessed 22 Feb. 2022].
- EPA (2004). *Primer for municipal wastewater treatment systems*. [online] Washington, Dc: U.S. Environmental Protection Agency, Office Of Water, Office Of Wastewater Management. Available at: <https://www.epa.gov/sites/default/files/2015-09/documents/primer.pdf> [Accessed 1 Mar. 2022].
- EPA (2014). *Storm Water Management Model (SWMM) | US EPA*. [online] EPA. Available at: <https://www.epa.gov/water-research/storm-water-management-model-swmm>.
- EPA (2016). *Report to Congress on Combined Sewer Overflows to the Great Lakes Basin Combined Sewer Overflows into the Great Lakes Basin*. [online] Environmental Protection Agency, pp.19–20. Available at: https://www.epa.gov/sites/default/files/2016-05/documents/gls_cso_report_to_congress_-_4-12-2016.pdf [Accessed 24 Feb. 2022].
- EPA (2021). *Managing and reporting environmental incidents*. [online] www.epa.ie. Available at: <https://www.epa.ie/our-services/compliance--enforcement/industry-and-waste-management/incidents/> [Accessed 2 Mar. 2022].
- EPSAR (2018). *Memoria de Gestión 2018*. [online] Available at: <http://www.epsar.gva.es/sanejament/quienes-somos/INFORME-DE-GESTION.pdf> [Accessed 27 May 2019].

- EPSAR (2020). 6. VERTIDOS INDUSTRIALES. In: *Memoria de Gestión 2020*. [online] pp.61–62. Available at: https://www.epsar.gva.es/sites/default/files/2021-06/Memoria%20de%20Gesti%C3%B3n%202020_firmado.pdf [Accessed 16 Feb. 2022].
- European Commission (2019). *Smart cities*. [online] European Commission. Available at: https://ec.europa.eu/info/eu-regional-and-urban-development/topics/cities-and-urban-development/city-initiatives/smart-cities_en [Accessed 7 Aug. 2022].
- FAO (2019). *1. Wastewater characteristics and effluent quality parameters*. [online] FAO. Available at: <http://www.fao.org/3/T0551E/t0551e03.htm> [Accessed 18 Feb. 2022].
- Faustine, A., Mvuma, A.N., Mongi, H.J., Gabriel, M.C., Tenge, A.J. and Kucel, S.B. (2014). Wireless Sensor Networks for Water Quality Monitoring and Control within Lake Victoria Basin: Prototype Development. *Wireless Sensor Network*, 06(12), pp.281–290. doi:10.4236/wsn.2014.612027.
- Ferrer Polo and Seco Torrecillas, A. (2007). *Tratamientos físicos y químicos de aguas residuales*. Valencia: Universidad Politécnica De Valencia.
- Fingas, M. and Brown, C. (2017). A Review of Oil Spill Remote Sensing. *Sensors*, 18(2), p.91. doi:10.3390/s18010091.
- Fisher, D.K. and Sui, R. (2013). An inexpensive open-source ultrasonic sensing system for monitoring liquid levels. *Agricultural Engineering International: CIGR Journal*, 15(4), pp.328–334.
- Forzani, E.S., Zhang, H., Chen, W. and Tao, N. (2005). Detection of Heavy Metal Ions in Drinking Water Using a High-Resolution Differential Surface Plasmon Resonance Sensor. *Environmental Science & Technology*, 39(5), pp.1257–1262. doi:10.1021/es049234z.
- Fujikura, M. (2011). Japan's Efforts Against the Illegal Dumping of Industrial Waste. *Environmental Policy and Governance*, 21(5), pp.325–337. doi:10.1002/eet.581.
- García, J.L., Parra, M., Parra, L., Rocher, J., Sendra, S. and Lloret, J. (2019). Practical Study of the Temperature Effect in Soil Moisture Measurements. In: *INNOV 2019 The Eighth International Conference on Communications, Computation, Networks and Technologies*. INNOV 2019 The Eighth International Conference on Communications, Computation, Networks and Technologies. IARIA XPS Press, pp.7–13.
- García, L., Jiménez, J.M., Taha, M. and Lloret, J. (2018). Wireless Technologies for IoT in Smart Cities. *Network Protocols and Algorithms*, 10(1), p.23. doi:10.5296/npa.v10i1.12798.
- García, M., Tomás, J., Boronat F., Lloret J., (2009). The Development of Two Systems for Indoor Wireless Sensors Self-location. *Ad Hoc Sens. Wirel. Networks*, 8 (3-4), p.235-258.

- Garrido, E., Camacho-Muñoz, D., Martín, J., Santos, A., Santos, J.L., Aparicio, I. and Alonso, E. (2016). Monitoring of emerging pollutants in Guadiamar River basin (South of Spain): analytical method, spatial distribution and environmental risk assessment. *Environmental Science and Pollution Research*, 23(24), pp.25127–25144. doi:10.1007/s11356-016-7759-x.
- Gippel, C.J. (1995). Potential of turbidity monitoring for measuring the transport of suspended solids in streams. *Hydrological Processes*, 9(1), pp.83–97. doi:10.1002/hyp.3360090108.
- Gong, W., Mowlem, M., Kraft, M. and Morgan, H. (2008). Oceanographic sensor for in-situ temperature and conductivity monitoring. In: *OCEANS 2008 - MTS/IEEE Kobe Techno-Ocean*. Oceans'08 MTS/IEEE KOBE-Techno-Ocean'08 (OTO'08). IEEE, pp.1–6.
- Gonzalez-Reyna, M.A., Alvarado-Mendez, E., Estudillo-Ayala, J.M., Vargas-Rodriguez, E., Sosa-Morales, M.E., Sierra-Hernandez, J.M., Jauregui-Vazquez, D. and Rojas-Laguna, R. (2015). Laser Temperature Sensor Based on a Fiber Bragg Grating. *IEEE Photonics Technology Letters*, 27(11), pp.1141–1144. doi:10.1109/lpt.2015.2406572.
- Gosling, S.N. and Arnell, N.W. (2013). A global assessment of the impact of climate change on water scarcity. *Climatic Change*, 134(3), pp.371–385. doi:10.1007/s10584-013-0853-x.
- Granlund, D. and Brännström, R. (2013). Smart City: The smart sewerage. In: *37th Annual IEEE Conference on Local Computer Networks - Workshops*.] 37th Annual IEEE Conference on Local Computer Networks. IEEE, pp.856–859. doi: 10.1109/LCNW.2012.6424074
- GSMA (2019). *Narrowband – Internet of Things (NB-IoT)*. [online] Gsma.com. Available at: <https://www.gsma.com/iot/narrow-band-internet-of-things-nb-iot/> [Accessed 26 Oct. 2022].
- Gupta, V.K. and Rastogi, A. (2008). Biosorption of lead from aqueous solutions by green algae *Spirogyra* species: Kinetics and equilibrium studies. *Journal of Hazardous Materials*, 152(1), pp.407–414. doi:10.1016/j.jhazmat.2007.07.028.
- Gutiérrez-Capitán, M., Baldi, A., Gómez, R., García, V., Jiménez-Jorquera, C. and Fernández-Sánchez, C. (2015). Electrochemical Nanocomposite-Derived Sensor for the Analysis of Chemical Oxygen Demand in Urban Wastewaters. *Analytical Chemistry*, 87(4), pp.2152–2160. doi:10.1021/ac503329a.
- Ha, N., Koike, K. and Nhuan, M. (2013). Improved Accuracy of Chlorophyll-a Concentration Estimates from MODIS Imagery Using a Two-Band Ratio Algorithm and Geostatistics: As Applied to the Monitoring of Eutrophication Processes over Tien Yen Bay (Northern Vietnam). *Remote Sensing*, 6(1), pp.421–442. doi:10.3390/rs6010421.
- Hancke, G.P., Silva, B. de C.E. and Hancke, G.P. (2012). The role of advanced sensing in smart cities. *Sensors (Basel, Switzerland)*, 13(1), pp.393–425. doi:10.3390/s130100393.

- Hauser, F.M., Metzner, T., Rößler, T., Pütz, M. and Krause, S. (2019). Real-time wastewater monitoring as tool to detect clandestine waste discharges into the sewage system. *Environmental Forensics*, 20(1), pp.13–25. doi:10.1080/15275922.2019.1566295.
- Hegab, H.M., ElMekawy, A., van den Akker, B., Ginic-Markovic, M., Saint, C., Newcombe, G. and Pant, D. (2018). Innovative graphene microbial platforms for domestic wastewater treatment. *Reviews in Environmental Science & Biotechnology*. 17(1), pp.147–158. doi:10.1007/s11157-018-9459-0.
- Hegazy, M.H. and Gawad, M.A. (2016). Measuring and Evaluating the Performance of a Wastewater Treatment Plant. In: *Proceedings of the World Congress on Civil, Structural, and Environmental Engineering*. World Congress on Civil, Structural, and Environmental Engineering (CSEE2016). Orléans, Canada: Avestia. doi:10.11159/awspt16.111.
- Hernández-Nolasco, J.A., Wister Ovando, M.A., Acosta, F.D. and Pancardo, P. (2016). Water Level Meter for Alerting Population about Floods. In: *2016 IEEE 30th International Conference on Advanced Information Networking and Applications (AINA)*. IEEE 30th International Conference on Advanced Information Networking and Applications (AINA). IEEE. doi: 10.1109/AINA.2016.76
- Hoes, O.A.C., Schilperoort, R.P.S., Luxemburg, W.M.J., Clemens, F.H.L.R. and van de Giesen, N.C. (2009). Locating illicit connections in storm water sewers using fiber-optic distributed temperature sensing. *Water Research*, 43(20), pp.5187–5197. doi:10.1016/j.watres.2009.08.020.
- Hossain, A., Canning, J., Ast, S., Rutledge, P.J., Yen, T.L. and Jamalipour, A. (2015). Lab-in-a-Phone: Smartphone-Based Portable Fluorometer for pH Measurements of Environmental Water. *IEEE Sensors Journal*, 15(9), pp.5095–5102. doi:10.1109/jsen.2014.2361651.
- Hou, Y., Li, Y., Liu, B., Liu, Y. and Wang, T. (2017). Design and Implementation of a Coastal-Mounted Sensor for Oil Film Detection on Seawater. *Sensors*, 18(2), p.70. doi:10.3390/s18010070.
- Hsu, T.-C., Teng, Y.-T., Yeh, Y.-W., Fan, X., Chu, K.-H., Lin, S.-H., Yeh, K.-K., Lee, P.-T., Lin, Y., Chen, Z., Wu, T. and Kuo, H.-C. (2021). Perspectives on UVC LED: Its Progress and Application. *Photonics*, 8(6), p.196. doi:10.3390/photonics8060196.
- Huang, W.-D., Cao, H., Deb, S., Chiao, M. and Chiao, J.C. (2011a). A flexible pH sensor based on the iridium oxide sensing film. *Sensors and Actuators A: Physical*, 169(1), pp.1–11. doi:10.1016/j.sna.2011.05.016.
- Huang, X., Pascal, R.W., Chamberlain, K., Banks, C.J., Mowlem, M. and Morgan, H. (2011b). A Miniature, High Precision Conductivity and Temperature Sensor System for Ocean

- Monitoring. *IEEE Sensors Journal*, 11(12), pp.3246–3252.
doi:10.1109/jsen.2011.2149516.
- Huang, Z., Long, J., Xu, W., Ji, H., Wang, B. and Li, H. (2012). Design of capacitively coupled contactless conductivity detection sensor. *Flow Measurement and Instrumentation*, 27, pp.67–70. doi:10.1016/j.flowmeasinst.2012.04.003.
- Hübner, M. and Minceva, M. (2020). Microfluidics approach for determination of the miscibility gap of multicomponent liquid-liquid systems. *Experimental Thermal and Fluid Science*, 112, p.109971. doi:10.1016/j.expthermflusci.2019.109971.
- Hur, J. and Cho, J. (2012). Prediction of BOD, COD, and Total Nitrogen Concentrations in a Typical Urban River Using a Fluorescence Excitation-Emission Matrix with PARAFAC and UV Absorption Indices. *Sensors*, 12(1), pp.972–986. doi:10.3390/s120100972.
- Ichinose, D. and Yamamoto, M. (2011). On the relationship between the provision of waste management service and illegal dumping. *Resource and Energy Economics*, 33(1), pp.79–93. doi:10.1016/j.reseneeco.2010.01.002.
- IEEE (2001). *[hibernating] IEEE 802.16 Working Group on Broadband Wireless Access Standards*. [online] IEEE802. Available at: <https://www.ieee802.org/16/> [Accessed 30 Sep. 2021].
- IEEE (2014). *IEEE 802.11, The Working Group Setting the Standards for Wireless LANs*. [online] www.ieee802.org. Available at: <https://www.ieee802.org/11/> [Accessed 30 Sep. 2021].
- IEEE (2018). *Welcome to the IEEE 802.1 Working Group*. [online] [Ieee802.org](http://www.ieee802.org). Available at: <https://1.ieee802.org/> [Accessed 30 Sep. 2021].
- IEEE (2020). *IEEE 802.15.4-2020 - IEEE Standard for Low-Rate Wireless Networks*. [online] standards.ieee.org. Available at: https://standards.ieee.org/standard/802_15_4-2020.html [Accessed 30 Sep. 2021].
- Ignatev, A. and Tuhkanen, T. (2019). Monitoring WWTP performance using size-exclusion chromatography with simultaneous UV and fluorescence detection to track recalcitrant wastewater fractions. *Chemosphere*, 214, pp.587–597.
doi:10.1016/j.chemosphere.2018.09.099.
- Iler, A.L. and Hamilton, P.D. (2015). Detecting oil on water using polarimetric imagin. In: *Ocean Sensing and Monitoring VII*. SPIE DEFENSE + SECURITY. SPIE.
- Iloms, E., Ololade, O.O., Ogola, H.J.O. and Selvarajan, R. (2020). Investigating Industrial Effluent Impact on Municipal Wastewater Treatment Plant in Vaal, South Africa. *International Journal of Environmental Research and Public Health*, 17(3), p.1096.
doi:10.3390/ijerph17031096.

- Irvine, K., Rossi, M.C., Vermette, S., Bakert, J. and Kleinfelder, K. (2011). Illicit discharge detection and elimination: Low cost options for source identification and trackdown in stormwater systems. *Urban Water Journal*, 8(6), pp.379–395. doi:10.1080/1573062x.2011.630095.
- Islam, S., Reza, M.N., Jeong, J.-T. and Lee, K.-H. (2016). Sensing Technology for Rapid Detection of Phosphorus in Water: A Review. *Journal of Biosystems Engineering*, 41(2), pp.138–144. doi:10.5307/jbe.2016.41.2.138.
- ISO (2011). *Information Technology—Radio Frequency Identification (RFID) for Item Management—Application Protocol: Encoding and Processing Rules for Sensors and Batteries*. [online] ISO. Available at: <https://www.iso.org/standard/51144.html> [Accessed 30 Sep. 2021].
- Jin, J., Gubbi, J., Marusic, S. and Palaniswami, M. (2014). An Information Framework for Creating a Smart City Through Internet of Things. *IEEE Internet of Things Journal*, 1(2), pp.112–121. doi:10.1109/jiot.2013.2296516.
- Jondhale, S.R., Maheswar, R. and Lloret, J. (2022). Fundamentals of Wireless Sensor Networks. In: *Received Signal Strength Based Target Localization and Tracking Using Wireless Sensor Networks*. Cham, Switzerland: EAI/Springer Innovations in Communication and Computing, pp.1–19. doi: 10.1007/978-3-030-74061-0_1
- Juarez-Leon, F.A., Soriano-Sánchez, A.G., Rodríguez-Licea, M.A. and Perez-Pinal, F.J. (2020). Design and Implementation of a Germicidal UVC-LED Lamp. *IEEE Access*, 8, pp.196951–196962. doi:10.1109/ACCESS.2020.3034436.
- Kandur, Y., Harms, J. and Kern, T.A. (2021). Uncertainty Analysis for Low-Cost Transformer-Type Inductive Conductivity Sensors. *Engineering Proceedings*, 6(1), p.52. doi:10.3390/i3s2021dresden-10145.
- Kang Hui, S., Jang, H., Kim Gum, C., Yu Song, C. and Kim Yong, H. (2020). A new design of inductive conductivity sensor for measuring electrolyte concentration in industrial field. *Sensors and Actuators A: Physical*, 301(1). doi:10.1016/j.sna.2019.111761.
- Khanafer, M., Guennoun, M. and Mouftah, H.T. (2009). WSN Architectures for Intelligent Transportation Systems. In: *2009 3rd International Conference on New Technologies, Mobility and Security*. IEEE. doi:10.1109/ntms.2009.5384685.
- Kim, C., Eom, J., Jung, S. and Ji, T. (2016). Detection of Organic Compounds in Water by an Optical Absorbance Method. *Sensors*, 16(1). doi:10.3390/s16010061.
- Kim, T.Y. and Yang, S. (2014). Fabrication method and characterization of electrodeposited and heat-treated iridium oxide films for pH sensing. *Sensors and Actuators B: Chemical*, 196, pp.31–38. doi:10.1016/j.snb.2014.02.004.

- Kim, Y.-C., Sasaki, S., Yano, K., Ikebukuro, K., Hashimoto, K. and Karube, I. (2001). Photocatalytic sensor for the determination of chemical oxygen demand using flow injection analysis. *Analytica Chimica Acta*, 432(1), pp.59–66. doi:10.1016/s0003-2670(00)01145-4.
- Kirhensteine, I., Cherrier, V., Jarrit, N., Farmer, A., Paoli, G. de, Delacamera, G. and Psomas, A. (2016). *EU-level instruments on water reuse : final report to support the Commission's impact assessment*. Luxembourg: Publications Office of the European Union. doi: 10.2779/974903.
- Kleinberg, R.L., Chew, W.C. and Griffin, D.D. (1989). Noncontacting electrical conductivity sensor for remote, hostile environments. *IEEE Transactions on Instrumentation and Measurement*, 38(1), pp.22–26. doi:10.1109/19.19992.
- Klemas, V. (2012). Tracking and monitoring oil slicks using remote sensing. In: *2012 IEEE/OES Baltic International Symposium (BALTIC)*. IEEE/OES Baltic International Symposium (BALTIC). IEEE, pp.1–7.
- Laneve, G. and Luciani, R. (2015). Developing a satellite optical sensor-based automatic system for detecting and monitoring oil spills. In: *International Conference on Environment and Electrical Engineering (EEEIC)*. 15th International Conference on Environment and Electrical Engineering (EEEIC). IEEE, pp.1653–1658.
- Leal-Junior, A., Frizera-Neto, A., Marques, C. and Pontes, M. (2018). A Polymer Optical Fiber Temperature Sensor Based on Material Features. *Sensors*, 18(2), p.301. doi:10.3390/s18010301.
- Lee, A.C.K. and Maheswaran, R. (2010). The health benefits of urban green spaces: a review of the evidence. *Journal of Public Health*, 33(2), pp.212–222. doi:10.1093/pubmed/fdq068.
- Lee, E., Han, S. and Kim, H. (2013). Development of Software Sensors for Determining Total Phosphorus and Total Nitrogen in Waters. *International Journal of Environmental Research and Public Health*, 10(1), pp.219–236. doi:10.3390/ijerph10010219.
- Li, C., Ning, T., Zhang, C., Wen, X., Li, J. and Zhang, C. (2016). Liquid level and temperature sensor based on an asymmetrical fiber Mach–Zehnder interferometer combined with a fiber Bragg grating. *Optics Communications*, 372(1), pp.196–200. doi:10.1016/j.optcom.2016.04.025.
- Li, P., Cai, Y., Shen, X., Nabuzaale, S., Yin, J. and Li, J. (2014). An Accurate Detection for Dynamic Liquid Level Based on MIMO Ultrasonic Transducer Array. *IEEE Transactions on Instrumentation and Measurement*, 64(3), pp.582–595. doi:https://doi.org/10.1109/TIM.2014.2357586.

- Li, T., Winnel, M., Lin, H., Panther, J., Liu, C., O'Halloran, R., Wang, K., An, T., Wong, P.K., Zhang, S. and Zhao, H. (2017). A reliable sewage quality abnormal event monitoring system. *Water Research*, 121, pp.248–257. doi:10.1016/j.watres.2017.05.040.
- Lin, S.-S., Shen, S.-L., Zhou, A. and Xu, Y.-S. (2020). Approach based on TOPSIS and Monte Carlo simulation methods to evaluate lake eutrophication levels. *Water Research*, 187, p.116437. doi:10.1016/j.watres.2020.116437.
- Lin, W.-C., Brondum, K., Monroe, C. and Burns, M. (2017). Multifunctional Water Sensors for pH, ORP, and Conductivity Using Only Microfabricated Platinum Electrodes. *Sensors*, 17(7), p.1655. doi:10.3390/s17071655.
- Liu, S., Che, H., Smith, K. and Chen, L. (2014). Contamination event detection using multiple types of conventional water quality sensors in source water. *Environ. Sci.: Processes Impacts*, 16(8), pp.2028–2038. doi:10.1039/c4em00188e.
- Liu, S., Smith, K. and Che, H. (2015). A multivariate based event detection method and performance comparison with two baseline methods. *Water Research*, 80, pp.109–118. doi:10.1016/j.watres.2015.05.013.
- Liu, Y., Fan, P.P., Hou, G.L., Sun, J.C., Cheng, Y. and Ma, R. (2012). Rapid Determination of Organic Matter Fractions by Ozonation Chemiluminescence. *Advanced Materials Research*, 468-471, pp.2842–2848. doi:10.4028/www.scientific.net/amr.468-471.2842.
- Liu, Y., Ma, X., Shu, L., Yang, Q., Zhang, Y., Huo, Z. and Zhou, Z. (2020). Internet of Things for Noise Mapping in Smart Cities: State of the Art and Future Directions. *IEEE Network*, 34(4), pp.112–118. doi:10.1109/MNET.011.1900634.
- Lloret, J., Garcia, M., Bri, D. and Sendra, S. (2009). A Wireless Sensor Network Deployment for Rural and Forest Fire Detection and Verification. *Sensors*, 9(11), pp.8722–8747. doi:10.3390/s91108722.
- Lopes, P.R.M., Montagnolli, R.N., de Fátima Domingues, R. and Bidoia, E.D. (2010). Toxicity and Biodegradation in Sandy Soil Contaminated by Lubricant Oils. *Bulletin of Environmental Contamination and Toxicology*, 84(4), pp.454–458. doi:10.1007/s00128-010-9945-8.
- Lora-alliance (2019). *Home page / LoRa Alliance™*. [online] Lora-alliance.org. Available at: <https://lora-alliance.org/> [Accessed 30 Sep. 2021].
- Maciel, V.B.V., Yoshida, C.M.P. and Franco, T.T. (2015). Chitosan/pectin polyelectrolyte complex as a pH indicator. *Carbohydrate Polymers*, 132, pp.537–545. doi:10.1016/j.carbpol.2015.06.047.

- MacLean, A., Moran, C., Johnstone, W., Culshaw, B., Marsh, D. and Parker, P. (2003). Detection of hydrocarbon fuel spills using a distributed fibre optic sensor. *Sensors and Actuators A: Physical*, 109(1-2), pp.60–67. doi:10.1016/j.sna.2003.09.007.
- Maksymiuk, K., Stelmach, E. and Michalska, A. (2020). Unintended Changes of Ion-Selective Membranes Composition—Origin and Effect on Analytical Performance. *Membranes*, 10(10), p.266. doi:10.3390/membranes10100266.
- Mamat, H., Ibrahim, B.H. and Sulong, M.P. (2020). Network Topology Comparison for Internet Communication and IoT Connectivity. In: *2019 IEEE Conference on Open Systems (ICOS)*. 2019 IEEE Conference on Open Systems (ICOS). IEEE. doi: 10.1109/ICOS47562.2019.8975702 [Accessed 27 Oct. 2022].
- Mannina, G. and Viviani, G. (2009). Separate and combined sewer systems: a long-term modelling approach. *Water Science and Technology*, 60(3), pp.555–565. doi:10.2166/wst.2009.376.
- Marcos Von Sperling (2007). 2. Wastewater characteristics. In: *Wastewater characteristics, treatment and disposal*. [online] London ; New York: Iwa Pub. Available at: <https://library.oapen.org/viewer/web/viewer.html?file=/bitstream/handle/20.500.12657/31053/640137.pdf?sequence=1&isAllowed=y> [Accessed 7 Mar. 2022].
- Martín, M., Hernández-Crespo, C., Andrés-Doménech, I. and Benedito-Durá, V. (2020). Fifty years of eutrophication in the Albufera lake (Valencia, Spain): Causes, evolution and remediation strategies. *Ecological Engineering*, 155, p.105932. doi:10.1016/j.ecoleng.2020.105932.
- McCarty, P.L. (2018). What is the Best Biological Process for Nitrogen Removal: When and Why? *Environmental Science & Technology*, 52(7), pp.3835–3841. doi:10.1021/acs.est.7b05832.
- McCue, R.P., Walsh, J.E., Walsh, F. and Regan, F. (2006). Modular fibre optic sensor for the detection of hydrocarbons in water. *Sensors and Actuators B: Chemical*, 114(1), pp.438–444. doi:10.1016/j.snb.2005.04.048.
- Mehmood, A., Lv, Z., Lloret, J. and Umar, M.M. (2020). ELDC: An Artificial Neural Network Based Energy-Efficient and Robust Routing Scheme for Pollution Monitoring in WSNs. *IEEE Transactions on Emerging Topics in Computing*, 8(1), pp.106–114. doi:10.1109/tetc.2017.2671847.
- Mekonnen, M.M. and Hoekstra, A.Y. (2016). Four billion people facing severe water scarcity. *Science Advances*, 2(2), p.e1500323. doi:10.1126/sciadv.1500323.
- Miček, J., Karpiš, O., Olešňaniková, V. and Kochláň, M. (2016). Monitoring of water level based on acoustic emissions. In: *2015 IEEE Symposium on Computers and Communication*

- (ISCC). IEEE Symposium on Computers and Communication (ISCC). IEEE. doi: 10.1109/ISCC.2015.7405515 [Accessed 19 Sep. 2022].
- Michailovsky, C.I., McEnnis, S., Berry, P.A.M., Smith, R. and Bauer-Gottwein, P. (2012). River monitoring from satellite radar altimetry in the Zambezi River basin. *Hydrology and Earth System Sciences*, 16(7), pp.2181–2192. doi:10.5194/hess-16-2181-2012.
- Microsoft (2021). *Overview of Azure IoT device types*. [online] docs.microsoft.com. Available at: <https://docs.microsoft.com/en-us/azure/iot-develop/concepts-iot-device-types> [Accessed 13 Aug. 2022].
- Microsoft (2022). *Define and solve a problem by using Solver*. [online] support.microsoft.com. Available at: <https://support.microsoft.com/en-us/office/define-and-solve-a-problem-by-using-solver-5d1a388f-079d-43ac-a7eb-f63e45925040> [Accessed 18 Feb. 2022].
- Mikosz, J. (2014). Determination of permissible industrial pollution load at a municipal wastewater treatment plant. *International Journal of Environmental Science and Technology*, 12(3), pp.827–836. doi:10.1007/s13762-013-0472-0.
- Mirosław Jonasz and Fournier, G.R. (2007). *Light scattering by particles in water : theoretical and experimental foundations*. 1st Edition ed. London: Academic Press.
- Moo, Y.C., Matjafri, M.Z., Lim, H.S. and Tan, C.H. (2016). New development of optical fibre sensor for determination of nitrate and nitrite in water. *Optik*, 127(3), pp.1312–1319. doi:10.1016/j.ijleo.2015.09.072.
- Moreira, N.A. and Bondelind, M. (2016). Safe drinking water and waterborne outbreaks. *Journal of Water and Health*, 15(1), pp.83–96. doi:10.2166/wh.2016.103.
- Morton, J., Havens, N., Mugweru, A. and Wanekaya, Adam K. (2009). Detection of Trace Heavy Metal Ions Using Carbon Nanotube- Modified Electrodes. *Electroanalysis*, 21(14), pp.1597–1603. doi:10.1002/elan.200904588.
- Moufid, M., Hofmann, M., El Bari, N., Tiebe, C., Bartholmai, M. and Bouchikhi, B. (2021). Wastewater monitoring by means of e-nose, VE-tongue, TD-GC-MS, and SPME-GC-MS. *Talanta*, 221, p.121450. doi:10.1016/j.talanta.2020.121450.
- Mousavi, S.A. and Khodadoost, F. (2019). Effects of detergents on natural ecosystems and wastewater treatment processes: a review. *Environmental Science and Pollution Research*, 26(26), pp.26439–26448. doi:10.1007/s11356-019-05802-x.
- Murphy, K., Heery, B., Sullivan, T., Zhang, D., Paludetti, L., Lau, K.T., Diamond, D., Costa, E., O'Connor, N. and Regan, F. (2015). A low-cost autonomous optical sensor for water quality monitoring. *Talanta*, 132, pp.520–527. doi:10.1016/j.talanta.2014.09.045.

- Naja, G.M. and Volesky, B. (2013). Sewage of Tripoli: a review of the current situation and of the future planning. *International Journal of Environmental Technology and Management*, 16(4), p.312. doi:10.1504/ijetm.2013.054879.
- Namour, Ph. and Jaffrezic-Renault, N. (2010). Sensors for measuring biodegradable and total organic matter in water. *TrAC Trends in Analytical Chemistry*, 29(8), pp.848–857. doi:10.1016/j.trac.2010.04.013.
- NASA (2022). *Using GPM Data for Water Resources, Agricultural Forecasting & Food Security | NASA Global Precipitation Measurement Mission*. [online] gpm.nasa.gov. Available at: <https://gpm.nasa.gov/applications/water> [Accessed 22 Feb. 2022].
- Neirotti, P., De Marco, A., Cagliano, A.C., Mangano, G. and Scorrano, F. (2014). Current trends in Smart City initiatives: Some stylised facts. *Cities*, 38, pp.25–36. doi:10.1016/j.cities.2013.12.010.
- Nezhad, M.M., Groppi, D., Laneve, G., Marzialetti, P. and Piras, G. (2018). Oil spill detection analysing ‘Sentinel 2’ satellite images: A Persian Gulf case study. In: *Proceedings of the 3rd World Congress on Civil, Structural, and Environmental Engineering*. 3rd World Congress on Civil, Structural, and Environmental Engineering (CSEE’18). Avestia.
- Nhapi, I. and Tirivarombo, S. (2004). Sewage discharges and nutrient levels in Marimba River, Zimbabwe. *Water SA*, 30(1), pp.107–113. doi:10.4314/wsa.v30i1.5033.
- Nienhuis, J., de Haan, C., Langeveld, J., Klootwijk, M. and Clemens, F. (2013). Assessment of detection limits of fiber-optic distributed temperature sensing for detection of illicit connections. *Water Science and Technology*, 67(12), pp.2712–2718. doi:10.2166/wst.2013.176.
- NodeMcu (2014). *NodeMcu -- An open-source firmware based on ESP8266 wifi-soc*. [online] [Nodemcu.com](http://www.nodemcu.com). Available at: http://www.nodemcu.com/index_en.html [Accessed 15 Feb. 2018].
- Nsenga Kumwimba, M., Meng, F., Iseyemi, O., Moore, M.T., Zhu, B., Tao, W., Liang, T.J. and Ilunga, L. (2018). Removal of non-point source pollutants from domestic sewage and agricultural runoff by vegetated drainage ditches (VDDs): Design, mechanism, management strategies, and future directions. *Science of The Total Environment*, 639, pp.742–759. doi:10.1016/j.scitotenv.2018.05.184.
- Núñez, L., Cetó, X., Pividori, M.I., Zanoni, M.V.B. and del Valle, M. (2013). Development and application of an electronic tongue for detection and monitoring of nitrate, nitrite and ammonium levels in waters. *Microchemical Journal*, 110, pp.273–279. doi:10.1016/j.microc.2013.04.018.

- Oconomowoc (2012). *Treatment Steps / City of Oconomowoc, WI - Official Website*. [online] Oconomowoc-wi.gov. Available at: <https://www.oconomowoc-wi.gov/270/Treatment-Steps> [Accessed 1 Mar. 2022].
- Oh, S. and Lee, M. (2012). Oil spill detection sensor using artificial illumination with blue LEDs. In: *2012 IEEE Sensors*. IEEE SENSORS 2012. Taiwan: IEEE. doi:10.1109/icsens.2012.6411264.
- ONU (2015). *Wastewater Management: A UN-Water Analytical Brief*. [online] UNWATER. ONU. Available at: <https://www.unwater.org/publications/wastewater-management-un-water-analytical-brief/> [Accessed 21 Feb. 2022].
- Pallarès, A., Fischer, S., France, X., Pons, M.N. and Schmitt, P. (2016). Acoustic turbidity as online monitoring tool for rivers and sewer networks. *Flow Measurement and Instrumentation*, 48, pp.118–123. doi:10.1016/j.flowmeasinst.2015.07.010.
- Panasiuk, O., Hedström, A., Marsalek, J., Ashley, R.M. and Viklander, M. (2015). Contamination of stormwater by wastewater: A review of detection methods. *Journal of Environmental Management*, 152, pp.241–250. doi:10.1016/j.jenvman.2015.01.050.
- Parameswari, M. and Moses, M.B. (2019). Efficient analysis of water quality measurement reporting system using IOT based system in WSN. *Cluster Computing*, 22(5). doi:10.1007/s10586-017-1581-1.
- Parra Boronat, M. (2019). *Design and development of a low-cost soil moisture sensor based on solenoid coils*. [Final degree project] *riunet.upv.es*. Available at: <http://hdl.handle.net/10251/130868> [Accessed 31 Oct. 2022].
- Parra, L. (2018). *Study of requirements and design of sensors for monitoring water quality and feeding process in fish farms and other environments*. [PhD] Available at: <https://doi.org/10.4995/Thesis/10251/106369> [Accessed 27 Jun. 2022].
- Parra, L., Lloret, G., Lloret, J. and Rodilla, M. (2018a). Physical Sensors for Precision Aquaculture: A Review. *IEEE Sensors Journal*, 18(10), pp.3915–3923. doi:10.1109/jsen.2018.2817158.
- Parra, L., Rocher, J., Escrivá, J. and Lloret, J. (2018b). Design and development of low cost smart turbidity sensor for water quality monitoring in fish farms. *Aquacultural Engineering*, 81, pp.10–18. doi:10.1016/j.aquaeng.2018.01.004.
- Parra, L., Rocher, J., García, L., Lloret, J., Tomás, J., Romero, O., Rodilla, M., Falco, S., Sebastiá, M.T., Mengual, J., González, J.A. and Roig, B. (2018c). Design of a WSN for smart irrigation in citrus plots with fault-tolerance and energy-saving algorithms. *Network Protocols and Algorithms*, 10(2), p.95. doi:10.5296/npa.v10i2.13205.

- Parra, L., Sendra, S., Lloret, J. and Bosch, I. (2015a). Development of a Conductivity Sensor for Monitoring Groundwater Resources to Optimize Water Management in Smart City Environments. *Sensors*, 15(9), pp.20990–21015. doi:10.3390/s150920990.
- Parra, L., Sendra, S., Lloret, J. and Mendoza, J. (2015b). Low-cost optic sensor for hydrocarbon detection in open oceans. In: *SIXTH INTERNATIONAL WORKSHOP ON MARINE TECHNOLOGY, Martech 201*. [online] SIXTH INTERNATIONAL WORKSHOP ON MARINE TECHNOLOGY, Martech 201. UPC, pp.85–88.
- Parra, L., Sendra, S., Lloret, J. and Rodrigues, J.J.P.C. (2014). Low cost wireless sensor network for salinity monitoring in mangrove forests. In: *IEEE SENSORS 2014*. IEEE SENSORS, 2014. IEEE. doi:10.1109/icsens.2014.6984949.
- Parra, M., Parra, L., Rocher, J., Lloret, J., Mauri, P.V. and Llinares, J.V. (2020). A Novel Low-Cost Conductivity Based Soil Moisture Sensor. In: M. Ezziyyani, ed., *Advanced Intelligent Systems for Sustainable Development (AI2SD'2019)*. Cham, Switzerland: Springer International Publishing, pp.27–35. doi:10.1007/978-3-030-36664-3_4.
- Pavanelli, D. and Bigi, A. (2005). Indirect Methods to Estimate Suspended Sediment Concentration: Reliability and Relationship of Turbidity and Settleable Solids. *Biosystems Engineering*, 90(1), pp.75–83. doi:10.1016/j.biosystemseng.2004.09.001.
- Pereda, O., Solagaistua, L., Atristain, M., de Guzmán, I., Larrañaga, A., von Schiller, D. and Elozegi, A. (2020). Impact of wastewater effluent pollution on stream functioning: A whole-ecosystem manipulation experiment. *Environmental Pollution*, 258, p.113719. doi:10.1016/j.envpol.2019.113719.
- Perera, C., Zaslavsky, A., Christen, P. and Georgakopoulos, D. (2013). Sensing as a service model for smart cities supported by Internet of Things. *Transactions on Emerging Telecommunications Technologies*, 25(1), pp.81–93. doi:10.1002/ett.2704.
- Péron, O., Rinnert, E., Lehaitre, M., Crassous, P. and Compère, C. (2009). Detection of polycyclic aromatic hydrocarbon (PAH) compounds in artificial sea-water using surface-enhanced Raman scattering (SERS). *Talanta*, 79(2), pp.199–204. doi:10.1016/j.talanta.2009.03.043.
- Peterson, S.H., Roberts, D.A., Beland, M., Kokaly, R.F. and Ustin, S.L. (2015). Oil detection in the coastal marshes of Louisiana using MESMA applied to band subsets of AVIRIS data. *Remote Sensing of Environment*, 159, pp.222–231. doi:10.1016/j.rse.2014.12.009.
- Philippart, C.J.M., Salama, Mhd.S., Kromkamp, J.C., van der Woerd, H.J., Zuur, A.F. and Cadée, G.C. (2013). Four decades of variability in turbidity in the western Wadden Sea as derived from corrected Secchi disk readings. *Journal of Sea Research*, 82, pp.67–79. doi:10.1016/j.seares.2012.07.005.

- Pisano, A., Bignami, F. and Santoleri, R. (2015). Oil Spill Detection in Glint-Contaminated Near-Infrared MODIS Imagery. *Remote Sensing*, 7(1), pp.1112–1134. doi:10.3390/rs70101112.
- Preisner, M., Neverova-Dziopak, E. and Kowalewski, Z. (2020). Analysis of eutrophication potential of municipal wastewater. *Water Science and Technology*, 81(9), pp.1994–2003. doi:10.2166/wst.2020.254.
- Prerana, Shenoy, M.R., Pal, B.P. and Gupta, B.D. (2012). Design, Analysis, and Realization of a Turbidity Sensor Based on Collection of Scattered Light by a Fiber-Optic Probe. *IEEE Sensors Journal*, 12(1), pp.44–50. doi:10.1109/jsen.2011.2128306.
- Promax (2019). *FUENTES DE ALIMENTACIÓN FA-363B, FA-376, FA-662B, FA-665*. [online] Promax. Available at: <https://www.promax.es/downloads/products/esp/FA-xxx.pdf> [Accessed 6 Nov. 2022].
- Purschke, K., Zoell, C., Leonhardt, J., Weber, M. and Schmidt, T.C. (2020). Identification of unknowns in industrial wastewater using offline 2D chromatography and non-target screening. *Science of The Total Environment*, 706, p.135835. doi:10.1016/j.scitotenv.2019.135835.
- Ramírez-Miquet, E., Perchoux, J., Loubière, K., Tronche, C., Prat, L. and Sotolongo-Costa, O. (2016). Optical Feedback Interferometry for Velocity Measurement of Parallel Liquid-Liquid Flows in a Microchannel. *Sensors*, 16(8), p.1233. doi:10.3390/s16081233.
- Ramos, H., Gurriana, L., Postolache, O., Pereira, M. and Girão, P. (2005). Development and characterization of a conductivity cell for water quality monitoring. In: *IEEE 3rd Int. Conf. Syst. Signals Devices (SSD)*. International Multi-Conference on Systems, Signals & Devices (SSD). IEEE.
- Rathee, D.S., Ahuja, K. and Hailu, T. (2019). Role of Electronics Devices for E-Health in Smart Cities. In: D. Singh Rathee, K. Ahuja and T. Hailu, eds., *Practice, Progress, and Proficiency in Sustainability*. IGI global, pp.212–233. doi:10.4018/978-1-5225-8085-0.ch009.
- Rawat, P., Singh, K.D., Chaouchi, H. and Bonnin, J.M. (2013). Wireless sensor networks: a survey on recent developments and potential synergies. *The Journal of Supercomputing*, 68(1), pp.1–48. doi:10.1007/s11227-013-1021-9.
- Reverter, F., Li, X. and Meijer, G.C.M. (2007). Liquid-level measurement system based on a remote grounded capacitive sensor. *Sensors and Actuators A: Physical*, 138(1), pp.1–8. doi:10.1016/j.sna.2007.04.027.

- Rice, E.W., Eaton, A.D. and Baird, R. (2017). *Standard methods for the examination of water and wastewater*. 23rd ed. Washington, Dc: American Public Health Association, American Water Works Association, Water Environment Federation.
- Rocher J., Aldegheishem A., Alrajeh N., and J. Lloret J, "Develop an Optical Sensor to Detect Pollution Incidents in Sewerage," in *IEEE Sensors Journal*, 2022, doi: 10.1109/JSEN.2022.3219931.
- Rocher, J., Basterrechea, D.A., Fawzy, M., Lloret, J. and Omar, M.Y. (2020). Sensors and Biosorption for Better Reuse of Wastewater. In: E. M. , ed., *Advances in Intelligent Systems and Computing*. Cham: Springer, pp.321–330. doi:10.1007/978-3-030-36664-3_36.
- Rocher, J., Basterrechea, D.A., Parra, L. and Lloret, J. (2019a). A New Conductivity Sensor for Monitoring the Fertigation in Smart Irrigation Systems. In: *Advances in Intelligent Systems and Computing*. Springer, pp.136–144. doi:10.1007/978-3-030-24097-4_17.
- Rocher, J., Garcia-Navas, J.L., Romero, O. and Lloret, J. (2019b). A WSN-based Monitoring System to Control Sewerage. In: *2019 Sixth International Conference on Internet of Things: Systems, Management and Security (IOTSMS)*. 2019 Sixth International Conference on Internet of Things: Systems, Management and Security (IOTSMS). IEEE. doi:10.1109/iotsms48152.2019.8939269.
- Rocher, J., Parra, L., Jimenez, J.M., Lloret, J. and Basterrechea, D.A. (2021a). Development of a Low-Cost Optical Sensor to Detect Eutrophication in Irrigation Reservoirs. *Sensors*, 21(22). doi:10.3390/s21227637.
- Rocher, J., Parra, L., Lloret, J. and Mengual, J. (2018a). An Inductive Sensor for Water Level Monitoring in Tubes for Water Grids. In: *2018 IEEE/ACS 15th International Conference on Computer Systems and Applications (AICCSA)*. 2018 IEEE/ACS 15th International Conference on Computer Systems and Applications (AICCSA). IEEE. doi:10.1109/aiccsa.2018.8612845.
- Rocher, J., Parra, M., Parra, L., Sendra, S., Lloret, J. and Mengual, J. (2021b). A Low-Cost Sensor for Detecting Illicit Discharge in Sewerage. *Journal of Sensors*, 2021, pp.1–16. doi:10.1155/2021/6650157.
- Rocher, J., Rego, A., Lloret, J. and Oliveira, L.M.L. (2022). Use of wireless sensor network system based on water level, rain, conductivity, oil and turbidity sensors to monitor the storm sewerage. *IET Wireless Sensor Systems*, 12((3-4)), pp.103–121. doi:10.1049/wss2.12040.
- Rocher, J., Sendra, S., Parra, L., Lloret, J. and Shu, L. (2018b). Low Cost Sensor to Measure Solid Concentrations in Wastewater. In: *IECON 2018 - 44th Annual Conference of the IEEE Industrial Electronics Society*. IEEE. doi:10.1109/iecon.2018.8591149.

- Rocher, J., Taha, M., Parra, L. and Lloret, J. (2018c). IoT Sensor to Detect Fraudulent Use of Dyed Fuels in Smart Cities. In: *2018 Fifth International Conference on Internet of Things: Systems, Management and Security*. 2018 Fifth International Conference on Internet of Things: Systems, Management and Security. IEEE. doi:10.1109/iotsms.2018.8554631.
- Rony, J.H., Karim, N., Rouf, MD.A., Islam, Md.M., Uddin, J. and Begum, M. (2021). A Cost-Effective IoT Model for a Smart Sewerage Management System Using Sensors. *J*, 4(3), pp.356–366. doi:10.3390/j4030027.
- RS online (2018). *SFH 203*. [online] RS Online. Available at: <https://docs.rs-online.com/9f58/0900766b816d8a09.pdf> [Accessed 20 Aug. 2022].
- RS online (2022). *Infrared Emitting Diode, 950 nm, GaAs*. [online] RS online. Available at: <https://docs.rs-online.com/f3b6/0900766b80e22d5c.pdf> [Accessed 20 Aug. 2022].
- Saeed, M.U., Hussain, N., Sumrin, A., Shahbaz, A., Noor, S., Bilal, M., Aleya, L. and Iqbal, H.M.N. (2022). Microbial bioremediation strategies with wastewater treatment potentialities – A review. *Science of The Total Environment*, 818, p.151754. doi:10.1016/j.scitotenv.2021.151754.
- Sahoo, P.K., Panigrahy, B., Sahoo, S., Satpati, A.K., Li, D. and Bahadur, D. (2013). In situ synthesis and properties of reduced graphene oxide/Bi nanocomposites: As an electroactive material for analysis of heavy metals. *Biosensors and Bioelectronics*, 43, pp.293–296. doi:10.1016/j.bios.2012.12.031.
- Salberg, A.-B., Rudjord, O. and Solberg, A.H.S. (2014). Oil Spill Detection in Hybrid-Polarimetric SAR Images. *IEEE Transactions on Geoscience and Remote Sensing*, 52(10), pp.6521–6533. doi:10.1109/tgrs.2013.2297193.
- Sandiego, G. (2021). *Sewer Spill Statistics | Public Utilities | City of San Diego Official Website*. [online] Sandiego.gov. Available at: <https://www.sandiego.gov/public-utilities/sewer-spill-reduction/sewer-spill-statistics> [Accessed 7 Mar. 2022].
- Sartorius (2022). *Entris® II Laboratory Balances*. [online] Sartorius. Available at: <https://www.sartorius.com/en/products/weighing/laboratory-balances/entris-ii> [Accessed 18 Feb. 2022].
- Schwarz, J., Kaden, H. and Pausch, G. (2000). Development of miniaturized potentiometric nitrate- and ammonium selective electrodes for applications in water monitoring. *Fresenius' Journal of Analytical Chemistry*, 367(4), pp.396–398. doi:10.1007/s002160000367.
- See, C.H., Horoshenkov, K.V., Tait, S.J., Abd-Alhameed, R.A., Hu, Y.F., Elkhazmi, E.A. and Gardiner, J.G. (2009). A Zigbee based wireless sensor network for sewerage monitoring. In: *2009 Asia Pacific Microwave Conference*. IEEE. doi:10.1109/apmc.2009.5384245.

- Sendra Compte, S. (2013). *Deployment of Efficient Wireless Sensor Nodes for Monitoring in Rural, Indoor and Underwater Environments*. [PhD] Available at: <https://doi.org/10.4995/Thesis/10251/32279> [Accessed 27 Jun. 2022].
- Sendra, S., Parra, L., Ortuño, V. and Lloret, J. (2013). A Low Cost Turbidity Sensor Development. In: *SENSORCOMM 2013, The Seventh International Conference on Sensor Technologies and Applications*. SENSORCOMM 2013, The Seventh International Conference on Sensor Technologies and Applications. IARIA.
- Sha, K., Shi, W. and Watkins, O. (2006). Using Wireless Sensor Networks for Fire Rescue Applications: Requirements and Challenges. In: *2006 IEEE International Conference on Electro/Information Technology*. IEEE. doi:10.1109/eit.2006.252145.
- Sigfox (2017). *SIGFOX 0G TECHNOLOGY*. [online] <https://www.sigfox.com/en/what-sigfox/technology>. Available at: <https://www.sigfox.com/en> [Accessed 30 Sep. 2021].
- Silva, C.R., Conceição, C.D.C., Bonifácio, V.G., Filho, O.F. and Teixeira, M.F.S. (2008). Determination of the chemical oxygen demand (COD) using a copper electrode: a clean alternative method. *Journal of Solid State Electrochemistry*, 13(5), pp.665–669. doi:10.1007/s10008-008-0580-9.
- Simitha, K.M. and Subodh Raj, M.S. (2019). IoT and WSN Based Water Quality Monitoring System. In: *2019 3rd International conference on Electronics, Communication and Aerospace Technology (ICECA)*. 3rd International conference on Electronics, Communication and Aerospace Technology (ICECA). IEEE. doi: 10.1109/ICECA.2019.8821859.
- Siregar, B., Menen, K., Efendi, S., Andayani, U. and Fahmi, F. (2018). Monitoring quality standard of waste water using wireless sensor network technology for smart environment. In: *2017 International Conference on ICT For Smart Society (ICISS)*. International Conference on ICT For Smart Society (ICISS). IEEE. doi: 10.1109/ICTSS.2017.8288865.
- Song, Q., Luan, F., Shi, Z., Li, T. and Wang, M. (2020). Design of Turbidity Remote Monitoring System Based on FX-11A Optical Fiber Sensor. In: *2020 Prognostics and Health Management Conference (PHM-Besançon)*. 2020 Prognostics and Health Management Conference (PHM-Besançon). IEEE. doi: 10.1109/PHM-Besancon49106.2020.00056.
- Sòria-Perpinyà, X., Miracle, M.R., Soria, J., Delegido, J. and Vicente, E. (2018). Remote sensing application for the study of rapid flushing to remediate eutrophication in shallow lagoons (Albufera of Valencia). *Hydrobiologia*, 829(1), pp.125–132. doi:10.1007/s10750-018-3741-6.

- Srivastava, H. and Singh, T.P. (2010). Assessment and development of algorithms to detection of oil spills using MODIS data. *Journal of the Indian Society of Remote Sensing*, 38(1), pp.161–167. doi:10.1007/s12524-010-0007-9.
- Statgraphics, S. (2022). *STATGRAPHICS | Data Analysis Solutions*. [online] www.statgraphics.com. Available at: <https://www.statgraphics.com/> [Accessed 18 Feb. 2022].
- Tang, I.H., Sundari, R., Lintang, H.O. and Yuliati, L. (2016). Detection of nitrite and nitrate ions in water by graphene oxide as a potential fluorescence sensor. In: *IOP Conference Series: Materials Science and Engineering*. IOP. doi:10.1088/1757-899x/107/1/012027.
- Taravat, A. and Del Frate, F. (2012). Development of band ratioing algorithms and neural networks to detection of oil spills using Landsat ETM+ data. *EURASIP Journal on Advances in Signal Processing*, 2012(1). doi:10.1186/1687-6180-2012-107.
- Taylor, E., Bonner, J., Nelson, R., Fuller, C., Kirkey, W. and Cappelli, S. (2015). Development of an in-situ total phosphorus analyzer. In: *OCEANS 2015 - MTS/IEEE Washington*. IEEE. doi:10.23919/oceans.2015.7404384.
- TBS1000. (2022). [online] Available at: <https://www.farnell.com/datasheets/2053056.pdf> [Accessed 18 Feb. 2022].
- Tchounwou, P.B., Yedjou, C.G., Patlolla, A.K. and Sutton, D.J. (2012). Heavy Metal Toxicity and the Environment. In: *Molecular, Clinical and Environmental Toxicology Volume 3: Environmental Toxicology*. Springer, pp.133–164. doi:10.1007/978-3-7643-8340-4_6.
- Tektronix (2022a). *Arbitrary/Function Generator AFG1000 Series Datasheet*. [online] Available at: <https://www.farnell.com/datasheets/2239457.pdf> [Accessed 19 Jan. 2022].
- Tektronix (2022b). *Digital Storage Oscilloscopes TBS1000 Series Datasheet*. [online] Available at: <https://www.farnell.com/datasheets/2053056.pdf> [Accessed 11 Mar. 2022].
- TENMA (2022). *Digital Multimeter*. [online] Available at: http://www.farnell.com/datasheets/1993717.pdf?_ga=2.177994341.1755120939.1591014303-1928794037.1591014303 [Accessed 18 Feb. 2022].
- Toronto Water (2018). *Sewers and Water Supply By-laws 2018 Compliance and Enforcement Annual Report and Report on the Lavender Creek Water Quality Assessment*. [online] Toronto. Available at: <https://www.toronto.ca/legdocs/mmis/2019/ie/bgrd/backgroundfile-140395.pdf> [Accessed 21 Feb. 2022].
- Trygar, R. (2009). *NITROGEN CONTROL IN WASTEWATER TREATMENT PLANTS Second Edition*. [online] University of Florida TREEO Center. Available at: <https://treeo.ufl.edu/media/treeoufledu/waterwastewater/student-resources/Nitrogen-control-in--wastewater-treatment-plants-v4.pdf>.

- UK government (2020). *Water and sewerage companies in England: environmental performance report for 2019*. [online] gov.uk. Environment Agency. Available at: <https://www.gov.uk/government/publications/water-and-sewerage-companies-in-england-environmental-performance-report-2019/water-and-sewerage-companies-in-england-environmental-performance-report-for-2019> [Accessed 2 Mar. 2022].
- Ukil, A., Braendle, H. and Krippner, P. (2012). Distributed Temperature Sensing: Review of Technology and Applications. *IEEE Sensors Journal*, 12(5), pp.885–892. doi:10.1109/jsen.2011.2162060.
- Ullah, N., Mansha, M., Khan, I. and Qurashi, A. (2018). Nanomaterial-based optical chemical sensors for the detection of heavy metals in water: Recent advances and challenges. *TrAC Trends in Analytical Chemistry*, 100, pp.155–166. doi:10.1016/j.trac.2018.01.002.
- UNESCO (2020). *World Water Development Report 2020*. [online] UNESCO. Paris (France). Available at: <https://unesdoc.unesco.org/ark:/48223/pf0000372985/PDF/372985eng.pdf.multi> [Accessed 21 Feb. 2022].
- Ungureanu, N., Vlăduț, V. and Voicu, G. (2020). Water Scarcity and Wastewater Reuse in Crop Irrigation. *Sustainability*, 12(21), p.9055. doi:10.3390/su12219055.
- Van De Werfhorst, L.C., Murray, J.L.S., Reynolds, S., Reynolds, K. and Holden, P.A. (2014). Canine Scent Detection and Microbial Source Tracking of Human Waste Contamination in Storm Drains. *Water Environment Research*, 86(6), pp.550–558. doi:10.2175/106143013x13807328848496.
- Verstraete, W. and Vlaeminck, S.E. (2011). ZeroWasteWater: short-cycling of wastewater resources for sustainable cities of the future. *International Journal of Sustainable Development & World Ecology*, 18(3), pp.253–264. doi:10.1080/13504509.2011.570804.
- Vieira, R.H. and Volesky, B. (2000). Biosorption: a solution to pollution? *International Microbiology: The Official Journal of the Spanish Society for Microbiology*, 3(1), pp.17–24.
- Völker, M., Eberheim, A. and Pechstein, T. (2008). *Inductive Conductivity Sensor*.
- Vosse, M., Schilperoort, R., de Haan, C., Nienhuis, J., Tirion, M. and Langeveld, J. (2013). Processing of DTS monitoring results: automated detection of illicit connections. *Water Practice and Technology*, 8(3-4), pp.375–381. doi:10.2166/wpt.2013.037.
- Wada, Y., van Beek, L.P.H., van Kempen, C.M., Reckman, J.W.T.M., Vasak, S. and Bierkens, M.F.P. (2010). Global depletion of groundwater resources. *Geophysical Research Letters*, 37(20), doi:10.1029/2010gl044571.

- Wahyuni, R.T., Wijaya, Y.P. and Nurmalasari, D. (2014). Design of Wireless Sensor Network for Drainage Monitoring System. *Innovative Systems Design and Engineering*, 5(5), pp.6–13.
- Wang, F., Tong, J., Li, Y., Bian, C., Sun, J. and Xia, S. (2014). An Electrochemical Microsensor Based on a AuNPs-Modified Microband Array Electrode for Phosphate Determination in Fresh Water Samples. *Sensors*, 14(12), pp.24472–24482. doi:10.3390/s141224472.
- Wang, J., Wu, C., Wu, K., Cheng, Q. and Zhou, Y. (2012). Electrochemical sensing chemical oxygen demand based on the catalytic activity of cobalt oxide film. *Analytica Chimica Acta*, 736, pp.55–61. doi:10.1016/j.aca.2012.05.046.
- Wang, J., Zhang, Y., Wang, Y., Xu, R., Sun, Z. and Jie, Z. (2010). An innovative reactor-type biosensor for BOD rapid measurement. *Biosensors and Bioelectronics*, 25(7), pp.1705–1709. doi:10.1016/j.bios.2009.12.018.
- Wang, Y., Rajib, S.M.S.M., Collins, C. and Grieve, B. (2018). Low-Cost Turbidity Sensor for Low-Power Wireless Monitoring of Fresh-Water Courses. *IEEE Sensors Journal*, 18(11), pp.4689–4696. doi:10.1109/jsen.2018.2826778.
- Warwick, C., Guerreiro, A. and Soares, A. (2013). Sensing and analysis of soluble phosphates in environmental samples: A review. *Biosensors and Bioelectronics*, 41, pp.1–11. doi:10.1016/j.bios.2012.07.012.
- Wear, S.L. and Thurber, R.V. (2015). Sewage pollution: mitigation is key for coral reef stewardship. *Annals of the New York Academy of Sciences*, 1355(1), pp.15–30. doi:10.1111/nyas.12785.
- Werner, A.D., Bakker, M., Post, V.E.A., Vandenbohede, A., Lu, C., Ataie-Ashtiani, B., Simmons, C.T. and Barry, D.A. (2013). Seawater intrusion processes, investigation and management: Recent advances and future challenges. *Advances in Water Resources*, 51, pp.3–26. doi:10.1016/j.advwatres.2012.03.004.
- Wood, R.T., Bannazadeh, A., Nguyen, N.Q. and Bushnell, L.G. (2010). A salinity sensor for long-term data collection in estuary studies. In: *OCEANS 2010 MTS/IEEE SEATTLE*. OCEANS 2010 MTS/IEEE SEATTLE. IEEE. doi: 10.1109/OCEANS.2010.5664602.
- Wu, X., Zheng, Y., Wu, B., Tian, Y., Han, F. and Zheng, C. (2016). Optimizing conjunctive use of surface water and groundwater for irrigation to address human-nature water conflicts: A surrogate modeling approach. *Agricultural Water Management*, 163, pp.380–392. doi:10.1016/j.agwat.2015.08.022.
- Xu, Z., Yin, H. and Li, H. (2014). Quantification of non-stormwater flow entries into storm drains using a water balance approach. *Science of The Total Environment*, 487, pp.381–388. doi:10.1016/j.scitotenv.2014.04.035.

- Xue, K., Zhang, Y., Duan, H., Ma, R., Loisel, S. and Zhang, M. (2015). A Remote Sensing Approach to Estimate Vertical Profile Classes of Phytoplankton in a Eutrophic Lake. *Remote Sensing*, 7(11), pp.14403–14427. doi:10.3390/rs71114403.
- Yang, L., Shin, H.-S. and Hur, J. (2014). Estimating the Concentration and Biodegradability of Organic Matter in 22 Wastewater Treatment Plants Using Fluorescence Excitation Emission Matrices and Parallel Factor Analysis. *Sensors*, 14(1), pp.1771–1786. doi:10.3390/s140101771.
- Yao, J., Wang, G., Xue, B., Wang, P., Hao, F., Xie, G. and Peng, Y. (2019). Assessment of lake eutrophication using a novel multidimensional similarity cloud model. *Journal of Environmental Management*, 248, p.109259. doi:10.1016/j.jenvman.2019.109259.
- Yeh, P., Yeh, N., Lee, C.-H. and Ding, T.-J. (2017). Applications of LEDs in optical sensors and chemical sensing device for detection of biochemicals, heavy metals, and environmental nutrients. *Renewable and Sustainable Energy Reviews*, 75, pp.461–468. doi:10.1016/j.rser.2016.11.011.
- Yeoh, S., Matjafri, M.Z., Mutter, K.N. and Oglat, A.A. (2019). Plastic fiber evanescent sensor in measurement of turbidity. *Sensors and Actuators A: Physical*, 285, pp.1–7. doi:10.1016/j.sna.2018.10.042.
- Yin, H., Xie, M., Zhang, L., Huang, J., Xu, Z., Li, H., Jiang, R., Wang, R. and Zeng, X. (2019). Identification of sewage markers to indicate sources of contamination: Low cost options for misconnected non-stormwater source tracking in stormwater systems. *Science of The Total Environment*, 648, pp.125–134. doi:10.1016/j.scitotenv.2018.07.448.
- Yin, W., Peyton, A.J., Zysko, G. and Denno, R. (2008). Simultaneous Noncontact Measurement of Water Level and Conductivity. *IEEE Transactions on Instrumentation and Measurement*, 57(11), pp.2665–2669. doi:10.1109/tim.2008.926054.
- Zgheib, S., Moillon, R. and Chebbo, G. (2012). Priority pollutants in urban stormwater: Part 1 – Case of separate storm sewers. *Water Research*, 46(20), pp.6683–6692. doi:10.1016/j.watres.2011.12.012.
- Zhang, Q. ed., (2016). *Precision agriculture technology for crop farming*. Boca Raton, Florida: Taylor & Francis. doi: 10.1201/b19336
- Zhang, X., Lu, S. and Chen, X. (2014). A visual pH sensing film using natural dyes from *Bauhinia blakeana* Dunn. *Sensors and Actuators B: Chemical*, 198, pp.268–273. doi:10.1016/j.snb.2014.02.094.
- Zhao, Y., Zhang, X., Zhao, T., Yuan, B. and Zhang, S. (2009). Optical Salinity Sensor System Based on Fiber-Optic Array. *IEEE Sensors Journal*, 9(9), pp.1148–1153. doi:10.1109/jsen.2009.2026527.

Zhou, W., Wang, S. and Zhou, Y. (2004). Determination of chlorophyll a content of the Lake Taihu, china using Landsat-5 TM data. In: *In IGARSS 2004. 2004 IEEE International Geoscience and Remote Sensing Symposium*. IEEE International Geoscience and Remote Sensing Symposium. IEEE.